

Late Pleistocene and Holocene sediments around South  
Georgia:

Archives for climate-induced signals in sub-Antarctica since  
the last glaciation

Dissertation

zur Erlangung des

Doktorgrades der Naturwissenschaften (Dr. rer. nat.)

am Fachbereich Geowissenschaften

der Universität Bremen

vorgelegt von

Nina-Marie Lešić

Bremen, August 2023



**Datum der mündlichen Prüfung:**

Freitag, 20.10.2023

**Gutachtende:**

Prof. Dr. Gerhard Bohrmann  
Universität Bremen  
MARUM – Zentrum für Marine Umweltwissenschaften  
Klagenfurter Straße 2-4  
28359 Bremen

Apl. Prof. Dr. Bernhard Diekmann  
Alfred-Wegener-Institut, Helmholtz-Zentrum für Polar- und Meeresforschung, Potsdam  
Telegrafenberg A45  
Wissenschaftspark Albert Einstein  
14473 Potsdam



## Preface

And there it was. South Georgia. After three years of thinking about it in most of my wake hours, I finally saw the island peeking through the misty and rainy weather. Even “joy” cannot accurately describe what I felt on the morning of November 26<sup>th</sup>, 2022, when the island was finally in sight. I began to laugh and jump on deck and some of the seafarers watched me amused and maybe a little bewildered. After three years of dedicated work, the hardships of social isolation during the pandemic and its consequences for my dissertation, and some doubt whether it was the right decision to join the expedition at the very end of my PhD, I remembered what had driven me to begin my PhD journey. Following our natural curiosity to understand nature and its complexity. The adventure of experiencing remote and harsh environments. The community of scientists, working together to achieve their goals. Seeing this island with my own eyes, going on land there, communicating face-to-face with scientists, who investigate the same areas, was the most beautiful experience and gift and will stay with me as much as the memories of countless days in front of the computer, unravelling South Georgia’s secrets from afar in my office in (the also mostly rainy) Bremen.

This PhD thesis was written at the Faculty of Geosciences at the University of Bremen in Germany and the Alfred Wegener Institute, Helmholtz Centre for Polar and Marine Research, in Bremerhaven and funded by the “Deutsche Forschungsgemeinschaft (DFG)” in the framework of the priority program SPP 1158 "Antarctic Research with comparative investigations in Arctic ice areas" with the grants BO 1049/23-1, KU 683/18-1 and DO 705/4-1. The work on this dissertation has been carried out from January 2020 until the end of August 2023 and relies on data from the South Georgia continental shelf, which were acquired during the expeditions PS81, M134, PS119 and PS133/2 (Bohrmann, 2013; Bohrmann et al., 2017; Bohrmann, 2019; Kasten, 2023). In eight chapters, including four manuscripts, already published, submitted or in preparation for submission, this thesis shows that the cross-shelf troughs on South Georgia’s continental shelf host a variety of excellent climate archives. Combined, they recorded the last 22-24.5 thousand years with different temporal resolutions, which depend on the highly variable sedimentation rates. Island-distal locations have recorded the maximum ice extents in two different trough systems and, partly, the timing of subsequent deglaciation, while island-proximal areas have archived climate signals during the Holocene that likely influenced the oceanographic setting.

## Table of Contents

Abbreviations.....	II
Abstract.....	III
Kurzfassung.....	IV
Outline and contributions to manuscripts.....	1
1. Introduction .....	9
1.1. Phanerozoic climate cycles.....	9
1.2. South Georgia’s geographical position within Southern Hemisphere climate drivers 13	
2. Motivation and objectives of this study .....	17
3. Study area.....	19
3.1. South Georgia’s South American heritage and its geological setting .....	19
3.2. Glacial History.....	22
4. Manuscript I: Glacimarine sediments from outer Drygalski Trough, sub- Antarctic South Georgia – evidence for extensive glaciation during the Last Glacial Maximum .....	27
4.1. Introduction.....	28
4.2. Study area.....	31
4.3. Methods.....	34
4.4. Results.....	37
4.5. Discussion .....	58
4.6. Conclusion .....	72
5. Manuscript II: Glacial history of the King Haakon Trough System, sub- Antarctic South Georgia .....	75
5.1. Introduction.....	76
5.2. Physiographic Setting .....	78

5.3. Methods.....	81
5.4. Results and Interpretation.....	81
5.5. Discussion – Glacial history.....	91
5.6. Conclusion .....	104
6. Manuscript III: Spatial and temporal variability in Holocene trough-fill sediments, King Haakon Trough System, sub-Antarctic South Georgia .....	106
6.1. Introduction.....	107
6.2. Study area.....	109
6.3. Methods.....	111
6.4. Results and Interpretation.....	113
6.5. Discussion .....	122
6.6. Conclusions.....	136
7. Manuscript IV: Climate-driven Holocene sedimentation in King Haakon Trough System, sub-Antarctic South Georgia .....	139
7.1. Introduction.....	140
7.2. Study area.....	142
7.3. Methods.....	146
7.4. Results and Interpretation.....	149
7.5. Discussion .....	165
7.6. Conclusion .....	176
8. Concluding remarks and perspectives.....	178
9. Acknowledgements.....	183
10. References .....	185
11. Appendices .....	205

## Abbreviations

AB	Acoustic basement
ACC	Antarctic Circumpolar Current
ACR	Antarctic Cold Reversal
AD	Anno Domini
AF	Acoustic facies
AI	Annenkov Island
AIF	Annenkov Island Formation
APIS	Antarctic Peninsula Ice Sheet
AWI	Alfred Wegener Institute (AWI), Helmholtz Centre for Polar and Marine Research
BH	Bathymetric high
BP	Before present
bSiO <sub>2</sub>	Biogenic silica
Cal	Calibrated
CBF	Cumberland Bay Formation
CBSZ	Cooper Bay Shear Zone
CIF	Cooper Island Formation
DBD	Dry bulk density
DFC	Drygalski Fjord Complex
DFS	Drygalski Fjord System
DHF	Ducloz Head Formation
DT	Drygalski Trough
GIA	Glacial isostatic adjustment
HU	Hounsfield Unit
HTM	Holocene Thermal Maximum
IRD	Ice rafted debris
JaB	Jacobsen Bight
JoB	Jossac Bight
JT(S)	Jacobsen Trough (System)
ka	Thousand years
KHB	King Haakon Bay
KHT(S)	King Haakon Trough (System)
LHC	Larsen Harbour Complex
(L)LGM	(Local) Last Glacial Maximum



---

MA	Million years
MRA	Marine reservoir ages
MS	Magnetic Susceptibility
MSCL	Multi-Sensor Core Logger
NB	Newark Bay
NEGR	Northeast Georgia Rise
NGF	Novosilski Glacier Formation
PF	Polar Front
RXCT	Rotating X-ray CT system
SACCF	Southern Antarctic Circumpolar Current
SAM	Southern Annular Mode
SB	Southern Boundary (of the Antarctic Circumpolar Current)
SBF	Sandebugten Formation
SG	South Georgia
SGF	Salomon Glacier Formation
SGIC	South Georgia Ice Cap
SHW	Southern Hemisphere Westerly Winds
TC	Total carbon
TOC	Total organic carbon
UoB	University of Bremen
WAIS	West Antarctic Ice Sheet

---

## Abstract

The island of South Georgia, along with a number of other smaller islands, is part of a microcontinent surrounded by oceanic crust in the Atlantic sector of the sub-Antarctic. Oceanographically, South Georgia lies within the Antarctic Circumpolar Current (ACC), the broad oceanic current system that is driven by the Southern Hemisphere Westerlies (SHW) and climatically isolates the Antarctic continent from the warmer Northern Hemisphere. Its location in the middle of the ACC and its isolation from continental influences makes South Georgia a sensitive region, where climate changes are registered earlier than on the more thermally isolated Antarctic continent. So far, however, the timing and extent of the Last Glacial Maximum on South Georgia have not been completely resolved, mostly because radiocarbon dated sediment investigations are missing. This is mainly due to the lack of marine geological studies on the continental shelf of the southern side of the island, which is climatically much harsher and therefore less accessible than the northern side. This information, however, is important to create and evaluate reliable climate and ice sheet models. This thesis, based on the investigations of sediment cores, sediment echosounder profiles and high-resolution bathymetry data, closes important knowledge gaps in the King Haakon Trough System and Drygalski Fjord System on the southern shelf of South Georgia. For the latter, the radiocarbon-dated sediments reveal an extensive ice cap before 30 ka BP during the Local Last Glacial Maximum. In the King Haakon Trough System, the bathymetric and sediment echo-graphic mapping of this thesis also reveal shelf-wide glaciation, possibly related to the last glacial period. Furthermore, this thesis investigates the subsequent deglaciation and the traces left by climate variability and its drivers within the sedimentary records in the two cross-shelf troughs. The results show that the southern shelf environments were ice-free since before the Antarctic Cold Reversal and thus exposed to currents at least since the start of the Holocene. These likely reacted to climate fluctuations of the present interglacial and, therefore, impacted trough sedimentation. Thus, this thesis does not only provide evidence for past ice-extent, which is crucial for benchmarking modelling approaches, but also gives further insight into the Holocene climate variability and sedimentary processes around South Georgia, potentially even archiving shelf-intruding behaviour of the nearby Southern Antarctic Circumpolar Current Front (SACCF) for at least the last 8 ka BP.

## Kurzfassung

Die Insel Südgeorgien ist Teil eines Mikrokontinents umgeben von ozeanischer Kruste im atlantischen Sektor der Subantarktis. Ozeanographisch liegt sie im Antarktischen Zirkumpolarstrom (ACC), jenem breiten ozeanischen Strömungssystem, das durch die südliche Westwindzone (SHW) angetrieben wird und den antarktischen Kontinent klimatisch von einer nördlichen wärmeren Hemisphäre isoliert. Die Lage mitten im ACC, und die Isolation von kontinentalen Einflüssen, macht Südgeorgien zu einer sensiblen Region, in der Klimaänderungen früher als auf dem thermisch isolierteren antarktischen Kontinent registriert werden. Bisher ist jedoch der Zeitrahmen und das Vereisungs-Ausmaß des Letzten Glazialen Maximums auf Südgeorgien noch nicht endgültig geklärt, da vor allem datierte Sedimentuntersuchungen fehlen. Dies liegt hauptsächlich an dem Mangel von marin-geologischen Untersuchungen auf dem breiten Kontinentalschelf der Südseite der Insel, der klimatisch sehr viel rauer und daher weniger zugänglich ist als auf der Nordseite. Solches Wissen ist jedoch wichtig, um verlässliche Modelle für Klima und Eisschilde zu generieren und diese bewerten zu können. Die Dissertation, die sich auf die erstmalige Untersuchung von Sedimentkernen, Echolot-Profilen und hochauflösende, bathymetrische Daten stützt, schließt wichtige Wissenslücken im King Haakon Trog System und Drygalski Fjord System auf dem südlichen Schelf von Südgeorgien. Für das Drygalski Trog System belegen die mit der <sup>14</sup>C-Methode datierten Sedimente eine weit ausgedehnte Eiskappe vor mindestens 30 000 Jahren während des Lokalen Letzten Glazialen Maximums. Im King Haakon Trog System verdeutlichen die bathymetrischen und sedimentechographischen Kartierungen dieser Arbeit außerdem eine schelfweite Vergletscherung, die möglicherweise auch während des letzten Glazials aktiv war. Darüber hinaus untersucht diese Arbeit den nachfolgenden Eisrückzug und die Spuren, die die Klimaschwankungen und deren Ursachen in den Sedimentpaketen der beiden glazialen Tröge hinterlassen haben. Die Ergebnisse zeigen, dass diese südlichen Schelfgebiete schon vor dem Antarktischen Kälterückfall (ACR) eisfrei und, spätestens ab dem Holozän, Meeresströmungen ausgesetzt waren. Diese Strömungen reagierten sensibel auf größere Klimaschwankungen des Holozäns und wirkten sich auf die Sedimentation in den Trögen aus. Diese Arbeit liefert nicht nur Beweise für vergangene Eisausdehnung, die für Klimamodelle von entscheidender Bedeutung sind, sondern ermöglicht auch weitere Einblicke in die Holozäne Klimavariabilität und die Sedimentationsprozesse um Südgeorgien. Prozesse, die

möglicherweise durch das Verhalten der nahegelegenen südlichen Front des Antarktischen Zirkumpolarstroms (SACCF) in den letzten 8000 Jahren beeinflusst wurden.

## Outline and contributions to manuscripts

This cumulative thesis focuses on the maritime sub-Antarctic climate in the Atlantic sector since the last glaciation and the associated waxing and waning of a sub-Antarctic ice cap based on the microcontinent South Georgia. Until now, climate archives and ice extent reconstructions from the region were mostly based on terrestrial or, if from the marine realm, near-coastal areas or the north-eastern shelf. In this thesis, archives from the southern and south-western shelf, which have not been investigated so far, are introduced and do not only provide evidence for an extensive ice sheet during the Local Last Glacial Maximum, but also highly resolve the subsequent Holocene interglacial. In Chapter 1, this thesis introduces glacial and interglacial periods, as well as the primary drivers of Southern Hemisphere climate and the importance of South Georgia's geographical position within the Southern Ocean. This is followed by a short summary of the state of the art and the consequential knowledge gaps in Chapter 2, which serve as the base for this thesis and its objectives. Chapter 3 introduces the study area of South Georgia and its geology, which builds the foundation for the climate archives retrieved for this work. The main body of this thesis, Chapters 4 - 7, consists of four manuscripts that were and will be published in scientific journals. Each of them focuses on different marine archives and acoustic data that allow to reconstruct different time periods and the primary processes that influence the continental shelf.

Chapter 4 investigates South Georgia's ice cap extent. the timing of its Local Last Glacial Maximum and the subsequent deglaciation in Drygalski Trough on the southern continental shelf. This study is based on a sedimentological dataset from gravity core PS119/5-1 and bathymetric and sub-bottom data from the Drygalski Fjord System and was published in "Quaternary Science Reviews" (Lešić et al., 2022).

Chapter 5 examines the geomorphology of King Haakon Trough System, based on the bathymetry and sub-bottom profiler data and aims to reconstruct its glacial history. This chapter is currently in preparation for submission to a scientific journal.

Chapter 6 focuses on the following interglacial period and the climate-associated depositional conditions within the King Haakon Trough System on the south-western shelf. It is based on sub-bottom profiles and uses radiocarbon dating of sediment cores from the area for chronological classification. This chapter was submitted to Quaternary Science Advances in August 2023.

Chapter 7 is dedicated to the detailed analysis of the sediment cores introduced in Chapter 6. The aim is to detect climate variability and the sedimentological characteristics of transitions between cold and warm periods during the Holocene. For this purpose, multi-proxy analysis was carried out on three gravity cores, giving us more insight into the Holocene climate that influenced King Haakon Trough System. This chapter is currently in preparation to be submitted for publication in a scientific journal.

In the final chapter 8, all findings are summarized and integrated into a larger context. This is followed by the Acknowledgements, a complete reference list and the appendices, which contain the supplementary materials for the three manuscripts and the grainsize data, physical and chemical properties. These data will be submitted to PANGAEA, along with the Multi-Sensor Core Logging data from Chapter 4. Nina-Marie Lešić is the main contributor to all Chapters and is responsible for the designing of all studies, except Chapter 5. A list of authors and their contributions to the respective manuscripts is provided below:

Chapter 4 - Manuscript I (published): Glacimarine sediments from outer Drygalski Trough, sub-Antarctic South Georgia – evidence for extensive glaciation during the Last Glacial Maximum	
Author	Contribution to Manuscript
Nina-Marie Lešić	Conceptualization, Methodology, Investigation, Writing – Original draft, Writing – Review & Editing, Visualization
Katharina Teresa Streuff	Investigation, Writing - Original draft (Chapter 4.3 and 4.4), Writing – Review & Editing, Visualization (Fig. 4.6, 4.7, 4.8, 4.10), Supervision
Gerhard Bohrmann	Chief scientist of PS119 research cruise, Funding Acquisition, Supervision, Project Administration, Writing – Review & Editing
Gerhard Kuhn	Funding Acquisition, Supervision, Project Administration, Writing – Review & Editing

Chapter 5 - Manuscript II (in prep.): Glacial history of the King Haakon Trough System, sub-Antarctic South Georgia	
Author	Contribution to Manuscript
Katharina Teresa Streuff	Conceptualization, Methodology, Investigation, Writing – Original draft, Writing – Review & Editing, Visualization
Nina-Marie Lešić	Conceptualization, Methodology, Investigation, Writing – Original draft (parts of Chapter 5.4 and 5.5), Review & Editing, Visualization (Fig. 5.5, 5.6)
Gerhard Kuhn	Funding Acquisition, Supervision, Project Administration, Writing – Review & Editing

Outline and contributions to manuscripts

Gerhard Bohrmann	Chief scientist of M134 research cruise, Funding Acquisition, Supervision, Project Administration, Writing – Review & Editing
------------------	---

Chapter 6- Manuscript III (submitted to Quaternary Science Advances): Spatial and temporal variability in Holocene trough-fill sediments, King Haakon Trough System, sub-Antarctic South Georgia	
Author	Contribution to Manuscript
Nina-Marie Lešić	Conceptualization, Methodology, Investigation, Writing – Original draft, Writing – Review & Editing, Visualization
Katharina Teresa Streuff	Investigation, Writing – Review & Editing, Supervision
Gerhard Bohrmann	Chief scientist of M134 research cruise, Funding Acquisition, Supervision, Project Administration, Writing – Review & Editing
Gerhard Kuhn	Funding Acquisition, Supervision, Project Administration, Writing – Review & Editing

Chapter 7 - Manuscript IV (in prep.): Climate-driven Holocene sedimentation in King Haakon Trough System, sub-Antarctic South Georgia	
Author	Contribution to Manuscript
Nina-Marie Lešić	Conceptualization, Methodology, Investigation, Writing – Original draft, Writing – Review & Editing, Visualization
Katharina Teresa Streuff	Conceptualization, Writing – Review & Editing, Supervision
Jürgen Titschack	CT scanning and Processing, Writing – Original draft (Methods in Appendix), Writing – Review & Editing
Tilo von Dobeneck	Funding Acquisition, Methodology, Investigation
Gerhard Kuhn	Funding Acquisition, Supervision, Project Administration, Writing – Review & Editing
Gerhard Bohrmann	Chief scientist of M134 research cruise, Funding Acquisition, Supervision, Project Administration, Writing – Review & Editing

### 1. Introduction

#### 1.1. Phanerozoic climate cycles

##### 1.1.1. Icehouse and greenhouse climate

The Earth's history of the Phanerozoic has been dominated by global climatic super-cycles of several 10s of million years, which oscillate between icehouse and greenhouse climate (Frakes et al., 1992). During icehouse climate, ice sheets are present at minimum one pole, while greenhouse climate does not feature continental ice at all. This cyclicity has been associated with the variability of global plate tectonics, tectonic-dependent volcanic activity, seafloor spreading and changes in ocean gateways and circulation, as well as chemical weathering and the balance of carbon dioxide release into the atmosphere and its removal from it, which is controlled by the entity of these factors (e.g. Raymo and Ruddiman, 1992; Smith and Pickering, 2003; Jovane et al., 2009). Within these large-scale cycles, ice-house climate is associated with periods of low carbon dioxide levels in the atmosphere (cf. Royer, 2006).

Currently, Earth is experiencing its most recent icehouse climate, the "Late Cenozoic Ice Age" (Elverhøi et al., 1998), which started around 34 Ma ago around the Eocene/Oligocene boundary with the onset of extensive glaciation of the Antarctic continent (Jovane et al., 2009 and references therein). This Antarctic glaciation has been tentatively associated with the roughly concurrent openings of the Drake Passage and Tasmanian gateway and the following establishment of the Antarctic Circumpolar Current, which thermally isolates the Antarctic continent (Smith and Pickering, 2003; Scher and Martin, 2006; Livermore et al., 2007), as well as with the closure of the Neotethys Ocean (Jovane et al., 2009). This long-lasting glaciation history and thermal isolation of the large Antarctic continent, together with the locally exceptionally low temperatures, make Antarctica and the thermally more sensitive adjacent sub-polar regions of the Southern Hemisphere especially interesting for polar climate research. Conversely, Late-Cenozoic ice sheets have been developing on the Northern Hemisphere only during the last 3 - 4 Ma (Mudelsee and Raymo, 2005; Hayashi et al., 2020), possibly due to the closure of the Central American Seaways (Bartoli et al., 2005), and intensified around the start of the Pleistocene after 2.7 Ma BP and is associated with the strengthening of the Atlantic meridional overturning circulation (Ruggieri et al., 2009; Hayashi et al., 2020).



## 1.1.2. Glacial and interglacial periods during icehouse climate

In addition to these changes on long time scales in glaciation, Earth's climate has been going through shorter  $\sim 100$  ka glacial cycles of periodically i) larger global ice sheets and lower eustatic sea-levels and ii) smaller global ice sheets and higher eustatic sea-levels within this current icehouse climate for at least the last 800-900 ka (Past Interglacials Working Group of PAGES, 2016; Weinans et al., 2021), which are defined as glacial and interglacials, respectively (Lang and Wolff, 2011). For instance, besides hosting large ice sheets in polar regions and low eustatic sea-levels, glacial periods exhibit low mean temperatures and carbon dioxide levels in the atmosphere. On the contrary, interglacials not only feature smaller ice sheets and higher eustatic sea-levels, but also higher temperatures and higher carbon dioxide levels, which usually are below 300 ppmv and are 80 to 100 ppmv higher than peak glacial values (Sigman and Boyle, 2000; Masson-Delmotte et al., 2010). The reconstruction of these cycles is based on an array of proxies from marine, cryospheric and terrestrial archives (Lang and Wolff, 2011). They can be traced, for instance, along the variability of stable oxygen isotopes from benthic foraminifera (Fig. 1.1) (Past Interglacials Working Group of PAGES, 2016).

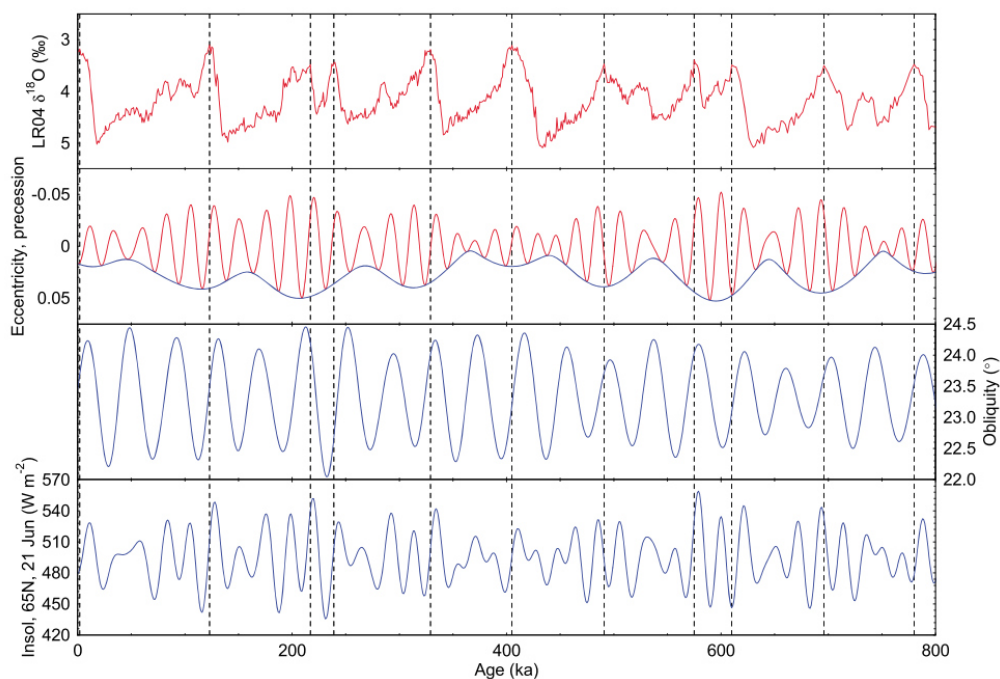


Fig. 1. 1: Interglacial/glacial cycles visualised by variability of oxygen isotope 18 in benthic foraminifera with maxima displaying interglacials and minima displaying glacial periods from the last 800 ka, correlated with changes in earth's orbital patterns, Figure taken from Past Interglacials Working Group of PAGES (2016)

Though these cycles (Fig. 1.1) might be triggered by recurring changes in the earth's orbital pattern of eccentricity, precession and obliquity, as well as resulting changes in solar insolation

(Berger, 1988; Bamber, 2021), they have varied in intensity (Masson-Delmotte et al., 2010), suggesting more complicated interactions of marine, atmospheric and terrestrial mechanisms. Indeed, the Southern Ocean has been suggested as a crucial driver of glacial/interglacial variability due to e.g. its large contribution to the global oceanic carbon reservoir (Sigman and Boyle, 2000; Sigman et al., 2010; Sikes et al., 2023). There, physical, chemical, and biological processes seem to contribute to carbon release, e.g. as carbon dioxide, and storage (Sikes et al., 2023 and references therein). These include the occurrence of sea-ice, which not only acts as an important barrier for ocean-atmosphere (carbon)-exchange but also influences global ocean circulation and the Earth's albedo, i.e. reflecting solar radiation from the Earth's surface back to space (Stephens and Keeling, 2000; Ferrari et al., 2014; Sévellec and Fedorov, 2015; Willeit et al., 2023).

Today, we live during the most recent interglacial, the Holocene, that started around 11.7 ka BP ago (Walker et al., 2009), after the end of the last Pleistocene glacial, which lasted from ~115 - 11.7 ka BP (Masson-Delmotte et al., 2010) and culminated in a maximum ice extent around 26 - 19 ka BP, the so-called Last Glacial Maximum (LGM; Clark et al., 2009). The LGM was associated with a global eustatic sea-level fall of ~130 m (Fig. 1.2) (Clark and Mix, 2002). However, this maximum ice extent did not occur simultaneously on a global scale and instead represents a temporal overlap of many ice sheet-specific glacial maxima with distinct individual timings, which are defined as "Local Last Glacial Maxima" and occurred as early as 32 - 29 ka BP in mid- and high latitudes of the Northern Hemisphere and e.g. the West Antarctic Ice-Sheet (WAIS) (Fig. 1.2) (LLGM; Clark et al., 2009). Temperature reconstructions from the LGM have shown that the Earth experienced a drop in global mean temperature by ~6 °C after the preceding interglacial, which might have been slightly warmer than today (Masson-Delmotte et al., 2010; Tierney et al., 2020; Bova et al., 2021; Seltzer et al., 2021).

During the LGM, >20 % of Earth's land surface was covered by ice, which can be reconstructed by geophysical, geologic and geomorphic surveys. They not only provide evidence for grounded ice and glacial isostatic adjustment, but also give information on the direction of ice sheet and glacier movements. This can be translated to the marine realm with bathymetric surveys, acoustic profiling and sediment cores (e.g. Velichko et al., 1997). The resulting evidence, when dated with radiometric dating methods, can be used for benchmarking ice sheet and climate models by testing their reliability to reproduce past-climate and ice-extents.

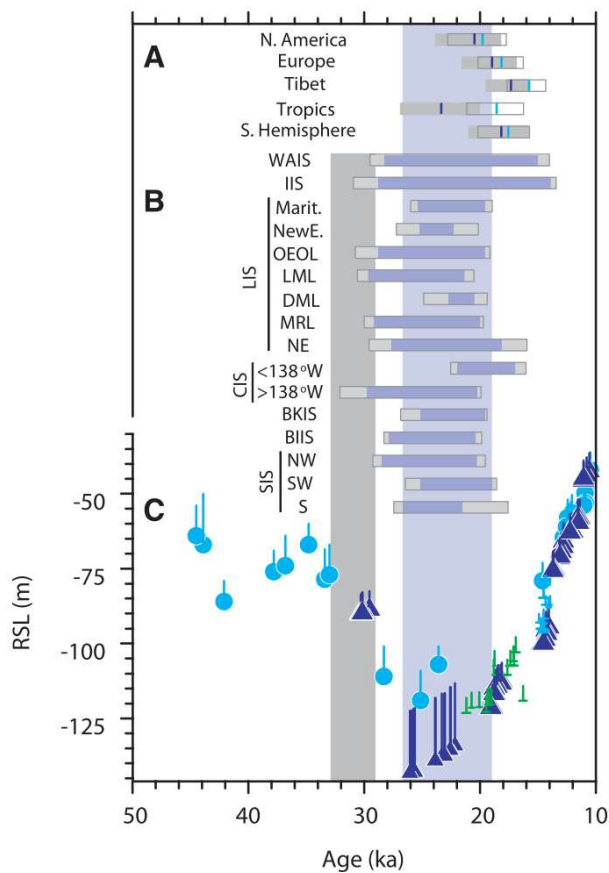


Fig. 1. 2: LLGM chronologies: The vertical purple bar represents LGM timing inferred from relative sea-level (RSL) data, while the vertical gray bar depicts the earliest interval of sea-level fall, corresponding to first LLGM. A) LLGM for mountain glaciation (small horizontal bars). The vertical purple segment and associated horizontal gray segment show the mean age and age range for the onset of deglaciation. The vertical blue segment and associated area outlined in gray represent the mean age and the range for the onset of deglaciation B) LLGM for ice-sheet sectors and ice sheets: small horizontal purple bars with gray bars on either end depict the LLGM and their errors. West Antarctic Ice Sheet (WAIS), Inuitian ice Sheet (IIS), the sectors of the Laurentide Ice Sheet (LIS): Maritimes (Marit.), New England (NewE.), Ohio-Erie-Ontario Lobe (OEOL), Lake Michigan Lobe (LML), Des Moines Lobe (DML), Mackenzie River Lobe (MRL), north-eastern margin (NE). Cordilleran Ice Sheet (CIS), the Scandinavian Ice Sheet (SIS) sectors: northwest (NW), southwest (SW), south (S). C) RSL data (including depth uncertainty from 10 to 50 ka). Locations: the Bonaparte Gulf (green half-pluses), New Guinea (blue circles), the Sunda Shelf (blue half-pluses), Barbados (purple triangles) (Figure and adapted caption from Clark et al., 2009)

Today, within the recent interglacial, ice masses still cover ~10 % of the Earth's land surface (Bartels-Rausch, 2013) and contain around 70 % of the global freshwater. However, the modern concentration of carbon dioxide in the atmosphere of 421 ppmv (Davis, 2023), along with other greenhouse gases, has been unprecedented in at least 800 ka and can be associated with anthropogenic emissions (Sigman and Boyle, 2000; Eyring et al., 2021; Davis, 2023), critically endangering the future of Earth's ice sheets, biodiversity and humans (Eyring et al., 2021; Davis, 2023). Indeed, if all ice sheets and glaciers melted, this would raise the global mean sea-level by ~66.5 m (Bamber, 2021). Thus, because of the alarming rate of anthropogenic global warming and its presumed effect on ongoing ice sheet melting (Masson-Delmotte et al., 2022), it is crucial to understand the natural causes for climate variability and ice sheet feedback (cf. e.g. Fyke et al., 2018). To achieve this, we have to investigate the past in order to understand the current anthropogenic influence and (more securely) predict (the degree of) future changes that will be influenced by both natural variability and humans.

## 1.2. South Georgia's geographical position within Southern Hemisphere climate drivers

Shifts between glacial and interglacial periods are not only recorded at the poles but also in various archives worldwide. One example is the sub-Antarctic region, which is a transitional zone between high and low latitudes and climatically depends on the Southern Hemisphere Westerly Winds (SHW) and the Antarctic Circumpolar Current (ACC) (cf. Strother et al., 2015; Moreno et al., 2018; Matano et al., 2020; Bakke et al., 2021; Yamazaki et al., 2021). In the sub-Antarctic, ice caps still exist today (e.g. Hodgson et al., 2014b), although their respective land masses are too small to host ice sheets comparable in size to those on the Antarctic continent, and, therefore, only have a relatively limited influence on the global eustatic sea level. However, the climate and the ice caps of sub-Antarctic islands have reacted comparably early to modern warming (Gordon et al., 2008; Cook et al., 2010; Nel et al., 2023). Therefore, they are not only considered as sensitive indicators of climate variability itself but also allow to investigate the influence of this variability on Southern Hemisphere ice sheet (in-)stability (Gordon et al., 2008; Cook et al., 2010; Hodgson et al., 2014b; Farías-Barahona et al., 2020).

One of the largest sub-Antarctic islands is the microcontinent South Georgia, which is located in the Atlantic sector of the Southern Ocean at 54-55° S and 35.5-38° W (Fig. 1.3) and is ~3456 km<sup>2</sup> large (calculated on ellipsoid WGS84 (EPSG: 7030) based on data by Gerrish (2020)). However, as a microcontinent, it also features a large continental shelf (<400 m water depth, calculated on ellipsoid WGS84 (EPSG: 7030), based on the bathymetric data from Hogg et al. (2016); (2017)), that is ~10 times the size of the island and shows evidence of intense glacial influence and is characterised by numerous cross-shelf troughs (cf. Clapperton, 1971; Graham et al., 2008; Hodgson et al., 2014a). Considering that the LGM caused an eustatic sea-level drop of ~130 m (Clark et al., 2009), additional parts of the shelf might have been emerged and subjected to grounded ice (cf. Barlow et al., 2016), increasing its potential to store freshwater during glacials.

Today, South Georgia is still covered by ice cap remains, whose outlet tidewater glaciers dominate the fjord heads (Cook et al., 2010; Farías-Barahona et al., 2020). Due to its remote location far from large continents (Fig. 1.3), it experiences the maritime climate of the Southern Ocean (Bentley et al., 2007; Hodgson et al., 2014a) and is a prime target to investigate maritime sub-Antarctic climate variability.

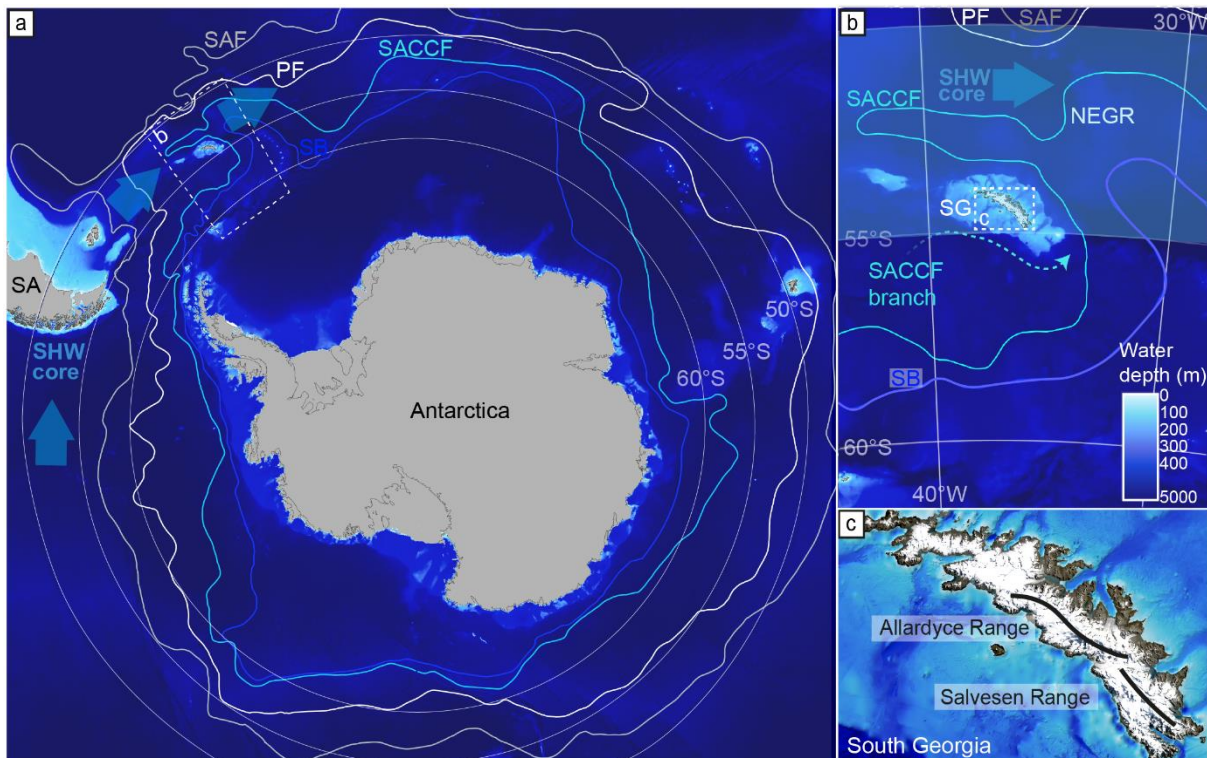


Fig. 1. 3: a) Overview of the Southern Ocean, including the Antarctica and South America (SA). South Georgia (SG), within the area highlighted by white dashed line, is located within the core belt of the Southern Hemisphere Westerly Wind (SHW) between 50-55°S (after Moreno et al. (2018), and between the Antarctic Circumpolar Current fronts SAF (Sub-Antarctic Front), PF (Polar Front), SACCF (Southern Antarctic Circumpolar Current Front), SB (Southern Boundary), based on Orsi and Harris (2019). (EPSG: 3031) map is based on IBCSO data from Dorschel et al. (2022), GEBCO Compilation Group (2023), land polygons are from Gerrish (2020); Gerrish et al. (2023). SA polygon <50°S is expanded by U.S. Department of State (2013) data b) SG is positioned between the PF and the SACCF, which features a branch that borders the SG shelf to the south (dashed blue line). (EPSG: 3762) c) SG features two mountain ranges, the Allardyce range and Salvesen range, after Curtis (2011) (EPSG: 3762). DEM shelf is based on Hogg et al. (2016); (2017). Map information for SG island is derived from Landsat imagery from South Georgia GIS (2023).

The island is located within the core belt of the SHW (~50 - 55°S during austral summer, Fig. 1.3a) and is therefore strongly influenced by these eastward-directed winds year-around (Lamy et al., 2010; Moreno et al., 2018; Bakke et al., 2021). They provide moisture and thus impact the distribution of temperature and precipitation on South Georgia. As a result, these winds do not only impact the extent of the South Georgia Ice Cap (SGIC) (Bakke et al., 2021), but also contribute to the regulation of island run-off, thus affecting water masses and biological processes like primary production on the continental shelf (Matano et al., 2020). Observations showed that the Allardyce and Salvesen mountain ranges (Fig. 1.3b) serve as an orographic barrier and lead to a declining south-north gradient in precipitation, which likely causes glaciers along the north-eastern coast of South Georgia to retreat faster than in the southwest (Gordon et al., 2008; Cook et al., 2010; Fariás-Barahona et al., 2020).

South Georgia's climate, its ice cap and surrounding environments seem to be sensitive to changes in SHW strength, which does not only vary (sub-)seasonally but also on decadal timescales (Zhang et al., 2022). This variability in strength is accompanied by changes in the latitudinal wind belt position and is described as the Southern Annular Mode (SAM), a shift in wind induced by changing air pressure over the Southern Ocean (Gong and Wang, 1998, 1999; Lee et al., 2019; Fogt and Marshall, 2020; Wright et al., 2022). A positive phase of the SAM is equivalent to low air pressure over the Antarctic continent and high air pressure over lower latitudes, causing a poleward contraction of the wind belt, which increases the strength of the SHW at higher latitudes. Conversely, a negative SAM is characterised by higher air pressure over Antarctica, forcing an expansion of the SHW belt towards the north, and thus effectively increasing wind strength in the sub-Antarctic and decreasing wind strength at high Antarctic latitudes (cf. Gong and Wang, 1999; Sallée et al., 2008; Lee et al., 2019; van der Bilt et al., 2022). Paleo-reconstructions of the mean SAM state (e.g. Abram et al., 2014) suggest that this variability is largely natural and a feedback to natural external forcing, like solar irradiance, or might even be intrinsic (Wright et al., 2022).

Since the SHWs are a key driver of the eastwards flowing ACC (Orsi et al., 1995), changes in SHW/SAM might cause a latitudinal shift of mean ACC transport, provoking changes in the ocean currents in its area of influence (Meredith et al., 2004; Meredith and Hogg, 2006; Sallée et al., 2008; Gille, 2014; Liao and Chao, 2017).

The ACC consists of multiple circumpolar features, which are ~20 000 km-long fronts that extend from the sea surface to the seafloor of the 1000's of m deep Southern Ocean due to strong meridional gradients in temperature, salinity, and density (Sokolov and Rintoul, 2009). Thus, the fronts depend on the Southern Ocean's bathymetry and are spaciouly distributed above abyssal plains but are deflected by large bathymetric features, where the fronts converge (Fig. 1.3a) (Sokolov and Rintoul, 2009). The density difference across each front generates movement and makes them the routes of main transport within the ACC, with elevated current speeds. Although they are mostly displayed as rather simplified and isolated jets of accelerated ACC transport, they all consist of multiple branches and filaments that form extensive jet structures throughout vast sectors of the Southern Ocean (Sokolov & Rintoul, 2009 and references therein; Matano et al., 2020; Combes et al., 2023).

The complicated front structure, as well as differences between methods to determine front positions, led to a slight variability of their circumpolar paths in the literature. In this thesis, the positions of oceanographic fronts on the large circumpolar scale (Fig. 1.3a) are adapted from Orsi et al. (1995), while, on the smaller regional scale around South Georgia, the position of individual branches of the Southern Antarctic Circumpolar Current Front (SACCF) is adapted from Matano et al. (2020).

Knowing the position of SACCF branches is crucial to investigate shelf environments, as South Georgia is positioned between two primary ACC fronts (Fig. 1.3b), which are, from north to south, the Polar Front (PF) and the Southern Antarctic Circumpolar Current Front (SACCF), which traces and intrudes across parts of South Georgia's continental shelf break, influencing the currents on the continental shelf (Matano et al., 2020; Combes et al., 2023). The position of the microcontinent within these large atmospheric and oceanographic systems makes South Georgia island and its continental shelf an ideal area to investigate i) past climate and ice extent on a broader Southern Hemisphere scale (Bentley et al., 2009; Strother et al., 2015), ii) dependent variations in SHW through time and iii) dependent changes in the SACCF transport.

## 2. Motivation and objectives of this study

The overarching objective of this thesis is to gain a deeper understanding of past sub-Antarctic ice extent and associated climate, which is, compared to Antarctica, relatively poorly understood and lacks extensive dated evidence. The sub-Antarctic ice caps only contribute a small fraction to global ice masses and, therefore, do not strongly influence the eustatic sea-level during interglacial/glacial cycles. However, the ice caps have been reacting early to the recent global warming, implying that they also might have been sensitive and highly responsive to past major and minor climate changes. This is associated with the position of these ice caps within the area of influence of the SHW and the ACC fronts at the margin of Antarctic realms. Especially in light of recent climate changes and the urgency of this climate crisis (Masson-Delmotte et al., 2022), it is crucial to collect information on past climate and ice masses to add boundary conditions to ice sheet simulations in order to estimate their future behaviour more securely.

Among the glaciated sub-Antarctic islands, South Georgia is one of the largest and, as a microcontinent, features a large continental shelf that expands South Georgia's capacity to host a rather extensive ice cap. Therefore, this thesis uses data from South Georgia's continental shelf to:

1. Enhance the knowledge of glacial evolution and LLGM ice extent, which is fundamental scientific research and crucial to improve climate models that simulate the future of the Earth's ice sheets and ice caps, especially in transitional climate zones as the sub-Antarctic. (Chapters 4 and 5).
2. Show the potential of South Georgia's cross-shelf trough fills as an archive for regional climate and potential associated changes in the ACC after the LLGM (Chapter 6).
3. Integrate the changes in South Georgia trough sedimentation within Holocene Southern Hemisphere climate variability (Chapter 7).

To achieve this, this thesis focuses on two study areas on the southern and south-western continental shelf, which, to our knowledge, entirely lack dated marine constraints for past ice extent or climate records (Fig. 2.1). In total, five gravity cores are investigated, along with bathymetric data and sub-bottom profiles within the two study areas.



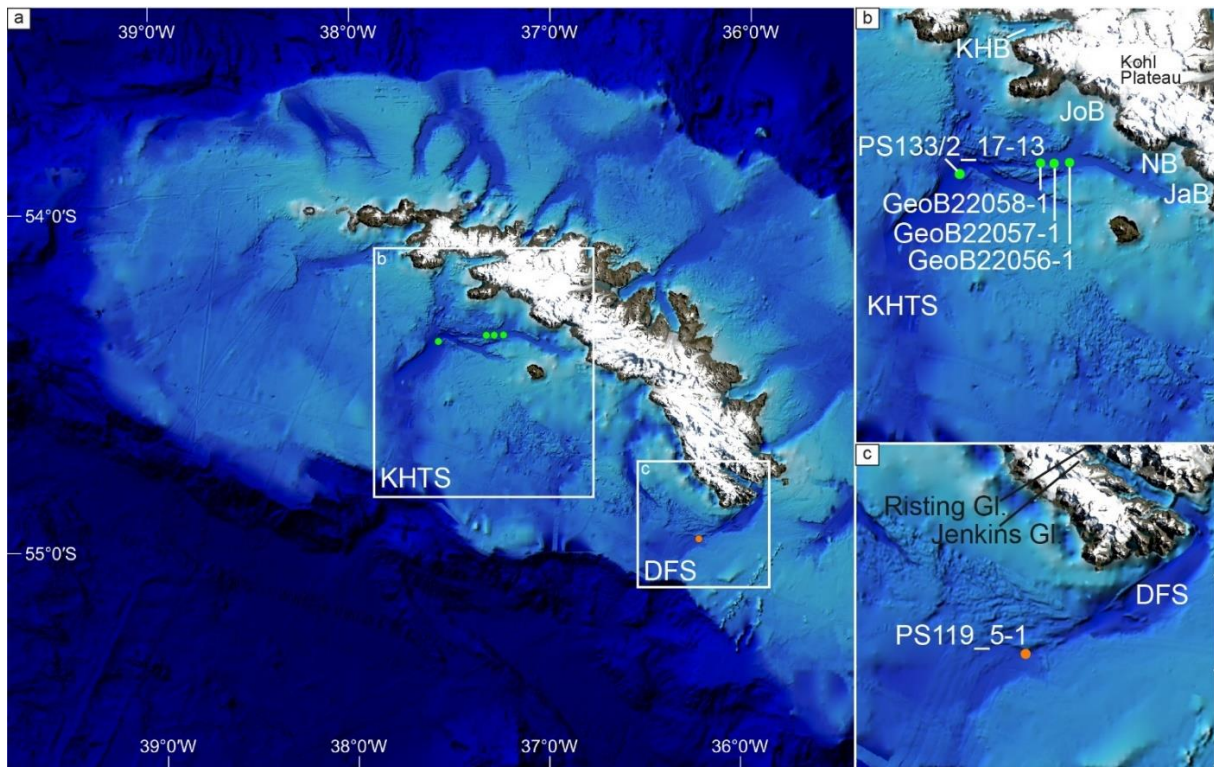


Fig. 2. 1: a) South Georgia and its continental shelf with two rectangles indicating the two study areas in this thesis, King Haakon Trough System (KHTS) and Drygalski Fjord System (DFS) with the respective core positions in green and orange. The study areas are represented by the two insets b and c. b) King Haakon Trough System (KHTS) with four gravity core locations (locations in green, Chapters 5,6,7). The trough feeding bays are indicated in white, KHB = King Haakon Bay, JoB= Jossac Bight, NB= Newark Bay, JaB= Jacobsen Bight. c) Drygalski Fjord System (DFS) with the core location from Chapter 4 and the two glaciers that feed into DFS, Risting Glacier and Jenkins Glacier. DEM information for the ocean and shelf areas is based on GEBCO Compilation Group (2023), and Hogg et al. (2016); (2017) overlain by data from PS81, M134 and PS119 (Bohrmann, 2013; Bohrmann et al., 2017; Bohrmann, 2019), while the map information for SG island is derived from Landsat imagery from South Georgia GIS (2023)

### 3. Study area

#### 3.1. South Georgia's South American heritage and its geological setting

Today, the microcontinent South Georgia's location in the Southern Ocean is ideal for paleoclimate and ice cap research. However, it has only been in a tectonically stable position for the last ~6 Ma, long after the Drake Passage first opened and the ACC started flowing eastwards (cf. Graham et al., 2008). Indeed, its long-term tectonic evolution and origin, though investigated since the 1820s (Dalziel et al., 2021), is still a subject to research. While a genetic relation between the tip of the South American Andes and the South Georgia microcontinent is widely accepted in literature, as the geologic formations of South Georgia can be correlated with the Tierra del Fuego area, the tectonic mechanisms behind its isolation and relative (to South America) eastwards translation are unclear (Dalziel et al., 2021). Indeed, only ~50 % of this relative translation towards South Georgia's new position can be attributed to seafloor spreading on the west Scotia Sea spreading centre and the remaining 50 %, though likely incorporating some degree of rotation, are yet to be resolved (Dalziel et al., 2021; Beaver et al., 2022).

Based on the geological evidence, it was reconstructed that South Georgia once was part of a South American marginal basin. This "Rocas Verdes" basin, amongst many others, was the result of extension tectonics and subsequently filled and tectonically closed in the mid- to Late Cretaceous (Dalziel et al., 2021; Beaver et al., 2022), deforming its fill during inversion. Despite the geological evidence, however, South Georgia's South American heritage is questioned completely by some scientists, inter alia in recent regional plate models based on geophysical data (Dalziel et al., 2021 and references therein).

Its modern location lies 1500 - 1700 km east of its reconstructed original position (Fig. 3.1), meaning that the continental splinter of South Georgia must have been displaced eastwards relative to South America during or/and after the basin closure around the mid- to late Cretaceous. Indeed, thermochronology has shown South Georgia was connected to South America until 45 - 40 Ma (Carter et al., 2014), indicating that South Georgia only finally separated afterwards, colliding with the "North East Georgia Rise" (NEGR; Fig. 1.3) around 12 - 10 Ma BP (Dalziel et al., 2021).

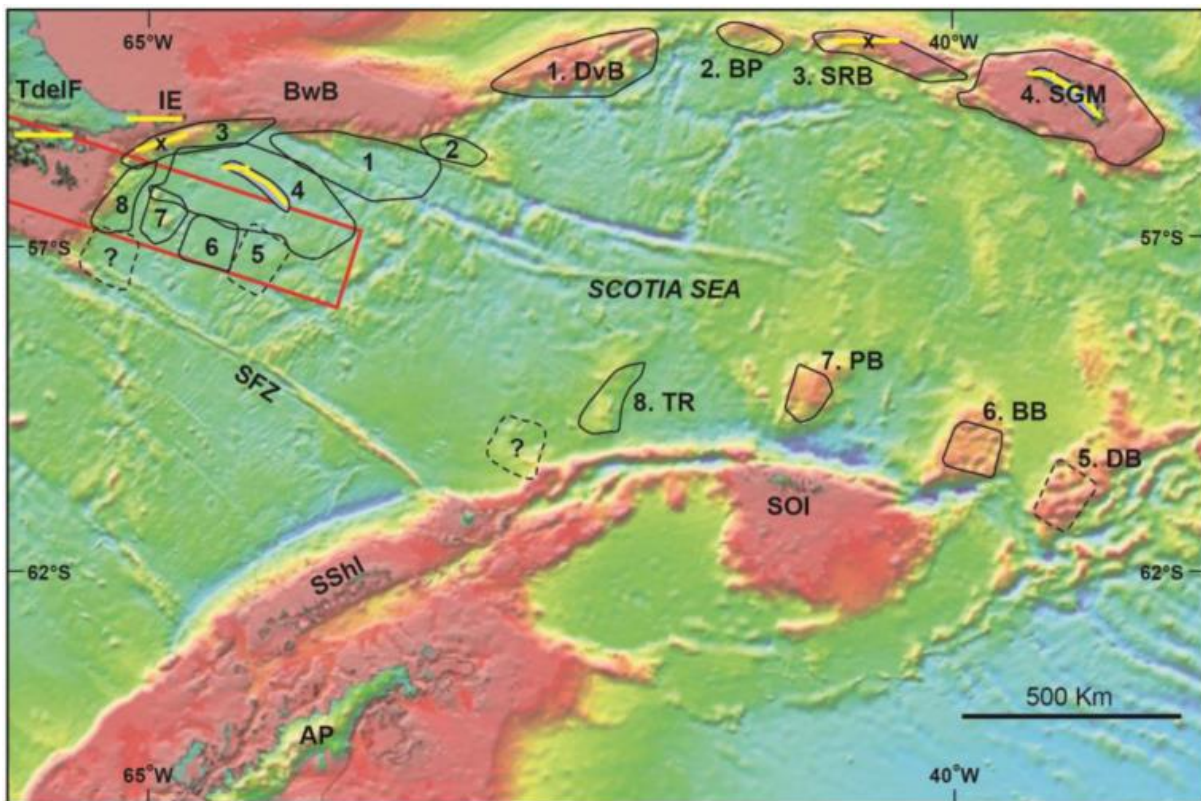


Fig. 3. 1: This map shows gravity data of the Scotia Arc with the present and (tentatively) reconstructed positions of South Georgia and other continental fragments. Left to right and top to bottom: TdelF= Tierra del Fuego, IE= Isla de los Estados, BwB= Burdwood Bank, DvB= Davis Bank, BP= Barker Plateau; SRB= Shag Rocks bank; SGM= South Georgia microcontinent, SFZ=Shackleton Fracture Zone, TR= Terror Rise, PB= Pirie Bank, BB= Bruce Bank, DB=, SShl= South Shetland Islands, SOI= South Orkney Islands, AP= Antarctic Peninsula. Red rectangle: batholith present on Tierra del Fuego, the South Georgia microcontinent and the continental blocks of the southern Scotia Sea. This Figure and the adapted caption are taken from Dalziel et al. (2021)

Due to South Georgia's origin from the "Rocas Verdes" marginal basin, a great variety of rocks can be found on the island and, consequentially, the whole basement of the continental block (Fig. 3.2). However, only small parts of the submerged continental shelf have been geologically mapped, leaving the extent of formations and fault zones to some degree of speculation (Storey, 1983; Macdonald et al., 1987; Mair, 1987; Curtis, 2011; Dalziel et al., 2021).

The island is largely built up by back-arc basin infill consisting of turbidite deposits of volcanoclastic sandstones and mudstones (e.g. Dalziel et al., 2021). This basin fill formation on South Georgia is defined as "Cumberland Bay Formation" (CBF) and builds up the Allardyce mountain range (Figs. 1.3b and 1.6). CBF is closely associated with the "Sandebugten Formation" (SBF), which also consists of turbidites and might represent either an older turbidite sequence than CBF, had a different provenance or both (Macdonald et al., 1987; Turnbull and Craw, 1988).

## Study area

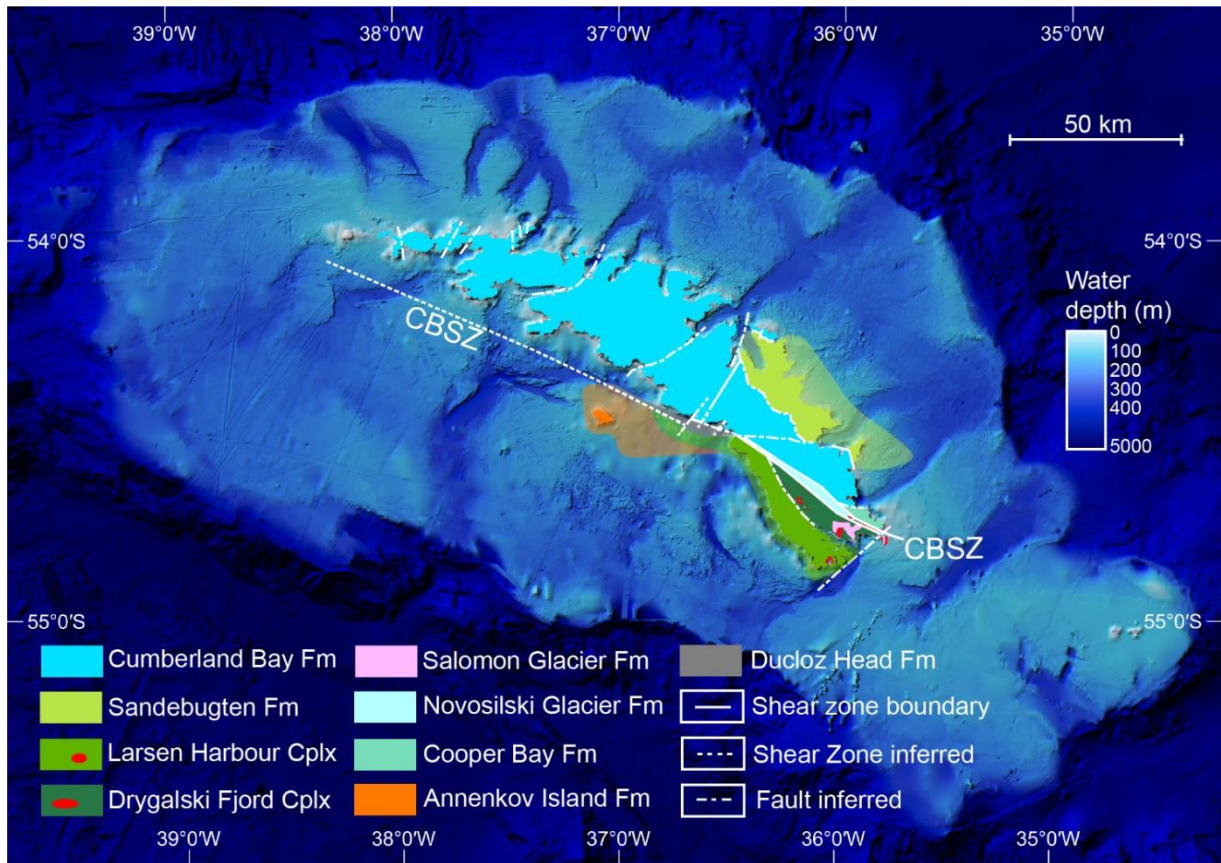


Fig. 3. 2: Geologic formations and faults of and around SG, including the major shear zone Cooper Bay Shear Zone (CBSZ), adapted from Macdonald et al. (1987), Curtis (2011) and Dalziel et al. (2021). DEM information for the ocean and shelf areas is based on GEBCO Compilation Group (2023), and Hogg et al. (2016); (2017) overlain by data from PS81, M134 and PS119 (Bohrmann, 2013; Bohrmann et al., 2017; Bohrmann, 2019), while the map information for SG island is derived from Landsat imagery from South Georgia GIS (2023).

This basin fill of CBF and SBF is likely separated from the southeast part of the island by a large shear zone, the “Cooper Bay Shear Zone” (CBSZ), which might affect large parts of the continental shelf as well (Fig. 3.2) (Curtis, 2007; Curtis, 2011; Dalziel et al., 2021).

The area south of the CBSZ contains three units that represent: i) a fraction of Pre-Jurassic basement, meaning continental crust, called the “Drygalski Fjord Complex” (DFC), which incorporates three additional sedimentary and metasedimentary formations called “Salomon Glacier” (SGF), “Cooper Island” (CIF) and “Novosilski Glacier” (NGF) formations and partly builds up the “Salvesen” mountain range (Fig. 1.3b) ii) parts of an ophiolitic complex called the “Larsen Harbour Complex” (LHC), which is mostly composed of gabbros, tholeiitic pillow basalts, pillow breccias, sheeted dolerite dykes, volcanoclastic rocks and silicic magmatites, and iii) Cretaceous tuff and volcanoclastic breccias, which belong to the “Annenkov Island” (AIF) and “Ducloz Head” (DHF) formations and were interpreted as volcanic-arc marginal deposits and might have been deposited in a deep shelf setting with large submarine canyons (Fig. 3.2)

(Storey, 1983; Storey and Macdonald, 1984; Macdonald et al., 1987; Mair, 1987; Curtis, 2011; Dalziel et al., 2021).

The position of (inferred) faults and shear zones on the island the shelf, as well as their spatial relation to the geological formations (Fig. 3.2) suggest that the individual past ice-streams and modern glaciers of the South Georgia Ice Cap (SGIC) have been flowing and eroding along structural weaknesses, e.g. the CBSZ. Thus, they should transport debris that depends on the geology of the feeding area. Orientation of fjords and cross-shelf troughs might therefore depend on these weaknesses (also see Chapters 5 and 6) and ice rafted debris sampled on the continental shelf should reflect the regional geology.

### 3.2. Glacial History

The South Georgia island and its surrounding continental shelf have been subjected to a climatically-controlled glacial evolution with repeated periods of ice sheet growth and decay and at least one advance all the way to the shelf edge (Sugden and Clapperton, 1977; Graham et al., 2008; Hodgson et al., 2014a; Graham et al., 2017). The formation of the deeply incised cross-shelf troughs is attributed to this long-term glacial evolution, whose start is thought to pre-date the LGM (e.g. Hodgson et al., 2014b; Graham et al., 2017). However, despite numerous studies concerning the (glacial) history of South Georgia, the timing of the LLGM Clark et al. (2009) and its corresponding ice extent have still been unclear, as dated offshore constraints for more accurate ice sheet models were lacking prior to this study (cf Graham et al., 2008; Hodgson et al., 2014b; Barnes et al., 2016).

Several studies on South Georgia's glacial history promote a restricted ice extent confined to the inner fjords during the LLGM. One of the first to introduce a model for such a restricted ice extent was Bentley et al. (2007), who relied on exposure-dating and mapping of a consistent glacial geomorphological pattern along the north-eastern coast of South Georgia, including moraines and their terrestrial equivalents in several bays around the island. This pattern suggested comparably late glacial ( $12.2 \pm 1.5$  ka BP) and interglacial ( $3.6 \pm 1.1$  ka BP) advances with similar maximum ice extents, which led both Bentley et al. (2007) and Hodgson et al. (2014a, 2014b) to interpret moraines in the inner fjord basins as markers of glacial limits during the LGM. Moraines in the outer fjord basins were assigned to a preceding glaciation. In addition to the geomorphological evidence, the presence of biological refugia on protected ridge areas on the island itself also suggested such a "little ice" (Fig. 3.3) scenario (Barnes et

al., 2016), as ice-free landscapes on South Georgia were thought to have formed as early as ~18.6 cal ka BP (e.g. Wasell, 1993; Rosqvist et al., 1999; van der Putten and Verbruggen, 2005). An explanation for restricted extent was, according to Bentley et al. (2007), limited precipitation as a result of widespread sea-ice cover, that “starved” the ice sheet, causing it to hardly advance past the coastline. However, the inner basin moraines were exposure-dated to a maximum 14.2 ka BP and are thus significantly younger than the accepted LGM timing (26 - 19 ka BP; Clark et al., 2009), leading some studies to conclude that these moraines possibly recorded post-LGM still-stands or re-advances instead (e.g. Graham et al., 2008; Graham et al., 2017), while the LGM ice-extent might have extended to the outer fjords without leaving onshore records (Bentley et al., 2007) (Fig. 3.3).

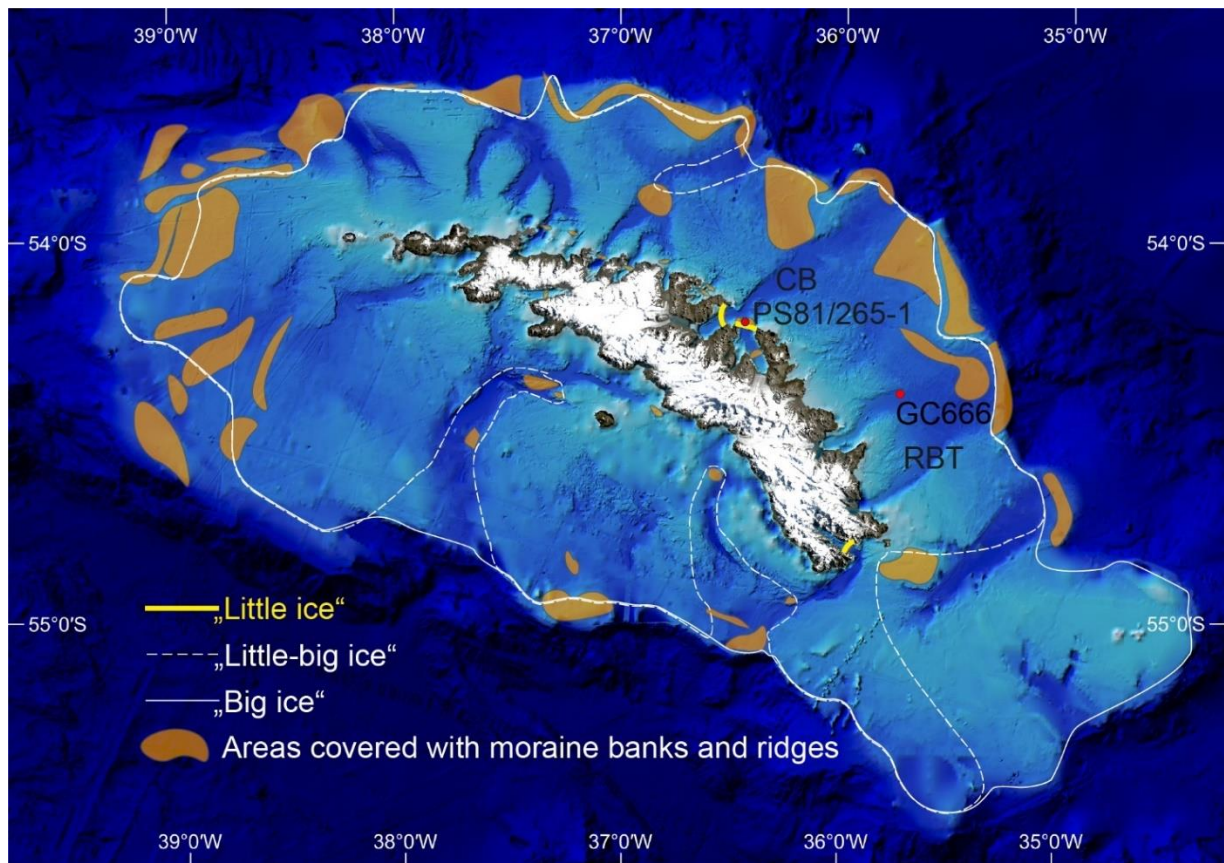


Fig. 3. 3: Overview over SG and mapped areas with moraine ridges and banks on its adjacent continental shelf. Moraine ridges and banks were mapped from Graham et al. (2008; 2017). Different scenarios of LGM ice extent are shown here as “little ice” scenario (restricted extent to the outer fjords; yellow), “big ice” scenario (shelf-wide extent everywhere on South Georgia; white) and “little-big ice” scenario (shelf-wide extent with selected ice-free areas; dashed white) after Barnes et al. (2016). Locations of sediment cores PS81/265-1 in Cumberland Bay (CB) and GC666 in Royal Bay Trough (RBT) from Graham et al. (2017) are indicated in red. DEM information for the ocean and shelf areas is based on GEBCO Compilation Group (2023), and Hogg et al. (2016); (2017) overlain by data from PS81, M134 and PS119 (Bohrmann, 2013; Bohrmann et al., 2017; Bohrmann, 2019), while the map information for SG island is derived from Landsat imagery from South Georgia GIS (2023).

In contrast to the studies promoting restricted LLGM ice-extent on South Georgia, some studies have uncovered evidence in favour of a shelf-wide glaciation (e.g. Sugden and Clapperton, 1977; Clapperton et al., 1978; Clapperton et al., 1989b; Clapperton, 1990; Graham et al., 2008; Barlow et al., 2016; Barnes et al., 2016; Graham et al., 2017; White et al., 2017). One of the first ice-sheet models for South Georgia relied on moraine positions, onshore weathering criteria e.g. along the north-eastern coast, interbedded raised beaches and till, as well as continental shelf morphology and evidence of extensive scouring above ~200 m water depth (Stone, 1974; Sugden and Clapperton, 1977; Clapperton et al., 1989b; Clapperton, 1990). The model suggested a shelf-wide ice extent prior to 18 ka BP, based on correlation with a drop in temperature investigated by Hays et al. (1976), that was related to a major global glaciation and associated sea-level lowstand that allowed for widespread ice grounding (Sugden and Clapperton, 1977; Clapperton et al., 1978; Clapperton et al., 1989b; Clapperton, 1990). The discovery of a complex shelf morphology, resulting in the mapping of over 2500 glacial landforms from bathymetric data, also supported a shelf-wide glaciation during the LGM (Graham et al., 2008; Graham et al., 2017), which was later confirmed by glacial isostatic adjustment models (GIA; Barlow et al., 2016). Streamlined landforms across the shelf, as well as multiple moraines at the shelf edge (Fig. 3.3), suggested several occasions, including the LGM, during which ice advanced all the way to the shelf edge (Graham et al., 2008; Graham et al., 2017). At the same time, recessional moraines on shallow shelf areas showed that grounded ice was not restricted to outlet glaciers or ice streams in the troughs. Accordingly, the shelf morphology overall implied faster-flowing ice with focused erosion in the troughs and slower ice flow with insignificant erosion or even aggradation on shallow banks for the LGM (Graham et al., 2008; Graham et al., 2017), defined as “big-ice” scenario (Fig. 3.3) by Barnes et al. (2016). Nevertheless, the seabed diversity study by Barnes et al. (2016) further refined this hypothesis and suggested that, while ice advanced to the shelf edge in the majority of locations around the island, comparatively high biodiversity in some cross-shelf troughs and on the far eastern shelf were an indicator for ice-free areas, where ice extent was less extensive, defined as a “little-big ice” scenario. This chronology was supported by rock hardness measurements on glacial deposits on ridgeline summits on the north-eastern side (Cumberland Bay area; White et al., 2017).

Evidence is scarce regarding glacial and deglaciation chronology around South Georgia. Indeed, the only relatively well-constrained chronology relying on data from the continental

shelf is from the Cumberland Bay (CB; Fig. 3.3) and Royal Bay Troughs (RBT; Fig. 3.3) in the north-east of South Georgia, where outer shelf moraines suggest a shelf-wide glaciation, followed by relatively rapid retreat into the fjords (Graham et al., 2017). A sediment core from Royal Bay Trough on the mid-continental shelf north-east of South Georgia (GC666, Fig. 3.3) and associated sub-bottom profiler data suggested an onset of trough sedimentation around 18 ka BP, while the presence of underlying subglacial till indicated erosion of pre-existing trough fill by the LGM ice sheet. This supports a maximum extent prior to 18 ka BP and is also in accordance with lake deposits from a nearby Peninsula, where autochthonous organic-rich lake sedimentation started around 18.6 cal ka BP, and thus constrained deglaciation onset on the island itself (Rosqvist et al., 1999).

Retreat continued until at least 15.2 cal ka BP, when renewed cooling and re-advance of the Antarctic Cold Reversal (ACR; 14.5 - 12.8 ka BP; Jouzel et al., 1995; Zech et al., 2007; Moreno et al., 2009; García et al., 2012; Jomelli et al., 2014; Stansell et al., 2015; Pedro et al., 2016; Graham et al., 2017; Stewart et al., 2021; Reynhout et al., 2022) led to the formation of a push moraine crossing the outer basin of East Cumberland Bay (PS81/265-1, Fig. 3.3, dated to max. 15.4 - 14.8 ka BP, Graham et al. (2017)). Re-advance ceased around 13.3 cal ka BP (PS81/265-1, dated to max. 13.5 - 13.2 ka BP, recalibrated to 12.8 cal ka BP), when ice had ungrounded from the outer basin moraine and sedimentation changed in the nearby RBT (GC666, Fig. 3.3, dated to max. 14.8 - 12.5 ka BP, Graham et al. (2017)). These dates indicate an early ACR and are in accordance with Bakke et al. (2021), which exposure-dated a maximum glacier position in East CB to ~13 ka.

After the ACR, ice retreated towards the island during the transition to the Holocene, reaching the coastline around 10 ka BP (e.g. Clapperton et al., 1989b). Since then, the tidewater glaciers have likely only been fluctuating within the fjords (Bentley et al., 2007; Hodgson et al., 2014a; Graham et al., 2017; Bakke et al., 2021) and thus sustainably exposed the whole continental shelf to ocean currents until today. Today, glaciers still cover large parts of the island and influence the marine realm significantly due to their meltwater run-off.

Consequently, the two investigated shelf areas Drygalski Fjord System (DFS) and King Haakon Trough System (KHTS) have been and still are proximally fed by numerous tidewater glaciers (Fig. 2.1). DFS is mostly fed by two marine-terminating glaciers, Risting and Jenkins Glaciers, as well as some minor tributaries along the fjord. In contrast, KHTS is fed by a multitude of



glaciers that, inter alia, drain from Kohl Plateau and into King Haakon Bay (KHB; e.g. Briggs Glacier), Jossac Bight (JoB; e.g. Esmark Glacier, Keilhau Glacier, Jewell Glacier), Newark Bay (NB; e.g. Lancing Glacier, Christensen Glacier, Kjerulf Glacier) and Jacobsen Bight (JaB; e.g. Christophersen) (nomenclature following South Georgia GIS, 2023). The locations of the KHTS feeding glaciers are presented in Chapters 5 and 6.

#### 4. Manuscript I: Glacimarine sediments from outer Drygalski Trough, sub-Antarctic South Georgia – evidence for extensive glaciation during the Last Glacial Maximum

This is the accepted manuscript version; published in *Quaternary Science Reviews*, Lešić et al. (2022)

Available under the DOI: <https://doi.org/10.1016/j.quascirev.2022.107657> under the license CC-BY-NC-ND 4.0: <https://creativecommons.org/licenses/by-nc-nd/4.0/legalcode.en>

Lešić, Nina-Marie<sup>1,2</sup> (nlesic@marum.de); Streuff, Katharina Teresa<sup>2</sup> (kstreuff@marum.de); Bohrmann, Gerhard<sup>2</sup> (gbohrmann@marum.de); Kuhn, Gerhard<sup>1,2</sup> (gerhard.kuhn@awi.de)

*1 Alfred Wegener Institute (AWI), Helmholtz Centre for Polar and Marine Research, Am Alten Hafen 26, 27568 Bremerhaven, Germany*

*2 MARUM, Centre for Marine Environmental Sciences, and Faculty of Geosciences, University of Bremen (UoB), Klagenfurter Str., D-28359 Bremen*

Corresponding author: Lešić, Nina-Marie (nlesic@marum.de)

Keywords:

Quaternary; LGM; Glaciation; South Atlantic; Geomorphology, glacial; Sedimentology-marine cores

### **Abstract**

South Georgia, one of the largest sub-Antarctic islands, is located within the Southern Ocean and is influenced by the moisture-supplying Southern Westerlies and the Antarctic Circumpolar Current, which are highly susceptible to Southern Hemisphere climate variability. Its unique location causes South Georgia's remaining ice masses to react sensitively to climate change, resulting in highly dynamic ice cap waxing and waning, as well as in geomorphological and sedimentological changes on the island and its continental shelf. Sediments around the island have been archiving this ice cap behaviour since at least the Last Glacial Maximum (LGM) and are therefore an important target to investigate past ice cap evolution and climate. Despite several interdisciplinary studies on land and in coastal areas, much of the glacial history is still poorly constrained due to a lack of offshore data. This study presents the, thus far, most distal marine sediment succession from outer Drygalski Trough on the mid-continental shelf of South Georgia. Composite multi-proxy-analyses, together with radiocarbon dating, sub-

bottom profiler and high-resolution bathymetric data provide first insights into the evolution of a large glacial trough south of South Georgia since the LGM. Several moraines close to the shelf edge indicate shelf-wide glaciation during the local LGM, which, based on extrapolation of the oldest reliable radiocarbon date, occurred before 30 ka BP at the earliest. Basal stratified diamicton at the core site was interpreted as waterlain till deposited in a subglacial cavity with restricted seawater access and suggests grounding zone-proximal sedimentation in the early phases of deglaciation. The ice margin remained stable until ~17.5 cal ka BP, when ice quickly retreated from the mid-continental shelf and sedimentation at the core site was dominated by hemipelagic suspension settling with some iceberg melting. Further retreat was interrupted by a local ice re-advance and associated increased hinterland erosion during the Antarctic Cold Reversal (14.5 – 12.8 ka), as indicated by peak sedimentation rates (>190 cm ka<sup>-1</sup>) between 13.4 and 12.4 cal ka BP. In contrast, the continuous deposition of ice-distal to open-marine mud at rates of only ~30 cm ka<sup>-1</sup> throughout the Holocene indicate that any other LGM-subsequent glacier re-advances reached significantly lesser extents and were probably confined to the fjord. Our data provide new evidence in support of a shelf-wide glaciation during the LGM and suggest rapid, but stepwise ice retreat during deglaciation.

#### 4.1. Introduction

The study of marine sediments from previously glaciated continental margins offers valuable insight into the past evolution of (marine-based) ice sheets. Apart from providing information about past depositional environments, (glaci-)marine sedimentation, and the dynamics of ice streams and tidewater glaciers (e.g. Domack, 1990; Evans and Pudsey, 2002; Kilfeather et al., 2011; Kuhn et al., 2017; Streuff et al., 2017a; Streuff et al., 2017b), marine sediments also archive past climatic and oceanographic changes (e.g. Schmieder et al., 2000; Denis et al., 2006; Moros et al., 2006; Ślubowska-Woldengen et al., 2007; Hass et al., 2010). They are therefore not only relevant for the development of ice sheet models that assess potential ice sheet and sea level response to ongoing global warming and rates of (glaci-)isostatic adjustment (cf. Clark et al., 2009; Hodgson et al., 2014a; Patton et al., 2015; Barlow et al., 2016), but can also be used to understand the influence of ocean currents and water mass properties

on present ice masses (e.g. Lloyd, 2006; Andresen et al., 2010; McCave et al., 2014; Xiao et al., 2016; Wu et al., 2021). While their contribution to global sea level response is considered minor (Barlow et al., 2016; Graham et al., 2017), sub-Antarctic ice caps mark the climatically more sensitive northern limit of the large, more isolated Antarctic system (sensu Barlow et al., 2016; Jomelli et al., 2017; Bakke et al., 2021). Understanding their past extents, retreat, and timing in the marine realm is hence crucial to evaluate and refine ice sheet models (Barlow et al., 2016; Graham et al., 2017).

South Georgia, one of the largest islands in the sub-Antarctic, is located in a climatically dynamic setting within the core belt of the Southern Westerly Winds (Moreno et al., 2018; Bakke et al., 2021) and between the Antarctic Circumpolar Current's (ACC) Polar Front to the north and the Southern Antarctic Circumpolar Current Front to the south (Fig. 4.1b) (Orsi et al., 1995). Shifts of the Westerlies and the oceanographic fronts induced by a changing climate thus cause the remains of the South Georgia Ice Cap (SGIC) to react sensitively to atmospheric changes, water mass configuration and ocean currents in the sub-Antarctic (cf. Gersonde et al., 2005; Toggweiler et al., 2006; Boex et al., 2013; Kohfeld et al., 2013; Sime et al., 2013; Gille et al., 2016; Waugh et al., 2020; Bakke et al., 2021; Wu et al., 2021). As a result, the marine sediments off the coast of South Georgia are of particular interest to study the growth and decay of lower-latitude ice masses during and since the LGM (26.5-19 ka BP; Clark et al., 2009). Nonetheless, most geological studies from South Georgia have focused on the reconstruction of LGM ice extent, as well as late Pleistocene and Holocene ice dynamics from the terrestrial and near-shore environment (Clapperton, 1971; Clapperton and Sugden, 1980; Clapperton et al., 1989b; Rosqvist et al., 1999; Bentley et al., 2007; Barlow et al., 2016; Graham and Hodgson, 2016; White et al., 2017; Oppedal et al., 2018; Bakke et al., 2021), while only few studies exist from the marine environment, including the sedimentary archives and the submarine geomorphology of the shelf (Sugden and Clapperton, 1977; Graham et al., 2008; Hodgson et al., 2014a; Graham and Hodgson, 2016; Graham et al., 2017). The scarcity of marine-based investigations and especially the lack of radiocarbon ages severely limits our understanding of the offshore depositional environments around South Georgia (cf. Graham et al., 2008; Hodgson et al., 2014b; Barnes et al.,

2016), which, in turn, has hampered accurate reconstructions of sub-Antarctic glacial dynamics.

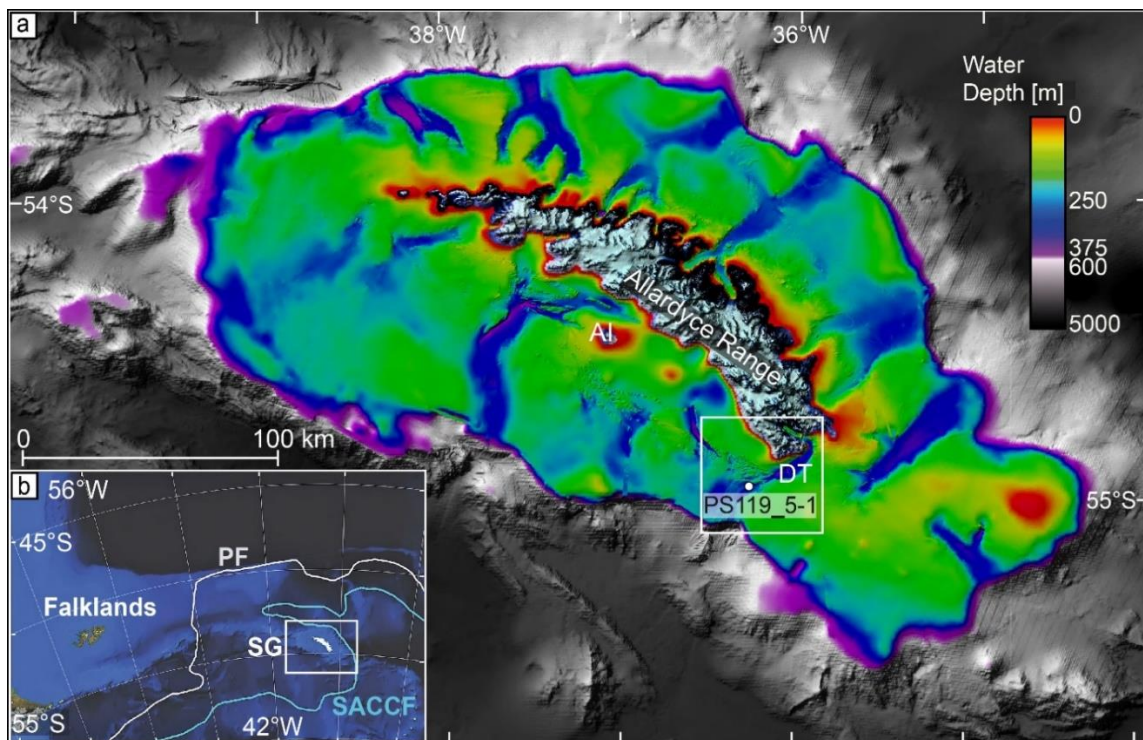


Fig. 4. 1: a) South Georgia Island with the Allardyce mountain range and the surrounding shelf bathymetry and the study area (see white box in a), the core site (white point). “DT” marks Drygalski Trough and “AI” the Annenkov Island b) Framed geographic and oceanographic position of South Georgia (SG) in the South Atlantic with respect to the Polar Front (PF) and the Southern Antarctic Circumpolar Current Front (SACCF). Frontal positions were modified after Graham et al. (2017). This map is based on GEBCO Compilation Group (2021) bathymetry data and data collected during PS81 (ANT-XXIX-4), M134 and PS119 (Bohrmann, 2013; Bohrmann et al., 2017; Bohrmann, 2019)

Here, we present research data of the first marine sediment core from the mid-continental shelf south of South Georgia and provide, to our knowledge, the oldest radiocarbon age around South Georgia thus far. The core archives the full sedimentary sequence from the LGM to the contemporary marine environment, including a time of renewed cooling known as the Antarctic Cold Reversal (ACR; 14.5-12.8 ka BP; Jouzel et al., 1995; Zech et al., 2007; Moreno et al., 2009; García et al., 2012; Jomelli et al., 2014; Stansell et al., 2015; Pedro et al., 2016; Graham et al., 2017; Stewart et al., 2021; Reynhout et al., 2022), and the subsequent Holocene (after 11.7 ka, Walker et al., 2009), and is therefore suitable to test previous hypotheses of extensive LGM ice and the following deglaciation (Clapperton et al., 1989b; Rosqvist et al., 1999; Bentley et al., 2007; Graham et al., 2008; Hodgson et al., 2014a; Hodgson et al., 2014b; Barlow et al.,

2016; Barnes et al., 2016; Graham et al., 2017; White et al., 2017). This study is based on bathymetric and sub-bottom profiler data from the continental shelf as well as dated lithofacies, all of which support shelf-wide glaciation during the LGM (Clapperton et al., 1989b; Graham et al., 2008; Barlow et al., 2016; Barnes et al., 2016; Graham et al., 2017) and provide further insights into ice cap behaviour during the subsequent deglaciation.

## 4.2. Study area

South Georgia is positioned between the ACC's Polar Front and the Southern Antarctic Circumpolar Current Front at approximately 54-55° S and 35.5-38° W (Fig. 4.1b). Its coast and continental shelf show evidence of intense glacial influence and are characterised by numerous fjords and cross-shelf troughs (Fig. 4.1a; Clapperton, 1971; Graham et al., 2008; Hodgson et al., 2014a). Today, South Georgia is still covered by ice cap remains, whose outlet tidewater glaciers dominate the fjord heads (Cook et al., 2010; Farías-Barahona et al., 2020).

The island is strongly influenced by the Southern Westerlies (Moreno et al., 2018; Bakke et al., 2021), which, besides driving the ACC (Orsi et al., 1995), provide moisture and thus directly control the distribution of temperature and precipitation on South Georgia. As a result, these winds not only play a key role in sustaining the SGIC (Strother et al., 2015; Waugh et al., 2020; Bakke et al., 2021), but also affect water masses and primary productivity on the continental shelf (Matano et al., 2020). Recent observations showed that the Allardyce mountain range (Fig. 4.1a) serves as an orographic barrier and leads to a declining south-north gradient in precipitation, which probably causes glaciers on the north-eastern coast of South Georgia to retreat faster than in the south-west (Gordon et al., 2008; Cook et al., 2010; Farías-Barahona et al., 2020).

Our study area is located in the Drygalski Fjord system (DFS), between ~54°45'-55°7' S and 35°48'-36°30' W, on the continental shelf south of South Georgia (Fig. 4.1a). The DFS is one of several fjord systems of South Georgia and is separated into the E-W-trending Drygalski Fjord (DF) and the adjoining NE-SW-trending Drygalski Trough. The fjord is approximately 14 km long, 0.9 km wide in the inner fjord to 3.5 km at the fjord mouth, and up to 220 m deep. It is fed by the marine-terminating Risting and Jenkins Glaciers at the fjord head and is further influenced by several smaller tributaries,

including the tidewater glaciers Philippi and Dead End Glaciers (cf. Cook et al., 2010; Hodgson et al., 2014a).

Beyond the coastline, the fjord merges into Drygalski Trough (DT; Fig. 4.1a), which is about 50 km long, 3-15 km wide, and up to 350 m deep. DT extends all the way to the shelf edge and represents one of several glacially-eroded cross-shelf troughs on the continental shelf around South Georgia (Fig. 4.1a).

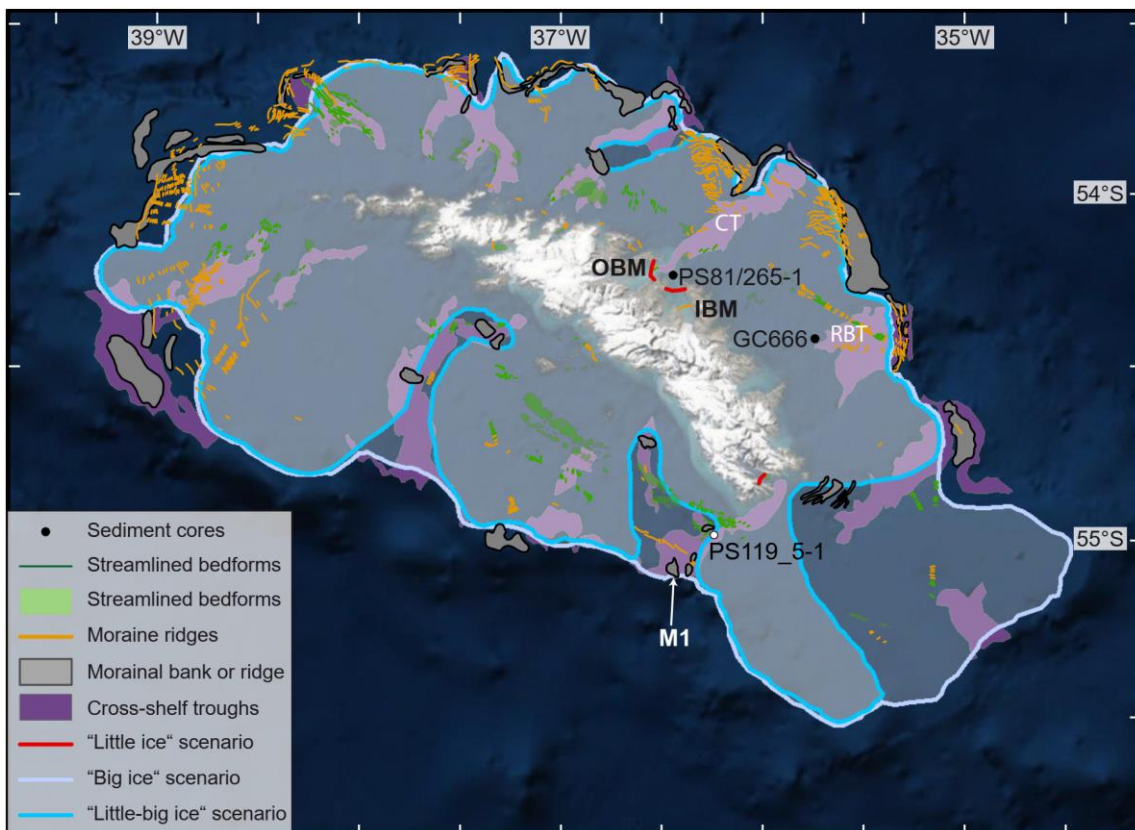


Fig. 4. 2: Overview over South Georgia and the glacial geomorphology on its adjacent continental shelf. Landforms were mapped from Graham et al. (2008; 2017) with IBM = Inner Basin Moraine and OBM = Outer Basin Moraines. Different scenarios of LGM ice extent have been debated in the literature and are shown here as "little ice" scenario (restricted extent to the outer fjords; red), "big ice" scenario (shelf-wide extent everywhere on South Georgia; light blue) and "little-big ice" scenario (shelf-wide extent with selected ice-free areas; blue) after Barnes et al. (2016). Locations of sediment cores PS81/285-1 in Cumberland Bay (adjacent to Cumberland Trough (CT)) and GC666 in Royal Bay Trough (RBT) from Graham et al. (2017) are indicated as black dots.

Repeated periods of climatically-controlled ice cap waxing and waning and at least one advance all the way to the shelf edge have formed streamlined bedforms, moraine ridges and deeply incised cross-shelf troughs (Figs. 4.1 and 4.2) (Sugden and Clapperton, 1977; Graham et al., 2008; Hodgson et al., 2014a; Hodgson et al., 2014b; Graham et al., 2017). However, these features were never clearly associated with the LGM. Instead,

numerous studies suggested different possible LGM ice extent scenarios (Fig. 4.2), which were summarised by Barnes et al. (2016) and are i) the “little ice” scenario with ice extent restricted to the fjords (Bentley et al., 2007; Hodgson et al., 2014a; Hodgson et al., 2014b), ii) the “big ice” scenario with ice extending all the way to the shelf edge, and iii) the “little-big ice” scenario, that suggests grounding to the continental shelf edge with the exception of some ice-free regions, especially on the eastern continental shelf and within some of the troughs. While the “little ice” scenario relied on fjord geomorphology and terrestrial exposure and radiocarbon ages, the “big ice” scenario was based on undated moraines at the shelf edge (see e.g. M1 in Fig. 4.2) (Sugden and Clapperton, 1977; Clapperton et al., 1978; Clapperton et al., 1989b; Graham et al., 2008). The “little-big ice” scenario was based on the ongoing re-establishment of seabed diversity and recolonisation on the shelf and was favoured by Barnes et al. (2016). Their findings were later confirmed and supported by glacial isostatic adjustment modelling (Barlow et al., 2016), by rock hardness measurements on glacial deposits on ridgeline summits in the north of South Georgia (White et al., 2017), by shelf-wide geomorphological maps (Graham et al., 2017), and by estimates of trough sedimentation onset in Royal Bay Trough (RBT; Fig. 4.2) (Graham et al., 2017).

However, dated offshore constraints for the LGM are still lacking (cf. Graham et al., 2008; Hodgson et al., 2014b; Barnes et al., 2016) with the oldest published marine date relating to the Late Pleistocene (13.9 ka BP, recalibrated, see also Table 4.1) in Royal Bay Trough from northern South Georgia (Graham et al., 2017). Studies on the subsequent deglaciation, and especially the Holocene (Clapperton et al., 1978; Clapperton et al., 1989a; Clapperton et al., 1989b; Oppedal et al., 2018; Berg et al., 2019; Bakke et al., 2021), also derive mainly from the northern shelf, where they revealed one significant ice readvance during the ACR inferred from only two gravity cores (PS81/265-1, GC666; Fig. 4.2) (Graham et al., 2017). Consequently, and since thus far no ice-proximal glacimarine sediments have been recovered from the shelf, much of the (glacial) history of South Georgia, including the timing of the Local Last Glacial Maximum (LLGM; Clark et al., 2009) and the subsequent deglaciation prior to the ACR, remains largely speculative.



### 4.3. Methods

Gravity core PS119\_5-1 (54° 59.136' S, 36° 13.884' W) is 822 cm long and was taken close to a bathymetric high from a water depth of 290 m during the RV Polarstern cruise PS119 in 2019 (Bohrmann, 2019). The penetration depth of the coring device was 10 m, implying core compression of ~18 % and/or potential core loss. After retrieval, the core was cut into 1 m-long sections, which were logged for magnetic susceptibility (volume-corrected), wet bulk-density, and p-wave velocity, using a GEOTEK Multi-Sensor Core Logger (MSCL) with a Bartington 140 mm magnetic susceptibility loop sensor (Bohrmann, 2019), and were stored at ~4° C. The core sections were split, photographed, and logged by assigning lithofacies. Sediment colour was determined using the Munsell Soil Colour Chart, while Computer Tomography Scans acquired with the AWI-based Rotating X-ray CT system (RXCT) from Geotek Ltd. provided information on internal sediment structures. Shear strength was measured with a hand-held shear vane approximately every ten centimetres between 820 and 439 cm core depth, but values (ranging from 3 to 18 kPa, Fig. A1 in the supplementary material) were considered inaccurate due to artefacts caused by the gravel fraction, and are therefore without relevance for past ice-stream overburden pressure. Two sets of sediment samples were taken in 10-cm intervals (occasionally 5-15 cm): 1) ~8 ml of sediment (extracted using 1.5-cm diameter syringes), and 2) ~1 cm-thick sediment slabs. A depth error of ±1 cm has to be considered. Syringe samples were weighed, freeze-dried, and weighed again to determine the water content. The samples were then ground and measured for i) dry bulk density (DBD) using a Micromeritics AccuPyc II 1340 gas pycnometer at AWI, for ii) total carbon (TC) and (iii) total organic carbon (TOC), both measured with a UoB-based LESO CS 744 through combustion and carbon-specific infrared wavelength absorption. TOC percentage results were corrected with a sample-specific factor that represents pre-analysis carbonate removal from the samples and were used for carbonate content calculation. 18 of the syringe samples were analysed for (iv) biogenic silicate (bSiO<sub>2</sub>), using the leaching method after Müller and Schneider (1993). Note that bSiO<sub>2</sub> is not equivalent to biogenic opal. The latter can be calculated with a factor of 100/90, assuming 10 wt% bound water content that is not accounted for in bSiO<sub>2</sub> (Müller and Schneider, 1993). Sediment slabs were dispersed in demineralised water and sieved for

grain size analysis (mud <63  $\mu\text{m}$ , sand 63  $\mu\text{m}$ -2 mm, and gravel >2 mm). We define all grains >2 mm as ice-rafted debris (IRD) and used the sieved gravel fraction to count IRD grains, normalised to a sample volume of 10  $\text{cm}^3$ .

Benthic foraminifera and bivalve fragments were isolated from the sand and gravel fraction of selected sediment depths and, together with two intact gastropods extracted during sampling, were used for Accelerator Mass Spectrometry (AMS)  $^{14}\text{C}$  dating at AWI's MICADAS laboratory (Mollenhauer et al., 2021). For quality control, the gastropods and the foraminifera *Buccella inusitata* (Andersen, 1952) and *Cassidulinoides parkerianus* (Brady, 1881) were dated separately and showed only minor age deviations within the reported lab error. This ensured consistent age determination from variable material from the same depths and the radiocarbon dates presented in this study are therefore considered analytically precise and comparable for different biogenic carbonate. They show lab errors of  $\pm 72$ -90  $^{14}\text{C}$  a for Holocene ages and  $\pm 103$ -359  $^{14}\text{C}$  a for Pleistocene ages.

Radiocarbon ages (Table 4.2 and A1) were calibrated in PaleoDataView (Langner and Mulitza, 2019) with the IntCal20 calibration curve (Reimer et al., 2020) and Marine Reservoir Ages (MRAs) modelled with a temporal resolution of 50 a (Butzin et al., 2019, 2020; Heaton et al., 2020). The present MRA of 900 a fits well with the weighted mean of four surface sample ages (meanMRA=812 a), and the used MRAs for the Holocene are based on three simulations. Median absolute deviations (MAD) lie within the laboratory error ( $\pm 60$ -90 a) and are therefore neglected. Pleistocene MRAs are based on nine simulations and show MADs of 700-780 a. These are not included due to inferred artificial jumps at the Pleistocene/Holocene boundary, but need to be considered for age interpretation. The reported Pleistocene age values are rounded to 100 a. Radiocarbon ages discussed in the text are calendar kiloyears before present (cal ka BP), where before present is equal to 1950 AD. The age model (script adapted from De Vleeschouwer and Zeeden, 2021) was constructed in R (R Core Team, 2021; R Studio Team, 2021) using the 'Bchron' programme after Haslett and Parnell (2008). It provides modelled ages for undated intervals with a 2.5 % Lower and a 97.5 % Upper Confidence Level (see "A1. Methods" in the supplementary material). Linear sedimentation rates were calculated between dated depths and significant undated lithofacies boundaries

using modelled ages. Since we cannot ascertain the degree of core compression, sedimentation rates will be reported for the logged depths. Three reverse radiocarbon ages, determined on mechanically altered material at 816 cm (one sample) and 625 cm (two samples) dated to >37.9 ka BP and were therefore excluded from both calibration and age model.

For the analysis of large-scale depositional environments bathymetry and sub-bottom profiler data were used. They were acquired on three separate cruises: PS81 (ANT-XXIX-4) and PS119 with RV Polarstern in 2013 and 2019, respectively, and M134 with RV Meteor in 2017 (Bohrmann, 2013; Bohrmann et al., 2017; Bohrmann, 2019). Bathymetry data from the Polarstern cruises were gathered with a hull-mounted Teledyne ATLAS HYDROSWEEP DS3 multibeam echo sounder operated at frequencies of 15 kHz (PS81) and between 14 and 17 kHz (PS119) with 600 beams on average. M134 bathymetry data were collected using a Kongsberg Maritime EM710 multibeam echo sounder with 432 beams for water depths <500 m, and a Kongsberg Maritime EM122 with 256 beams for water depths exceeding 500 m. The shallow-water echo sounder was operated at a frequency between 70 and 100 kHz, the deep-water echo sounder at a nominal frequency of 12 kHz. Bathymetry data from both cruises were processed using MB-System Suite (Caress and Chayes, 2017) and gridded to a resolution of 100 m (4 m for the Drygalski Fjord system). They were visualised and interpreted with the software QPS Fledermaus v7.7.2 and Global Mapper v20.1, while maps were made using ESRI ArcMap™ 10.4.1 and QGIS 3.16.15.

Sub-bottom profiler data were collected with a parametric Teledyne ATLAS PARASOUND P70 sub-bottom profiler on all cruises. The systems were operated at a secondary low frequency of ~4 kHz in a narrow 19kHz beam for high lateral resolution (Bohrmann, 2019). Sub-bottom profiler data were visualised and interpreted using SMT The Kingdom Suite 2020. All hydroacoustic systems were frequently calibrated during data acquisition using sound velocity profiles from both a probe and repeated Conductivity-Temperature-Depth measurements.

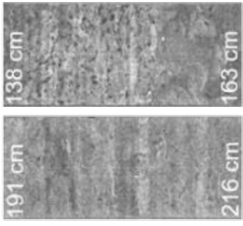

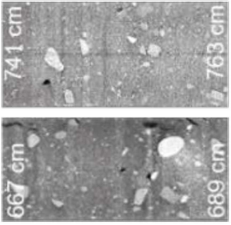
## 4.4. Results

### 4.4.1. Lithology

We define three lithofacies for PS119\_5-1 from bottom to top, which were classified according to a refined nomenclature for glacimarine sediments (Eyles et al., 1983; Streuff et al., 2022) and the relative abundance of dropstones (d), sand (S) and bioturbation (b). These are stratified (st) diamicton (Dm), hence *Dmst*, laminated (l) mud (F) with sand and dropstones (*Fl(d,S)*), and stratified, partially bioturbated sandy mud with dropstones (*Fst(S,d,b)*; Table 4.1).

*Dmst* (822-617 cm) consists of grey (N5/) stratified diamicton with a sandy matrix, black (2.5Y 2/0) sand patches and (sub-)angular pebbles (Table 4.1; Fig. 4.3). The stratification is imparted by almost regularly-spaced cm-thick IRD-rich sand layers (>50 wt% sand) alternating with IRD-rich clayey silt layers. Larger IRD clasts seem to show a preferentially horizontal orientation within the core (Fig. A3-11). Mud content is considerably lower than in overlying facies, with a maximum of ~45wt% (Fig. 4.3). High magnetic susceptibility (MS) varies between 2420 and 6600  $\times 10^{-6}$  SI units, roughly matches the high sand content (40-70 wt%), and is also elevated where IRD occurs. IRD content is highly variable throughout the facies, ranging from 1-29 wt% and 5.5-92.5 grains per  $10 \text{ cm}^{-3}$  (Fig. 4.3). Water content is low (13-21 wt%) and dry-bulk density (DBD) values vary between 1.6 and 1.86  $\text{g cm}^{-3}$ . Maximum carbonate values in the core occur in *Dmst* (1.61 and 3.3 wt%), but few microfossils are present (Fig. 4.3). TOC and bSiO<sub>2</sub> are low with values of 0.21-0.35 wt% and 0.81-2.69 wt%, respectively (Fig. 4.3). *Dmst* was dated to 24.3 cal ka BP at 816 cm (Table 4.2 and A1), while the upper boundary was dated to 17.5 cal ka BP at 617 cm.

Table 4.1: Characteristics and exemplary CT scan slices of the three identified lithofacies in gravity core PS119-5-1

Depth (cm)	CT Scan slice	Lithofacies code	Lithology	Sedimentary structures	Description	Physical properties	Palaeoenvironment
541-0		Fst(S,d,b)	Sandy mud	st	Stratified sandy mud with dropstones at the base, bioturbated intervals and occasional sand-rich layers	MS = 690-3400 10 <sup>-6</sup> SI units, DBD = 0.69-1.37 gcm <sup>-3</sup> Water content = 26-53 wt% TOC = 0.36-0.69 wt% Carbonate = 0.13-1.61 wt%	Open-marine environment, Declining glacimarine influence, Possible influence by shelf currents
617-541		Fl(d,S)	Gravelly mud	l-lw	Laminated clayey mud with dropstones, low sand content	MS = 1490-2600 10 <sup>-6</sup> SI units DBD = 0.73-0.98 gcm <sup>-3</sup> Water content = 38-50 wt% TOC = 0.49-0.56 wt% Carbonate = 1.22-1.84 wt%	Iceberg-influenced zone
822-617		Dmst	Stratified diamicton	st	Stratified diamicton with dropstones	MS = 2420-6600 10 <sup>-6</sup> SI units DBD = 1.6-1.86 gcm <sup>-3</sup> Water content = 13-21 wt% TOC = 0.21-0.35 wt% Carbonate = 1.61-3.27 wt%	Grounding zone-proximal glaciomarine environment

Based on its diamictic composition, its stratified appearance, and the inferred late glacial age, *Dmst* is interpreted as a waterlain till. High sand and gravel contents, along with exceptionally high MS values indicate strong terrestrial input. The almost cyclic change between coarser sand layers and finer clayey-silt layers resembles deposits from turbid waters immediately in front of a tidally-influenced glacier grounding zone (Anderson et al., 1980; Smith et al., 2019). These properties, as well as the low shear strength (3-18 kPa, Fig. A1), are also similar to waterlain tills described from other glacimarine environments (Smith et al., 2011; Pieńkowski et al., 2012; Pieńkowski et al., 2013), which supports our interpretation of ice margin-proximal sedimentation. The comparably low water content could be caused by either predominating coarse grain sizes or glacial overburden. The lack of evidence for substantial overburden and the increase of water content with decline of coarse grain sizes along the core indicates a grain size effect on the water content (Fig. 4.3). Deposition reminiscent of grounding-zone proximal environments is also indicated by low shear strength, aligned clasts (Fig. A9-11), as well as TOC contents (0.21-0.35 wt%) and TC/N ratios (~23, Fig. A2) comparable to those observed in front of Antarctic grounding zones (TOC = 0.13-0.35 wt%; TC/N = 13-33; Smith et al., 2019). Overall low mud contents with a predominating silt component indicate that a large portion of fines may have been removed by tidal currents (Kuhn et al., 2017).

Low TOC and bSiO<sub>2</sub>, as well as the presence of only few intact foraminifera attest to some, albeit low, biogenic productivity (Smith et al., 2019). The enhanced carbonate content compared to overlying facies seems to contradict the low biogenic productivity proxies and may hence indicate increased supply of terrigenous carbonates (e.g. marble). Such input would mask the overall low biogenic carbonate content, which is implied by the rare carbonate microfossils and scarce biogenic, mechanically eroded carbonate particles. Sediment reworking and transport, possibly by ice, is implied by mechanical erosion on carbonate particles of marine biogenic origin that produced three reverse ages >37.9 ka BP.

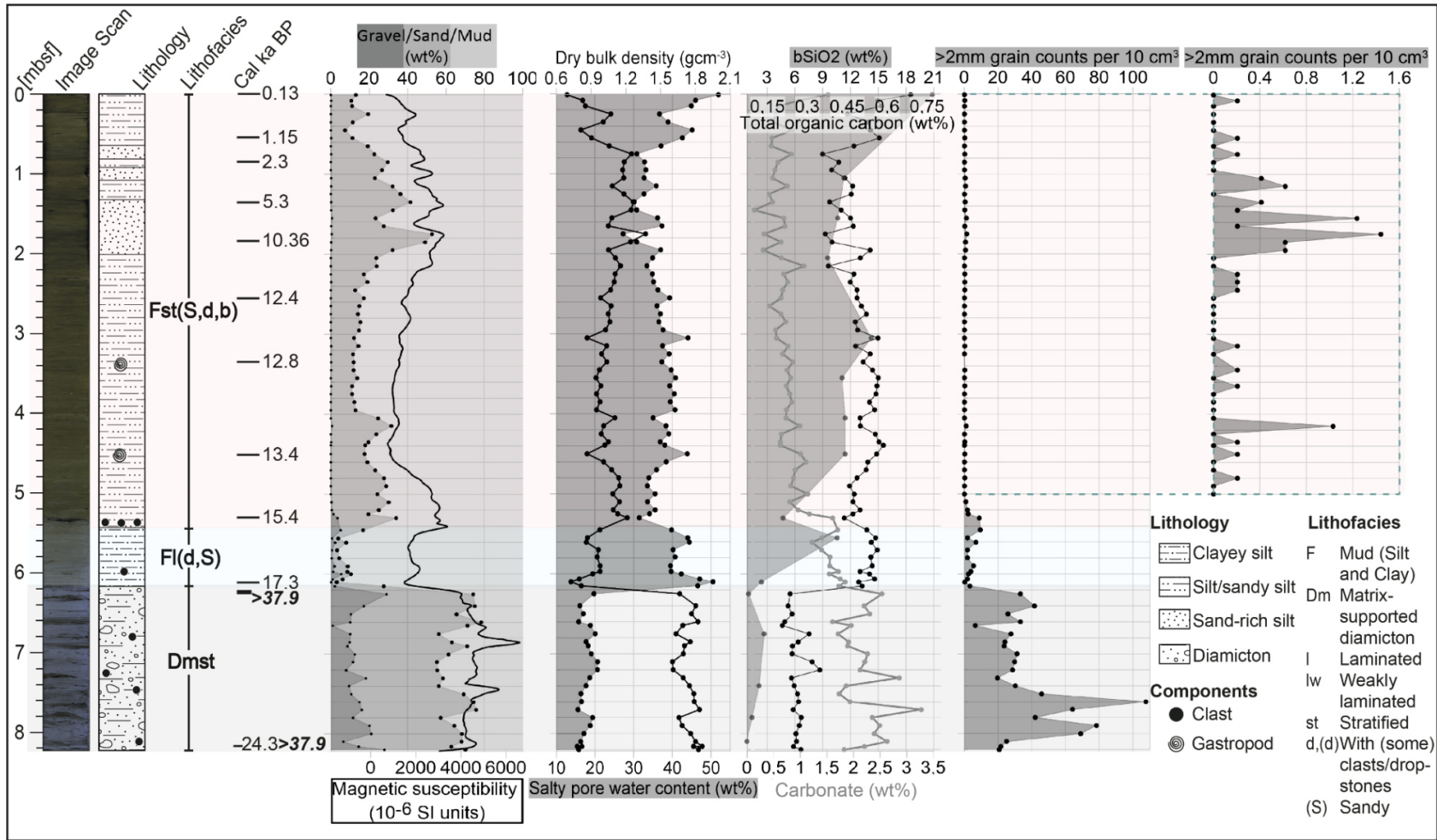


Fig. 4.3: Lithological analyses from gravity core PS119-5-1 including three defined lithofacies (colored), calibrated radiocarbon ages, grain size distribution, Magnetic susceptibility, the biogenic productivity proxies TOC and bSiO<sub>2</sub>, carbonate, physical properties and IRD grain size counts. Image scans, lithofacies logs and radiocarbon ages are shown for reference. Ages in italic bold font are uncalibrated <sup>14</sup>C ages, reported in ka. Note that the rightmost panel shows the grain size counts in the top 500 cm of the core at a higher resolution.

*Fl(d,S)* directly overlies *Dmst* and extends from 617-541 cm. It has a gradational lower contact which is characterised by a continuous up-core decrease in MS (Fig. 4.3). *Fl(d,S)* consists of weakly laminated to stratified (mm- to cm-scale) dark grey (5Y 4/1), sand-bearing clayey silt (83-97 wt% mud). The sand content is generally <10 wt% and gravel-sized IRD decreases to a maximum of 5 wt% ( $0.18-8.13 \text{ grains} \cdot 10 \text{ cm}^{-3}$ ) while larger IRD is still abundant. The facies is characterised by an overall lower MS compared to *Dmst* ( $1490-2600 \times 10^{-6}$  SI units, Fig. 4.3) that peaks at 593.5 cm. However, sand content and MS increase considerably at both facies boundaries to 11-25 wt% and  $>2180 \times 10^{-6}$  SI units, respectively (Fig. 4.3). Water content is moderate to high (38-50 wt%) and DBD low to moderate ( $0.73-0.89 \text{ gcm}^{-3}$ ). TOC increases to 0.49-0.56 wt% above the lower facies contact (Fig. 4.3).

TOC is accompanied by bSiO<sub>2</sub> and a sudden abundance of the foraminifera *Fursenkoina fusiformis* (Williamson, 1858) and bivalve fragments at 615 cm (17.3 cal ka BP). The carbonate signal is significantly weaker than in the underlying facies and continuously decreases from 1.61-3.27 wt% to 1.2-1.8 wt% (Fig. 4.3).

*Fl(d,S)* is interpreted as glacimarine mud provided mainly through meltwater and deposited in a progressively ice-distal environment with occasional input from icebergs (cf. Kirshner et al., 2012; Streuff et al., 2017a; Lepp et al., 2022). The shift in grain size distribution towards the fine fraction, the gradational lower contact, and the weakly laminated to stratified character indicate suspension settling to be the predominant sedimentation process (Ó Cofaigh and Dowdeswell, 2001). Decreasing and overall low contents of coarser grain sizes point towards increasingly suppressed sand and gravel supply by the ice cap, likely related to a retreating ice front. This is also indicated by the decrease in terrigenous carbonate content and enhanced TOC and bSiO<sub>2</sub> (Fig. 4.3). These, in addition to the appearance of the foraminifera *Fursenkoina fusiformis* (Williamson, 1858), indicate increasingly favourable living conditions for opportunistic microorganism assemblages (Anderson, 1975; Ishman and Domack, 1994; Alve, 1995; Ishman and Szymcek, 2003; Smith et al., 2019), thus further supporting progressively ice-distal conditions. Occasional larger dropstones, interpreted to have melted out directly from icebergs, suggest deposition within the calving zone.



The upper 541 cm of the core contain *Fst(S,d,b)*, a dark grey (5Y 4/1), irregularly stratified (cm- to dm-scale) clayey silt with variable sand content, dropstones and bioturbated intervals. Bioturbation is most prominent in the uppermost 200 cm. Several distinct sand-rich layers with gradual lower and upper boundaries occur (Fig. 4.3). Sand content varies between 11 and 52 wt%, exceeding minimum 25 wt% in sand-rich layers. MS ranges from 690 to 3390  $\times 10^{-6}$  SI units and follows the sand content, with increased MS coinciding with higher sand content (Fig. 4.3). IRD is abundant at the base of *Fst(S,d,b)* from 541 to 530 cm, decreases up-core, and is insignificant above 518 cm, where it only occurs in occasional clusters. The mud fraction varies between 48 and 93 wt% (Fig. 4.3). Water content is moderate to high (26-53 wt%) and negatively correlates with the low to moderate DBD (0.69-1.37  $\text{gcm}^{-3}$ ; Fig. 4.3). TOC (0.36-0.69 wt%) shows a slight overall increase up-core, but is lower in sand-rich layers than in silt-dominated intervals. bSiO<sub>2</sub> increases up-core, with a maximum value of around 21 wt% at the core top (Fig. 4.3). Carbonate content is lowest in *Fst(S,d,b)* and decreases to 0.13-1.6 wt%. Nevertheless, the maximum carbonate value is 1.6 wt% at the core top (Fig. 4.3). Deposition of *Fst(S,d,b)* was dated to before 15.4 cal ka BP at 530 cm above the lower contact (Table 4.2). Three sand-rich layers above 200 cm were dated to 10.36 cal ka BP (185 cm), 5.3 cal ka BP (135 cm) and 2.3 cal ka BP (85 cm).

*Fst(S,d,b)* is interpreted as ice margin-distal glacimarine to open-marine mud, which is supported by elevated productivity proxies and onset of more intensive bioturbation at 200 cm (Ó Cofaigh and Dowdeswell, 2001). Diminishing glacial influence is also implied by decreasing IRD abundance after 15.4 cal ka BP (530 cm). The comparably lower, facies-internal MS values and the decreasing values up-core of ~180 cm also indicate increasingly lower terrestrial and marine erosional input, which is further supported by the generally low carbonate values. However, MS values along the core remain exceptionally high (Bohrmann et al., 2017). This may be connected with the regional geology of the DFS, which, inter alia, features an ophiolitic complex and mafic intrusions (Storey, 1983; Mair, 1987). Our findings are in accordance with a continuously retreating glacier front and increasingly exposed continental shelf settings, which may also be responsible for the isolated sand layers as along-shelf currents could both bring in coarser grains and wash out fines.

4.4.2. Age model and sedimentation rates

Radiocarbon dates are displayed in Table 4.2, while linear sedimentation rates, calculated between consecutive dated and modelled depths are shown in Table 4.3. The age model (Fig. 4.4) implies that *Dmst* was deposited over a max. period of ~7 ka from 24.5 cal ka BP at the core base (822 cm) to 17.5 cal ka BP at a minimum average sedimentation rate of 29 cm ka<sup>-1</sup> (Table 4.2 and 4.3, Fig. 4.4). Throughout the deposition of *Fl(d,S)* from 17.5 until 15.7 cal ka BP, sedimentation rates were slightly elevated at ~44 cm ka<sup>-1</sup> and minimally decreased during initial deposition of *Fst(S,d,b)* until 13.4 cal ka BP (Fig. 4.4). From 13.4 until ~12.4 cal ka BP, a period that partially coincides with the ACR (14.5-12.8 ka BP; Graham et al., 2017), sedimentation rates spiked to values exceeding 190 cm ka<sup>-1</sup>, but decreased again to ~34 cm ka<sup>-1</sup> before the end of the Pleistocene (Fig. 4.4). After ~12.4 cal ka BP and throughout the Holocene, sedimentation rates were generally at or below 34 cm ka<sup>-1</sup>, except for the uppermost 55 cm of the core, which were deposited after 1.15 cal ka BP at a higher rate of 53 cm ka<sup>-1</sup> (Fig. 4.4).

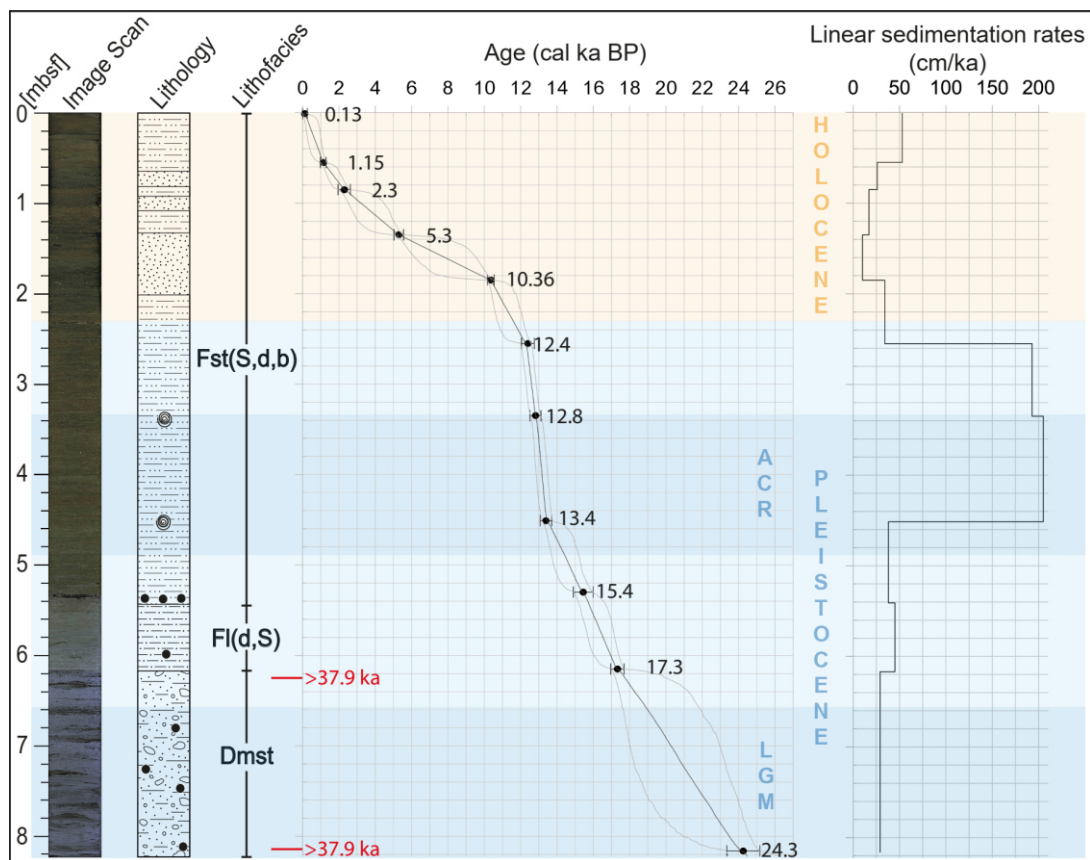


Fig. 4.4: Age model and calculated sedimentation rates for PS119\_5-1, with age anchors and their respective errors. Uncalibrated 14C ages (reported in ka, italic bold font) and are excluded from the age model.

Manuscript I: Glacimarine sediments from outer Drygalski Trough, sub-Antarctic South Georgia – evidence for extensive glaciation during the Last Glacial Maximum

Table 4.2: Conventional radiocarbon ages and calibrated weighted mean ages (cal ka BP) obtained in this study and discussed in the text. For a complete overview of calibration and age ranges, see Table A1 in Annex.

<b>Sample details</b>			<b>Conventional radiocarbon ages</b>		<b>IntCal20 calibration</b>	Lab Code
Gravity core	Depth (cm)	Carbonate source	Age ( <sup>14</sup> C ka BP)	Age error (ka)	Weighted mean (cal ka BP)	
PS119_5-1	1	Benthic foraminifera	0.913	±0.072	0.131	AWI 5705.1.1
PS119_5-1	55	Benthic foraminifera	2.190	±0.084	1.146	AWI 6154.1.1
PS119_5-1	85	Benthic foraminifera	3.199	±0.085	2.295	AWI 5706.1.1
PS119_5-1	135	Benthic foraminifera	5.515	±0.073	5.299	AWI 6155.1.1
PS119_5-1	185	Benthic foraminifera	10.017	±0.09	10.361	AWI 6156.1.1
PS119_5-1	255	Benthic foraminifera	12.263	±0.103	12.406	AWI 6157.1.1
PS119_5-1	335	Gastropod	12.590	±0.154	12.821	AWI 5707.1.1
PS119_5-1	451.5	Gastropod	13.365	±0.163	13.389	AWI 5708.1.1
PS119_5-1	530	Benthic foraminifera	14.854	±0.179	15.441	AWI 5709.1.1
PS119_5-1	615	Shell fragments	15.897	±0.124	17.328	AWI 6160.1.1
PS119_5-1	625	Carbonate fragments	>37.908	-	-	AWI 5710.1.1
PS119_5-1	625	Benthic foraminifera	>37.908	-	-	AWI 5711.1.1
PS119_5-1	816	Mixed foraminifera	22.192	±0.359	24.262	AWI 5713.1.1
PS119_5-1	816	Carbonate fragments	>37.908	-	-	AWI 5712.1.1
Recalibrated radiocarbon ages from Graham et al. (2017)						
PS81/265-1	251-254	Benthic foraminifera	12.59	±0.04	12.778	BETA- 444223
PS81/265-1	305.5	Gastropod	13.85	±0.04	13.902	BETA- 402961
GC666	388	Gastropod	11.926	±0.08	11.75	ETH- 51518.1
GC666	510	Shell fragments	13.301	±0.135	13.375	ETH-51520
GC666	815	Benthic foraminifera	13.572	±0.211	13.581	ETH-51522

Manuscript I: Glacimarine sediments from outer Drygalski Trough, sub-Antarctic South Georgia – evidence for extensive glaciation during the Last Glacial Maximum

Table 4.3: Linear sedimentation rates of core PS119\_5-1 calculated between dated and modelled lithological boundaries, the latter are indicated\*.

<b>Depth range (cm)</b>	<b>Thickness (cm)</b>	<b>Age range (ka)</b>	<b>Time period (ka)</b>	<b>Sedimentation rate (cm ka<sup>-1</sup>)</b>
1 - 55	54	0.131 - 1.146	1.015	53
55 - 85	30	1.146 - 2.295	1.149	26
85 - 135	50	2.295 - 5.299	3.004	17
135 - 185	50	5.299 - 10.361	5.062	10
185 - 255	70	10.361 - 12.406	2.045	34
255 - 335	80	12.406 - 12.821	0.415	193
335 - 451.5	116.5	12.821 - 13.389	0.568	205
451.5 - 541*	89.5	13.389 - 15.723	2.334	38
541* - 617*	76	15.723 - 17.466	1.743	44
617* - 816	199	17.466 - 24.262	6.796	29

#### 4.4.3. Submarine geomorphology

The DFS is characterised by a deep central trough valley and shallower flanks (Fig. 4.5) reaching down to water depths of 320 m with slope gradients of up to 25°. Based on its morphology, the DFS can be separated into four basins from north to south: 1) inner fjord basin, 2) outer fjord basin, 3) inner trough basin, and 4) outer trough basin (see Fig. 4.5a and Hodgson et al., 2014a). The basins are characterised by a smooth seafloor, indicating enhanced sediment deposition, and are separated by bathymetric highs, often occurring as ridges (Fig. 4.5a). The inner and outer fjord basins are shallowest with water depths of 180-200 m, while the inner trough basin is the deepest part of the study area (up to 340 m). The landforms observed on the continental shelf around the DFS are shown in Figures 4.6 and 4.7.

##### *Large transverse ridges – bedrock highs and ice-marginal moraines*

A total of five distinct ridges, R1-R5, occur in the Drygalski Fjord system and are orientated transverse to the main fjord/trough axis (Figs. 4.5a and 4.6). R1, a subtle, small bathymetric plateau in the inner fjord, stretches across the width of the fjord and is 350 m long and up to 550 m wide. Note that length and width of the landforms described in this paragraph refer to along-fjord and across-fjord extent, respectively. R1 is up to 6 m high and has a steeper proximal and a flatter distal flank, with the latter being characterised by a distinct bathymetric step (Fig. 4.5c), at which water depth abruptly increases from 192 to 198 m. The second ridge, R2, separates the inner from the outer fjord basin, is symmetrical in cross-section and is ~700 m long, 800 m wide, and up to 85 m high. Its distal flank has several protruding peaks and shows some indication of mass-wasting in the form of sedimentary lobes. R3 separates outer fjord and inner trough basins and is up to 1.3 km long and up to 150 m high. It stretches across the outer fjord, extends beyond the limits of our bathymetric data and therefore exceeds a minimum width of 1 km (Fig. 4.5e).

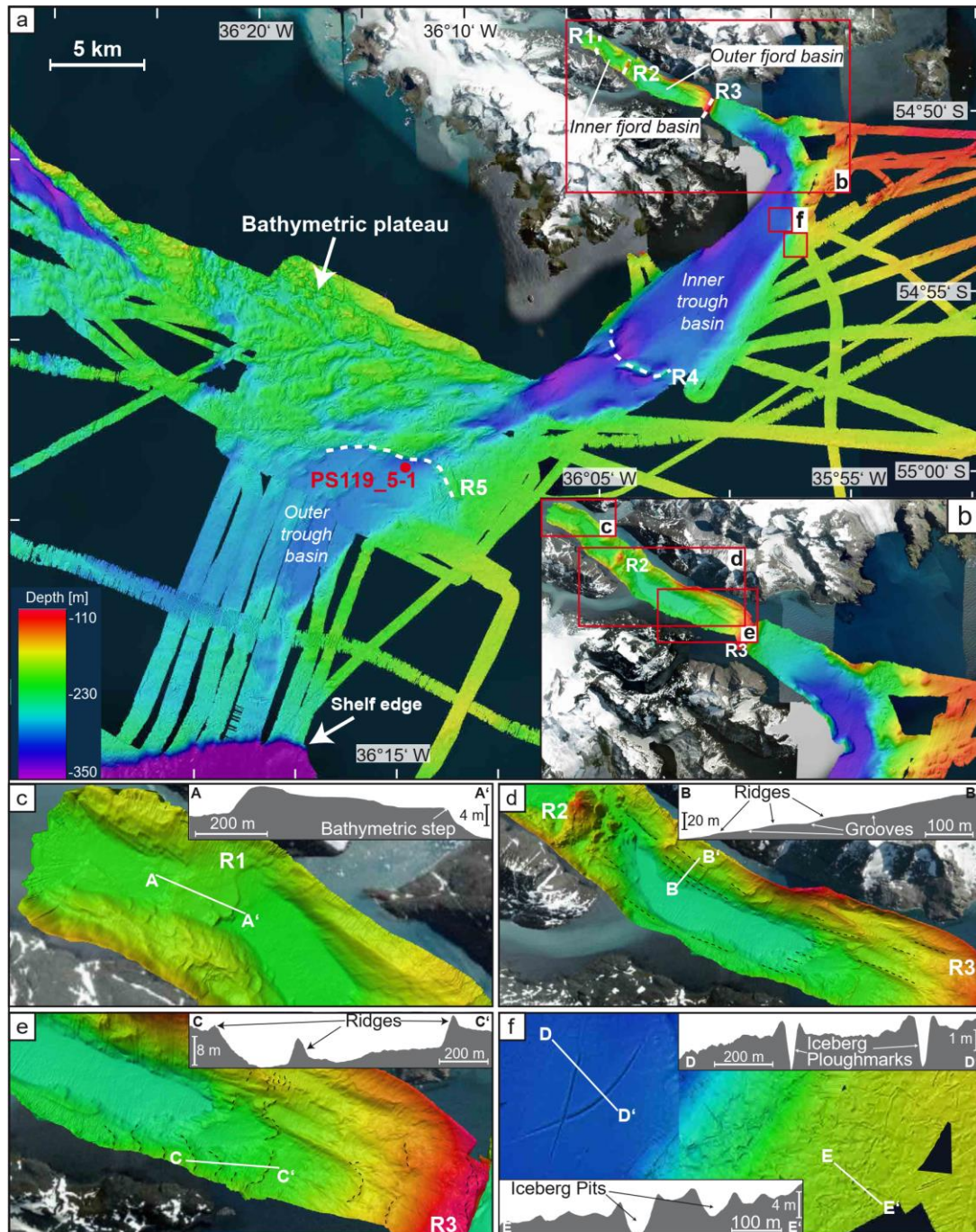


Fig. 4.5: a) Bathymetry of the Drygalski Fjord system (projection: WGS84 UTM, 25S) and the adjacent continental shelf as gathered during M134, PS81 and PS119 cruises. Inner and outer fjord and trough basins are labelled. Large-scale morphological features and bathymetric highs (R1-R5) are indicated. Note the location of sediment core PS119\_5-1 (red) and the small red boxes to the right showing the location of subpanel f). b) Bathymetry of Drygalski Fjord with red boxes showing the locations of subpanels c), d), and e). c) R1 in the innermost fjord with its cross-profile A-A'. d) Detailed fjord bathymetry with stippled black lines marking streamlined seafloor and groove-ridge features interpreted as glacial lineations. Cross-profile B-B' inset to the top right-hand corner shows the subtle morphology of individual grooves and ridges. e) Detailed fjord bathymetry of small fjord-transverse ridges (black stippled lines) interpreted as De Geer moraines. Their distinct morphology is visible in cross-profile C-C'. f) Examples of iceberg ploughmarks (left) and iceberg pits (right) in the area around Drygalski Fjord and Trough with respective cross-profiles D-D' and E-E'. The locations of b) and f) are marked by red boxes in subpanel a).

R3, like R1, is asymmetrical in cross-section but characterised by a flatter proximal and a steeper distal flank (see Fig. 4.5e). R3 has previously been described as a “marked inner basin moraine [...] with a wedge-like asymmetric profile” (Hodgson et al., 2014a), and was inferred to represent a former ice-marginal limit. R4 stretches across the distal part of the inner trough basin south-east of South Georgia with its crest located at 220-260 m water depth (Fig. 4.5a). It is ~5 km wide, 600-1100 m long, and has a relief of 120 m at its highest point. Unlike the other bathymetric highs, R4 is characterised by an 800 m-wide breach in its central part, where the ridge crest is indistinguishable from the surrounding seafloor (Fig. 4.5a).

The transition between inner and outer trough basins is marked by a ~4 km-long bathymetric high, where water depths decrease from >300 to ~225 m. It is part of a large bathymetric plateau of >10 km length and >25 km width, that extends beyond our dataset coverage (Fig. 4.5). The bathymetric plateau is incised by abundant small, chaotically orientated furrows and some channel-like depressions and is characterised by a rugged surface morphology. R5 represents part of the distal boundary of this plateau, and is up to 300 m long, up to 60 m high and >1.5 km wide. Its exact width cannot be determined as it is difficult to say where the ridge ends and the bathymetric plateau begins (Fig. 4.5).

Due to their more rugged and irregular appearance, ridges R2 and R5 are suggested to have their origin in bedrock. Although the bedrock was likely subglacially altered to some degree and may have been superimposed by subglacial till, the symmetrical shape of R2 along with the protruding peaks and overall roughness is more characteristic of bedrock than of glacial deposits (see also Graham et al., 2009; Freire et al., 2015; Hogan et al., 2016; Streuff et al., 2017a). Moreover, the morphological character of R5 is unlike any reported from glacial deposits elsewhere. Its dimensions are similar to grounding-zone wedges, but the rugged overall appearance, the lack of a distinct asymmetry, as well as the extent beyond the boundaries of DT are at odds with such an interpretation (cf. Batchelor and Dowdeswell, 2015 and references therein), and thus reinforce an origin unrelated to glacial activity. As the continental shelf is only around 200-250 m deep in that area, the bathymetric plateau (and thus R5) could simply be part of the original continental shelf. However, it is somewhat questionable how streaming ice

could have been erosive enough to carve out a subglacial trough of >50 km length, but then encountered an area of  $\sim 16 \text{ km}^2$ , where the substrate was too resistant. It might therefore be possible that the bathymetric plateau formed after the trough as a separate feature, and locally changed the latter's morphology. Indeed, a similar area of rugged seafloor in West Greenland has been interpreted as a glacially modified and eroded oceanic flood basalt (Hogan et al., 2016). Although no such provinces have been mapped around South Georgia, the geology bears evidence of widespread magmatic activity (Frakes, 1966), which could hence provide a feasible explanation for the formation of a bathymetric plateau. Nevertheless, as high-resolution data to detect internal structures are currently missing, and resistant bedrock obstacles beneath grounded ice are reported elsewhere (see Alley et al., 2021; Wild et al., 2022), we keep the rather general interpretation of R5 (and the bathymetric plateau) having its origin in till-covered and glacially modified bedrock.



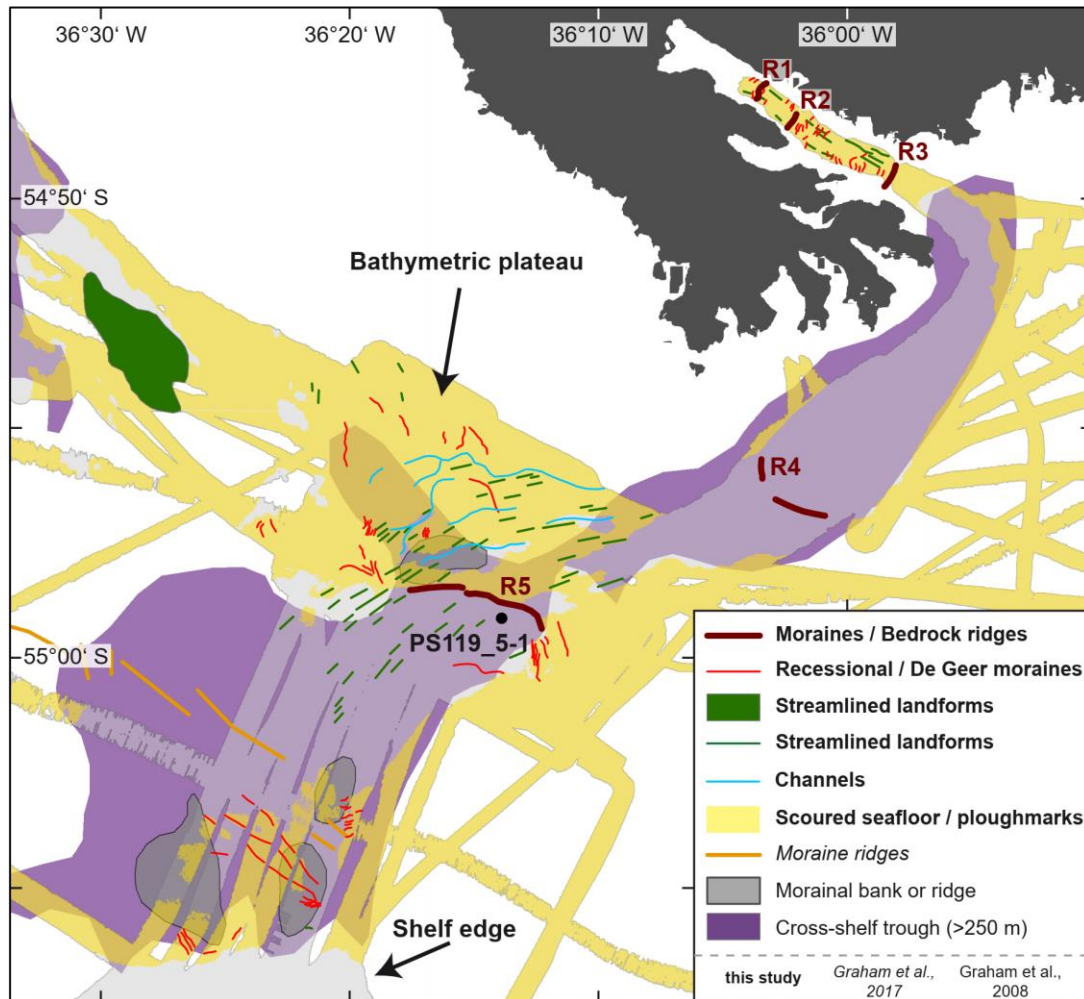


Fig. 4.6: Map of the landforms observed in the Drygalski Fjord system and the adjacent continental shelf (projection: UTM 24S). Bold landforms in the legend are properly georeferenced and based on high-resolution bathymetric data (4 m), while the location of the landforms from other studies is likely to be approximate at best, as features were mapped from published figures (Figures 9 and 2 from Graham et al., 2008 and 2017, respectively) at a much lower resolution.

The smooth appearance of R1 as well as the asymmetry of both R1 and R3 suggest that these ridges represent either terminal or retreat moraines deposited during readvances or longer still-stands of the ice front (see also Winkelmann et al., 2010; Klages et al., 2013; Dowdeswell et al., 2016b; Graham and Hodgson, 2016). Alternatively, due to similar characteristics, R1 could also be a grounding-zone wedge formed during overall ice retreat (see Batchelor and Dowdeswell, 2015). Based on their good preservation in the fjord, where we would expect local glacier readvances to episodically modify the pre-existing seafloor, both R1 and R3 likely formed during post-LGM glacial readvances.

The origin of R4 is difficult to ascertain. There is no clear identifying characteristic to this feature, as two protruding peaks and a variable asymmetry in cross-profile might

indicate a non-glacial origin, while the partially complete erosion as suggested by the breach could hint at soft, easily erodible material. Dimensions of R4 are well within the range of terminal moraines documented from other glacial settings but are not uncommon for bedrock ridges either. The available sub-bottom profiler data suggest bedrock to be the more likely interpretation in some places, but glacial till in others (see section 4.4.3 below); R4 may therefore represent a composite feature with subglacial till emplaced on a bedrock high.

*Streamlined seafloor and elongate grooves – glacially scoured bedrock and sediments*

Several fjord/trough-parallel groove and ridge-features as well as areas of streamlined seafloor can be observed in DF and parts of the trough (Figs. 4.5d and 4.6). Individual features are up to several hundred metres wide, up to 10 m high and commonly 1 - 2.5 km long; shorter landforms are restricted to the innermost fjord. Within DF, such features have previously been described and interpreted as grooves related to subglacial erosion (Hodgson et al., 2014a), while on the continental shelf they were interpreted as *roche moutonnées* and streamlined bedforms formed underneath faster-flowing sectors of the SGIC (Graham et al., 2017). We maintain this interpretation and suggest that the ridges, and in some cases the associated grooves, represent bedrock and/or sedimentary substrate that was streamlined by overriding ice (Graham et al., 2008). Although elongation ratios may not be reliable for the bedrock features, most exceed 10:1 and therefore suggest streaming ice (*sensu* Stokes and Clark, 2002) analogous to outlet glaciers and palaeo-ice streams observed in Antarctica, Greenland, and Svalbard (e.g. Ó Cofaigh et al., 2002; Ottesen et al., 2007; Evans et al., 2009).

*Small, transverse ridges – recessional and De Geer moraines*

Small, subdued ridges perpendicular to the main fjord axis are present on the seafloor of DF and can also be observed in parts of the outer trough basin (Figs. 4.5e and 4.6). They are mostly symmetrical in cross-section with slightly sinuous crests, and are commonly around 2 m high, 25-150 m long and only a couple hundred metres wide. Several larger ridges were also observed on the continental shelf, both in outer DT and on the bathymetric plateau. Those ridges have more variable orientations, but are generally perpendicular to the streamlined features, and therefore to the inferred

direction of past ice flow. They are up to 1 km wide, 50-100 m long and usually ~5 m high and sometimes occur in clusters of closely-spaced parallel ridges (Fig. 4.6). Close to the shelf edge, one such ridge cluster consists of three ridges between 200 and 500 m long, up to 6.5 km wide and ~10 m high, which are spaced at distances of approximately 400 m (Fig. 4.6).

The smaller ridges are similar to De Geer moraines described from other glacimarine settings and were likely formed through a combination of sediment push and squeeze during still-stands or minor readvances in overall ice retreat (cf. e.g. Lundqvist, 1981; Boulton, 1986; Zilliacus, 1989; Streuff et al., 2017b). This interpretation is in accordance with Hodgson et al. (2014a), who interpreted similar ridges in the innermost part of DF as small moraines marking respective ice-marginal advance or retreat limits of Jenkins and Risting Glaciers, and with Graham et al. (2008), who compared parallel sets of ridges on the continental shelf to De Geer moraines. For the slightly larger features, formation through sediment squeezing seems less likely and we therefore interpret them as recessional moraines, following the nomenclature for glacial landforms proposed in Streuff et al. (2022). This is in accordance with Graham et al. (2008; 2017), who previously mapped and interpreted the ridges close to the shelf edge as morainal banks or ridges related to brief still-stands of the ice cap grounding zone during overall retreat (Fig. 4.6).

#### *Curvilinear, chaotically orientated furrows – iceberg ploughmarks*

Numerous, randomly oriented furrows are 100-2000 m long and up to 15 m deep, with widths <100 m (Fig. 4.5f). They cover the continental shelf outside the margins of the cross-shelf trough (Fig. 4.6), but are absent in water depths exceeding 250 m. The furrows are often associated with small, quasi-circular depressions at one end, which are ~100 m in diameter and usually <10 m deep (Fig. 4.5).

The furrows are interpreted as iceberg ploughmarks, which attest to the presence of icebergs with sufficiently large keels to erode the seafloor (cf. Barnes and Lien, 1988; Dowdeswell and Forsberg, 1992; Dowdeswell et al., 1993). Because of their close association with the furrows, the small circular depressions are interpreted as iceberg

pits, marking the locations where icebergs either grounded on or lifted off of the seafloor.

*Curvilinear to slightly sinuous depressions – subglacial channels*

The bathymetric plateau on the continental shelf is incised by several channel-like depressions (Fig. 4.6), which are curvilinear to slightly sinuous in planform, have changing orientations, vary in width between ~200 and 500 m and are normally 20-40 m deep. They can be as short as 1 km. These “channels” represent locally developed depressions with no clear inflow or outflow point and can be rather subtle without clear evidence of actual incision (e.g. steep flanks, sharp edges). Because only few of the features are interconnected (Fig. 4.6) they appear as scattered, relatively short, elongate, individual depressions, rather than as part of a well-developed channel system.

The features are reminiscent of either an ancient channel system that was later modified by sedimentation, or of a “slow drainage system” (Greenwood et al., 2016), formed by subglacial flow of water and/or turbidity currents. The almost sinuous morphology as well as the fact that some of the depressions are interconnected support this interpretation. Variable orientations of the channel segments seem to suggest meltwater as the most likely agent, because its flow intensity and pathways are controlled by, often highly variable, internal ice configuration and meltwater discharge (cf. e.g. Nienow et al., 1998; Greenwood et al., 2016).

4.4.4. Acoustic facies

Sub-bottom profiler data from the South Georgia continental shelf record complex sedimentation regimes, which will be discussed in a separate paper. This paper will therefore only focus on the acoustic stratigraphy observed at the site of gravity core PS119\_5-1, which is shown in Fig. 4.7. The sub-bottom profile crosses the trough basin on the mid-continental shelf, which, at this location, is separated into a north-western and a south-eastern basin by a NE-SW-orientated ridge, interpreted as streamlined seafloor (section 4.4.3, Figs. 4.5, 4.6 and 4.7).

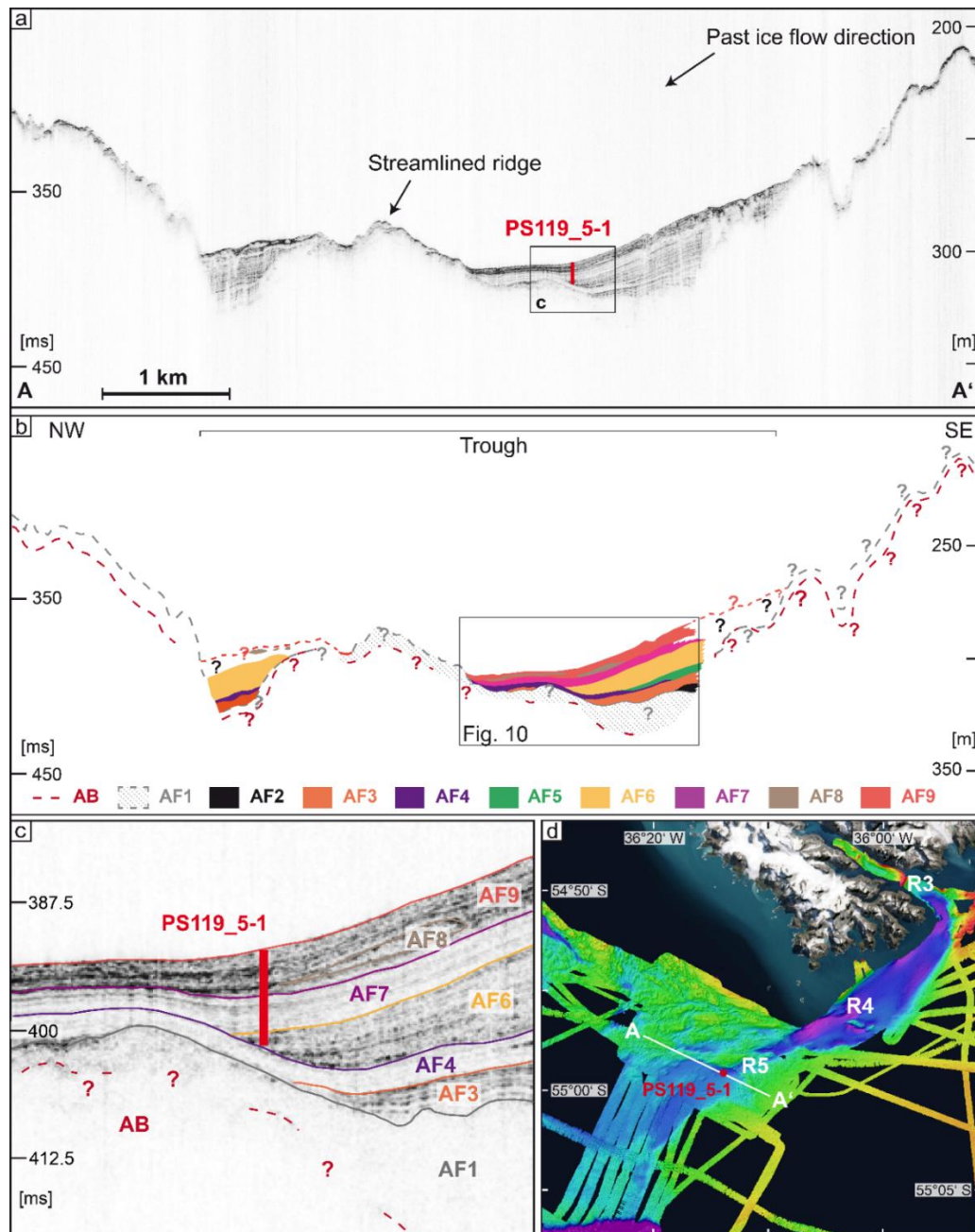


Fig. 4.7: Acoustic facies and depositional environments at the site of gravity core PS119\_5-1. a) Sub-bottom profiler data along profile A-A' (location indicated in subpanel d)) with approximate penetration depth (10 m,  $\neq$  recovery, see Bohrmann (2019) of PS119\_5-1. Conversion between two-way travel time (TWT) ms and m was done using a p-wave velocity of 1563 m/s, the measured average in the sediments of the gravity core. b) interpretation of the acoustic facies as observed on the sub-bottom profile A-A'. AB = acoustic basement. c) Close-up of the core site and the surrounding acoustic facies with approximate core and lithofacies penetration shown by the bold vertical line. d) Map of the Drygalski Fjord system with the core location (red) and the location of sub-bottom profile A-A' (white line).

Although in the vicinity of the core site the seafloor of DT consists of the acoustic basement, an acoustically transparent facies, and an overlying succession of acoustically

stratified sediments, the variable intensity of internal reflections and the individual facies geometry indicate a dynamic sedimentation regime with several depositional events. We define nine acoustic facies, AF1–AF9, in addition to the acoustic basement AB (Fig. 4.7b, c). AB is the lowest and therefore oldest facies and AF1 to AF9 were successively deposited on top. AB seems to frequently crop out at the seabed and is acoustically impenetrable with a highly irregular and chaotic hummocky upper boundary. The latter is of variable amplitude with a (semi-)transparent to opaque acoustic appearance (Fig. 4.7a) and is sometimes accompanied by diffraction hyperbolae.

The visible part of AB is normally only up to 6 ms ( $\approx$ 5 m) thick. Its base and all overlying facies are partially obliterated by acoustic blanking, which supports previous findings of methane gas in subsurface sediments around South Georgia (cf. Römer et al., 2014; Geprägs et al., 2016).

AF1 is acoustically transparent with very few, chaotic, internal reflections (Fig. 4.7) and a clear, relatively continuous semi-opaque top reflector, that often coincides with the acoustic basement (Fig. 4.7). Indeed, AF1 is very similar to and in large parts of the study area impossible to differentiate from AB. AF1 is up to 18 ms ( $\approx$ 14 m) thick.

AF2, AF3, AF5, and AF6 are all acoustically stratified with parallel internal reflections of moderate strength and a smooth, mostly continuous, (semi-)opaque upper reflection (Fig. 4.7a). AF2 is only present as a small wedge-shaped deposit in the SE part of the trough and is 6 ms ( $\approx$ 5 m) at its thickest. AF3 directly overlies and possibly downlaps onto AF2 in the SE, although this is difficult to see due to a weakened signal (Fig. 4.7a). It is 1-7 ms ( $\approx$ 1–5.5 m) thick and thins out in a northwestward direction, but reappears as a small patch in the NW of the trough basin (Fig. 4.7a, b). AF5 and AF6 show onlap geometry and pinch out towards the NW (Fig. 4.7a, b). Both facies are thickest in the southeastern part of the trough with a maximum thickness of 2 ms ( $\approx$ 1.5 m, AF5) and 15 ms ( $\approx$ 12 m, AF6). The upper parts of AF6 were sampled by PS119\_5-1 and revealed stratified, water-rich diamicton interpreted as waterlain till of LGM age, dated in PS119\_5-1 (section 4.4.1).

AF4 and AF7 were deposited as relatively thin (3-4 ms  $\approx$  2-3 m) layers of acoustically (semi-)transparent, faintly stratified sediment with a number of continuous, parallel, regular internal low-amplitude reflections (Fig. 4.7a, c). Both facies are conformable and drape the underlying topography. In the north-western part of the trough basin a hiatus (non-deposition of AF5 and AF6) causes AF7 to directly overlie AF4 (Fig. 4.7). AF7 was sampled by PS119\_5-1 and revealed generally stratified to laminated glacimarine mud with variable contents of coarser grains. Because  $Fl(d,S)$  in the core is much thinner (76 cm) than AF7 appears on sub-bottom profiler data ( $\sim$ 300 cm), AF7 probably represents  $Fl(d,S)$  and parts of  $Fst(S,d,b)$ .

AF8 is easily distinguished from surrounding facies on the basis of its lenticular geometry (Fig. 4.7). It is acoustically semi-transparent with few chaotic internal reflections and often pinches out laterally. Lenses of AF8 conformably drape the underlying topography and are up to 3 ms ( $\approx$ 2 m) thick in their central parts. AF8 commonly occurs in the vicinity of bathymetric highs.

AF9 is the topmost facies at the core site. It is acoustically stratified with frequent internal reflections of generally high amplitude (Fig. 4.7a) and is characterised by a strong, continuous lower boundary. Its upper boundary coincides with the seabed reflector. Unlike the other facies, AF9 has a slightly chaotic appearance, with more irregular and acoustically variable internal reflections. This is especially pronounced in the SE of the trough basin, where the internal stratification is partially obscured by a disturbed signal and the scattered occurrence of lenses of AF8 (Fig. 4.7a). AF9 is also thicker (up to 8 ms, i.e.  $\sim$ 6 m) in the SE of the trough basin and thins in a north-westward direction, where it onlaps onto the flank of the ridge previously interpreted as streamlined seafloor (Figs. 4.6 and 4.7a).

The impenetrable character of the acoustic basement AB indicates a hard and resistant material, which is further supported by outcrops of this facies as distinct bathymetric highs at the seafloor. This, a semi-transparent appearance, as well as irregular and discontinuous, often hummocky upper reflectors have been reported from both bedrock and basal till in other glacimarine settings (Stewart and Stoker, 1990; Kempf et al., 2013; Streuff et al., 2017a), but, due to the overlying, acoustically similar AF1, we favour an interpretation as bedrock. Accordingly, AF1 is probably composed of

subglacial till, which is supported by its acoustic character and the occasional internal reflections, which, if in bedrock, would not be picked up by the sub-bottom profiler instrument. The overlying acoustic facies, AF2-AF7, have the typical characteristics of basin-fill sediments (Ó Cofaigh et al., 2016) and are interpreted as ice-proximal to increasingly ice-distal glacimarine sediments, deposited in front of a retreating ice front. AF8, based on its lenticular geometry, its chaotic acoustic character and its vicinity to bathymetric slopes is interpreted as mass-flow deposits of reworked (glaci-)marine sediments (cf. e.g. Hogan et al., 2011). AF9 as the topmost unit is similar to Holocene sediments deposited in an increasingly deglacial setting, forming as a result of open-marine, hemipelagic suspension settling and the occasional input from sea ice and icebergs (cf. e.g. Forwick and Vorren, 2011; Streuff et al., 2017b). In total, approximately 11.7 m (15 ms) of stratified basin-fill sediments were deposited at the core site. Of these, gravity core PS119\_5-1 sampled between 8.2 and 10 m including AF6, AF7, and AF9. These sediments show a sequence of waterlain till and subsequent post-LGM/Holocene ice margin-distal glacimarine mud with variable influence from icebergs and tidal/winnowing currents, and hence provide the necessary evidence for our acoustic facies interpretation.



#### 4.5. Discussion

PS119\_5-1 is the first core from the southern South Georgia continental shelf that covers the entire sedimentary sequence from the LGM until today. It thus provides new insight into the glacial history of South Georgia and offers the opportunity to test previously proposed models of LGM ice sheet extent (Sugden and Clapperton, 1977; Clapperton et al., 1989b; Bentley et al., 2007; Graham et al., 2008; Hodgson et al., 2014a; Barlow et al., 2016; Barnes et al., 2016; Graham et al., 2017; White et al., 2017). Together with the sub-bottom data and radiocarbon ages from outer DT, the core reveals that all sediments in the trough have likely been deposited as a result of the LGM, its subsequent deglaciation, and the following interglacial period. Our findings, which will be discussed in the sections below, imply the following scenarios for the island's (post-)LGM evolution: i) a glacial maximum (possibly LLGM) palaeo-ice margin reached at least as far as the mid-shelf and likely all the way to the shelf edge in DT; ii) during, or shortly after the LGM, ice must have been grounded close to the core site; iii) the ice margin remained in a stable position for several thousand years.

##### 4.5.1. Full glacial to early deglacial (LGM-17.5 cal ka BP)

###### 4.5.1.1. *Ice extent*

The stratified nature of the waterlain till (*Dmst*), dated to 24.5 cal ka BP at the core base (modelled at 822 cm, Fig. 4.4), is probably the result of periodic changes in the predominant sedimentary processes, i.e. meltout of basal debris and suspension settling from meltwater close to grounded ice (cf. Powell, 1984). As a possible corresponding grounding zone, we suggest R5 (see Fig. 4.5; note that, following the recommendation by Batchelor and Dowdeswell (2015), rather than using the in our opinion restrictive “grounding line”, we define the term “grounding zone” as the area where the ice margin detaches from the seafloor). Such processes are common in the transitional zone between glacial and ice-proximal glacimarine sedimentation, where they are usually accompanied by turbidity currents and mass flows (e.g. Powell, 1984). Together with subglacial till and the glacial landform assemblage (Figs. 4.6 and 4.7), ice-proximal glacimarine sediments this far on the continental shelf provide evidence for an extensive palaeo-SGIC during the LGM. Our findings therefore directly contradict the “little ice” (Barnes et al., 2016) scenario (cf. Bentley et al., 2007; Hodgson et al., 2014a; Hodgson

et al., 2014b) and are hence considered proof for a glaciation far beyond the mouths of South Georgia fjords. In consequence, our study provides proof for LGM ice extent at least until the mid-continental shelf of South Georgia. Streamlined bedrock and glacial lineations are indicative of streaming, possibly fast-flowing, ice not only in DT but also on the shallower bathymetric plateau, which, contrary to previous assumptions (Graham et al., 2008; Graham et al., 2017), shows that fast-flowing ice extended beyond the trough. The fact that the recessional moraines are relatively well-preserved and, especially in DF, overprint streamlined seafloor, is a sign that the landforms were formed during different glaciation stages: streamlined seafloor likely formed during wide-spread ice advance, while the recessional moraines formed during episodic still-stands or small readvances (cf. e.g. Ó Cofaigh et al., 2002; Ottesen and Dowdeswell, 2009; Dowdeswell et al., 2016b). This implies that ice also grounded on the shallow shelf areas at one point in the past. Given the relatively small height of glacial lineations (commonly below 100 m, more often <10 m; cf. Spagnolo et al., 2014 and references therein), and the overall flat relief of the streamlined seafloor, we would expect any pre-LGM landforms to have, at least partially, been buried beneath postglacial sedimentation (cf. Graham et al., 2008). It follows that the streamlined landforms in the DFS probably derive from the LGM, while the recessional moraines were formed during subsequent retreat.

While the basal core age of 24.5 cal ka BP fits the LGM time period of 26.5-19 ka BP (Clark et al., 2009), we cannot rule out that the date of 24.3 cal ka BP at 816 cm overestimates the age of our diamicton. This is based on two observations: 1) the few available foraminifera for dating showed subtle signs of mechanical alteration as would be expected from glacial transportation, and 2) age calibration in high latitudes is generally difficult (Butzin et al., 2019, 2020; Heaton et al., 2020), because the influence of freshwater and glacially transported terrestrial carbon on the radiocarbon signal in the waters the calcifying organisms used is impossible to quantify precisely (Berg et al., 2020). As a consequence, the marine reservoir effect cannot be estimated as reliably as one would hope (Butzin et al., 2019; Berg et al., 2020; Butzin et al., 2020; Heaton et al., 2020), leading to some variability in calibrated radiocarbon ages (see also Table A1). If the age of 24.3 cal ka BP at 816 cm is in fact erroneous, the oldest reliable age in PS119\_5-1 would be 17.3 cal ka BP in 615 cm close to the base of *F/d,S* (Table 4.2 and

A1, Fig. 4.3). *Dmst* is, in contrast to *Fl(d,S)*, an ice margin-proximal facies (Figs. 4.8 and 4.9), a setting for which the originally calculated sedimentation rate of 29 cm ka<sup>-1</sup> seems uncommonly low, as rates close to grounding zones often exceed 92 cm ka<sup>-1</sup> (Domack and Powell, 2018). Since sedimentation rates in glacimarine environments are non-uniform and vary spatially (Lešić, unpublished data, chapter 6), depending, inter alia, on the local erosion by meltwater and ice, its flow speed, and the associated sediment supply to the depositional environment (Cowan et al., 1991), ineffective erosion due to a slower-flowing, more cold-based ice cap could also result in low sedimentation rates (Powell, 1984; Domack and Powell, 2018). This, however, contrasts with the streamlined bedrock and glacial lineations, observed on the bathymetric plateau, that seem to be indicative of faster-flowing ice, and, with it, more efficient erosion. In consequence, we would expect at least similar, if not higher sedimentation rates for *Dmst* compared to *Fl(d,S)*, which was deposited upwards of 617 cm core depth at 44 cm ka<sup>-1</sup> on average. Using an age of 17.3 cal ka BP and a higher sedimentation rate of 44 cm ka<sup>-1</sup> for *Dmst* gives a maximum basal core age of ~22 cal ka BP, which indicates that grounding zone-proximal conditions might have established significantly later than previously thought.

Correlation of the acoustic facies with the core penetration depth showed that PS119\_5-1 recovered the majority of the visible acoustic facies succession at the core site (Fig. 4.7a,c). The subglacial till (AF1) atop the acoustic basement (AB; Fig. 4.7) suggests that an extensive ice cap covered the continental shelf at least until the core site some time before *Dmst* deposition. Since the core did not sample the entire sediment succession, however, it is unclear whether the trough fill can solely be associated with (post)-LGM sedimentation. Although DT itself was interpreted to be the result of glacial erosion, trough formation on the South Georgia shelf was never connected to a specific glaciation and is therefore not necessarily tied to the LGM. Indeed, extrapolation of the most conservative sedimentation rate for *Dmst* (29 cm ka<sup>-1</sup>, Table 4.3) to the 11.7 m of stratified basin-fill sediments at the core site yields a basal age of ~36.5 cal ka BP for the trough fill above AF1, which would pre-date the LGM (cf. Clark et al., 2009). Accordingly, both AB and the lower parts of AF1 could represent glacial till from a pre-LGM glaciation (Peltier et al., 2021), specifically when assuming a “litte-big ice” scenario (Barnes et al., 2016), where ice-free areas in an otherwise extensive LGM would have locally preserved

older landforms (see Fig. 4.2). Furthermore, as age constraints are lacking from the moraines at the shelf edge (including M1; Fig. 4.2), these could also be older than LGM. Considering the long geological history of the island (Frakes, 1966; Stone, 1974; Storey, 1983; Macdonald et al., 1987; Mair, 1987), which has been tectonically stable for ~6.4 Ma (Graham et al., 2008), and the rather complex continental shelf morphology (Graham et al., 2008; Graham et al., 2017), it does seem reasonable to assume that South Georgia, like Antarctica and Patagonia, was covered by ice also prior to the LGM (cf. Kennett, 1977; Mörner and Sylwan, 1989; Rabassa et al., 2000; Goldner et al., 2014; Carter et al., 2017). Deposition of *Dmst* at the core site some time at or after 24.5 and before 17.5 cal ka BP would then imply that R5, where the ice margin was probably grounded at this time, marks the maximum LGM extent of the SGIC. However, if this were the case, we would expect to see more evidence for this in the glacial landform assemblage, namely large transverse moraine features on the continental shelf positioned at a similar distance from the coast as R5 or pronounced lateral moraines along the trough edges. Furthermore, the continuous pattern of streamlined landforms both northeast and southwest of R5 (Fig. 4.6) suggests coeval deposition beneath the same ice stream. If AB and parts of AF1 do pre-date the LGM, the absence of erosive reflections within AF1 makes it unlikely that its base was deposited during a different glacial period than its top. While AF1 could thus entirely represent a pre-LGM glacial unit, in this case we would expect to see a much thicker sedimentary sequence underneath AF6/*Dmst*, deriving from the subsequent interglacial. This is based on the absence of clear erosive boundaries between both AF1 and the overlying AF3, and AF4 and the overlying LGM-dated diamicton (AF6). Moreover, in the case of a “big-ice” LGM (see Fig. 4.2) we would have expected the ice cap to erode any older subglacial till and corresponding post-glacial sediments at the core site. Indeed, the mechanically eroded, transported carbonate material at the bottom of PS119\_5-1, dating to >37.9 ka BP, was likely incorporated into basal debris and does seem to provide evidence for an erosive ice cap base further inland during the LGM. Extrapolating the more plausible sedimentation rate of  $\geq 44 \text{ cm ka}^{-1}$ , which possibly still underestimates true sedimentation rates (Domack and Powell, 2018) and neglects potential sediment compression during coring, yields an absolute maximum age for the trough fill of ~30 cal ka BP. This, in turn, suggests grounding associated with the last glaciation phase

within the outer trough, possibly substantially after 30 cal ka BP, which could support the “big ice” scenario (Barnes et al., 2016) during the LGM (Fig. 4.2). We therefore propose, that AF1 represents glacial till from the last glaciation, while AB is either bedrock or glacial till from a previous glaciation. Unfortunately, the acoustically impenetrable character of both AB and AF1 prevents a definitive interpretation at this point and further evidence, possibly from deep drilling or seismic data specifically in the marine realm, is needed to resolve the question of pre-LGM sediments preserved in South Georgia.

Assuming that a maximum trough fill age of 30 cal ka BP is correct and that the upper boundary of AF1 marks the shift from glacial to glacimarine conditions in outer DT, deglaciation may have started as early as 30 cal ka BP at the core site. This would be in accordance with the presence of waterlain till, which is often associated with the first lift-off of a previously grounded ice margin marking immediate deglaciation (Murdmaa et al., 2006; Pieńkowski et al., 2012). An onset of deglaciation in South Georgia as early as 30 cal ka BP, following a consequential early LLGM before 30 cal ka BP, is technically feasible and would even be in accordance with the earliest Southern Hemisphere LLGMs (~32-30 cal ka BP; Clark et al., 2009; Hillenbrand et al., 2010). Nevertheless, this would be difficult to reconcile with an assumed deglaciation onset around 18 ka ago, calculated from sub-bottom data and the derived basal trough fill age in Royal Bay Trough (Fig. 4.2) (Graham et al., 2017). Early deglaciation around 30 cal ka BP would also be at odds with observations from palaeo-ice sheets at similar latitudes, and would suggest a fairly short time period for the LLGM on South Georgia. In the Strait of Magellan, for instance, the maximum LGM ice extent was dated to ~25 ka (Kaplan et al., 2008), with even later deglaciation. In contrast, a fairly early advance towards LGM limits, possibly later than 32.7 ka BP (corrected <sup>14</sup>C ages), was indicated for the West Antarctic Ice Sheet (WAIS) and the Antarctic Peninsula Ice Sheet (APIS) in the Bellingshausen Sea (Hillenbrand et al., 2010). Similar to the Strait of Magellan, however, subsequent retreat of both WAIS and APIS was dated to considerably later, with a first deglaciation step from the outer shelf at ~25.5 ka BP (corrected <sup>14</sup>C ages) and a second step from the mid-shelf at 19.8 ka BP (Hillenbrand et al., 2010). While this could imply that our age of 30 cal ka BP significantly overestimates the deglaciation onset on South Georgia, one has to keep in

mind that the island is located considerably further north than the Bellinghousen Sea and is far more exposed to ocean currents than the Strait of Magellan. Accordingly, the SGIC was probably more vulnerable to external forcing like early deglacial warming at low latitudes and moisture supply by the Southern Westerlies (Strother et al., 2015; Moreno et al., 2018; Waugh et al., 2020; Bakke et al., 2021) and is therefore likely to have started its deglaciation earlier than the climatically more isolated WAIS/APIS and Strait of Magellan.

The presence of AF1 would further suggest that ice extended beyond R5 during the LLGM. This, in turn, implies that glaciation all the way to the shelf edge is feasible during the LGM and that the moraines at the shelf edge (including M1, see Fig. 4.2) would indeed derive from the LGM (Graham et al., 2008; Graham et al., 2017). Furthermore, deposition of *Dmst* at the core site on the mid-continental shelf provides evidence that, assuming a common ice-cliff/-shelf configuration, the ice margin probably grounded at R5 *after* the LGM. This could, for instance, have been achieved if R5 served as an ice cap pinning point in overall retreat. Indeed, if the assumption of a 24.5 to 22 ka-old core base is correct, the thickness of *Dmst* ( $\geq 205$  cm) implies that the ice margin must have remained in a somewhat stable position for a period of 4.7-7 ka. However, although extended periods of still-stand after the LGM have been reported for marine-based ice sheets in general (e.g. Hillenbrand et al., 2010), this would be an exceptionally long time for an ice margin to remain in the same stable position specifically for a small ice cap such as the SGIC (Bart et al., 2017). Its exposure to climatic forcing at the time of deglaciation would likely have prevented this. This means that either the basal core age is erroneous and that *Dmst* was deposited over a much shorter time frame at sedimentation rates exceeding even  $44 \text{ cm ka}^{-1}$ , or that the ice configuration during deglaciation was more complex than previously thought.

4.5.1.2. *Ice configuration*

The configuration of the ice margin in DT during *Dmst* deposition is difficult to understand. Deposition of waterlain till suggests generally grounded ice, but with the presence of a water-filled cavity between the glacier sole and the bed of the ice sheet, through which basal debris falls before settling at the seafloor (Kellogg and Kellogg, 1988). While waterlain till formation is possible in diverse glacial settings, a maritime sub-polar system with a polythermal ice cap like the SGIC (Breuer et al., 2006) might not have been able to sustain typical polar ice margins such as floating ice shelves (see Smith et al., 2019). However, with postulated shifts of oceanographic fronts to the north (Wu et al., 2021), we cannot exclude more polar conditions in the sub-Antarctic during the LGM. (Smith et al., 2019). Although sedimentation in glacial environments is complex and whole traces of distinct depositional environments can be absent in the geological record (Smith et al., 2019), based on the lack of distinct evidence for sub-ice shelf sedimentation, we consider the presence of an extensive floating ice shelf unlikely in DT. We therefore propose two possible configurations of the SGIC margin for the time it was grounded at R5: i) ice-cliff, with the ice terminating more or less at the bathymetric high R5 (Fig. 4.8a, b) and ii) lightly or intermittently grounded ice-cap, with a subglacial cavity forming between R5 and the shelf edge (Fig. 4.8c, d).

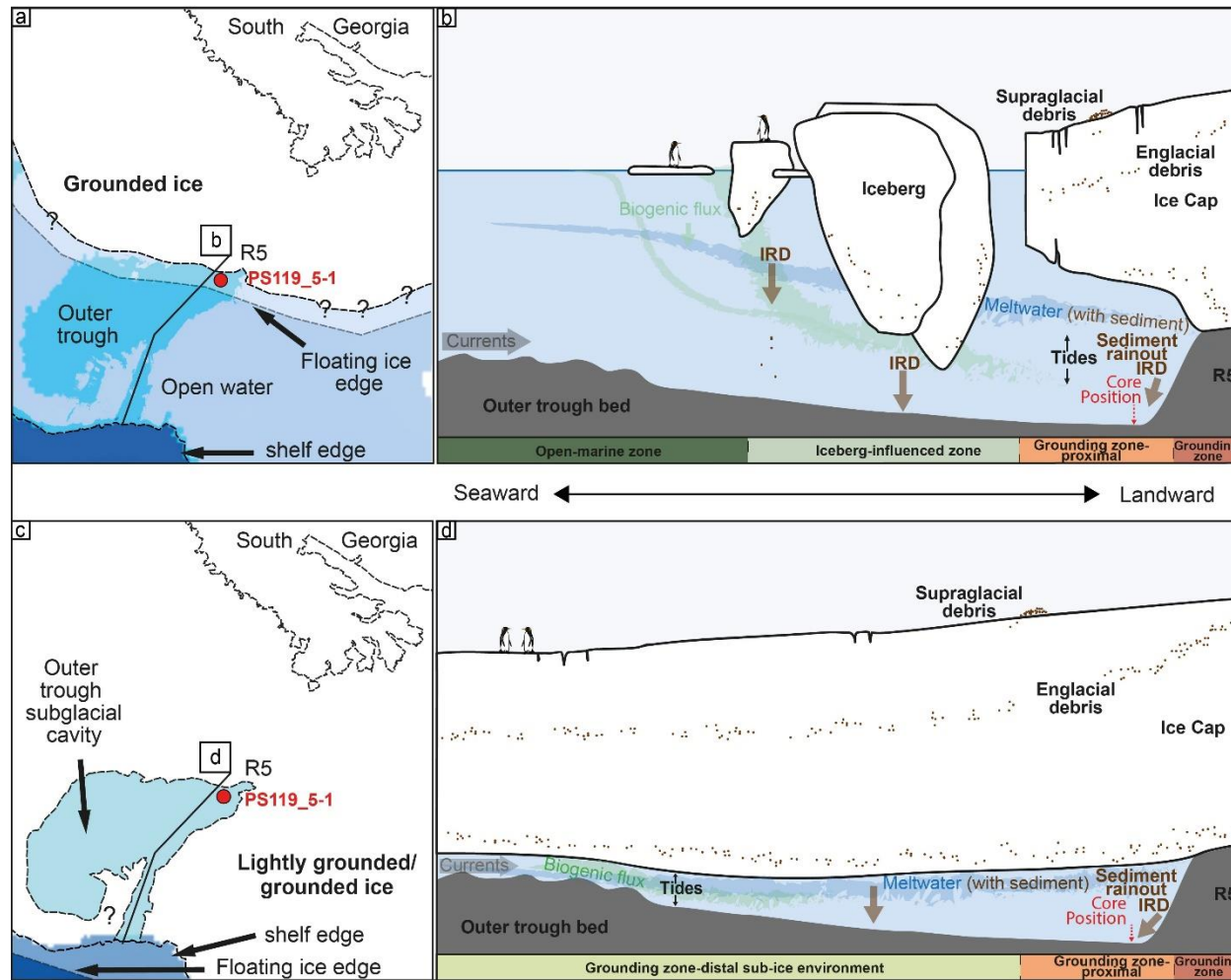


Fig. 4.8: 8a, c show a birds-eye view of outer DT and the core position, showing possible extent and configuration of the SGIC in three different scenarios. 8b, d show cross sections through the grounding zone towards the shelf edge (for locations, see black line in subpanels 8a, c). The most important sedimentary processes are indicated and different depositional zones defined at the bottom of the panels. (a) Ice grounded at R5 and a potential short ice tongue (corresponds to ice-cliff scenario in 9b). (c) Grounded ice extending all the way to the shelf edge, but a large subglacial cavity present underneath the ice sheet (corresponds to subpanel 8d. Subpanels b and d are inspired by Smith et al. (2019)).



Alongside a sudden upcore increase in productivity proxies (Fig. 4.3), the stratigraphy of waterlain till (*Dmst*) deposited underneath increasingly distal glacimarine muds (*Fl(d,S)* and *Fst(S,d,b)*) indicates rapid establishment of progressively open sedimentation regimes associated with a continuously retreating ice margin (cf. e.g. Smith et al., 2019). During this time, the ice margin could have been configured as an ice-cliff margin, which would also be supported by the thin gradational facies boundary and decreasing sedimentation rates (Fig. 4.3). However, for a common ice-cliff configuration (Fig. 4.8a, b), we would not only expect a weaker gradient in productivity proxies across the *Dmst-Fl(d,S)* boundary due to good water circulation underneath the ice margin, but would also expect the water column to be thicker than suspected for waterlain till formation. Furthermore, we would assume the sub-bottom profiler data to show “common” basin-fill sedimentation with horizontal and uniform layering of trough sediments. Instead, the complex facies geometry with onlap, downlap, local thickening and frequent pinching out is somewhat atypical for glacimarine sediments. While this effect could certainly be exacerbated by the NW-SE orientation of the sub-bottom data (the profile cuts the trough, and hence the inferred past ice-flow direction, at an angle of approximately 45°), their uncharacteristic bedding also suggests that the sediments were deposited in a dynamic setting that seems to contradict an ice-cliff configuration.

We therefore favour the second scenario and suggest that the SGIC was either lightly or intermittently grounded on the shelf during *Dmst* deposition and allowed for the formation of a sub-ice cavity within the trough (see also Greenbaum et al., 2015; Kuhn et al., 2017). The establishment of such a cavity seems likely when considering the regional bathymetry, as the presence of a long, overdeepened basin extending between R5 and the shelf edge could have facilitated the inflow of, likely warmer, open ocean waters from beyond the shelf (modelled onshelf transport by Matano et al., 2020) beneath the ice. Ice-cap thinning and increased subglacial melt would then have caused early ungrounding in the trough while the rest of the ice cap remained in contact with the seabed in shallower shelf areas (today in ~200-240 m water depth, see Figs. 4.5, 4.8 and 4.9). The morphology of the subglacial cavity would have likely been controlled by the pre-existing bathymetry, which, assuming it was comparable to the seafloor observed today, would have favoured formation of an up to 171 km<sup>2</sup> large cavity along

the present 250 m depth contour line (Fig. 4.8a, c). All surrounding shelf areas, including the areas west and east of outer DT, R5, and a local area of shoaling close to the shelf edge (marked M1 in Fig. 4.2), are located in considerably smaller water depths and would therefore have served as an effective barrier for currents invading the shelf even further (Matano et al., 2020). This, in turn, would have protected the SGIC from extensive sub-basal melting and associated collapse, enabling it to be grounded on the shelf for much longer than in DT itself. Light or intermittent grounding of the ice margin, specifically on the shelf edge moraine M1 (Figs. 4.2 and 4.8c, d), would have regulated water exchange in the cavity beyond by restricting it to a narrow passage between the base of the ice and the seabed (Fig. 4.8d). On the one hand, this would have provided the necessary environment for the formation of waterlain till and its rather long deposition (section 4.5.1.1). If *Dmst* was indeed deposited in a sub-ice cavity, this could further explain its maximum deposition period of ~4.7-7 ka, because conditions resembling a grounding zone-proximal environment could already have established at the core site beneath the ice, while the “proper” ice edge could have remained at the shelf edge. On the other hand, light or intermittent grounding would have restricted constant inflow of oceanic waters into the predominantly fresh meltwater setting of the subglacial cavity, thus likely hampering biogenic flux to the core site. The tidal influence thought to be responsible for the washing out of fines and sorting into sand and silt layers, would have likely been exacerbated in a subglacial cavity, which, owing to its partial connection to the adjacent shelf edge and the significant influence of tides on the SG continental shelf today (Matano et al., 2020), would have been subjected to a strong tidal pumping effect (Fig. 4.8 c,d; Greenbaum et al., 2015; Kuhn et al., 2017; Smith et al., 2019). With ongoing deglaciation, the ice would have progressively thinned, thus enlarging the glacial cavity and allowing for continuously more accommodation space for glacimarine sediments (Fig. 4.8d). Either at the same time or prior to this, and in any case before 17.5 ka BP, the ice margin would have started to withdraw from its maximum position at the shelf edge, intermittently at first, causing the formation of the moraine ridges on the shallower shelf areas (Fig. 4.2; Graham et al., 2017). Faster subsequent retreat is indicated by the lack of further recessional landforms (Fig. 4.6).

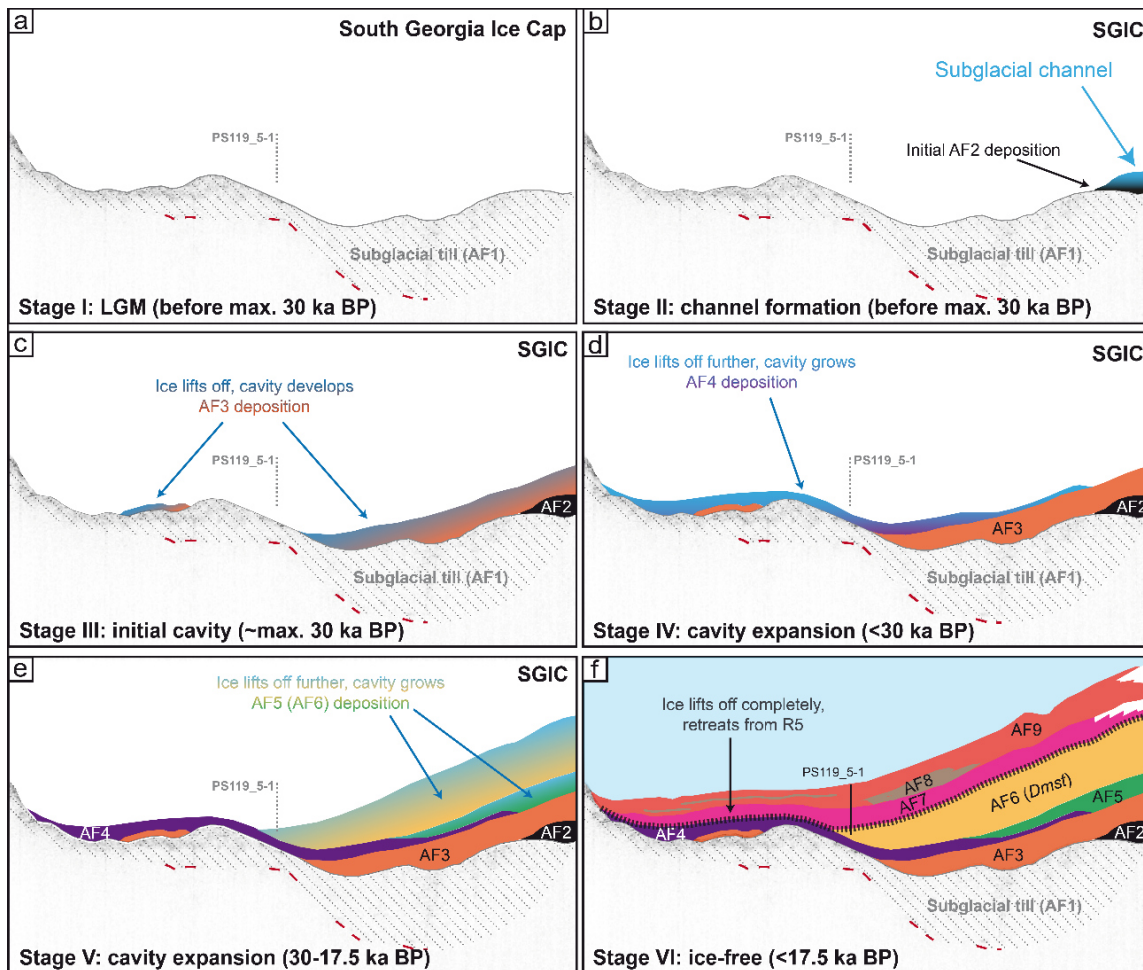


Fig. 4.9: Conceptual model for the ice margin configuration (not to scale) and stages of sediment deposition at PS119\_5-1 during and since the LGM. The configuration scenarios are shown using the sub-bottom profile across the trough and core site (for location see Fig. 4.7b, d), that is orientated from north-west (left-hand side) to south-east (right-hand side). Note that the reader is looking landward a) During the LGM the SGIC is completely grounded within the trough, and deposits AF1, interpreted as subglacial till. b) A subglacial meltwater channel develops, possibly still during the LGM, creating accommodation space for AF2. c) The ice cap thins and lifts off parts of the trough. A cavity forms by restricted inflow of ocean waters as far as R5, thus creating accommodation space for AF3 in the south-eastern part of the trough and on top of the streamlined ridge. d) Further lift-off and associated cavity growth lead to the deposition of AF4 across most of the trough, while parts of the ice cap remain grounded atop AF3 in the south-easternmost trough basin. e) As the ice cap thins further and the cavity is extended, AF5 and, subsequently, AF6 are deposited through a water column in the south-east. f) After deposition of AF6 the ice cap lifts off the trough floor completely (dashed black line) and begins a rapid retreat towards the coastline. At this time the ice margin also ungrounds from R5, thus exposing the core site to increasingly open-marine conditions.

Although the asymmetric trough fill (Figs. 4.7 and 4.9) could have been caused by meandering meltwater governing a complex regime of deposition and erosion, the absence of clear erosional contacts between the acoustic facies seems to be at odds with such an interpretation. Instead, we believe that the variable facies geometry and

uncommon stratigraphy in DT may also be explained by deposition in a subglacial cavity, dependent on the spatially variable thinning of the overlying ice. We propose that AB at the core site may represent bedrock, plastered with glacial till (AF1) deposited beneath LGM-ice advancing all the way to the shelf edge before 30 ka BP at the earliest (Fig. 4.9a). Deposition of AF2 as a small, spatially restricted wedge immediately on top of the acoustic basement may have been the result of a meltwater channel forming beneath the ice cap and being abandoned before cavity formation (Fig. 4.9b).

At the onset of deglaciation, ice cap thinning and partial lift-off, potentially further reinforced by the inflow of ocean water (cf. Matano et al., 2020), may have caused the formation of a subglacial cavity that allowed the deposition of early glacimarine sediments (AF3). During this time, the ice margin may have still been mostly grounded on the shallower streamlined ridge in the northwestern part of the trough (Figs. 4.6 and 4.9d). Continuous cavity growth likely led to the deposition of AF4 across the entire trough basin, and later AF5 and AF6 (*Dmst*) only in the south-east (Fig. 4.9d, e). Early post-LGM sea level rise around this time (Clark et al., 1996; Clark et al., 2009) then would have caused the ice to lift off the trough floor and R5 completely (Fig. 4.9f) and likely forced fast subsequent retreat, indicated by the almost instantaneous onset of biogenic productivity at the *Dmst-Fl(d,S)* facies transition (Fig. 4.3) and the rapid decline in gravel-sized IRD (Fig. 4.3). The more uniform, conformable deposition of subsequent facies (AF7-AF9) further supports this interpretation. In essence, the presence of a sub-ice cavity as depicted for the SGIC implies that the ice margin was grounded within outer Drygalski Trough during the LLGM and therefore supports the “big ice” scenario (Barnes et al., 2016) of shelf-wide glaciation in South Georgia.

#### 4.5.2. Deglaciation after 17.5 cal ka BP

The onset of *Fl(d,S)* deposition with decreasing IRD and sand content marks the transition from ice-proximal to more ice-distal conditions and therefore provides a minimum age for ice-margin retreat from R5 around 17.5 cal ka BP (Fig. 4.3). During the early stages of deglaciation ice retreat probably occurred mainly calving. High iceberg activity is indicated by abundant iceberg ploughmarks and associated “keeling points” on the shallower shelf areas around the trough, that, albeit of unknown age, are likely to at least partially derive from this time. A new exposure of the core site to iceberg

calving and melting from 17.5 ka BP can also be seen in  $F(d,S)$ , which despite low gravel content (only up to 5 wt%), contains several larger dropstones (see grain counts, Fig. 4.3). A low overall IRD signal in the core can probably be explained by icebergs surpassing the core site before melting.

$Fst(S,d,b)$  is characterised by a significant up-core decrease in IRD from 541 to 518 cmbsf (corresponding to the time frame between  $\sim 15.7$  and 15 cal ka BP) and peak sedimentation rates between 450 and 255 cmbsf (13.4-12.4 cal ka BP, Figs. 4.3 and 4.4). The fast decrease in IRD content above the bottom of the facies suggests quickly diminishing iceberg influence at the core site, and is considered indicative of further significant retreat towards the island. The almost absent IRD above 518 cm (i.e. after 15 cal ka BP, see Fig. 4.4) attests to open-marine sedimentation with negligible iceberg melting in the outer trough. The dramatic increase in sedimentation rates around 13.4 cal ka BP (Tab 4.3, Fig. 4.4) coincides with the ACR, which marked significant glacier readvances in the Southern Hemisphere and, accordingly, around South Georgia (14.5-12.8 ka BP; Putnam et al., 2010; García et al., 2012; Graham et al., 2017; Bakke et al., 2021). While peak readvances during the ACR were dated to as late as 13 ka ago in New Zealand (Putnam et al., 2010), environmental changes, high sedimentation rates, and outer fjord moraines associated with the ACR in the Royal Bay and Cumberland Bay areas northeast of South Georgia were originally dated to 15.2-14 cal ka BP (Graham et al., 2017). However, recalibration of these ages (Table 4.2 and A1) shifts the ACR period for South Georgia to  $\sim 14$ -13 cal ka BP and suggests that ice lift-off from the outer basin moraine in Cumberland Bay (OBM, see Fig. 4.2) occurred already at 12.8 cal ka BP. Sedimentation rates  $>190$  cm ka<sup>-1</sup> (Table 4.3, Fig. 4.4) are probably related to enhanced erosion on South Georgia and surrounding sediments, likely occurring as a result of higher precipitation, glacier readvance and higher meltwater input. Such high sedimentation rates would not only inhibit traces of bioturbation (Ó Cofaigh and Dowdeswell, 2001), which we would normally expect to see in such an ice-distal environment, but also indicate that, during the late ACR, glaciers in South Georgia advanced sufficiently to affect and significantly enhance sediment input on the mid-continental shelf. This calls into question the interpretation of small moraines in innermost Drygalski Fjord as retreat moraines related to the ACR (cf. Hodgson et al.,

2014a), and also suggests that glaciers reached beyond R3 at the mouth of DF during the ACR. The latter would be reasonable given the south-north precipitation gradient across South Georgia that provided more precipitation south of the Allardyce mountain range, and could thus have resulted in especially pronounced advance of the glaciers in Drygalski Fjord and Trough. Possible advance beyond the fjord mouth could attribute the formation of R3 (previously termed inner basin moraine by Hodgson et al., 2014a) to a post-ACR readvance and R4 to the formation as the ACR terminal moraine. Indeed, due to its preservation within the trough, R4 should be younger than the last glacial. The breached centre of the ridge (Figs. 4.5 and 4.6) indicates erosion, likely by focussed fluvial energy possibly related to a significant meltwater outburst. While this would support a grounded ice margin at R4 for an extended period of time, this could have also been the case during early retreat rather than during the ACR, especially because it seems unlikely that the short ACR period produced sufficient meltwater. Furthermore, if glaciers during the ACR had advanced all the way to R4, we would have expected a return from *Fst(S,d,b)* to slightly more proximal glacimarine mud in PS119\_5-1. In addition to this, the position of R4 is rather far away from the fjord mouth, especially when compared to the ACR moraines in Cumberland Bay (Graham et al., 2017; Bakke et al., 2021). Accordingly, R4 must have formed either in bedrock, thus providing a pinning point for the SGIC, or as a recessional feature during LGM-subsequent deglaciation. The former seems a bit more likely considering the relatively symmetrical crest morphology. The above, alongside the lack of a distinct facies change and very low IRD concentrations in PS119\_5-1 between ~14 and 12.8 cal ka BP (see Figs. 4.3 and 4.4), therefore lead us to conclude that the ACR readvance was limited in comparison to the LGM extent, did not reach as far as the core site and probably did not quite reach the extent of R4, making R3 a likely end moraine for this time interval after all (see also Hodgson et al., 2014a; Hodgson et al., 2014b; Graham et al., 2017).

#### 4.5.3. Holocene (after 11.7 cal ka BP)

The uppermost ~230 cm in gravity core PS119\_5-1 are dated to the Holocene (Table 4.2; Fig. 4.4) and were interpreted, based on scarce IRD and increasing biogenic flux, to have accumulated in an open-marine environment. The absence of glacial fluctuation signals, i.e. the continuity of *Fst(S,d,b)* deposition, this far on the shelf is in accordance with van

der Putten and Verbruggen (2005), who, albeit for the north-eastern side of the island, suggested an ice-free coastal environment by 10 cal ka BP. The lack of specific facies changes in PS119\_5-1 after 15.4 cal ka BP also means that any glacier response to Holocene climate signals recorded on land or in near-coastal areas on the northern side of the island and on Annenkov Island (Fig. 4.1a) (Clapperton et al., 1989b; Rosqvist et al., 1999; Rosqvist and Schuber, 2003; Strother et al., 2015; Oppedal et al., 2018; Berg et al., 2019; Bakke et al., 2021) may not have been as pronounced in the south of the island or may simply have not been extensive enough to affect the depositional environments at the core site.

The upper 200 cm of the core are characterised by low sedimentation rates and spontaneous increase in bioturbation after 11 cal ka BP. Post-ACR sedimentation rates dropped to 34 cm ka<sup>-1</sup> and decreased even further after ~10.4 cal ka BP to <26 cm ka<sup>-1</sup> (Table 4.3). These rates are significantly lower than those in other DT cores (PS119\_6-1 and PS119\_7-1; for location see Bohrmann, 2019) and the neighbouring Jacobson Trough, where rates generally >80 cm ka<sup>-1</sup> were observed (Lešić, unpublished data; Flenner, 2019). While this could be a result of shorter distances between cores and sediment source (all cores are located nearer to the shore than PS119\_5-1), the rates for the early Holocene also fall a little short of sedimentation rates reported from GC666 in Royal Bay Trough (Graham et al., 2017), which is located at a similar distance from the shore as PS119\_5-1. A possible explanation for the comparably low rates in the outer DT could be either partial erosion (not observed in the core) or some kind of “bypass environment” due to exposure of the core site to shelf currents. Indeed, multiple sand-rich layers in the core interval between ~200 and 60 cm would support this theory, as they imply enhanced current speeds that kept fine fractions in suspension and caused winnowing.

#### 4.6. Conclusion

This study presents the first continuous marine archive from the LGM to modern environmental conditions in a gravity core (PS119\_5-1) taken from the southern shelf of South Georgia. Our findings elucidate parts of the glacial history of the island, which was probably controlled by its vulnerability to climatic forcing. Waterlain till dated to before 17.5 cal ka BP at the base of the core provides unequivocal evidence for glacimarine

sedimentation on the mid-continental shelf. Together with bathymetry and sub-bottom profiler data this indicates that the SGIC was not restricted to the fjords but was probably grounded on the entire southern shelf close to the Drygalski Fjord system during the LGM and possibly former glaciations. Based on the waterlain till, which, during deposition, was affected by tidal pumping, and a complex acoustic stratigraphy, we propose the presence of a subglacial cavity with restricted seawater access in outer Drygalski Trough during early deglaciation, which probably developed as a result of early ice cap thinning and accompanied lift-off in the deeper parts of the trough. Although it is possible that the entire ice margin started retreating from the shelf edge during this time already, parts of the ice cap must have remained in a stable position on the mid-shelf, likely pinned to a distinct morphological ridge. When the ice cap disintegrated further, it caused ice above the cavity to retreat by intensive calving, as indicated by abundant ploughmarks on the continental shelf. It probably became ungrounded from R5 around 17.5 cal ka BP, leading to the deposition of laminated mud with dropstones and sand, indicating progressively distal environments at the core site. Outer Drygalski Trough was under the influence of icebergs until 15 cal ka BP, when IRD in the core dropped to negligible amounts and the ice margin had retreated too far to still affect the depositional environment at the core site. Fast environmental changes observed in the lithofacies and several recessional moraines on the continental shelf imply rapid, but step-wise retreat of the ice margin until 15 cal ka BP. A significant glacier re-advance in response to the ACR resulted in peak sedimentation rates, which were likely driven by increased hinterland erosion. A distinct ridge at the mouth of Drygalski Fjord is interpreted as a terminal moraine marking the maximum ACR extent of the local glaciers. After the ACR the glaciers retreated back into the fjord where a sequence of De Geer moraines either indicates frequent still-stands or smaller re-advances since then.

Our data provide the first dated evidence for an expansive ice cap during the LGM, thus confirms findings from previous studies, and further contributes an important piece of the puzzle that is South Georgia's glacial history. However, due to its vulnerability to Southern Hemisphere climate change, the glacial evolution is likely to have been much more complex than one dataset can resolve. As a consequence, further data, specifically



from the marine realm, are needed to better understand sub-Antarctic climate history and associated ice cap dynamics.

## Acknowledgements

This work was funded by the “Deutsche Forschungsgemeinschaft” (DFG) in the framework of the priority program SPP 1158 "Antarctic Research with comparative investigations in Arctic ice areas" by the grants BO 1049/23-1, KU 683/18-1 and DO 705/4-1. We thank the captain and crew from RV Polarstern cruise PS119, A. Höfken and M. Seebeck, V. Schumacher, S. Wiebe, P. Daub and C. Gebhardt from Alfred Wegener Institute, Helmholtz Centre for Polar and Marine Research in Bremerhaven for support with coring, core and sample processing, as well as J. Klages and J. Wollenburg for scientific guidance. Further, we thank B. Kockisch, M. Klann and J. Malnati for excellent laboratory support during the hardships of the pandemic. Our most sincere thanks go to all students involved in laboratory work on board and land, especially A. Ivanova and A. Lemire. We appreciate the comments and helpful recommendations of two anonymous reviewers that contributed to this publication. Figures 4.2, 4.5, 4.6, 4.7 in this publication were created using ArcGIS® software by Esri ArcGIS® and ArcMap™ that are the intellectual property of Esri and are used herein under license. Figure 4.1 was created using QGIS 3.16.15. and Figure 4.3 and 4.4 with Grapher 15. Figure 4.8 were produced in Adobe Illustrator 2022, which was also used to finish all Figures.

## 5. Manuscript II: Glacial history of the King Haakon Trough System, sub-Antarctic South Georgia

In preparation for submission (August 2023)

This manuscript is a preprint and has been submitted to Quaternary Science Reviews in a more advanced and modified version on 20.12.2023.

Streuff, Katharina Teresa<sup>1</sup> (kstreuff@marum.de); Lešić, Nina-Marie<sup>1,2</sup> (nlesic@marum.de); Kuhn, Gerhard<sup>1,2</sup> (ge\_ku@uni-bremen.de); Bohrmann, Gerhard<sup>1</sup> (gbohrmann@marum.de)

*1 MARUM – Centre for Marine Environmental Sciences and Faculty of Geosciences, University of Bremen, Klagenfurter Strasse, 28359 Bremen, Germany*

*2 Alfred Wegener Institute (AWI), Helmholtz Centre for Polar and Marine Research, Am Alten Hafen 26, 27568 Bremerhaven, Germany*

Corresponding author: Streuff, Katharina (kstreuff@marum.de)

### **Abstract**

The glaciated island of sub-Antarctic South Georgia is a key area for climate reconstructions, because it is positioned in the Southern Ocean amidst the core belt of the Southern Westerlies and the main fronts of the Antarctic Circumpolar Current. This makes it particularly susceptible to changes in local, regional, but also Southern Hemisphere-wide climate characteristics. Marine-geological records recovered from its vast continental shelf therefore offer enormous potential to better constrain how ice masses in the Southern Ocean responded to Quaternary climate change. Despite this, little research has been done offshore South Georgia. We present a new set of high-resolution bathymetric data supplemented with sub-bottom profiles, in order to reconstruct the pre-Holocene glacial history of the King Haakon Trough System on the southern continental shelf. Our data show numerous landforms common for phases of ice advance and retreat, which are interpreted to document the confluence of two major trunk glaciers during peak glaciation. Progressively elongated linear bedforms imply accelerated ice flow towards the shelf edge, probably during the Last Glacial Maximum, suggesting that the South Georgia Ice Cap behaved somewhat similarly to ice masses around the Antarctic Peninsula. Recessional moraines close to the shelf edge show both shelf-wide ice extent during the Local Last Glacial Maximum and staggered retreat at least during the initial phase of deglaciation. Multiple extensive ice advances, postulated

to have occurred during at least three separate glaciations, are indicated by several distinct reflectors within an acoustically transparent facies on the mid- and outer shelf. This paper complements two others focusing on the Holocene depositional environments and their associated sedimentary processes, in an effort to illuminate another part of the Quaternary evolution of South Georgia's marine environment.

### 5.1. Introduction

The geomorphology of previously glaciated regions offers valuable insights into past ice sheet behaviour, because glacially modified landscapes act as an archive for glacial footprints. The (palaeo-)bed surface, especially in the marine environment, often hosts a plethora of glacial landforms, which, amongst others, can be used to spatially reconstruct specific ice sheet configuration (e.g. Evans et al., 2004; Ottesen et al., 2005; Andreassen et al., 2008; Bradwell et al., 2008; Ottesen and Dowdeswell, 2009; Dowdeswell et al., 2016a; Arndt et al., 2017), phases of advance/retreat (Ó Cofaigh et al., 2002; Dowdeswell et al., 2007; Dowdeswell et al., 2008b; Andreassen et al., 2014; Ottesen et al., 2017; Streuff et al., 2017a), and maximum ice or glacier extent (Clark et al., 2012; Arndt et al., 2015; Streuff et al., 2015; Brouard and Lajeunesse, 2017; Dowdeswell et al., 2020). Furthermore, although dependent on the degree of preservation, the cross-section of any given glacial trough may hold information about the role the (pre-existing) morphology played during ice advance and retreat, as, in addition to the nature of the glacier bed (soft/hard, flat/hummocky etc.), topography may significantly impact how ice masses configure themselves, where advancing ice may be directed, and what type of obstacles the ice will have to overcome (cf. Anandakrishnan and Alley, 1994; Anandakrishnan et al., 1998). Similarly, the newly modified morphology after an ice advance may then affect deglacial ice dynamics. Larger bathymetric plateaus or bedrock highs, for example, may hamper ice retreat by acting as so-called pinning points, where the ice margin intermittently gets stuck (cf. Alley, 1993; Morlighem et al., 2016). Unpinning, or, alternatively, the presence of deep basins or a wide fjord geometry may then foster accelerated retreat, firstly by reducing drag and potential buttressing effects and secondly by allowing the potential for increased basal melt (cf. Motyka et al., 2003; Holland et al., 2008; Post et al., 2011; Åkesson et al., 2018; Wild et al., 2022).

Reconstructions of former ice dynamics, such as the above, are needed to improve modelling efforts, which aim to illustrate the potential ramifications of the two remaining ice sheets, the Greenland and the Antarctic Ice Sheet, melting in response to a warming climate. However, because the potential of many palaeo-archives is still covered by (grounded) ice, researchers often rely on the reconstruction of suitable analogues. Although the investigation of glacial geomorphology, in combination with radiocarbon dating, has been used to successfully reconstruct palaeo-ice sheets in the northern hemisphere (e.g. Ottesen et al., 2007; Clark et al., 2012; Hughes et al., 2016), it is difficult to find good alternative study sites for the evolution of the Antarctic Ice Sheet, which, due to its location in the Southern Hemisphere, is presumably exposed to a completely different climate.

In this context, the sub-Antarctic island of South Georgia (SG) is a valuable target for past climate studies. It is located in the Southern Ocean within two large climatic systems, the Southern Hemisphere Westerly Winds and the Antarctic Circumpolar Current Front, both of which impact the climate of the Southern Hemisphere (SH) (cf. Strother et al., 2015; Moreno et al., 2018; Matano et al., 2020; Bakke et al., 2021; Yamazaki et al., 2021). Despite its potential, however, the glacial evolution of the South Georgia Ice Cap (SGIC) is still poorly understood, most of which is due to a lack of (published) data from the marine realm. Although the large-scale glacial history as well as the more recent ice dynamics in the fjords have been crudely reconstructed on the basis of bathymetric data and scattered submarine glacial landforms (Graham et al., 2008; Hodgson et al., 2014a; Graham et al., 2017), the majority of the numerous cross-shelf troughs, with the exception of Drygalski Trough in the southeast of SG, remains unstudied in terms of glacial landforms and shelf morphology (Lešić et al., 2022).

This study presents hydroacoustic data from a large and complex cross-shelf trough system, the King Haakon Trough System, on the southern continental shelf of SG. By describing and interpreting the glacial footprints archived in bathymetry and sub-bottom profiler data, we aim to elucidate the glacial evolution of one of the, presumably major, pathways, carved into the continental shelf during past glacial(s). Focusing exclusively on the trough evolution prior to ~10 ka BP, this paper will complement two other studies on the Holocene depositional environments in the same trough (Lešić et

al., in prep.; Lešić et al., *subm.*) and therefore make a valuable contribution to the, thus far very limited, literature about the marine environment around SG.

## 5.2. Physiographic Setting

SG is one of the largest islands in the sub-Antarctic and is located in the Southern Ocean, between 54° and 55° southern latitude and 35°30' and 38° western longitude (Fig. 5.1). It is technically part of a microcontinent, which is unique in terms of a very large continental shelf, that is roughly ten times as large as the island itself. Bathymetric data have revealed a number of large cross-shelf troughs that spread more or less radially from the coast all the way to the continental shelf edge and have been interpreted as the product of large ice streams draining the SGIC during past glacial periods (Fig. 5.1b; Graham et al. (2008); Graham et al. (2017)). King Haakon Trough is one of these and is located on the southern SG continental shelf (Fig. 5.1b). Because it is joined by several other troughs, including Jacobsen and Annenkov Troughs (nomenclature according to Bohrmann et al. (2017)), it has been previously defined as the King Haakon Trough System (KHTS; Fig. 5.1b,c; Lešić et al., *subm.*).

KHTS is up to 12 km wide, up to 100 km long and up to 400 m deep (Fig. 5.1c). It consists of a main, N-S orientated trough valley, the King Haakon Trough (KHT), which is fed by Cheapman, King Haakon, and Queen Maud Bays from the north (Fig. 5.1c). All inlets host a minimum of one tidewater glacier, with Peters and Price Glaciers feeding into Cheapman Bay, Briggs Glacier, an outlet of the Murray Snowfield, draining into King Haakon Bay, and Hawkesbury Glacier terminating in Queen Maud Bay (Fig. 5.1c; nomenclature after South Georgia GIS, 2023).

Jacobsen Trough (JT) and Annenkov Trough (AT) join KHT from the east at approximately 12 km from the coast. They are separated by a prominent bathymetric high (BH1) located ~4.5 km east of the confluence zone with KHT (Fig. 5.1c). Both troughs are joined by several tributary bays from the north and northeast, which include Jossac Bight, Newark Bay, and Jacobsen Bight (Fig. 5.1c; nomenclature according to Bohrmann et al., 2017). These inlets are separated from Queen Maud Bay, i.e. the northernmost part of KHT, by the Nuñez Peninsula (Fig. 5.1c).

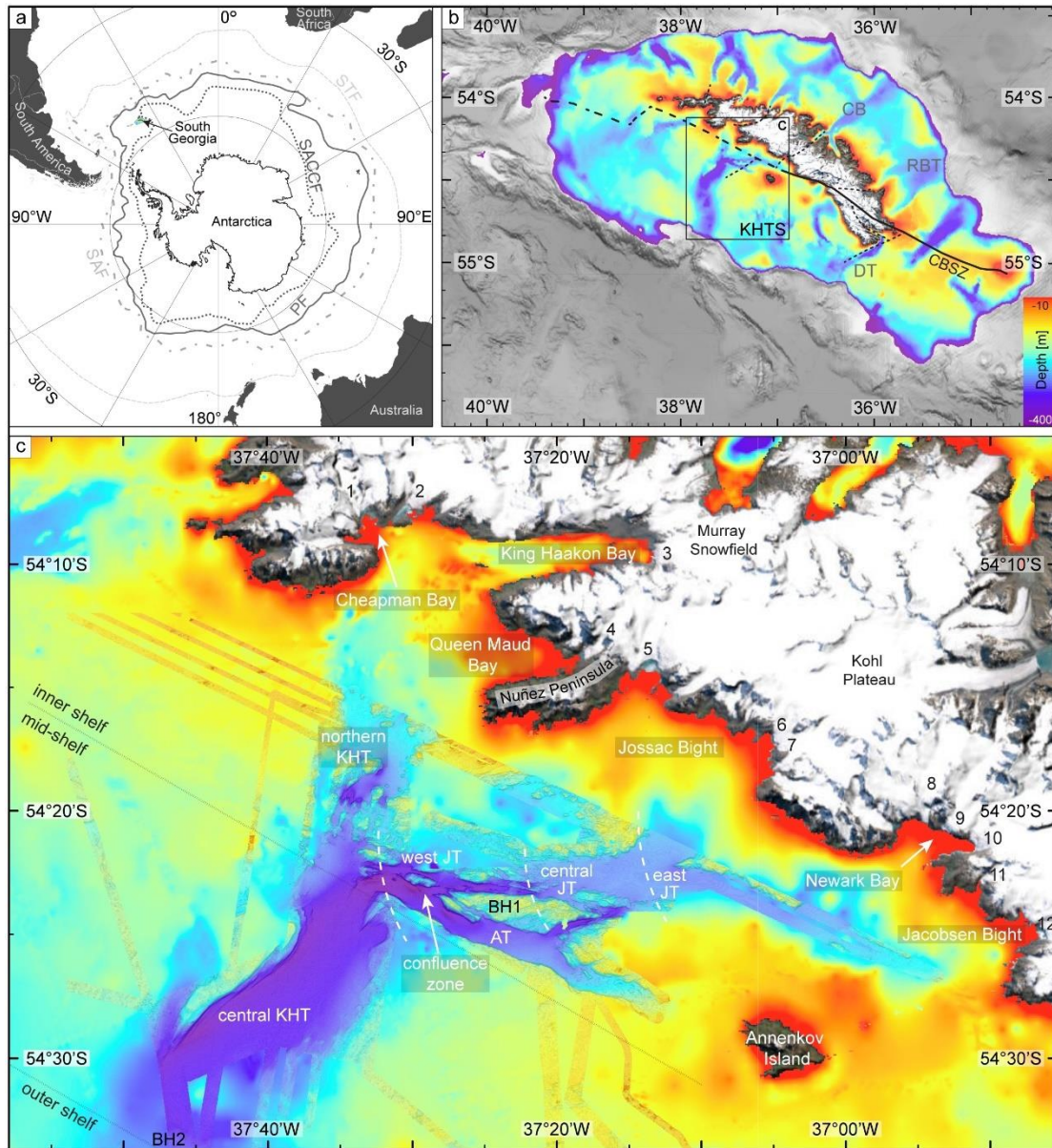


Fig. 5.1: a) Location of South Georgia in the Southern Ocean with respect to the different oceanographic fronts. STF = Subtropical Front, SAF = Sub-Antarctic Front, PF = Polar Front, and SACCF = Southern Antarctic Circumpolar Current Front. Nomenclature and frontal positions are based on Orsi et al. (1995). b) Marine environment around South Georgia. The continental shelf is here defined as the area between 0 and 400 m water depths and depicted in colour. A greyscale hillshade map marks the extent below 400 m. The location of the study area, the King Haakon Trough System (KHTS) is indicated by the black rectangle. Other troughs include DT = Drygalski Trough, RBT = Royal Bay Trough, and CB = Cumberland Bay. The major fault zone, the Cooper Bay Shear Zone (CBSZ) runs ~NE-SW across the southern island. Several additional faults were inferred to branch away from the CBSZ at an angle by Graham et al. (2008) and are shown by black dotted lines. Bathymetric data derive from GEBCO Compilation Group (2023) and Hogg et al. (2016); Hogg et al. (2017) with the island DEM from the ArcMap™ imagery basemap, courtesy of ESRI ArcGIS®. c) Overview of the King Haakon Trough System with all troughs and tributaries. A number of tidewater glaciers are present along the coast: 1= Peters Glacier, 2 = Price Glacier, 3 = Briggs Glacier, 4 = Hawkesbury Glacier, 5 = Esmark Glacier, 6 = Keilhau Glacier, 7 = Jewell Glacier, 8 = Lancing Glacier, 9 = Christensen Glacier, 10 = Kjerulf Glacier, 11 = Eclipse Glacier, 12 = Christophersen Glacier. Nomenclature from South Georgia GIS (2023). For easier reference the Jacobsen Trough System has been subdivided into east, central and west Jacobsen Trough (JT),

*Annenkov Trough (AT) as well as the tributaries. Throughout this study we will also use the terms northern, central and outer King Haakon Trough (KHT) and inner, mid- and outer shelf, which are marked here for reference..*

All JT tributaries also have a number of tidewater glaciers at their heads, including Esmark, Keilhau and Jewell Glaciers in Jossac Bight, Lancing, Christensen and Kjerulf Glaciers in Newark Bay, and Eclipse, Christophersen and Bary Glaciers for Jacobsen Bight (nomenclature after South Georgia GIS (2023); Fig. 5.1c). JT and AT, in combination with their three tributaries, have previously been referred to as the Jacobsen Trough System (JTS; Lešić et al., *subm.*).

For easier identification, and in accordance with Lešić et al. (*subm.*), JT is divided into west JT, extending from the confluence zone to roughly the centre of BH1, central JT, including the eastern part of BH1 and extending almost to the point where Jacobsen Bight and Newark Bay join Jossac Bight, and east JT, which includes the easternmost trough and its tributaries (Fig. 5.1c).

The tributaries, which join KHT and JT, show distinct differences in their appearance. Although bathymetric data for the coastal regions of SG is still very poorly resolved, aerial imagery as well as compiled bathymetry data (including the General Bathymetric Chart of the Oceans (GEBCO Compilation Group, 2023), as well as datasets by Hogg et al. (2016); (2017) and Hodgson et al. (2014b) show that King Haakon Bay, with a length of ~13 and a width of up to ~3 km, a fjord basin and an outer sill/moraine, looks like a “proper” fjord, and is, accordingly, similar to other major fjords in SG (Hodgson et al., 2014a). Comparable to the Drygalski Trough System, where Drygalski Fjord is orientated nearly perpendicular to Drygalski Trough (Lešić et al., 2022), King Haakon Bay is orientated predominantly E-W, i.e. perpendicular to the major trough basin of KHT (Fig. 5.1). Cheapman and Queen Maud Bay, while also “fjord-like” in appearance, are smaller embayments, whose shorter, more open morphology seems to implicate them as less important tributaries to a potential trunk glacier draining through KHT (Fig. 5.1c). Similarly, the tributaries of JT are much shorter (mostly <3 km) than King Haakon Bay, and appear to be wider and much more open. Although the GEBCO and Hogg et al. (2016); (2017) data rely largely on interpolation and may thus not necessarily be too reliable this close to the coast, the bathymetric information also seems to indicate a

relatively shallow seafloor and an associated lack of fjord basins and sills/moraines for the latter (Fig. 5.1c).

### 5.3. Methods

Bathymetric and sediment echo sounder data used in this study were gathered during the cruise M134 on RV *Meteor* in 2017 (Bohrmann et al., 2017). Onboard the *Meteor* bathymetric data were predominantly acquired using the Kongsberg Maritime EM710 multibeam echo sounder, which is the superior system for waters with depths below 500 m. It operates at nominal frequencies between 70 and 100 kHz with a total of 432 beams. In greater depths, or where the acquisition of good-quality backscatter data was prioritised, the alternate deep-water system, the Kongsberg Maritime EM122, was used, operating with 256 beams at a frequency of 12 kHz (Bohrmann et al., 2017). All bathymetric data were processed in MB-Systems, gridded to a resolution between 5 and 50 m, depending on data quality, and visualised and interpreted in QGIS 3.22.11, Global Mapper 24.0, and ESRI ArcGIS® Pro. All maps were produced in the World Mercator projection. Landform mapping and measuring using the UTM projection for zone 24S.

The Teledyne ATLAS PARASOUND P70 sub-bottom profiler was used to acquire the sediment echo sounder data for this study. The system operates at two main frequencies, a primary high frequency (PHF) between 18 and 20 kHz, and a secondary low frequency (SLF) of ~4 kHz, the latter of which is used for seafloor stratigraphy. Sub-bottom profiler data were visualised and interpreted using SMT The Kingdom Suite v. 2019.

### 5.4. Results and Interpretation

#### 5.4.1. Seafloor morphology

The bathymetric data from this study show that KHTS is characterised by a variable seafloor morphology. The most distinct features are the trough basins of KHT, JT and AT within the otherwise much shallower, surrounding shelf regions (Fig. 5.2a). KHT is around 250 m deep in its northern parts, deepens to ~350 m toward the mid-shelf and shoals to around 300 m at the shelf edge. At least on the outer and mid-shelf it thus shows a slightly reverse bed slope common for many cross-shelf troughs around the island and elsewhere (cf. Graham et al., 2008; Rydningen et al., 2013; Ryan et al., 2016).



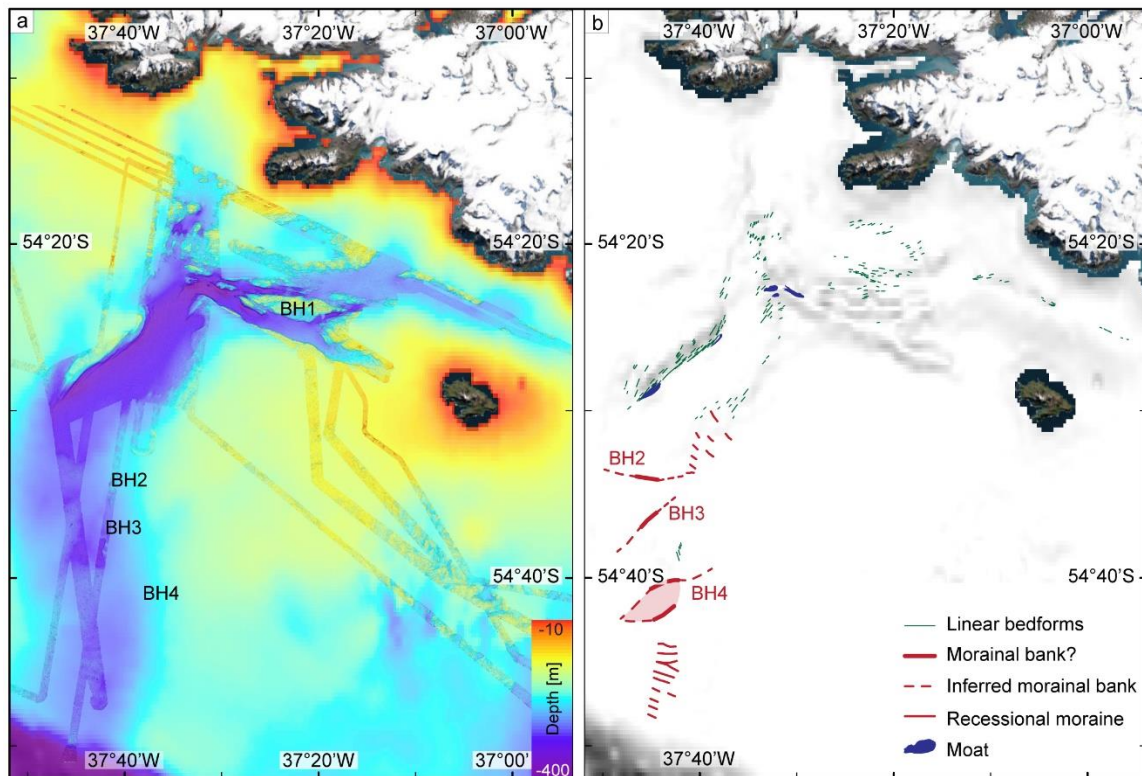


Fig. 5.2: a) Overview of the bathymetry used for the geomorphological interpretation. b) Map of the distribution of the landforms within KHTS. The island DEM is from the ArcMap™ imagery basemap, courtesy of ESRI ArcGIS®

Several basins are overdeepened with respect to the remaining trough basin and are between 850 and 3100 m long, up to 700 m wide, and >360 m deep (Fig. 5.2b). They have previously been interpreted as moats in moat-drift systems, developing from a dynamic regime of increased, or at least maintained, bottom-currents (Lešić et al., subm.). The largest moat is located at the confluence zone between KHT and JT, but several smaller ones are clustered along KHT's western flank (Fig. 5.2b). JT and AT, on the other hand, have their deepest parts close to the confluence zone with KHT and shallow towards the coast, ranging in depth between 350 and 380 m.

Several bathymetric shoals can be observed on the seafloor. These often appear as larger plateau areas, especially around the trough flanks, and usually have rugged surfaces (Figs. 5.2, 5.3), which is especially visible in the data gridded at a higher resolution. Based on this, as well as the sub-bottom data (cf. section 5.4.2 below), the bathymetric shoals are interpreted as outcropping bedrock. Many of their surfaces host a number of small, elongate, ridge-like features, that, on the inner and mid-shelf, are on average about 350 m long and 5-10 m high. On the outer shelf, these features are much

longer, averaging around 850 m and reaching up to 2.5 km in length (Figs. 5.2b, 5.3). Their width of ~70 m is relatively uniform across the entire trough system. The ridges are generally E-W orientated in JT and NE-SW orientated in KHT (Fig. 5.2b). Such characteristically aligned bedrock has previously been classified as streamlined seafloor (Dowdeswell et al., 2016b), and is in accordance with similar observations around SG (Graham et al., 2008; Hodgson et al., 2014a; Graham et al., 2017; Lešić et al., 2022). Individual lineations are here interpreted as streamlined bedrock and crag-and-tails (cf. Ó Cofaigh et al., 2005a; Graham et al., 2008; Graham et al., 2017), forming when grounded ice moulds pre-existing substrate and deposits material in the lee of erosion-resistant bedrock obstacles (e.g. MacLean et al., 2016).

Although characteristic sedimentary glacial lineations appear to be absent in KHTS, the orientation of the linear features implies ice moving westwards in JT and south- then southwestwards in KHT. On the outer shelf their elongation ratios often exceed 10:1 and may therefore be considered indicative of fast-flowing ice (cf. Stokes and Clark, 1999).

Several semi-arcuate ridges on the mid- and outer shelf are orientated roughly perpendicular to the main trough axis and occur in two clusters, one on the eastern trough flank of KHT, and one in the main trough basin close to the shelf edge (Fig. 5.2a,b). The ridges along KHT are 500-700 m wide, 5-10 m high, and have a crest-to-crest spacing of ~1000 m. Close to the shelf edge the ridges are generally 6-8 m high and around 400 m wide, although one feature is 16 m high and 1 km wide. Because the ridges extend beyond the coverage of our dataset, their length cannot be determined accurately, but they generally appear to be longer than 2 km. Note that length in this context refers to the cross-trough extent, while width describes the along-trough extent. Because the ridges are similar to morainal ridges observed in Drygalski Trough (Lešić et al., 2022), and partially coincide with the location of previously documented ice-marginal moraines (eastern KHT flank; Graham et al., 2008), they are interpreted as recessional moraines, forming through intermittent still-stands of an overall retreating ice margin (e.g. Dowdeswell et al., 2008b; Ottesen and Dowdeswell, 2009). The larger feature may accordingly represent a longer period of ice margin stagnation, possibly due to a climatically colder or wetter period lasting several years or even decades.

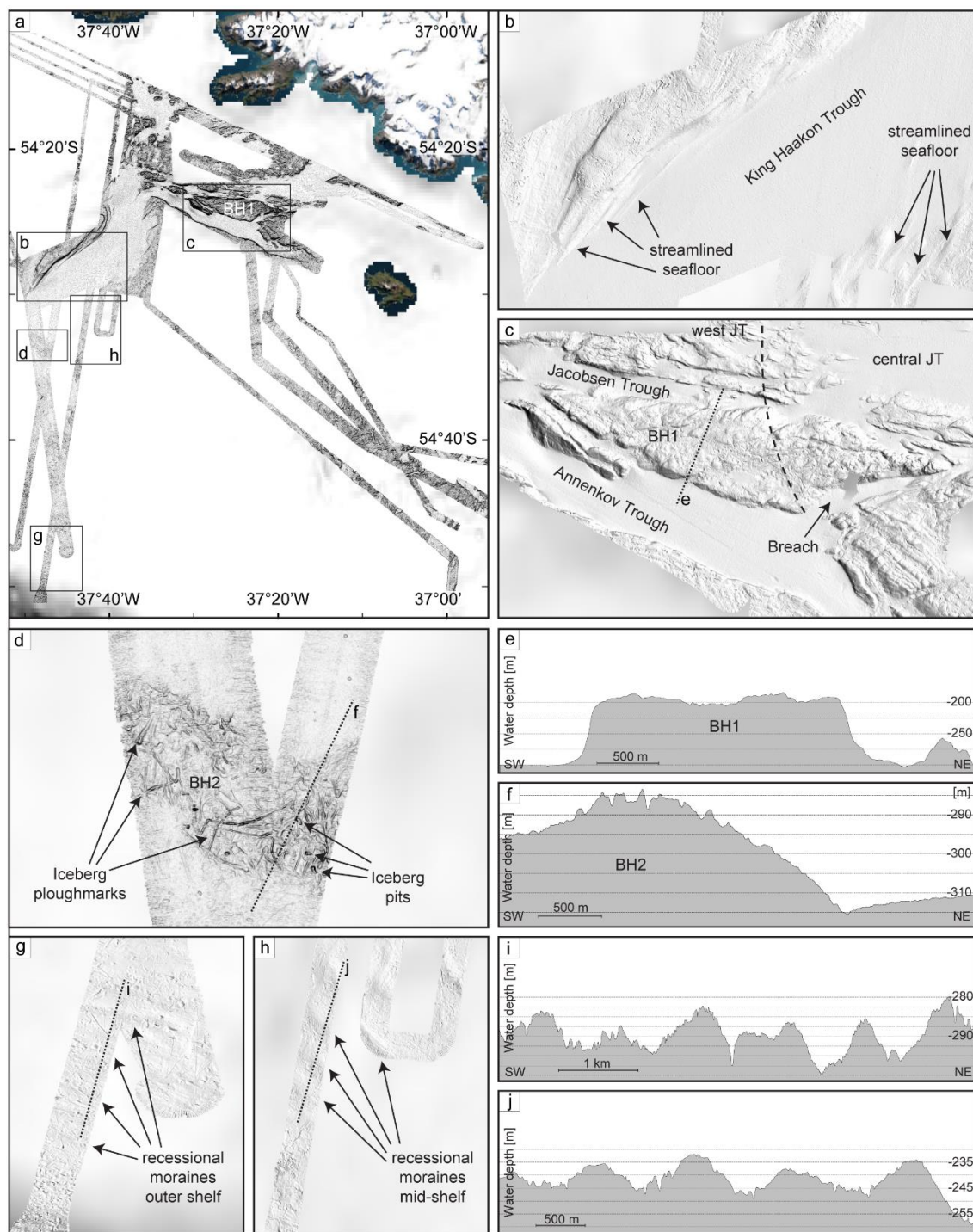


Fig. 5.3: Examples of the landforms observed in the bathymetric data from KHTS. a) Overview map of the computed slope of the bathymetry used in this study. Background is the GEBCO bathymetry. Island DEM is part of the World Imagery Basemap in ArcMap, courtesy of ESRI AcGIS. Black rectangles show the locations of individual sub-panels. b) Detail image of streamlined seafloor in central KHT. c, d) Close-ups of the bathymetric high BH1 and BH2 in JTS and on the mid-shelf in KHT. The transition from central to west JT is marked by a black dashed line in c. Note the obvious iceberg ploughmarks and pits on the surface of BH2 in d. Black dotted lines in c and d mark the position of cross-profiles shown in sub-panels e and f, respectively. g, h) Close-ups of the recessional moraines observed on the outer and on the mid-shelf in KHT, respectively. i, j) Cross-profiles across the recessional moraines. The locations of the profiles are indicated by the black dotted lines in g and h.

In addition to the smaller, well-defined moraines, we identify four large bathymetric highs, BH1 to BH4. BH1 is located in JTS, is orientated roughly E-W, and was previously documented to separate JT from AT (Fig. 5.1c, section 5.2). Its surface is rugged and, in parts, intensely furrowed (Fig. 5.3). It is up to 130 m high, up to 2.6 km wide, and about 11 km long, but extends beyond our bathymetric coverage, suggesting that these could be minimum dimensions. Geometrically, BH1 seems to be symmetric, with equally steep ( $\sim 15^\circ$  incline) proximal and distal flanks (Fig. 5.3). A notable, straight, channel-like feature characterised by a very smooth surface breaches BH1 at an  $\sim 270^\circ$  angle and eventually connects into AT (Fig 5.3). While the overall orientation of BH1 is parallel to an inferred extension of the Cooper Bay Shear Zone (CBSZ, Fig. 5.1b, Dalziel et al., 2021); also referred to as the Cooper Bay or Cumberland Bay Dislocation Zone (Macdonald et al., 1987; Graham et al., 2008), a large tectonic boundary that crops out on the island, the breach coincides with the location of an additional fault inferred by Graham et al. (2008) (Fig. 5.1b). BH2, BH3, and BH4 are more subtle, trough-transverse bathymetric highs that occur consecutively more landward of the shelf-edge moraines in KHT (Figs. 5.2a,b; 5.3). Geometry and dimensions of these highs differ significantly from the previously described moraines, because they are both higher (16-18 m) and much wider, with a minimum width of  $\sim 3$ -7 km along-trough. Since only parts of these features are covered by the hydroacoustic data, their geometry and exact dimensions are difficult to assess. While they are difficult to position reliably, profiles across the best-imaged BH2 seem to indicate asymmetry, with a steeper proximal and a flatter distal side (Fig. 5.3). It is unclear how exactly BH1-BH4 formed, although an interpretation as bedrock highs or morainal features seems reasonable. Indeed, BH2 was previously interpreted as a morainal bank (Graham et al., 2008). We suggest that BH1 represents a large bedrock high, whereas BH2 to BH4 all formed as ice-marginal features. This is further discussed in section 5.5 below.

Those parts of KHTS located in water depths below 310 m are characterised by smooth seafloor, probably imparted by locally enhanced sediment accumulation, and contrast the rugged surfaces of some of the landforms documented above (cf. Fig. 2a). Indeed, many of the shallower areas, including the moraines and bathymetric highs, appear to be heavily dissected, and exhibit a wide array of, mostly chaotically orientated, partially

cross-cutting, ridges and furrows (Fig. 5.3d). These are highly variable in length, width and height/depth and are often accompanied by small, up to 10 m-deep, circular to angular depressions with a diameter between 30 and 50 m (Fig. 5.3). The chaotic orientation and the variable dimensions of the furrows are common characteristics of iceberg ploughmarks (cf. e.g. Barnes and Lien, 1988; Dowdeswell et al., 2010; Arndt and Forwick, 2016). Since icebergs with keel depths up to ~600 m have been documented from Antarctica (Dowdeswell and Bamber, 2007), water depths <310 m are a likely target for iceberg scouring in SG, and we thus interpret the furrows as iceberg ploughmarks. Although the associated depressions could represent pockmarks, serving as outlet craters for free gas that has been documented in the subsurface of SG trough sediments (Römer et al., 2014; Geprägs et al., 2016), we would mainly expect pockmarks to appear in the deeper trough basins amidst thicker sediment sequences. Instead, the close connection between the iceberg ploughmarks and the depressions suggests that the latter represent iceberg pits, marking the grounding or lift-off zones of the respective icebergs.

#### 5.4.2. Seafloor stratigraphy

##### 5.4.2.1. *Acoustic Facies - Description*

Sub-bottom profiler data reveal a total of two acoustic facies, AF1 and AF2. Although difficult to discern, as it is acoustically impenetrable and the signal is often obliterated by overlying stratigraphic sequences, we also identify the acoustic basement, AB, in some places (Fig. 5.4). AB is acoustically impenetrable and almost entirely transparent, with very few discontinuous, semi-opaque internal reflections. AB's top reflector, where present, coincides with the seabed, giving it an opaque and irregular, hummocky appearance. In steep terrain, the reflector is characterised by a diffuse appearance. AB crops out locally, specifically in central and west JT, as well as in northern KHT (Figs. 5.4, 5.5). Because AB represents the acoustic basement, we would expect it to be present everywhere in KHTS and to represent the oldest material. Nevertheless, AB's top reflector is only resolved locally, as it is often subject to acoustic blanking or hampered signal penetration through the overlying stratigraphic sequences. Along bathymetric slopes the irregular top reflector becomes more diffuse and partially diffracted (Fig. 5.4f).

AF1 seems to mainly occur on the outer shelf in KHT. However, thick sediment sequences, disturbed signal returns as well as acoustic blanking commonly occur in the mid- and inner shelf regions, and could therefore obliterate any appearances of AF1. In very few locations AF1 may be present as a thin veneer on top of outcropping AB or beneath the overlying facies. AF1 is acoustically transparent at the surface and increasingly blank with depth (Fig. 5.4d,e). It appears internally homogeneous, with generally scattered and chaotic, discontinuous reflections of vertically decreasing amplitude. It is characterised, however, by several distinct reflectors, marked R1-R4 in Fig. 5.4e. The lowermost visible reflector, R1, is highly discontinuous and is present only in a few locations on the outer shelf (Fig. 5.4d,e).

Because of hampered signal penetration, it is impossible to say whether R1 marks the top reflector of AB, and, thus, the bottom reflector of AF1, or whether it represents a facies-internal reflector. R2 and R4, where visible, are similarly discontinuous but are generally more defined (Fig. 5.4d,e). In contrast, R3 is continuous across large areas of the continental shelf, where it takes on a wavy appearance (Fig. 5.4d,e). It extends all the way to the shelf edge where it becomes increasingly flat. AF1 occasionally crops out at the seafloor, where it appears to form the previously described ice-marginal moraines (Fig. 5.4e; Graham et al., 2008; Graham et al., 2017), as well as BH2 (Fig. 5.4c,d), which was interpreted as an ice-marginal morainal bank by Graham et al. (2008).

Outcrops of AF1 also coincide with the location of the recessional moraines in the outermost trough (Fig. 5.4b,e). Especially in the outer-shelf regions, the top of AF1 is hummocky with a chaotic, mostly opaque appearance. Because it generally seems to coincide with the strong and opaque, rather thick, seabed reflector, this makes it difficult to discern the actual seabed and the top of AF1 from a potentially present thin sediment cover. Underneath thick sedimentary sequences AF1's top reflector is either acoustically transparent and hard to distinguish, or it takes on the appearance of the overlying facies' base reflector (Figs. 5.4, 5.5). Although difficult to assess, AF1's maximum thickness in our data is ~28 m, close to the moraines on the outer shelf.

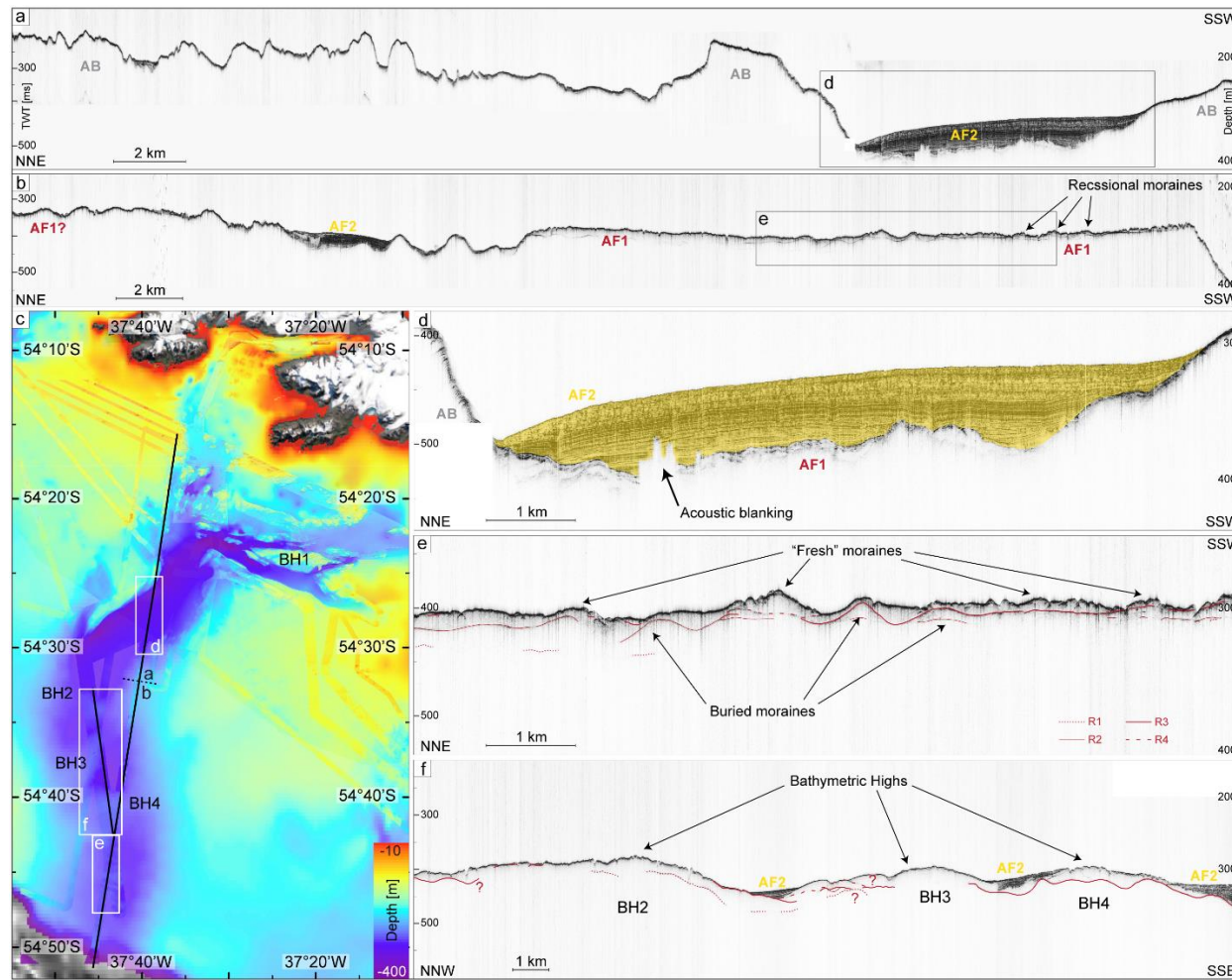


Fig. 5.4: Examples of the sub-bottom profiler data across KHT. a, b) Part 1 and 2, respectively, of a NNE-SSW profile across the shelf. The distribution of the identified acoustic facies, AB, AF1, and AF2 is indicated. Black rectangles show the morphological excerpt of sub-panels d and e. c) Bathymetric map of KHTS showing the location of the two illustrated sub-bottom profiles. The four bathymetric highs, BH1-BH4, are labelled. d, e) Detail image of a section through the main trough basin of KHT with the thick sequences of AF2. Note the diffuse top reflector of AB and the acoustic blanking in the subsurface. e) Detail image of AF1 on the outer shelf with the internal reflectors, R1-R4, depicted in red. Buried and fresh moraines are arrowed. f) NNW-SSE profile across three of the bathymetric highs, BH2-BH4, interpreted to be potential morainal banks. Small deposits of AF2 are labelled and some internal reflectors of AF1 are indicated.

AF2 conformably overlies stratigraphically older facies in KHTS, and is commonly confined to the bathymetric basins. It has been described in detail by Lešić et al. (subm.). AF2 is present everywhere on the inner and mid-shelf of KHTS, but is absent on the outer shelf. It is characterised by acoustic stratification, imparted by generally well-defined, parallel, internal reflectors of variable amplitude (Fig. 5.4f,5). On the basis of three distinct and continuous internal reflectors, AF2 was subdivided into four sub-units, A (oldest), B, C, and D (youngest). Unit AF2-A is seen to directly overlie AF1 in several locations on the mid- and outer shelf (example in Fig. 5.4f), but is not resolved in east JT, although this may be due to an obliterated acoustic signal (Fig. 5.5). AF2 was sampled by four gravity cores and consists of silty mud with frequent diatom layers (Lešić et al., in prep.; Lešić et al., subm.).

#### 5.4.2.2. *Acoustic Facies - Interpretation*

Based on its acoustic character, AB could represent either bedrock or glacial till (cf. e.g. Forwick et al., 2010; Forwick and Vorren, 2011; Streuff et al., 2017b). Because AB is difficult to distinguish where it underlies younger sequences, there is insufficient evidence for an unequivocal interpretation. However, based on the fact that, in contrast to AF1, it is acoustically completely impenetrable, and because outcrops of AB often coincide with the position of the previously described bathymetric shoals, we consider an interpretation as bedrock more likely. This is supported by its diffuse character particularly on bathymetric slopes and its irregular top reflector (e.g. Ó Cofaigh et al., 2001; Ó Cofaigh et al., 2002; Evans et al., 2004).

The acoustic character of AF1 is not only similar to that of AB, but also to till observed in other glaciated regions (e.g. Pine Island Bay, Antarctic Peninsula; Evans et al., 2006b). Indeed, acoustically transparent till from the Antarctic shelf is associated with the same continuous, opaque, sometimes wavy reflectors as those observed within AF1 (Ó Cofaigh et al., 2002). Furthermore, similar reflectors to R1-R4 have previously been identified as the top of buried ice-marginal moraines or grounding-zone wedges (Ó Cofaigh et al., 2005a) and as glacial erosional surfaces (Ó Cofaigh et al., 2004). A hummocky reflector atop an acoustically transparent unit is also often associated with glacial lineations (cf. e.g. Evans et al., 2005; Ó Cofaigh et al., 2005a; Evans et al., 2006b; 2007). We hence interpret AF1 to be composed predominantly of subglacial till.



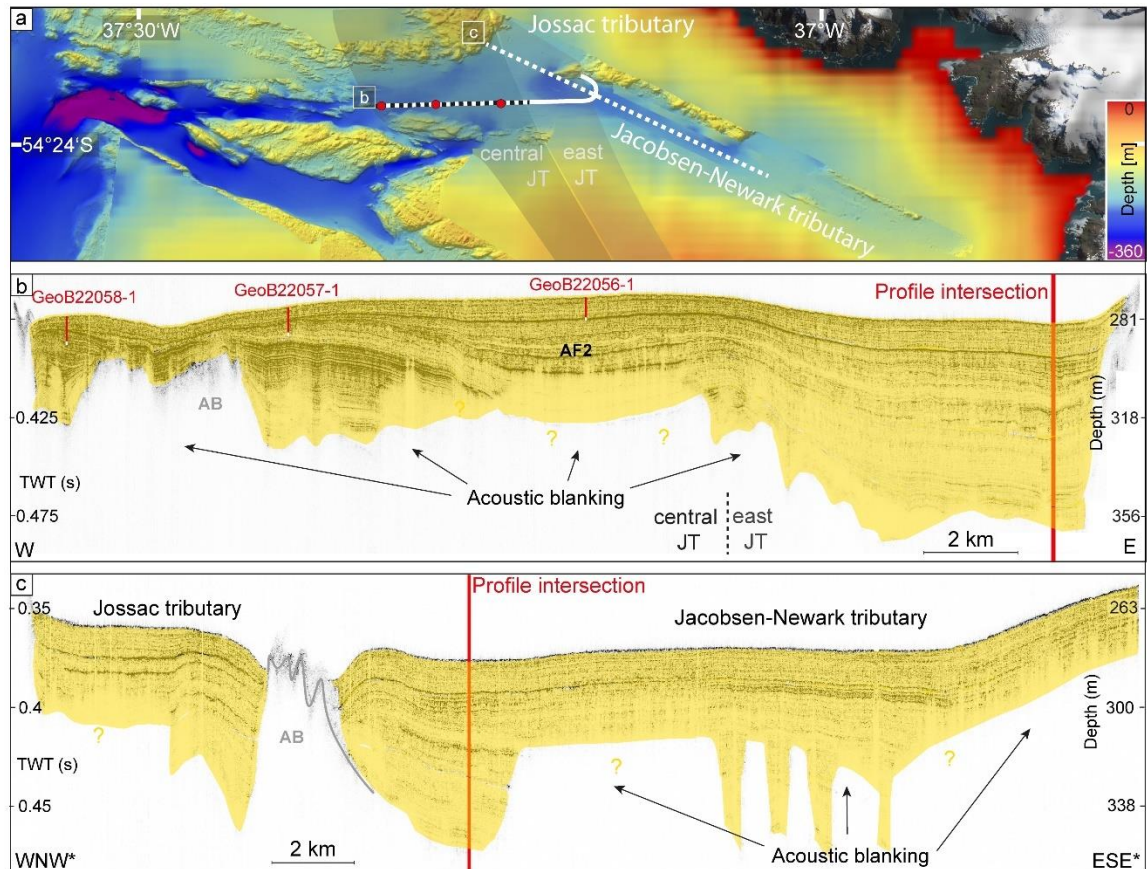


Fig. 5.5: Examples of sub-bottom profiler data through JTS. a) Bathymetric map of JTS showing the location of the two profiles shown in sub-panels b and c. The position of three gravity cores from Jacobsen Trough are marked in red. b) Sub-bottom profile through JT. Note the acoustic blanking in the subsurface and the thick sequence of AF2. AF1 appears to be absent. The locations and approximate recovery depths of the sediment cores are shown by the vertical red lines, whereas the white portion at their bottoms shows the assumed actual penetration depth when accounting for 16% sediment compression as a result of the coring process. c) Sub-bottom profile through Jossac Bight and the Jacobsen-Newark Bay, both tributaries to JT. Acoustic blanking is intensive and partially obliterates the signal. AB crops out in Jossac Bight and AF1 appears to be absent. Figure modified after Lešić et al. (subm.).

AF2 was interpreted as basin-fill sediment, deposited from mainly hemipelagic sedimentation (Lešić et al., subm.). Radiocarbon dating revealed Units AF2-B, AF2-C and AF2-D to be of Holocene age (Lešić et al., in prep.; Lešić et al., subm.), which is why they are considered to be outside the scope of this paper and the reader is instead referred to Lešić et al. (subm.) and Lešić et al. (in prep.). It was possible to date the upper parts of AF2-A in two locations, one in KHT close to the confluence zone (core PS133/2\_17-13), and one in central JT (core GeoB22058-1). Two ages from each location were used to provide relative age validation and to determine linear sedimentation rates (Lešić et al., in prep.; Lešić et al., subm.). The construction of an age model and an age of 10.2 cal

ka BP revealed that the upper 388 cm of AF2-A were deposited over a time period of  $\sim 2.6$  ka at assumed linear rates between 92 and 211 cm ka<sup>-1</sup> in central JT, whereas the upper 582 cm in KHT were deposited after 9 ka BP at rates between 359 and 837 cm ka<sup>-1</sup> (Lešić et al., in prep.). Since both gravity cores only sampled a fraction of AF2-A, the two ages derive from a position located relatively high in AF2-A.

## 5.5. Discussion – Glacial history

### 5.5.1. Trough origin

KHTS was interpreted as one of several cross-shelf troughs around SG, formed from glacial erosion (Graham et al., 2008; Graham et al., 2017). The presence of (sub-)glacial till (AF1) deposited as, presumably, the first sedimentary sequence on top of the acoustic basement, and the occurrence of glacial landforms observed in our acoustic data provide evidence that KHT indeed hosted grounded ice that likely carved out the trough valley over the course of one or more glaciations. The N-S orientation of KHT is in accordance with other cross-shelf troughs spreading roughly radially from the island and the slightly retrograde along-trough profile of an ancient KHT is in accordance with other cross-shelf troughs (e.g. Graham et al., 2008; Rydningen et al., 2013; Ryan et al., 2016), thus further strengthening the postulated origin of KHT.

Looking at the bathymetry from central KHT, it is obvious that the western side of the flank is much deeper than the eastern side (Fig. 5.2a). This asymmetry is also apparent in the sub-bottom profiler data, where, in lieu of an actual cross-profile, the comparison between several adjacent NE-SW profiles revealed the AF1-AF2 boundary to be in progressively deeper waters from east to west (Fig. 5.6). Accordingly, the asymmetry appears to have already been established during the deposition of, at least the upper parts of, AF1. This is comparable to cross-profiles of glacial troughs around the Antarctic Peninsula and Iceland, where asymmetric trough incisions have been related to preferential erosion of weaker bedrock/subglacial substrate on one side over the other (Evans et al., 2006a; Spagnolo and Clark, 2009). A similar mechanism in KHTS is feasible, because of the location of the CBSZ; indeed the NE-SW orientation of central KHT is parallel to a fault inferred by Graham et al. (2008), which might represent a potential extension of the dislocation zone (Fig. 5.1b). Although asymmetric trough incisions could also be the result of the Coriolis force, either directly, causing preferential ice flow along

the western flank, or by affecting its subglacial meltwater system and thus indirectly influencing ice stream dynamics (Karukäpp, 2004), we consider this unlikely in SG, where one would expect a deflection to the left-hand side of ice flow, i.e. to the eastern flank of KHTS. Asymmetric trough formation could also explain the occurrence of moats predominantly along the western flank. Moats in KHTS were related to bottom-currents establishing after the last glacial (Lešić et al., subm.), which are likely to be deflected to the west trough flank by the Coriolis force as shelf waters would have entered the trough from the south (Bressan and Constantin, 2019).

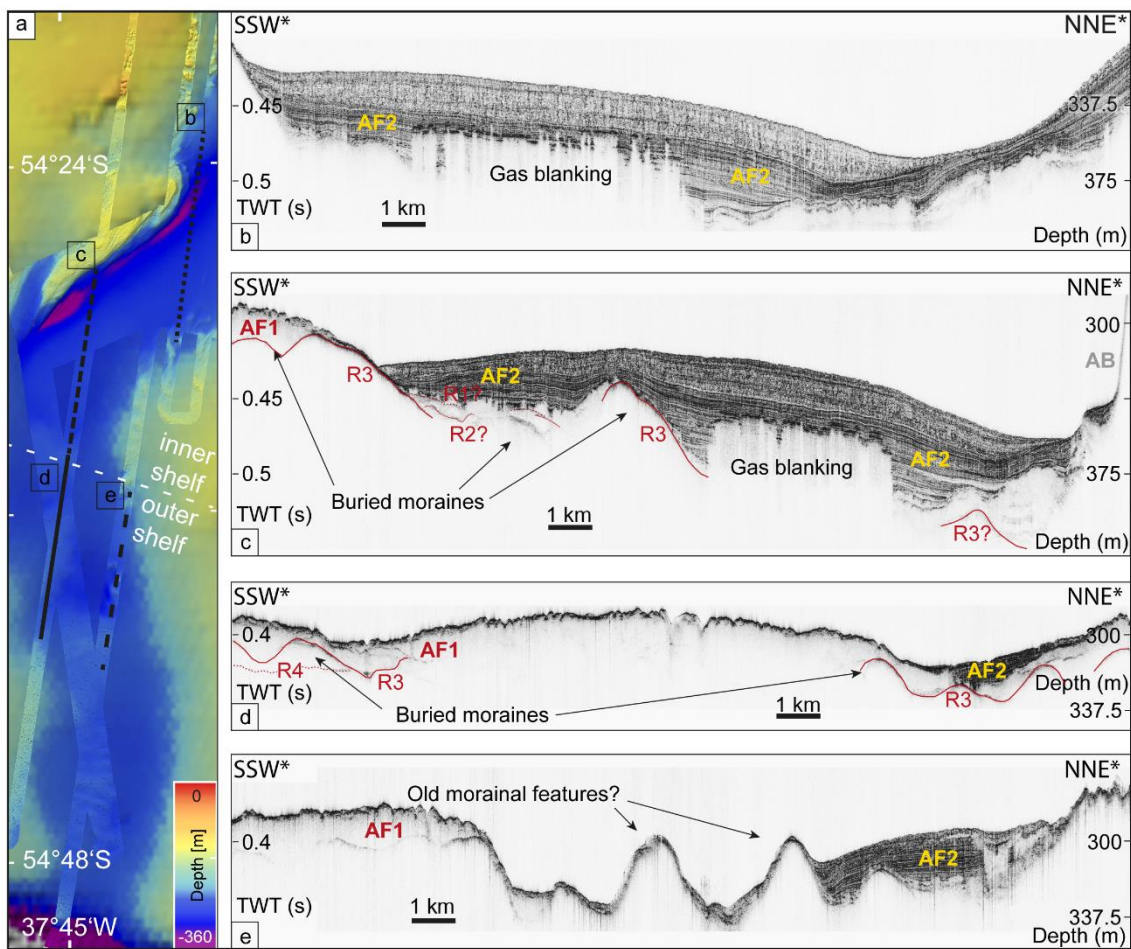


Fig. 5.6: Parallel sub-bottom profiles from KHT showing asymmetric trough incision. A) Reference map for location of sub-panels b-e. b-e) individual sub-bottom profiles showing crude facies interpretation. Note the different depths of the AF1-AF2 facies boundary between SSW and NNE when comparing sub-panels.

In contrast to the N-S orientation of KHT, the E-W, and de facto *along*-shelf, orientation of JTS is at odds with formation as a regular cross-shelf trough. However, the presence of the parallel, streamlined glacial landforms in JTS shows that ice must have also been grounded in this trough. Additionally, their orientation along the flanks of the trough

provide evidence for ice flowing from generally (north)east to west through JT (Fig. 5.2b). Although it is unclear why an ice stream or trunk glacier would have followed an along-shelf direction before joining KHT and changing to a cross-shelf direction, it is possible that pre-existing tectonic weaknesses in the bedrock dictated an ice-flow route, thus facilitating erosion in an E-W direction. This seems likely considering that the suggested extension of the CBSZ, and associated structural weakness, exactly matches the orientation of JTS, and especially its Jacobsen-Newark tributary (Fig. 5.1b; cf. e.g. Dalziel et al., 2021). Furthermore, an additional inferred fault is thought to run along the eastern part of Jossac Bight (Fig. 5.1b, cf. Graham et al., 2008), thus reinforcing the theory of a facilitated formation of JTS, including its tributaries, as a result of structural weakness and glacial erosion. Since neither AB nor AF1 can be observed in JTS, there is no indication for (sub-)glacial sediment in the subsurface of that trough system. Although this might imply that the origin of JTS is solely related to tectonic processes, this is unlikely given the presence of streamlined landforms and the connection to a series of glacier-fed tributaries. This is similar to Drygalski Fjord System, where an inferred fault is thought to run along DT (Fig. 5.1b cf. Graham et al., 2008).

#### 5.5.2. Ice advance

Glacial landforms are present in JTS and KHT and therefore provide evidence for grounded ice on the southern SG continental shelf during peak glaciation. We established above that streamlined landforms in JTS indicate palaeo-ice flow from (north)east to west, whereas the N-S orientation of such lineations in KHT is at odds with this interpretation. Nonetheless, as both KHT and JTS have a number of tidewater glaciers at their heads, it is entirely plausible to assume that several glaciers were involved in trough formation. We hence postulate that an extended Briggs Glacier, likely as the main trunk glacier, drained the SGIC from east to west through King Haakon Bay, thus forming the pronounced fjord basin, and joined the Peters and Price Glaciers, draining N-S through Cheapman Bay, just west of the sill or moraine (see Figs. 5.1c, 5.2b and section 5.2). The combined three glaciers would then have drained through northern KHT, being joined by Hawkesbury Glacier southwest of Queen Maud Bay. Although this may be an artefact from the lack of high-resolution bathymetry north of the Nuñez Peninsula, the first appearance of short and crude streamlined bedforms just

north of the KHT-JTS confluence zone would be consistent with such an interpretation, as the combined force of several glaciers at this point was probably sufficient to erode and modulate the underlying bedrock. This is further supported by the consistent deepening of the major trough basin, at least until close to the shelf edge (cf. Fig. 5.1c,2a). Similarly, the distribution of streamlined bedforms in JTS suggests that a palaeo-trunk glacier, presumably composed of Christophersen, Eclipse and Bary Glaciers, drained the SGIC in an E-W direction through Jacobsen Bight and was then joined by the three glaciers draining through Newark Bay from the northeast, thus forming the eastern parts of JTS (cf. Figs. 5.1c, 5.2b). Esmark, Keilhau and Jewell Glaciers would have drained through Jossac Bight in a general NE-SW direction (cf. Figs. 5.1c, 5.2a), joining the Christophersen trunk glacier in east JT (Fig. 5.1c). The combined force of those glaciers would then probably have been sufficient to carve out JT and partly AT, while the position of AT with respect to Annenkov Island and its ESE-WNW orientation suggests additional ice draining from there (Fig. 5.1). Just west of the confluence zone the Briggs and Christophersen trunk glaciers would have merged, developing into an ice stream draining the SGIC further, first in a NNE-SSW, then in a ~N-S direction, all the way to the shelf edge. This hypothesis seems reasonable, especially when considering that the confluence zone of KHT and JTS marks the deepest part of the ancient trough morphology - it could thus easily represent a locus for concentrated erosion from trunk glaciers joining to form an ice stream. Despite the fact that this scenario is based on the SGIC configuration of today, which, very likely, does not represent configurations of past glacial maxima, we still argue that this is a feasible explanation for the distribution of the troughs and their glacial landforms, especially for the more recent glaciations.

The bathymetric data show that the glacial linear features in KHTS evolve from crudely streamlined seafloor and shorter crag-and-tails on the inner and mid-shelf to much more elongate glacial lineations towards the outer shelf. Such consecutive elongation is consistent with observations from other glacial cross-shelf troughs, specifically around the Antarctic Peninsula, where it was associated with a change from harder to softer substrate on the one hand, and progressive flow acceleration on the other (Ó Cofaigh et al., 2005a; Ó Cofaigh et al., 2005b). Indeed, some of the linear bedforms in the outer trough appear in the, presumably softer, sediment sequences of the trough basin. Flow

acceleration is also supported by the increasing length:width ratios towards outer KHTS (Stokes and Clark, 1999), which would also support the idea of a cumulative force of conjoining trunk glaciers draining a palaeo-SGIC through KHT and JTS.

### 5.5.3. Peak Glaciation

A terminal moraine marking maximum ice extent is lacking in KHTS, but the continental shelf edge slopes upwards for the outermost 2.6 km, thus generating a ~20 m-high “wedge” with a flatter proximal and a steeper distal slope (Fig. 5.4b). Dimensions are at the lower spectrum of smaller grounding-zone wedges (GZWs) in the northern hemisphere and the overall morphology appears somewhat similar to a GZW documented from the shelf break off Melville Bay in NW Greenland (#45 in Batchelor and Dowdeswell (2015)). While this might therefore suggest a GZW to be present at the southern SG shelf break, the observation is based on a single Parasound line, making such an assumption highly speculative. Nonetheless, a GZW at this position could indicate ice extending all the way to the shelf break, as these large sedimentary depocentres form along the grounding lines of large ice streams and are associated with high sediment delivery (Batchelor and Dowdeswell, 2015). A characteristic outward bulge, commonly associated with progradation of the continental slope as a result of glacial sediment delivery, appears to be either absent or very weakly pronounced at the mouth of KHTS, and the same seems to be true for trough-mouth fans frequently found at such locations (cf. Laberg and Vorren, 1995; Taylor et al., 2002; Evans et al., 2006b; Dowdeswell et al., 2008a; Lucchi et al., 2012; Ó Cofaigh et al., 2013; Camerlenghi et al., 2016). However, both the presence of subglacial till and recessional moraines this close to the shelf edge make the latter a very likely target, which has indeed been suggested to be the position of maximum ice extent during the Local Last Glacial Maximum (Sugden and Clapperton, 1977; Clapperton et al., 1989b; Graham et al., 2008; Barlow et al., 2016; 2017; Lešić et al., 2022).

#### 5.5.3.1. *Timing of peak glaciation*

Timing of the glacial period excavating the trough and producing the landforms is difficult to estimate. KHTS was previously interpreted as one of several cross-shelf troughs on the continental shelf of SG, formed from glacial erosion related to the LLGM, and likely also to preceding glaciations (Graham et al., 2008; Graham et al., 2017). While

the presence of the (sub-)glacial till of AF1 deposited as the presumably first sedimentary sequence on top of the acoustic basement might provide evidence for rather early glacial till (SG has been tectonically stable since ~6.4 Ma (Graham et al., 2008) and we would accordingly expect bedrock to be quite old), we have no age control from AF1, which makes it difficult to pinpoint the exact time of formation or deposition. We do, however, suggest that AF1 represents multiple generations of subglacial till, related to a minimum of three separate glaciations. This is based on the presence of four internal reflectors, one of which, R3, likely represents a buried glacial landscape (cf. Fig. 5.4e), comparable to reflectors observed in TOPAS data from the Antarctic peninsula (Ó Cofaigh et al., 2005a). R1 to R4 would then indicate surfaces of glacial erosion associated with renewed ice advance and obliteration of any deposits from preceding glaciations. This is in accordance with similar findings from Northeast Greenland, where stacked acoustically transparent units, separated by (semi-)continuous opaque reflectors, were also interpreted as stacked till sequences (Ó Cofaigh et al., 2004). Repeated episodes of ice (re-)advance were also concluded for the northern shelf of SG from the presence of both truncated and well-preserved ice-sheet end moraines (Clapperton et al., 1989b; Graham et al., 2008; Graham et al., 2017). An interpretation of several till generations is further supported by the fact that AF1 forms moraines both in the subsurface as well as at the seafloor. Although the latter could simply be related to draping, and thus maintenance, of the buried R3 landscape (cf. Fig. 5.4e), R3 is present as a flat reflector with superimposed moraines on the outer shelf, which immediately negates this possibility (Recessional moraines in Fig. 5.4b). One might further argue that the portion of AF1 above R3 could represent mass-flow deposits rather than glacial till. We consider this unlikely, however, as this part of AF1 occurs in a generally flat terrain where triggers for such widespread gravitational mass movements are inconceivable. Moreover, Ó Cofaigh et al. (2005a,b) suggested a similar acoustic unit on the western Antarctic Peninsula to represent a sheet of (deformation) till. Such an interpretation is also supported by the absence of characteristically dipping reflectors and/or lenticular sediment bodies, which we would expect if, at least parts of AF1, were formed from mass flows. Although it is technically possible that the different till generations merely relate to separate phases of ice advance, the stacked till sequences can be traced over a distance of ~28 km from the mid- to the outer shelf. As we consider it unlikely that ice

margin positions oscillated this much within a single glacial period, we conclude that an interpretation of AF1 as several generations of glacial till is entirely feasible and would, in turn, provide evidence that KHT and JTS did, in fact, form over the duration of several glacial periods (cf. also Graham et al., 2008; Graham et al., 2017; Lešić et al., 2022).

The stacked sequences cease to exist about 2.5 km from the shelf edge, so only one sequence of AF1 is present on the outermost shelf. Since it would seem odd that the acoustic profiler signal managed to pick up underlying sequences on the mid- and outer shelf, but not at the shelf edge, this may suggest that out of at least three shelf-wide glaciations, only one reached the actual shelf edge. However, assuming that the interpretation of R3 as the surface of a buried glacial landscape is true, the apparent lack of more sequences of glacial till must be related to a lack of signal penetration into the stiff till. Again, this speculation is based on a single profile and more data would be needed to reliably answer this question. Assuming that this is true, this then raises the question which of the glacial periods was the most extensive. Contradictory evidence from the bathymetry and sub-bottom data makes this difficult to answer, and is discussed in the following section.

#### *Local Last Glacial Maximum*

One might argue that the LGM (Marine Isotope Stage (MIS) 2) would be the most likely candidate for glaciation all the way to the shelf edge. This is indicated by the following: (i) several studies from SG favour shelf-wide glaciation for the LLGM (e.g. Sugden and Clapperton, 1977; Clapperton et al., 1989b; Graham et al., 2008; Barlow et al., 2016; Lešić et al., 2022). As the LGM forced shelf-wide ice extent for several areas around the Antarctic Peninsula and West Antarctica (Dowdeswell et al., 2004; Evans et al., 2005; Ó Cofaigh et al., 2005b; Klages et al., 2014), and an extensive LGM was also proposed for other sub-Antarctic islands (Hodgson et al., 2014b), maximum ice extent during MIS 2 is entirely plausible for SG. (ii) It seems unlikely that the glacial landforms observed on the seafloor of KHTS date back much further. Apart from the fact that we would expect glacial landforms from a previous ice extent to have been either modified into overridden features (cf. Ottesen and Dowdeswell, 2006; Ottesen and Dowdeswell, 2009; Greenwood and Kleman, 2010; Streuff et al., 2015) or obliterated altogether by a renewed, and more extensive ice advance at a later stage, Graham et al. (2008) already



argued that rates of typical post-glacial sedimentation for continental shelves (they assumed 5-800 cm ka<sup>-1</sup> on the basis of such rates documented from the Norwegian shelf) would likely be sufficient to bury any low-relief landforms within a, geologically speaking, relatively short period of time. Indeed, both Graham et al. (2017) and Barlow et al. (2016) already tentatively attributed outer-shelf moraines to the LLGM. (iii) At first glance, the three bathymetric highs, BH2 to BH4, in outer KHT appear to be similar to grounding-zone wedges observed from other glacial settings and their orientation and positions within the trough basin would fit an interpretation as large sedimentary depocentres formed during still-stands in ice recession since the LLGM (Batchelor and Dowdeswell, 2015). Formation as recessional features (cf. Hunter et al., 1996) would also be in accordance with Graham et al. (2008), who previously interpreted BH2 as a morainal bank. The same study also documented similar mid-trough moraines on the NW continental shelf of SG, where one suggested possibility for their formation included marginal still-stands during overall deglaciation (Graham et al., 2008). (iv) Ice-proximal sediments, dating to before 17.5 cal ka BP, were documented from the mid-shelf of the adjacent Drygalski Trough (Fig. 5.1b), the position of which is significantly further south than the shelf edge in KHTS. The waterlain till was suggested to provide evidence that DT also experienced shelf-wide ice extent during the LLGM (Lešić et al., 2022), consistent with MIS 2.

#### *Pre-LLGM*

Most of the above arguments for the LLGM may just as easily be discounted again, opening the possibility of a pre-LGM age for the maximum ice extent. (i) Pleistocene glaciations have been shown to be rather extensive in, for instance, Patagonia, where ice extents were inferred to be larger during MIS 3 than during the LGM (Darvill et al., 2015), but have also been postulated for South Georgia and Kerguelen (Hodgson et al., 2014b). In addition to this, several studies have actually suggested a restricted LLGM ice extent on SG, hence, at least indirectly, implying more extensive glaciation during earlier glacials (Bentley et al., 2007; Hodgson et al., 2014a). (ii) The good preservation of the landforms in KHTS merely provides evidence that they are relatively “fresh”. Accordingly, if subsequent re-advances of the SGIC were less extensive than the one forming the streamlined bedrock and recessional moraines, this would explain why none

of the landforms show signs of glacial modification. This also applies to BH2-BH4, whose rugged surfaces are associated exclusively with iceberg scouring (Fig. 5.3). Moreover, we consider sedimentation rates as low as  $5 \text{ cm ka}^{-1}$  plausible for the outermost shelf areas (Graham et al., 2008). Consequently, it would take about 200 ka to bury the 10 m-high streamlined bedforms and recessional moraines in KHTS, suggesting that at least on the outer shelf the landforms may derive from as far back as the Saalian glacial (MIS 6, cf. Gibbard and Cohen, 2008; Ehlers et al., 2018). Note, however, that because mean sedimentation rates were shown to exceed  $180 \text{ cm ka}^{-1}$  on the inner shelf (Lešić et al., in prep.), we would argue that at least the streamlined landforms on the inner shelf derive from the LLGM. (iii) At second glance, BH2, 3 and 4 actually appear to be significantly smaller than GZWs documented from elsewhere (Batchelor and Dowdeswell, 2015). They also lack the characteristic asymmetry, with BH2 even showing the opposite, i.e. a steeper proximal and flatter distal flank (see section 5.4.1). The latter is more commonly found in terminal moraines, marking maximum extents of glaciers or large palaeo-ice streams (e.g. Ottesen and Dowdeswell, 2006; Streuff et al., 2015). Consequently, the recessional moraines at the shelf edge could indeed derive from the Penultimate Glacial Maximum (PGM), while BH4, BH3 and BH2 would mark the maximum extents of three subsequent glacial re-advances. Ice sheet re-advances were also the second possibility suggested for the formation of the mid-trough moraines in NW SG (Graham et al., 2008). Given their good preservation, BH4 would then be older than BH3, which, in turn, would be older than BH2, suggesting consecutively more restricted ice advances until formation of BH2 at the LLGM. This is at odds with the distribution of the multiple till sequences, however, which extend at least until the position of BH3 (Fig. 5.4d). Climatic periods between the PGM and the LGM could have caused ice to repeatedly advance all the way to the outer shelf may include, for instance, MIS 3, which was shown to have been extensive in Patagonia (Darvill et al., 2015), MIS 4, or potentially colder substages of MIS 5 (see e.g. Diekmann et al., 2000; Hagemann, 2023).

The above shows that the glacial evolution of KHTS offers much potential for debate. Both scenarios are possible and would, in their own way, seem plausible, but since chronological age control is still extremely scarce on the entire marine environment of

SG, it is impossible to definitively assign glacial periods to either the till sequences or the landforms. Because the majority of studies from SG seem to support most extensive ice advance during the LLGM, having since refuted the restricted ice scenarios proposed by Hodgson et al. (2014a) and Bentley et al. (2007), we cautiously adapt this theory and would then suggest that BH2-BH4 may indeed represent morainal banks, deposited during still-stands of a generally receding ice margin after the LLGM. Maximum ice extent during the LLGM rather than a previous glaciation would also make the behaviour of the SGIC more comparable to the West Antarctic and Antarctic Peninsula, rather than Patagonia, and would further imply a post-LLGM age for the recessional moraines at the shelf edge. This, in turn, would then suggest that R3 marks the erosive surface of a preceding glaciation. Assuming that R3 indeed represents the surface of a buried landscape, and that it extends all the way to the shelf edge, we would then assume that an equally extensive ice extent occurred during one of the previous glaciations. We stress, however, that until undisputable evidence emerges, we have no way of determining the age of the peak glaciation(s) in KHTS.

#### 5.5.4. Deglaciation

A study from outer Drygalski Trough, approximately 90 km to the southeast of KHTS (Fig. 5.1b), has shown that the ice cap reached all the way to the shelf edge during the considerably early LLGM, with post-LLGM deglaciation and subsequent sedimentation hypothesised to have started as early as 30 ka BP (Lešić et al., 2022). Deglaciation was suggested to be asynchronous, with formation of a subglacial cavity initiating around 30 ka BP, allowing for the subsequent deglaciation of DT much earlier than the surrounding shallower shelf areas. A radiocarbon date of 17.5 cal ka BP from ice-proximal sediments was interpreted to mark the time frame when the entire ice sheet started to retreat from the mid-shelf (Lešić et al., 2022). If conditions for the two trough systems were similar, the uppermost sequence of AF1 (above R3) in KHTS would indeed represent glacial till from the LLGM. This is supported by the 13 m of overlying basin-fill sediments (AF2) on the outer shelf (cf. Fig. 6.8 in Chapter 6), which, assuming a maximum deposition time of 30 ka, indicate average sedimentation rates of 43 cm ka<sup>-1</sup>. These would be within the range of average sedimentation rates in Drygalski Trough (~32-68 cm ka<sup>-1</sup>, ex- and including peak sedimentation rates during the ACR, respectively; cf.

Lešić et al., (2022). Extrapolations to the bottom of Unit AF2-A suggest that the onset of AF2 in KHTS occurred sometime after 31 and before 12 ka BP based on linear sedimentation rates (Lešić et al., in prep.; Lešić et al., subm.), which might further strengthen a hypothesis of upper AF1 as LLGM till. Although we can only speculate about the mode of retreat, the recessional moraines and potential morainal banks on the mid- and outer shelf (BH2-BH4) seem to suggest step-wise retreat, at least during the initial phase of deglaciation, with several shorter and three longer periods of still-stand (cf. Batchelor and Dowdeswell, 2015; Dowdeswell et al., 2016b). The widespread signs of intensive iceberg scouring indicate that ice recession happened predominantly by calving and that icebergs had keel depths exceeding 300 m.

If KHTS and the adjacent Drygalski Trough are indeed comparable, the radiocarbon age of 17.5 cal ka BP would imply deglaciation prior to or around this time also for the former. This would increase sedimentation rates from 43 to 74 cm ka<sup>-1</sup> for the outer shelf, which is still plausible as the recessional moraines on the outer shelf may have been partially buried. The fact that the vast majority of streamlined bedforms can only be observed on the mid-shelf (Fig. 5.2b) could further support this, as these, typically lower-relief, landforms may have been buried more quickly on the outer shelf.

A deglaciation age of 17.5 cal ka BP would also imply rates exceeding 300 cm ka<sup>-1</sup> for the thickest, complete sequence of post-glacial AF2, which is located in central KHT. Similar rates between 359 and 837 cm ka<sup>-1</sup> have since been confirmed on the basis of additional radiocarbon ages from Unit AF2-A sampled in a nearby sediment core (PS133/2\_17-13; Lešić et al., in prep.), but actually seem to be slightly lower than sedimentation rates in central JT (367-966 cm ka<sup>-1</sup> in GeoB22056-1; Lešić et al., in prep.). Although both rates would be significantly higher than those observed in Drygalski Trough (max. ~190 cm ka<sup>-1</sup>; Lešić et al., 2022), higher sedimentary input into KHTS could easily be accounted for by the cumulative deposition of sedimentary material from the numerous tributaries and their associated tidewater glaciers. Furthermore, the rates are comparable to inferred post-glacial linear sedimentation rates from the mid-shelf in Royal Bay Trough (RBT, Fig. 5.1b) in north-eastern SG (306-632 cm ka<sup>-1</sup>; Graham et al., 2017). Here, the onset of post-glacial trough infill was postulated to have occurred around 18 ka BP, thus

further implying that deglacial conditions may have been similar for the larger cross-shelf troughs around SG.

We previously mentioned that neither AF1 nor AB are resolved in the sub-bottom data of JT (Fig. 5.5) and discarded the possibility that this is related to an absence of glacial influence in the trough system. Although this apparent lack could very easily be (and was likely) caused by the very thick sediment sequences, placing AF1 and AB outside the resolution limits of the echosounder system, a second possibility could be the presence of a subglacial cavity establishing below the LLGM ice cap, just as reconstructed for Drygalski Trough (Lešić et al., 2022). While this would be feasible on the grounds of the pre-existence of a sufficiently deep basin (cf. Pine Island Bay, Antarctic Peninsula; Kuhn et al., 2017) and the presence of streamlined seafloor along the trough flanks, we would, in that case, expect to find cavity-characteristic deposits in JT (Lešić et al., 2022). The acoustic signature of the waterlain diamicton in Drygalski Trough is very similar to the acoustic stratification of AF2-A in KHTS and may suggest that such deposits are indeed present in JT and KHT. Furthermore, the cores sampling AF2-A were almost certainly too short to recover such sediments - the oldest recovered sediments dated to 10.2 ka BP, suggesting that a considerably higher amount of sediment would have needed to be obtained in order to yield sediments dating to ~17.5 ka BP.

It should be mentioned, that while considered somewhat unreliable, an extrapolated time frame between 31 and 12 ka BP for AF2-A onset may not only support an origin of the upper portions of AF1 as LLGM till. Instead, the time frame also covers part of the Antarctic Cold Reversal (ACR), a renewed cold period associated with a temperature drop of 2-3°C (Bakke et al., 2021) and significant glacier advance on the north-eastern side of SG (Graham et al., 2017; Bakke et al., 2021). This could mean that AF1 actually represents glacial till from this renewed cold period. Indeed, a number of arguments could potentially support a more extensive ACR advance in JTS than elsewhere: (i) a previous interpretation that ACR advances were restricted to the fjord regions was predominantly based on bathymetric data from the major fjords around SG (e.g. Hodgson et al., 2014a). Although this included King Haakon Bay, the JTS tributaries appear to be morphologically very different and their seemingly flat and wide bathymetry (see Fig. 5.1c and section 5.2) might have facilitated more extensive glacier

advance due to reduced lateral drag. (ii) Most of the major fjords used for the ACR reconstructions are located on the northern side of the island, but a north-south climate gradient across SG actually favours precipitation, and potentially associated larger glacier extents, in the south (Gordon et al., 2008; Cook et al., 2010; Farías-Barahona et al., 2020; Lešić et al., 2022). (iii) Age control for ACR deposits exists only from Royal Bay Trough and Cumberland Bay (RBT and CB, respectively; Fig. 5.1b), where onset of glacial marine sedimentation post-ACR was dated to 13.3 cal ka BP (Graham et al., 2017), a timing consistent with the extrapolated time frame for the deposition of Unit AF2-A. (iv) A bathymetric ridge feature in Drygalski Trough (R4) could potentially derive from a more extensive ACR advance, despite the fact that this was considered less likely (Lešić et al., 2022). (v) The large bathymetric high separating AT from JT, BH1, was previously interpreted as a morainal bank or ridge (Graham et al., 2008), which would be a feasible interpretation when considering ACR re-advance.

Despite the above, we actually consider such an extensive ACR advance improbable. This is mainly based on the presence of the uppermost portion of AF1 all the way to the shelf edge, which seems highly unlikely for the ACR. Neither has there been a record of a grounded ice sheet even as far as the mid-shelf during the ACR. Furthermore, the bathymetric data currently available from the JTS tributaries as well as Cheapman and Queen Maud Bays have a low resolution of 500 m, which, on the one hand might indicate that the morphological assessment of the embayments is sporadic at best, and on the other could easily obliterate any potential fjord moraines relating to the ACR. In addition to that, AF2-A was actually interpreted to include the ACR (Lešić et al., in prep.; Lešić et al., *subm.*), as according sediment in DT seemed to record the ACR only through an increase in sedimentation rates. Otherwise, the sediments were found to be remarkably similar to post-LLGM deposits, i.e. characterised by acoustic stratification and a composition of predominantly (glaci-)marine mud (Lešić et al., 2022). Lastly, symmetry and large height of BH1 seem to be at odds with an interpretation as a terminal moraine. Instead, based on its E-W orientation, the previously established connection of JTS to the CBSZ, and the much rougher appearance compared to other glacial landforms identified in this study, we consider it more likely that BH1 actually represents a bedrock high.

The acoustic profiles from the mid- and inner shelf demonstrate that during and after the LLGM-subsequent ice retreat, acoustically stratified, post-glacial (glaci-)marine basin-fill sediments (Units A-D of AF2) were deposited onto the pre-existing glacial landscape, i.e. AF1. These recorded several distinct changes in depositional environments throughout the Holocene, which are subject of Lešić et al. (in prep.) and Lešić et al. (subm.).

## 5.6. Conclusion

Seafloor bathymetry and sub-bottom profiles from the King Haakon Trough System offer new insights into the glacial evolution of a large cross-shelf trough system on the southern South Georgia continental shelf. The data confirm an interpretation of a main trough, King Haakon Trough (KHT), as a common cross-shelf trough, formed by glacial erosion, preferentially on the western side, throughout consecutive glacial periods. Its nearly perpendicular tributary trough system, the Jacobsen Trough System (JTS), on the other hand also formed from glacial erosion, but its development was probably largely controlled by an adjacent tectonic boundary, the Cooper Bay Shear Zone, causing considerable structural weaknesses in the pre-existing bedrock. Several glacial landforms visible on the contemporary seafloor allow for the reconstruction of two main trunk glaciers, conjoining on the inner shelf to form an accelerating ice stream. Ice flow direction is indicated by streamlined seafloor and numerous crag-and-tails, and was shown to be E-W through JTS and roughly N-S through KHT. Recessional moraines and possible morainal banks are present on the outer and mid-shelf and the shallower areas of the seafloor are intensively scoured. Together with several stacked till sequences observed in the sub-bottom profiler data, these landforms reveal that during at least one peak glaciation the South Georgia Ice Cap reached all the way to the shelf break from where it retreated in a step-wise manner predominantly by iceberg-calving. Although the onset of deglaciation is difficult to determine, several arguments are in favour of a similar evolution to both the adjacent Drygalski Trough and Royal Bay Trough in northeast South Georgia, where ice retreat was already underway by 17.5 ka BP. Although the data elucidate a further piece of South Georgia's glacial history, we call for further investigations and, most importantly, age control on the marine environment, in

order to be able to fully reconstruct the Quaternary evolution of this sub-Antarctic ice cap.

### **Acknowledgements**

This work was funded by the “Deutsche Forschungsgemeinschaft” (DFG) in the framework of the priority program SPP 1158 "Antarctic research with comparative investigations in Arctic ice areas", grants BO 1049/23-1 and KU 683/18-1. We thank the captain, chief scientist and crew from *RV Meteor* cruise M134. Processing of the bathymetric data by C. dos Santos Ferreira was greatly appreciated. All maps in this publication, except Fig. 5 and 6, which were created in QGIS 3.22.11, were created using ArcMap™ as part of the ArcGIS® Pro software by Esri and are used herein under license. Figures were partially created and finalised in Adobe Illustrator 2022/2023.



6. Manuscript III: Spatial and temporal variability in Holocene trough-fill sediments, King Haakon Trough System, sub-Antarctic South Georgia

Submitted to Quaternary Science Advances (August 2023)

The following manuscript version is a preprint (DOI: <http://dx.doi.org/10.2139/ssrn.4563255>). It has since been peer-reviewed and published in Quaternary Science Advances (DOI: <https://doi.org/10.1016/j.qsa.2023.100156>) under the license CC-BY-NC-ND 4.0 (<https://creativecommons.org/licenses/by-nc-nd/4.0/legalcode.en>)

Reference: Lešić, N. M., Streuff, K. T., Bohrmann, G., Kasten, S., & Kuhn, G. (2024). Spatial and temporal variability in Holocene trough-fill sediments, King Haakon Trough System, sub-Antarctic South Georgia. *Quaternary Science Advances*, 13, 100156.

Lešić, Nina-Marie<sup>1,2</sup> (nlesic@marum.de); Streuff, Katharina Teresa<sup>1</sup> (kstreuff@marum.de); Bohrmann, Gerhard<sup>1</sup> (gbohrmann@marum.de); Kuhn, Gerhard<sup>1,2</sup> (ge\_ku@uni-bremen.de)

*1 MARUM, Centre for Marine Environmental Sciences, and Faculty of Geosciences, University of Bremen (UoB), Klagenfurter Str.2-4, 28359 Bremen, Germany*

*2 Alfred Wegener Institute (AWI), Helmholtz Centre for Polar and Marine Research, Am Alten Hafen 26, 27568 Bremerhaven, Germany*

Corresponding author: Lešić, Nina-Marie (nlesic@marum.de)

Keywords: Sub-Antarctic, Acoustic data, Marine Sedimentology, Pleistocene reconstruction;  
Depositional Environments

## Abstract

The climate in the South Atlantic sector of the sub-Antarctic, and therefore on and around South Georgia island, is dependent on the Southern Hemisphere Westerlies (SHW) and the Antarctic Circumpolar Current (ACC), which, in turn, are strongly associated with climate variability in the Southern Hemisphere. Accordingly, thick sediment sequences in the troughs across South Georgia's continental shelf should archive past climate in the Southern Ocean. Since Holocene climate fluctuations led to only minimal oscillations in glacier margin positions within the fjords, the entire shelf was exposed to dynamic ocean currents around this time. Its depositional systems are therefore a suitable target for the reconstruction of Holocene dynamics of both SHW and ACC. Sub-bottom profiler data and radiocarbon ages from four gravity cores from the southern continental shelf provide evidence for a complex interplay between island run-off and ocean currents intruding into a unique cross-shelf trough system

during the last ~10 ka. The data record several prominent changes in sediment and Holocene climate dynamics, the most significant occurring between 8.5 and 7.7 cal ka BP and between 2.6 and 2.2 cal ka BP, both of which represent transitions from warmer to cooler and windier conditions in South Georgia and the Southern Hemisphere. Our record from the King Haakon Trough System is the first highly resolved Holocene archive from the marine realm on the south-western continental shelf of South Georgia that seems to reflect large-scale Southern Hemisphere climate changes during the mid- to late Holocene.

## 6.1. Introduction

The deposition of marine sediments, especially in previously glaciated areas, depends not only on local and regional climate, glacier dynamics and (associated) terrestrial runoff, but is also influenced by the ocean floor geomorphology and its resulting exposure to cross- and along-shelf currents. The latter can be highly variable and are often intrinsically linked to the presence of, e.g., exposed bathymetric highs or deeply incised glacial troughs, particularly on continental shelves (Dunbar et al., 1985; Dickens et al., 2014; Graham et al., 2017; Dickens et al., 2019). In climatically dynamic regions, such as the sub-Antarctic microcontinent South Georgia (SG), the already complex interplay between ocean, atmosphere and, still partially glaciated, landmasses is complicated even further by frequent shifts in the predominant climatic systems, i.e. the Southern Hemisphere Westerlies and the Antarctic Circumpolar Current fronts (SHW and ACC, respectively, Fig. 6.1a; Moreno et al., 2018); Orsi et al., 1995), as well as a wide and exposed shelf, making the entire region vulnerable to changing ocean configuration (cf. Anderson et al., 1984; Dunbar et al., 1985; Nicholls et al., 2009; Graham et al., 2017; Hillenbrand et al., 2017). As a result, (glaci-)marine sediments around the island archive not only the multitude of processes affecting their deposition, but also the evolution of such processes over time. The thick sedimentary sequences accumulated in the glacially-incised cross-shelf troughs around SG (Graham et al., 2008) are therefore particularly suitable for climate reconstructions, because they should provide insights into Holocene climate variability and resulting environmental changes - also in the broader context of Southern Hemisphere atmospheric oscillations - at a high temporal resolution.

Despite its potential for climate research, data on the SG microcontinent is mostly restricted to the island itself. Most studies investigating Holocene climate records (after 11.7 ka; Walker et al., 2009) have focused on a small area of the terrestrial north-eastern part of the island

(e.g. Clapperton et al., 1989b; Rosqvist et al., 1999; Rosqvist and Schuber, 2003; van der Putten et al., 2004; van der Putten and Verbruggen, 2005; van der Putten et al., 2009; Oppedal et al., 2018; Berg et al., 2019; Zwier et al., 2021; van der Bilt et al., 2022), while only two studies exist on the southern side of SG (Strother et al., 2015; Foster et al., 2016). Even fewer studies investigate the marine environment, where, to our knowledge, the only climate archive that focuses on the Holocene has been documented from a coastal inlet in Cumberland Bay, also located in north-eastern SG (Berg et al., 2019).

This study presents, for the first time, hydroacoustic data in combination with radiocarbon ages from a large cross-shelf trough system, the King Haakon Trough System (KHTS; Fig. 6.1), in order to elucidate marine Holocene climate records from the southern SG continental shelf. Apart from presenting and interpreting the Holocene acoustic record, it seeks to correlate sedimentological signatures observed from the local marine environment with climate events from other SG records and the Atlantic sector of the Southern Ocean. Our dataset is the first highly resolved Holocene record from the marine environment south of SG and not only shows repeated changes in KHTS sedimentation consistent with regional Holocene climate variability, but also demonstrates that depositional environments even in the inner-shelf regions were influenced by large-scale Southern Hemisphere-related processes (Bentley et al., 2009; Voigt et al., 2015; Moreno et al., 2018; Berg et al., 2019; Zwier et al., 2021; van der Bilt et al., 2022).

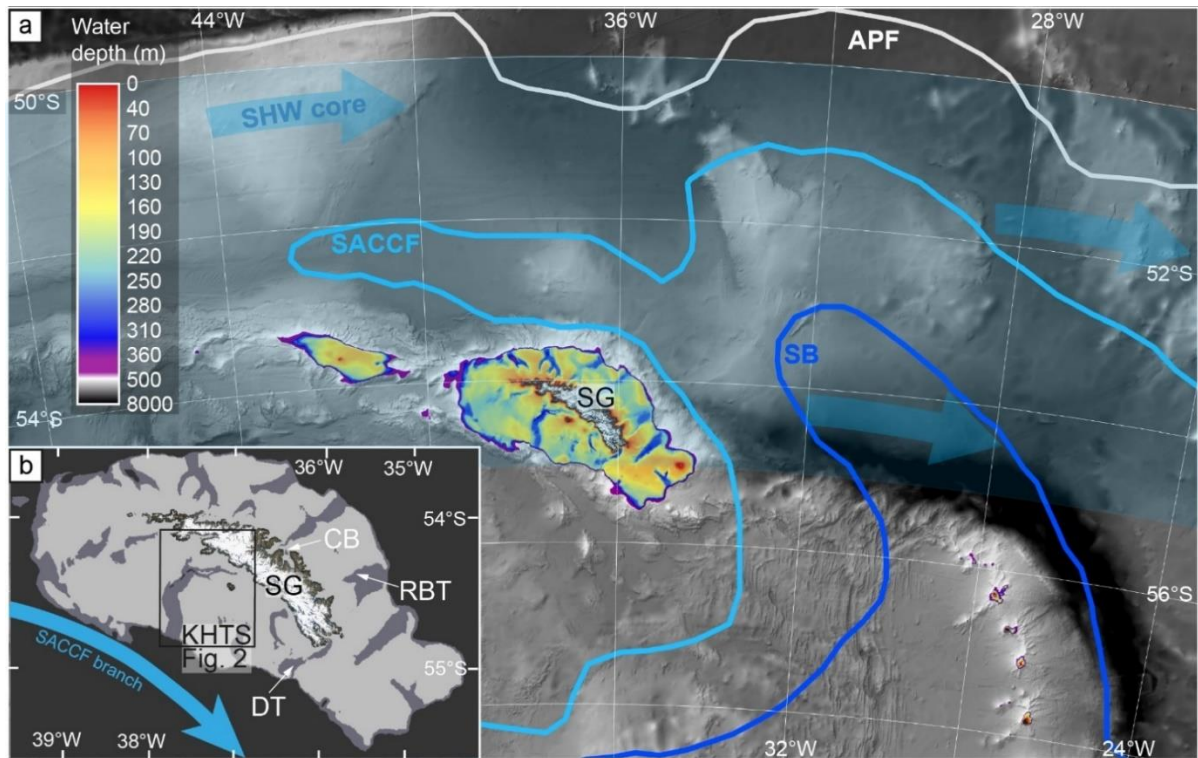


Fig. 6.1: a) Location of South Georgia (SG) with respect to the core belt of the Southern Hemisphere Westery Winds (SHW; 50-55°S; blueish shading and blue arrows; Lamy et al., 2010) and three of the major oceanographic Antarctic Circumpolar Current (ACC) fronts in the Southern Ocean. PF = Polar Front, SACCF = Southern Antarctic Circumpolar Current Front, and SB = Southern Boundary of the ACC, their positions inferred from Orsi et al. (1995). b) Broad overview of the SG shelf morphology and an adjacent SACCF branch (adapted after Matano et al., 2020). Dark grey areas show the numerous, likely glacially-incised, cross-shelf troughs, e.g. Drygalski Trough (DT) and Royal Bay Trough (RBT; >250 m water depth). The location of King Haakon Trough System (KHTS) is shown by a black rectangle that simultaneously shows the extent of Fig. 6.6.2. Light grey areas on the shelf show water depths <250 m, including Cumberland Bay (CB; Graham et al., 2017). DEM information for the shelf and surrounding ocean is based on GEBCO Compilation Group (2023), while map information for the island derives from Landsat imagery provided by South Georgia GIS (2023). (EPSG: 3762)

## 6.2. Study area

### 6.2.1. Physiographic Setting

SG is located in the South Atlantic (54-55° S, 35.5-38°W; Fig. 6.1) and is one of the few large islands in the sub-Antarctic (Gordon et al., 2008; Berg et al., 2019). It is not only positioned within the core of the SHW belt (Fig. 6.1a), but also between two primary fronts of the ACC, i.e. the present-day Polar Front (PF) and the Southern Antarctic Circumpolar Current Front (SACCF), with the latter tracing the continental shelf break (Orsi et al., 1995; Thorpe et al., 2002; Matano et al., 2020; Combes et al., 2023). These circumpolar fronts are ~20,000 km long and feature enhanced latitudinal gradients of water properties that extend from the sea surface to the seafloor. Despite their mostly simplified depiction as the main (isolated) jets of

ACC transport, they actually consist of several intertwined branches, thus forming an extensive jet structure in many areas (Sokolov and Rintoul, 2009; Matano et al., 2020; Combes et al., 2023). SG's position within these atmospheric and oceanographic systems therefore makes the island and its continental shelf sensitive to changes in position and strength of both SHW and ACC (cf. Strother et al., 2015; Graham et al., 2017; Moreno et al., 2018; Matano et al., 2020; Bakke et al., 2021; Yamazaki et al., 2021).

KHTS is located between 54°08' and 54°50'S and 37°14' and 37°39'W on the SG continental shelf and is bordered by the southern SG coast to the north, Annenkov Island to the east and the continental shelf edge to the south (Fig. 6.2). It is closely associated with the Cooper Bay Shear Zone (CBSZ, Fig. 6.2b), which divides rock formations on land and is inferred to continue onto the continental shelf, likely passing through KHTS tributaries.

KHTS consists of a main trough on the mid- and outer shelf, i.e. King Haakon Trough (KHT, Fig. 6.2b), an adjoining smaller trough system on the inner shelf, which we define as the Jacobsen Trough System (JTS), to the east, and some additional, albeit smaller, arms and feeding systems. KHT strikes north-south (Fig. 6.2a) and is connected to the coast by the shallower conjoined Cheapman and King Haakon Bays, from here on referred to as King Haakon Bay (Fig. 6.2; Hodgson et al., 2014a). King Haakon Bay is mostly fed by the Briggs tidewater Glacier and extends first E-W, then N-S, before it joins KHT on the inner continental shelf (Fig. 6.2a).

JTS is composed of two main troughs, Jacobsen Trough (JT, ~22.5 km long) to the north and Annenkov Trough (AT; ~28 km long with tributaries) to the south, both of which strike east-west and are separated by a prominent bedrock feature (Fig. 6.2; unofficially named in Bohrmann et al., 2017). For easier identification, we subdivide JT into an eastern, a central, and a western part (Fig. 6.2a, Fig. A.1). East JT represents the junction of JT with both the 3.4 km-wide Jossac Bight and the Jacobsen-Newark Tributary, an around 5 km wide, ESE-WNW striking and ~23 km-long tributary composed of Newark Bay and Jacobsen Bight (Fig. 6.2a), which likely follows the CBSZ (Fig. 6.2b). Central JT marks the initial separation of JTS into JT and AT, while west JT includes the deepest parts of JT and extends all the way to the confluence with KHT (Fig. 6.2). According to patchy bathymetric data towards the coast, JTS is fed by multiple fjords and bays, all of which are outlets for an array of marine-terminating tidewater glaciers (Fig. 6.2; U.S.G.S., 1981; Gordon et al., 2008; Cook et al., 2010).

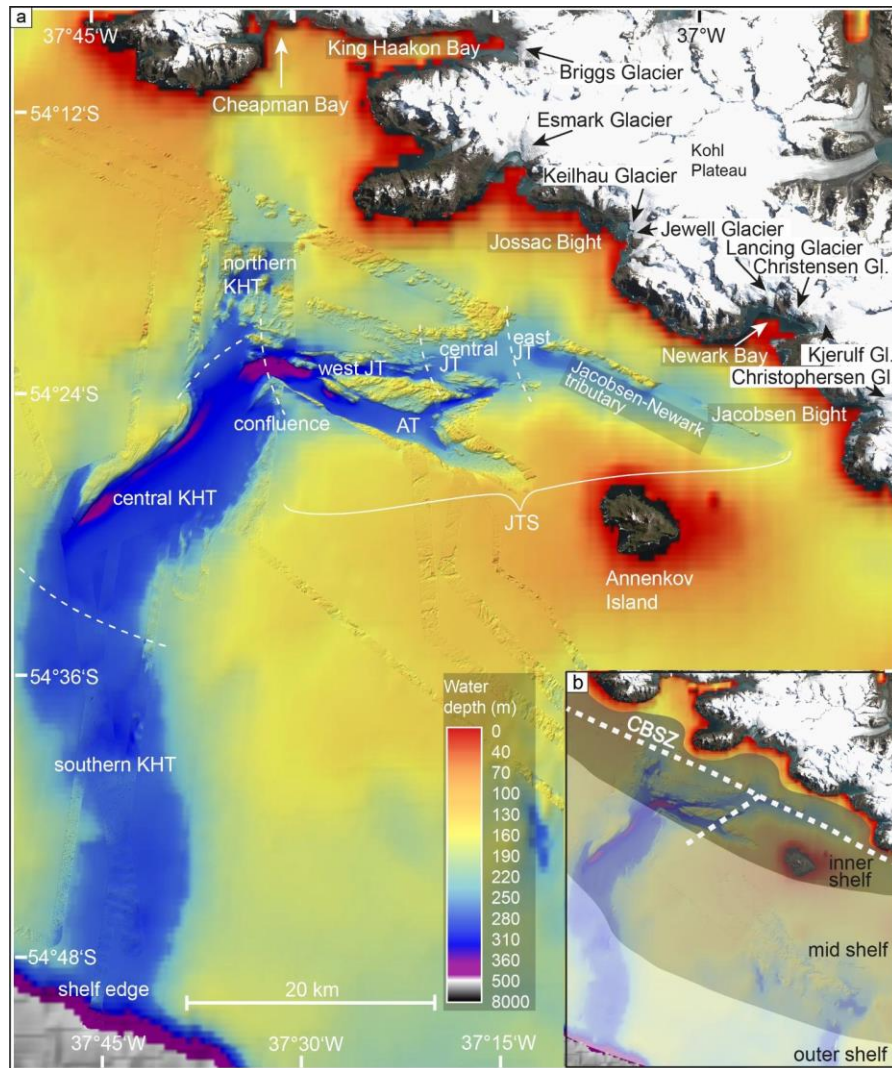


Fig. 6.2: a) Overview of the bathymetry of the King Haakon Trough System and the glaciers within its catchment area. In addition to the main trough, King Haakon Trough (KHT), Jacobsen Trough (JT) and Annenkov Trough (AT) are the predominant tributaries, which, in turn, are joined by Jossac Bight from the north and the Jacobsen-Newark tributary from the east. AT and JT together with their tributaries form the Jacobsen Trough System (JTS). JT is subdivided here into an eastern, a central and a western part. b) Visualisation of the different shelf areas referred to in the manuscript, including inner shelf (comprising King Haakon Bay, Cheapman Bay, and JTS with all tributaries), sediment-rich mid-shelf (comprising central KHT), and sediment-starved outer shelf (comprising the distal part of KHT until the shelf edge). The inner shelf and the eastern part of JTS are cross-cut by the inferred extension of the Cooper Bay Shear Zone (CBSZ; modified after Macdonald et al., 1987) and Dalziel et al. (2021), also referred to as Cooper Bay Dislocation Zone. (EPSG: 3762)

### 6.3. Methods

Hydroacoustic data, acquired on cruise M134 with RV Meteor in 2017 (Bohrmann et al., 2017), complemented with radiocarbon dates from four sediment cores, were used to analyse the regional Holocene depositional environments in KHTS (Fig. 6.3). While this paper focuses on sediment echosounder data from the Holocene, two forthcoming papers will concentrate on

(i) the core lithologies and associated local environments (Lešić et al., in prep.) and (ii) the pre-Holocene glacial history (Streuff et al., in prep.).

Bathymetric data were collected using a Kongsberg Maritime EM710 multibeam echosounder with 432 beams for water depths <500 m, and a Kongsberg Maritime EM122 with 256 beams for water depths exceeding 500 m. The shallow-water echosounder was operated at a frequency between 70 and 100 kHz, the deep-water echosounder at a nominal frequency of 12 kHz. Bathymetric data were processed using MB-System Suite (Caress and Chayes, 2017), gridded to a resolution of 5 m, and visualised and interpreted with the software QGIS 3.22.11.

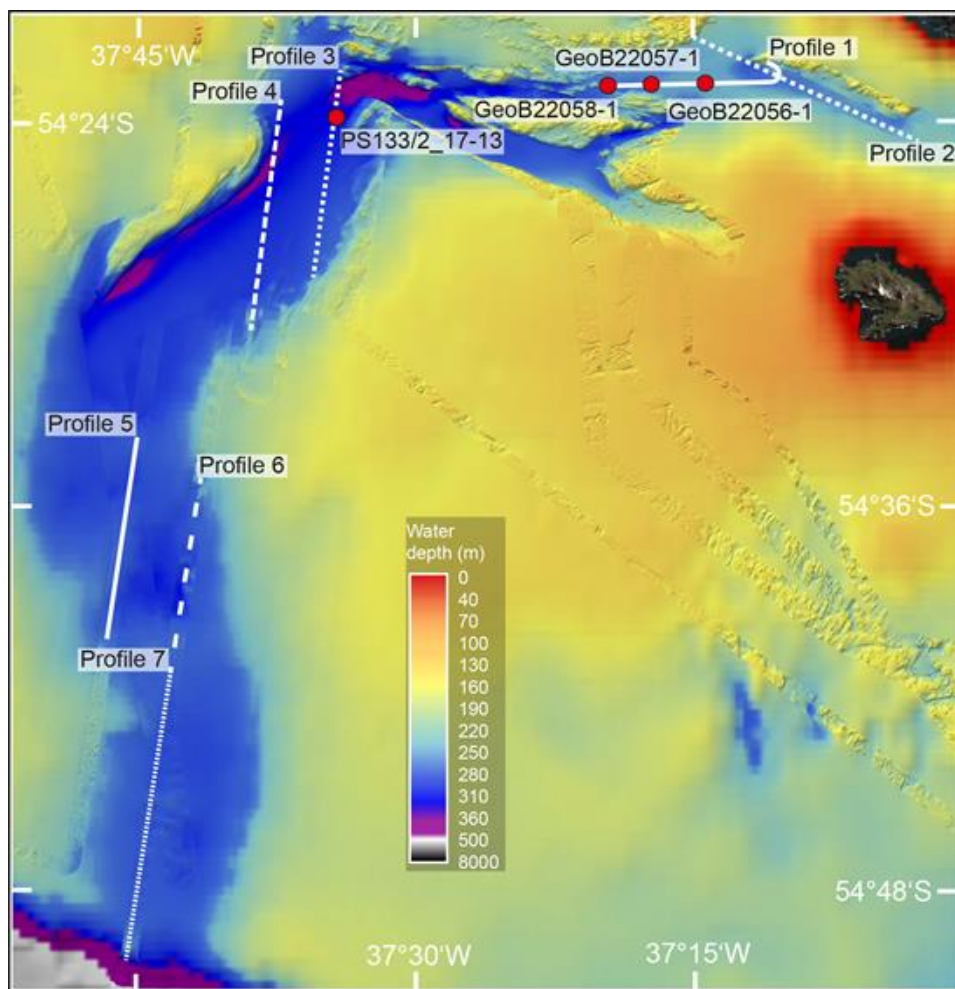


Fig. 6.3: Overview of the data, including the location of the seven sub-bottom profiles (Profile 1-7) and four sediment cores (GeoB22056-1, GeoB22057-1, GeoB22058-1 and PS133/2\_17-13). (EPSG: 3762)

Sediment echosounder data were collected with a parametric Teledyne ATLAS PARASOUND P70 sub-bottom profiler. The system was operated at a secondary low frequency of ~4 kHz. The data were visualised and interpreted using SMT The Kingdom Suite 2019. Interpretations for this study were restricted to seven profiles, 1-7, deemed representative for the entire

trough system (Fig. 6.3). All hydroacoustic systems were frequently calibrated during data acquisition using sound velocity profiles and repeated Conductivity-Temperature-Depth measurements. All depth conversions are based on an assumed sound velocity of 1500 ms<sup>-1</sup> within the sediments (Figs. 6.4-6.7, Table 6.1).

For stratigraphic information on the sub-bottom profiles, radiocarbon dating was performed on four gravity cores, GeoB22056-1, 57-1 and 58-1 taken during M134 from JT (Fig. 6.3; Bohrmann et al., 2017), and PS133/2\_17-13 taken from KHT during RV Polarstern cruise PS133/2 (Kasten, 2023). While the detailed lithology of these cores will be subject of Lešić et al. (in prep.), crude lithofacies logs allowed for the correlation with acoustic data and the identification of distinct lithological boundaries, interpreted to represent acoustic unit boundaries. Biogenic carbonate was isolated from >63 µm sample fractions and the sediment surface of the split core halves above and below these boundaries as well as at the core base and sent for Accelerator Mass Spectrometry (AMS) 14C dating as CO<sub>2</sub> samples at the MICADAS laboratory at AWI (Mollenhauer et al., 2021). Lab errors are between ±0.036-0.108 ka. Radiocarbon age calibration was carried out with the IntCal20 calibration curve (Reimer et al., 2020), using modelled Marine Reservoir Ages (MRAs) with a temporal resolution of 0.05 ka that are based on three simulations. Their median absolute deviations (MAD) lie within the laboratory error and are therefore neglected (Butzin et al., 2019, 2020; Heaton et al., 2020; Heaton et al., 2022). All boundary-specific ages were taken within a max. vertical distance of 20 cm from the lithological boundaries, except in PS133/2\_17-13, where a sample at 434 cm was taken 126 cm below the according boundary. All obtained ages lie (within their errors) in the expected stratigraphic order and are based on a variety of biogenic carbonate, rather than just foraminifera. Accordingly, we consider the ages reliable, despite the fact that radiocarbon dating and calibration, especially on foraminifera, can be difficult in (polar) oceans (cf. Heaton et al., 2022), also in the SG region (Berg et al., 2020). All ages are presented in calibrated kiloyears before present (cal ka BP; see Tables 6.2 and 6.3 in section 6.4 below).

## 6.4. Results and Interpretation

### 6.4.1. Trough morphology

The mapped extent of KHT, which we separate into a northern, central and a southern part (Fig. 6.2a), is approximately 70 km long, up to 10 km wide and shoals from its deepest part at the confluence between central KHT and JTS (401 m; Fig. 6.2a) to ~275 m at the shelf edge. In



contrast, JTS, with all its mapped tributaries, is ~74 km long, up to 4 km wide, with shallow, rugged flanks (<200 m) and some deeper central basins (Fig. 6.2a). A small bedrock high splits west JT into a shallower northern (<240 m) and a deeper (370-401 m) southern arm, the latter of which we interpret to represent the main water/ice pathway, based on its larger depth (Fig. 6.2a). The presence of several shoals creates a funnel-like geometry around the boundary of central and west JT, causing it to narrow and constrict into a bottleneck shape just before joining KHT (Fig. 6.2a). AT on the other hand is relatively uniform in width (~2 km), but similar in depth (200-370 m; Fig. 6.2). AT's deepest part is marked by a bathymetric depression at a water depth of 370 m, close to the conjuncture with west JT (Fig. 6.2a).

KHTS is characterised by a smooth seafloor in the majority of its trough valleys, especially within JTS (Fig. 6.2a) and in central KHT (Fig. 6.2a). This indicates locally enhanced sedimentation that (partially) obliterates the trough relief. In contrast, shallower areas of the trough (<300 m), specifically flanks and bathymetric highs, exhibit a variety of geomorphological features, some of which were previously mapped and described for other areas of SG (Hodgson et al., 2014a; Graham and Hodgson, 2016; Lešić et al., 2022) and will be subject of Streuff et al. (in prep.). However, there are several prominent depressions in KHTS that we will describe in the following. They are elongated, orientated parallel to the trough flank, and commonly associated with confluence zones of tributaries and troughs (Fig. 6.2a), as well as the western flank of KHT (Fig. 6.3a). They are ~1-6 km long and exceed 360 m water depth, meaning they are overdeepened with respect to the remaining trough system. Accordingly, these areas seem to have formed from locally enhanced erosion, possibly related to focused and potentially accelerated ice and/or water flow, and are somewhat comparable to subglacial meltwater channels (e.g. Nitsche et al., 2013; Kirkham et al., 2020), tunnel valleys (e.g. Ó Cofaigh, 1996; van der Vegt et al., 2012; Kirkham et al., 2022), canyons (e.g. Inman et al., 1976) or deep-sea trough settings (e.g. Stow et al., 2002). In this context, feasible agents would probably be streaming ice, subglacial meltwater, or directed bottom-currents. However, since the depressions along the western KHT flank are often adjacent to mound features observed in the sub-bottom profiler data (see section 6.4.2 below), and this combination between erosion and deposition is reminiscent of bottom-current related moat-drift systems observed in various contourite settings (Wilckens et al., 2023), we interpret the bathymetric depressions as 'moats' and the adjacent sediment bodies as 'mounded drifts' after Rebesco et al. (2014).

## 6.4.2. Acoustic Units

### 6.4.2.1. Description

The seven sub-bottom profiles from KHTS show three acoustic facies: The acoustic basement (AB), and two overlying acoustic facies, AF1 and AF2. Because this paper focuses exclusively on the Holocene trough-fill sequences, AB and AF1, both consecutively referred to as pre-basin-fill sequence, are subject of a forthcoming paper (Streuff et al., in prep.). In the following sections, we accordingly describe only the uppermost acoustic facies, AF2. AF2 conformably overlies and onlaps onto the underlying pre-basin fill sequence (Fig. 6.5c,e). It effectively fills the topography in the majority of KHTS basins, except on the outer shelf (Fig. 6.6f). AF2 is at least 80 m thick in east JT (Fig. 6.4), but significantly thins to 10-30 m towards central JT. In central KHT, on the other hand, AF2 is significantly thinner, decreasing from 52 to 24 m on the mid-shelf (Fig. 6.5), to 13 m on the outer shelf (Fig. 6.6b-e), and negligible amounts at the continental shelf edge (Fig. 6.6f). Note that thicknesses are only approximations due to partial obliteration by acoustic blanking. Where acoustic blanking occurs, the overlying reflectors are often enhanced, strongly opaque, and prone to upwards doming (Fig. 6.4b,d).

AF2 is acoustically stratified, with generally well-defined, parallel internal reflections of variable amplitude. Based on clearly defined reflectors between stratified sequences, as well as vertically variable degrees of stratification, AF2 is subdivided into Units A-D. Especially the lowermost parts of AF2 can be partially obliterated by overlying sediment packages or acoustic blanking. All units show significant variability in thickness, implying spatial and/or temporal variations in their deposition. Their characteristics are summarised in Table 1. AF2 was sampled by all four cores in KHTS and consists of silty mud.

Table 6.1: Characteristics of the four subunits of AF2.

Unit	Acoustic signal	distribution	KHT thickness	JT thickness
A	Distinct stratification	Widespread	6-48 m	8-35 m
B	Weak stratification, semi-transparent	Conformably overlies A in most parts, pinches out towards bathymetric highs in KHT	1-8.5 m	0->27
C	Weak stratification, higher amplitude & higher impedance in JT	Pinches out towards bathymetric highs	1-10 m	0-> 30 m
D	continuous, perfectly parallel mostly horizontal reflector, medium to high amplitude	Draping	2-4	4-15

Unit A occurs in central KHT and in central JT with a relatively uniform thickness between 6 and 48 m, the latter occurring within the mounded drift of the “moat-drift” system (Table 6.1, Fig. 6.5c). However, partial obliteration of the acoustic data hampers not only detailed thickness determination in east JT (Fig. 6.4b,c), but also gauging its exact distribution, specifically in the Jacobsen-Newark tributary (Fig. 6.4d,e). In western KHT, diverging reflectors within Unit A (Fig. 6.5c,e) imply increased sediment aggradation in the form of mound-like structures, which were related to the formation of moat-drift systems (section 6.4.1). Truncated upper reflectors of Unit A within individual moats (Figs. 6.5b, 6.6b,d) indicate erosion of its uppermost parts. Unit A was sampled by GeoB22058-1 and PS133/2\_17-13 and is the only unit that contains diatom-layers intercalated into the very fine silty mud (Lešić et al., in prep.). Unit B is mainly present in central and east JT and on the mid-shelf around the confluence zone of JTS and KHT (Fig. 6.4; 6.5b-e). Where visible, it overlies older sediments in basins and bathymetric depressions and pinches out towards bathymetric highs in KHT (Fig. 6.5c,e). It is generally much thinner on the mid-shelf (<8.5 m) than on the inner shelf, where it progressively thins westwards from ~27 m in east JT/ Jacobsen-Newark tributary to 7 m at the location of GeoB22057-1 (Fig. 6.4c). In central JT, Unit B directly underlies Unit D with local cut-off of its reflectors (Fig. 6.4c). Unit C occurs everywhere on the inner shelf, but is locally absent from the stratigraphic record (Figs. 6.4; 6.5; 6.6). Its thickness progressively decreases in a westward direction from a maximum of >30 m in east JT to a minimum close to the core location of GeoB22057-1, where it pinches out (Fig. 6.4b,c). Unlike Unit A and B, its strong and continuous upper boundary shows that Unit C was not eroded in central JT. Similarly, Unit C pinches out towards bathymetric highs and the flanks in central KHT (Fig. 6.5c,e).

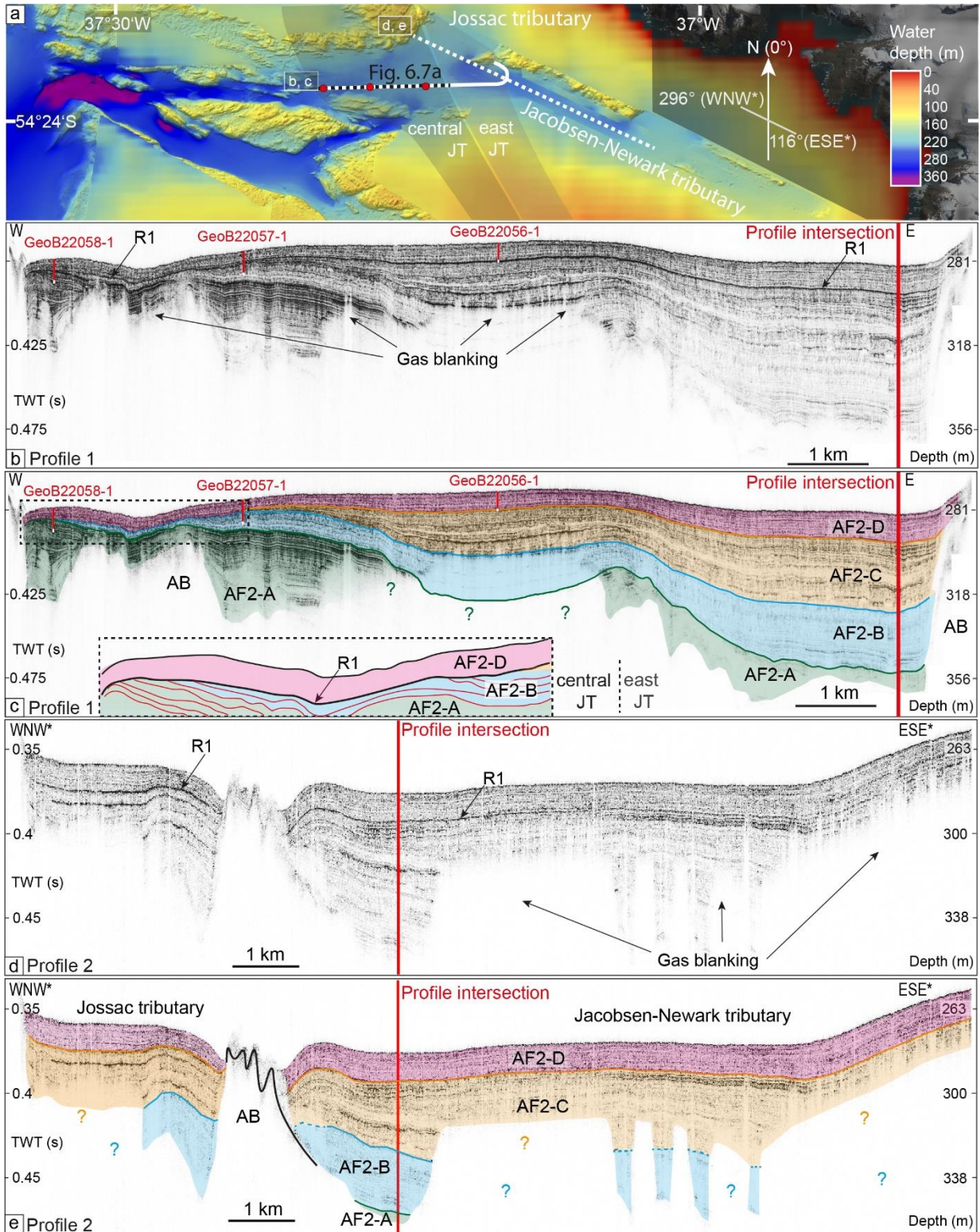


Fig. 6.4: a) Overview of the position of the sub-bottom profiles in JT, Profiles 1 and 2. b, d) Profile 1 with core locations indicated in red solid lines. White intervals at the bottom of the cores show the estimated true core recovery when accounting for 16% sediment compression. Red vertical lines show the position where Profiles 1 and 2 intersect. c) interpretation of acoustic units in Profile 1. AB = Acoustic Basement, AF2 = basin-fill. AF2-A to D mark the acoustic sub-units of AF2. The inset shows a zoom-in to the unconformity in west JT, demonstrating the presence of cut-off reflectors. d,e) Analogous to b,c) but for Profile 2. Gas blanking is present and affects the mapping of acoustic units in all profiles. (EPSG: 3762)

Unit D is the uppermost acoustic unit and drapes almost the entire trough system except for the outer shelf (Fig. 6.4; 6.5; 6.6). Its thickness decreases from 15 m in the JTS tributaries to ~4 m in central JT (Fig. 6.4c,e), which is also the average thickness in KHT (Fig. 6.5c,e). Its distinct and opaque basal reflector, R1, is characterised by high continuity across the entire trough system and a higher amplitude in JTS than in KHT (Fig. 6.4b,d; 6.5b,d). Unit D directly overlies the acoustic basement on bathymetric highs (Fig. 6.5c), Unit A in central KHT (Fig. 6.5d) and east of the bottleneck in central JT (Fig. 6.4c), as well as Unit B in central JT (Fig. 6.4c).

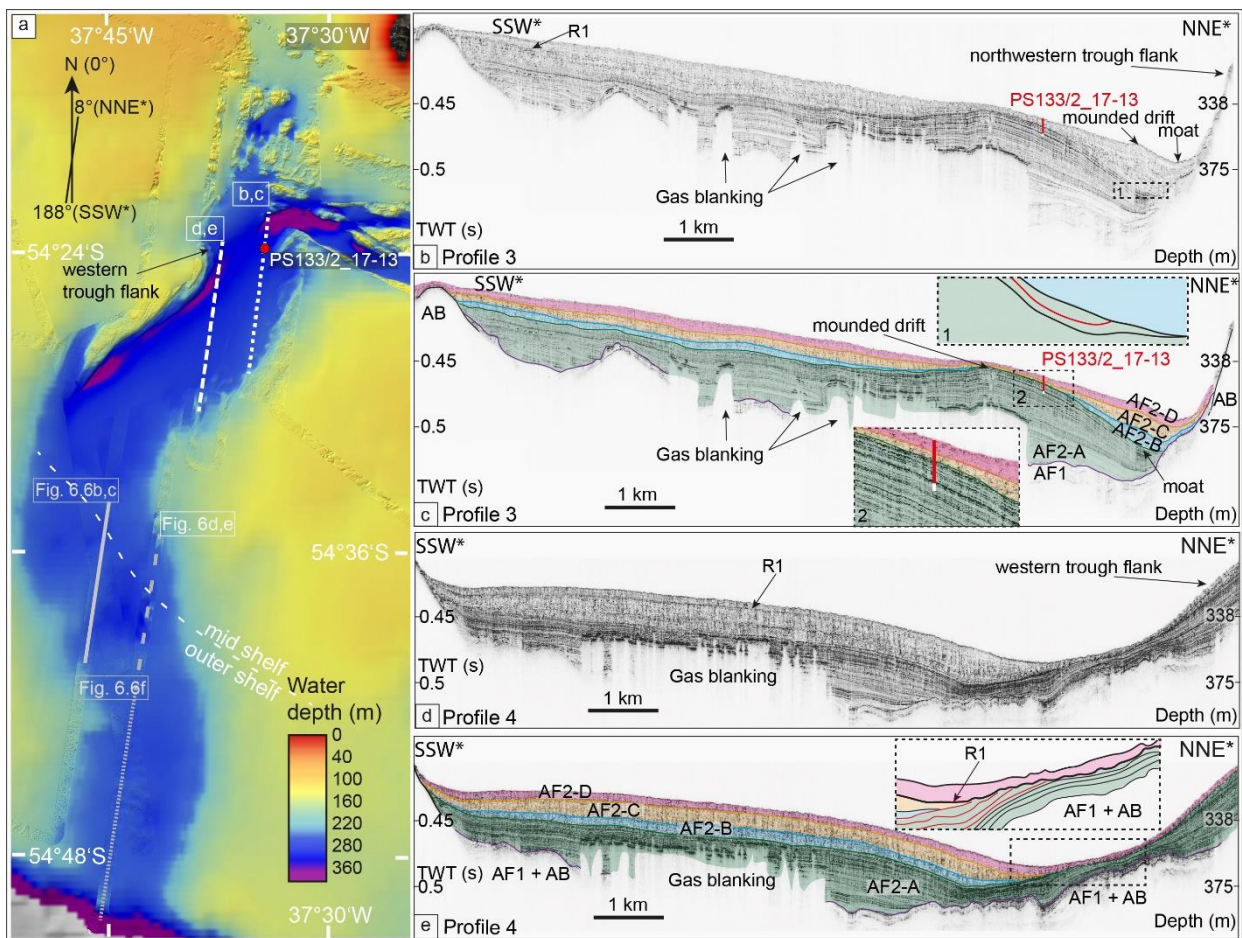


Fig. 6.5: a) Overview of the position of the sub-bottom profiles in KHT and the core location of PS133/2\_17-13. b) Mid-shelf Profile 3 with its stratigraphic interpretation in c). Black dashed rectangle (in b) shows the location of inset 1, while the arrowed R1 refers to a prominent reflector at the base of Unit D. Inset 1 in c) illustrates a truncated reflector of Unit A (red line). Inset 2, illustrated by black dashed rectangles in c) shows a zoom-in to the core location PS133/2-17-13 and the respective unit interpretation. d) Mid-shelf Profile 4 with its stratigraphic interpretation in e). The inset in e) outlined by two black dashed rectangles, shows truncated reflectors of Unit A (red lines). AB + AF1 form the pre-basin fill sequence and are subject of Streuff et al., (in prep.). AF2 in all sub-panels refers to the trough fill, with AF2-A to D representing the acoustic sub-units of AF2. The presence of gas blanking makes unit extents difficult to determine. (EPSG: 3762)

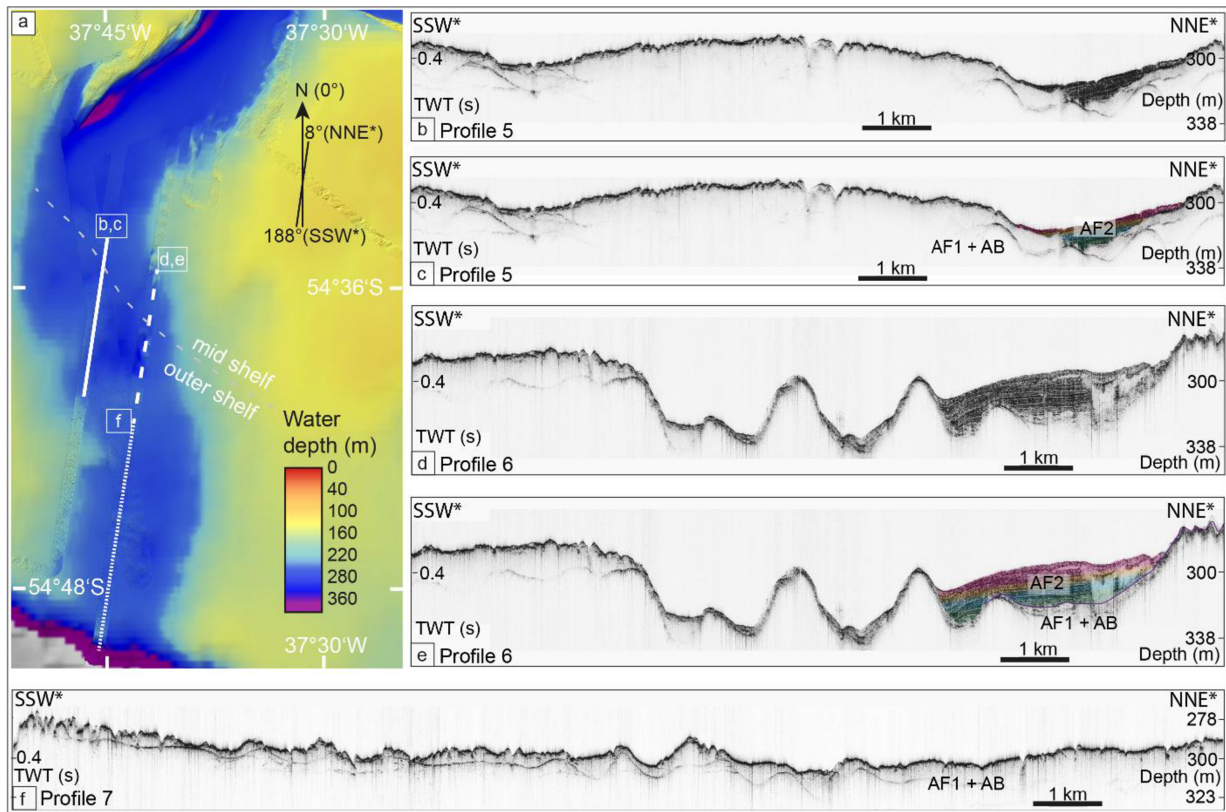


Fig. 6.6: a) Overview of the sub-bottom profiles on the outer shelf. b,c) Mid- to outer shelf Profile 5 and its acoustic unit interpretation. AB and AF1 mark the pre-basin fill sequence and are subject of another paper. AF2 is Holocene trough-fill with according sub-units A-D. Note the very restricted presence of AF2 in the north-eastern part (illustrated in sub-panel c). d,e) Mid- to outer shelf Profile 6 and its interpretation of acoustic units. Again, the presence of AF2 is limited to a small basin in the NNE (sub-panel e). f) Outer shelf Profile 7. Note the complete absence of trough-fill AF2. (EPSG: 3762)

#### 6.4.2.2. Interpretation

Based on its mostly conformable, draping geometry and the stratified appearance, AF2 is interpreted as basin-fill sediment (Ó Cofaigh et al., 2016). On continental margins around previously glaciated areas, such deposits may originate predominantly from (glaci-)marine hemipelagic suspension rainout from turbid meltwater plumes and the water column, which is periodically interrupted by ice rafting, downslope and current-induced re-sedimentation processes, and (seasonal) changes in primary production (e.g. Seramur et al., 1997; Forwick et al., 2010; Dowdeswell and Vásquez, 2013; Ó Cofaigh et al., 2016). Although the acoustic appearance of Units A-D is generally similar, the clearly defined boundaries of the four sub-units suggest periodic changes in the depositional environment across the entire trough system, while the variably pronounced stratified appearance indicates frequent impedance contrasts, probably caused by the intercalation of at least two different lithologies. In this context, stronger stratification might indicate pronounced differences in physical properties,

while weaker stratification may be related to the interbedding of strata with more similar physical properties. This interpretation is consistent with the acoustic signal of glacial marine sediments in Royal Bay Trough (RBT; Fig. 6.1b), where strong stratification was correlated with the occurrence of frequent intercalation of terrigenous diatom-rich muds with individual layers of diatomaceous ooze (Graham et al., 2017).

The fact that Unit D directly overlies the pre-basin-fill sequence in central KHT is probably related to steeply dipping bedrock (Fig. 6.5c) preventing the preservation of thick sediment accumulations beneath the youngest stratigraphic unit. Conversely, the distinct cut-off reflectors as well as the stratigraphic relationships between Units A, B and D in central JT and western KHT provide evidence for local erosion and an associated stratigraphic unconformity. In KHT, Unit A forms the lower, “pre-erosion”, part, while Unit D forms the upper “post-erosion” sequence. In JT, Unit A and B show truncated reflectors and thus both constitute the unconformity’s lower part.

#### 6.4.3. KHTS sediment ages

Radiocarbon dating shows that Units B-D and the uppermost part of Unit A are of Holocene age and cover the last ~10 ka, with the oldest age (10.2 cal ka BP; Table 6.2) recovered from Unit A in GeoB22058-1 in central JT. Individual units were deposited roughly simultaneously in KHT and JT (Fig. 6.7). The upper boundary of Unit A in JT can be constrained to 7.7-7.1 cal ka BP (GeoB22058-1 and 57-1, respectively, Table 6.2) and to after 8.5 cal ka BP in KHT (PS133/2\_17-13; Table 6.2; Fig. 6.7b). The overlying Unit B was deposited over the subsequent ~4 ka until ~3.9 cal ka BP in JTS (Fig. 6.7a), dated by GeoB22057-1. A hiatus in PS133/2\_17-13 between 8.5 and 4.1 cal ka BP not only indirectly dates Unit B to this time in KHT, but also shows that a change in depositional environment at ~4 cal ka BP led to the sedimentation of Unit C (Fig. 6.7b). Deposition of Unit C also appears to have been simultaneous in both troughs, lasting until 2.6-2.1 cal ka BP, when the last distinct change in sedimentary environments led to the deposition of Unit D. Unit D drapes most of the trough system, and, because it is the uppermost acoustic unit, probably represents contemporary sedimentation in the study area (Fig. 6.7).

According to the age data, sedimentation rates have fluctuated throughout the Holocene trough-fill evolution and differ within individual units. While the core locations in central JT tend to show an increase or only slight decrease in sedimentation rates across the A-B and A-

D unit boundaries, sedimentation rates drop by a magnitude of 10 at the core location of PS133/2\_17-13 in central KHT (Table 6.3), although this might be an artefact related to the core location at the margin of a 'mounded drift' (cf. Rebesco et al., 2014).

Table 6.2: Conventional radiocarbon ages and calibrated weighted mean ages (cal ka BP) discussed in the text. Note that the Unit boundaries are up to 12 cm thick in the core.

<b>Sample details</b>			<b>Conventional radiocarbon ages</b>		<b>IntCal20 calibration</b>	<b>Unit</b>	<b>Vertical distance to Units Boundaries (cm)</b>	<b>Lab Code</b>
Gravity core	Depth (cm)	Carbon(ate) source	Age ( <sup>14</sup> C ka BP)	Age error (ka)	Weighted mean (cal ka BP)			
GeoB22056-1	645	Mollusc	2.504	±0.06	1.483	D	-	AWI 4455.1.1
GeoB22057-1	430	Mollusc	3.403	±0.066	2.598	D	4 cm above C-D boundary	AWI 4458.1.1
GeoB22057-1	460	Mollusc	4.443	±0.067	3.899	B	14 cm below B-D boundary	AWI 4459.1.1
GeoB22057-1	750	Mollusc	7.285	±0.079	7.129	B	304 cm below B-D boundary	AWI 4463.1.1
GeoB22058-1	380	Bryozoa	2.983	±0.062	2.143	D	20 cm above A-D boundary	AWI 6171.1.1
GeoB22058-1	430	Benthic Forams	7.879	±0.087	7.718	A	18 cm below A-D boundary	AWI 4465.1.1
GeoB22058-1	800	Benthic Forams	9.896	±0.09	10.167	A	388 cm below A-D boundary	AWI 4470.1.1
PS133/2_17-13	183.5	Mollusc	3.323	±0.062	2.557	D	13.5 cm above C-D boundary	AWI 10474.1.1
PS133/2_17-13	303.5	Mollusc	4.65	±0.073	4.144	C	1.5 cm above A-C boundary	AWI 10476.1.1
PS133/2_17-13	434	Benthic Forams	8.696	±0.084	8.511	A	126 cm below A-C boundary	AWI 10477.1.1
PS133/2_17-13	885.5	Fish scale	9.038	±0.036	9.028	A	582 cm below A-C boundary	AWI 10480.1.1



Table 6.3: Average linear sedimentation rates for the Units A-D based on the ages provided in Table 2. Note that these simple sedimentation rates assume that 0 cm in the core represents recent sedimentation and are rates for unit D are therefore only estimated. More precise age data and sedimentation rates throughout the units can be found in Lešić et al. (in prep.)

Core	Unit	Thickness (cm)	Time period (ka)	Sedimentation rate (cm ka <sup>-1</sup> )	Sedimentation rates A and (B+C+D)
GeoB22056-1	D	645	1.483	435	435
GeoB22057-1	D	430	2.598	166	93
GeoB22057-1	B	110	3.23	34	
GeoB22058-1	D	380	2.143	177	177
GeoB22058-1	A	370	2.449	151	151
PS133/2_17-13	D	183.5	2.557	72	73
PS133/2_17-13	C	120	1.587	77	
PS133/2_17-13	A	451.5	0.517	873	873

## 6.5. Discussion

The seven sub-bottom profiles from KHTS generally show uniform trough-fill with mostly horizontal, conformable sediment sequences. The exception is a distinct unconformity observed in central JT (Fig. 6.4b,c) and the western part of central KHT (Fig. 6.5d,e) indicated by truncated upper reflectors within Units A and B. AF2 is almost entirely absent on the outer shelf, so it stands to reason that it is composed of predominantly terrigenous material, sourced directly from the island. The exception are the diatom layers, which indicate a marine component, at least during the deposition of Unit A.

### 6.5.1. Sediment ages

Based on the calibrated radiocarbon ages, the majority of AF2 was deposited after ~10.2 cal ka BP. This date derives from close to the base of GeoB22058-1 and is located 388 cm beneath the erosional unconformity in central JT (Table 6.2). When assuming constant deposition of Unit A, a reconstructed sedimentation rate of 151 cm ka<sup>-1</sup> from the same core (GeoB22058-1; Table 6.2; Fig. 6.7) would date the onset of Unit A deposition to ~31 ka BP, given the 35 m maximum thickness in central JT (Fig. 6.4).

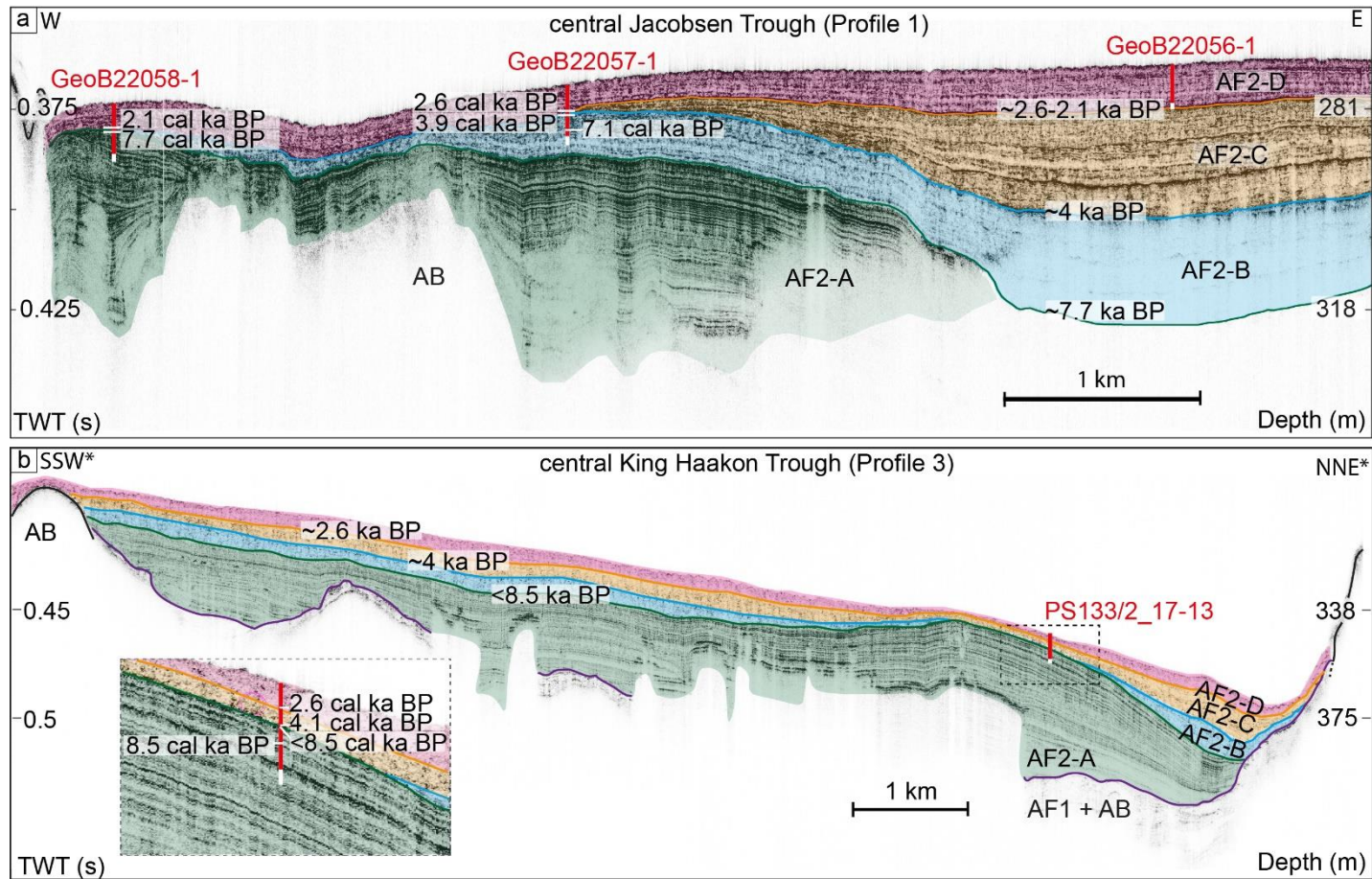


Fig. 6.7: a) shows the western part of Profile 1 from central JT (Fig. 6.4a,b,c) with the core locations of GeoB22058-1, GeoB22057-1, GeoB22056-1 and their true length in red, while the possible core compression of 16% is depicted in white. The calibrated radiocarbon ages closest to the unit boundaries are shown along the cores. Age approximations, based on the radiocarbon ages, for the unit boundaries are indicated by ka BP. b) shows Profile 3 from central KHT with the core location of PS133/2\_17-13 and its true length in red, while the possible core compression of 16% is depicted in white. The calibrated radiocarbon ages closest to the unit boundaries are shown along the cores. Age approximations, based on the radiocarbon ages, for the unit boundaries are indicated by ka BP. AB = Acoustic basement, AF1 = acoustic facies 1 (glacial till), AF2 = glacimarine trough fill, AF2-A-D = acoustic Units A-D of AF2. (EPSG: 3762)

While this might imply that AF2 actually represents LLGM sediment, the acoustic stratification is at odds with an interpretation as (sub-)glacial till. Moreover, since the mid-shelf of the nearby Drygalski Trough (DT; Fig. 6.1b) was glaciated during an early LLGM and remained so until the onset of an early deglaciation around 17.5 cal ka BP (Lešić et al., 2022), it seems unlikely that the mid-/inner shelf in KHTS was ice-free much earlier. Indeed, extrapolated sedimentation rates for Unit A from KHT (873 cm ka<sup>-1</sup> from PS133/2\_17-13; Table 6.2; Fig. 6.7) would instead date its base either to the beginning (14 ka BP; max. thickness 48 m) or the end (12.5 ka BP; 35 m) of the Antarctic Cold Reversal (ACR; 14.5-12.8 ka; Jouzel et al., 1995; Putnam et al., 2010; Pedro et al., 2016; Graham et al., 2017), thus possibly implicating Unit A as the first (post-)ACR deposit. Nevertheless, because ACR maximum extent was actually attributed to a number of outer fjord moraines around SG (Hodgson et al., 2014a; Graham et al., 2017; Lešić et al., 2022), it seems unlikely that such thick sediment sequences would accumulate as far away from the active glacier margins as the core site of PS133/2\_17-13. Moreover, sedimentation rates in KHT are likely overestimated, because the core location is situated at the margin of a 'mounded drift' within Unit A (cf. Rebesco et al., 2014; Wilckens et al., 2023), where sediment was accumulated preferentially (Fig. 6.5c). Indeed, an assumption of linear sedimentation rates for Unit A is likely unreasonable altogether, considering that sedimentation rates were shown to not only fluctuate between the core sites but also within individual units (section 6.4.3). In fact, sediments with similar acoustic signatures as Unit A were interpreted to represent the onset of marine sedimentation in RBT (Fig. 6.1b), which was extrapolated to ~18 ka BP. A similar age for Unit A is not only in accordance with the deglaciation onset on the mid-shelf in DT at 17.5 cal ka BP (Lešić et al., 2022), but would also be supported by the inferred glacial origin of the pre-basin-fill sequences (Streuff et al., in prep.). This would further imply that Unit A represents the first marine sequence after the LLGM. As this would mean that any ACR record must be included in Unit A, it may seem odd that Unit A shows no distinct change in sedimentation pattern. Nonetheless, we actually observed a similar pattern in outer DT (Fig. 6.1b) (Lešić et al., 2022), where, apart from the post-LLGM deglaciation, the strongest change in sedimentation occurs with the transition to the Holocene, while the ACR can only be determined by changes in sedimentation rates but not the types of sediments deposited (Lešić et al., 2022). We therefore maintain that similar to the lowermost acoustic Unit in RBT (Graham et al., 2017), Unit A is the result of post-glacial marine sedimentation that likely initiated after 18 ka BP and continued throughout the ACR

and into the Holocene, but would like to stress that better age control would be necessary to definitively determine the origin of Unit A.

Contrary to Unit A, the radiocarbon ages place the onset of deposition of Unit B between 8.5 cal ka BP (PS133/2\_17-13) and 7.1 cal ka BP (GeoB22057-1; Table 6.2; Fig. 6.7). Because the age from KHT derives from a depth of 126 cm below the A-B unit boundary, it is likely that an age of 8.5 cal ka BP is slightly overestimated. Likewise, the date from GeoB22057-1 originates from right within Unit B, 304 cm below the B-C unit boundary (Fig. 6.7a), and thus probably significantly underestimates the onset of Unit B deposition. Since an age from just below the A-D unit boundary in GeoB22058-1 dates the uppermost 18 cm of Unit A to ~7.7 cal ka BP (Table 6.2, Fig. 6.7), we propose that deposition of Unit B initiated between ~7.7 and roughly 8 cal ka BP, with a slight delay in JT compared to KHT, and that a change in depositional environment associated with marine erosion around this time led to the truncation of Unit A's upper reflectors in KHT (Fig. 6.5b,d).

Much less ambiguous are Units C and D, the onset of which is clearly dated to 4.1-3.9 cal ka BP (PS133/2\_17-13 in KHT and GeoB22057-1 in JT, respectively; Table 6.2, Fig. 6.7) for Unit C and to 2.6 (GeoB22057-1 and PS133/2\_17-13) to 2.1 cal ka BP (GeoB22058-1; Table 6.2, Fig. 6.7) for Unit D. Because Unit D marks the uppermost stratigraphic unit in the acoustic data, we interpret it to represent contemporary conditions in the trough system, but point out that more recent changes might not have been resolved by the echosounder.

#### 6.5.2. Spatial variability in sediment deposition

Notwithstanding a presumably identical provenance for all basin-fill units, i.e. island-runoff and some marine matter, there are substantial differences in their distribution across the trough system, which become especially obvious in the conceptual model of trough sedimentation (Fig. 6.8). This shows that first, sediment cover strongly increases from a negligible amount in outer KHT to up to 78 m on the inner shelf in east JT. Second, albeit rather expectedly, sediment cover is thicker in bathymetric basins than on the shallow banks. Third, while Unit A is of similar thickness in both central KHT and JT, Units B-D, deposited in the same time frame of ~8 ka, are significantly thicker in JT than in the entire KHT (Fig. 6.8). This suggests that not only the main sedimentary processes in KHTS, indicated by variable degrees of acoustic stratification, but also their magnitude within the troughs, were subjected to a

number of potential factors throughout the Holocene, which will be discussed in detail in the following paragraphs.

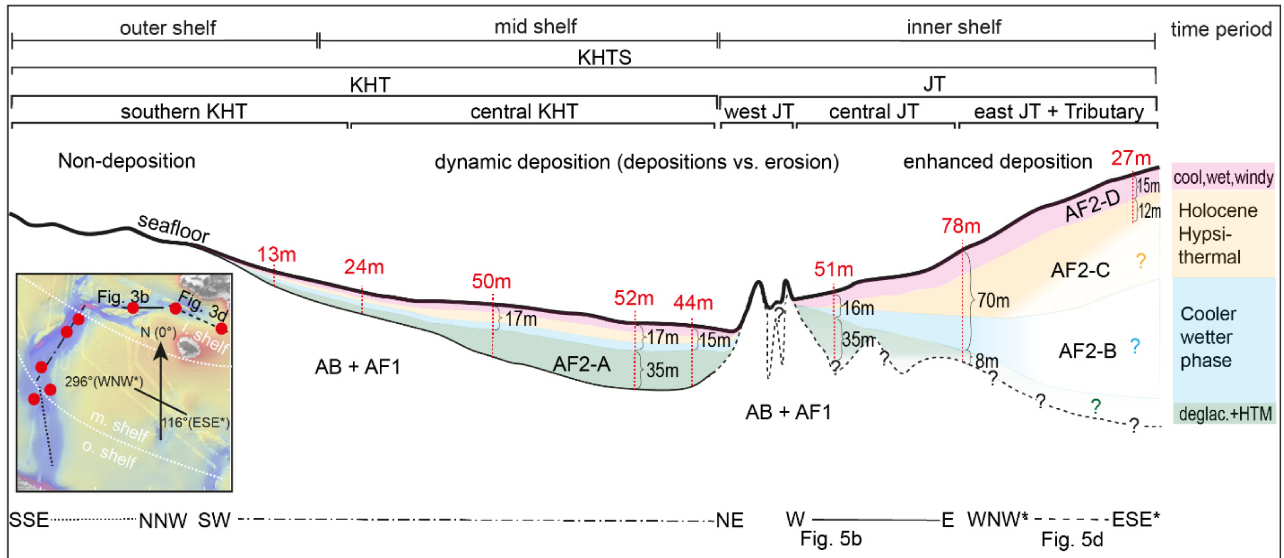


Fig. 6.8: conceptual model of trough fill thickness associated with the described acoustic units, based on the unit distribution and thickness along the trough. Calculations are based on 1500 m/s sound velocity. Red numbers refer to the visible thickness of AF2, while black numbers refer to either individual Units or the Units B-D. Note that this is a conceptual model and not to scale, nor includes it all bathymetrical features. Find the profile through west JT in the Appendix (Fig. A.1). Where thickness cannot be determined the features are transparent or indicated by dashed lines. Possible climatological interpretation in the right column (HTM= Holocene Thermal Maximum).

#### 6.5.2.1. Processes controlling sedimentation in KHTS

##### 6.5.2.1.1. Trough morphology and accommodation space

Glacially formed cross-shelf troughs, specifically around Antarctica, tend to flatten towards the shelf edge but slope towards the continents (Anderson et al., 1983; Dunbar et al., 1985; Klages et al., 2013), thus providing more near-shore accommodation space in land-proximal areas than close to the shelf edge. Because the sub-bottom profiler data show the same trend for central and southern KHT, with the deepest basins around the confluence zone of JTS and KHT, along the western flank of central KHT (Fig. 6.2), and quite deep basins in the subsurface of east JT (Fig. 6.4b-e), we suggest that this specific morphology favours sedimentation on the mid- and inner shelf compared to the outer shelf. Furthermore, the deeper trough morphology in the subsurface of east JT and its spatial association with a large shear zone, the CBSZ (Fig. 6.2b), probably facilitated (glacial) erosion due to structural weaknesses, thus promoting the formation of additional deeper basins, i.e., more accommodation space than

elsewhere. It is noteworthy, however, that in the case of simple relief-fill by AF2, we would expect a relatively uniform seafloor reflector in JT, placing it at roughly the same water depths throughout. In contrast, individual units of AF2 thicken eastwards in JT (Figs. 6.4, 6.7a, 6.8), thus filling not only the deeper basins in east JT but also causing the seafloor to slope upwards towards the east and the coast (Fig. 6.4d). This could be caused by the bottleneck-morphology of west JT (Fig. 6.2), which might hold back sediment coming from the east, thus preventing it to travel further westward into central KHT. Nevertheless, it then remains questionable why sediment continued to be held back even after enough had accumulated to effectively fill the basins and flatten the relief, which suggests that trough morphology likely was not the only factor affecting deposition.

#### 6.5.2.1.2. Sediment source

Sediment sources and their relative position to the depositional environments within KHTS likely also impacted sediment distribution. Preferential accumulation on the inner rather than on the outer shelf is consistent with distally decreasing sedimentation rates in glacial settings and a retreating ice-margin after maximum extent (Elverhøi et al., 1983). The proximity to the sediment source could also explain thicker sediment sequences in JT compared to central KHT, specifically when considering configuration and morphology of both troughs, implying that i) more glaciers and tributaries are draining the ice cap into JT (Fig. 6.2a) than into King Haakon Bay, together likely delivering larger amounts of sediment, ii) that central KHT is further away from the feeding bay than east and central JT (Fig. 6.2a), and iii) that King Haakon Bay (Fig. 6.2a) features a distinct fjord basin with an outer moraine (cf. Hodgson et al., 2014), which probably held back sediment. The remaining sediment that passed, could then have easily been deflected by along-shelf currents when entering northern KHT (Fig. 6.2a). In contrast, the seemingly flat morphology of Jossac Bight, Newark Bay, Jacobsen Bight and the JT tributaries, though not mapped entirely (Fig. 6.2a), might not have served as an efficient sediment trap, but rather have permitted sediment distribution across wider areas of east and central JT (Figs. 6.2, 6.4).

While enhanced proximal sedimentation would also be in accordance with an upward-sloping seafloor reflector towards east JT, it seems odd that the progressive thickening of AF2 within JT, did not affect the entire basin-fill sequence, but only Units B-D. This suggests that the influence of the different sediment sources also varied over time, which will be further

discussed in section 6.5.3 below. However, this could also be a grainsize effect and result from relatively coarse grains that were deposited closer to a variable distance to a source.

Because we derived the majority of AF2 to be supplied by SG island, Holocene sediment sources were probably fluctuating glacier margins, residual and seasonal meltwater, as well as sediment-laden run-off from rain, rivers and potential reworking processes. Accordingly, the changes between Units A-D could be related to changes in the depositional environment due to small-scale glacier fluctuations during the Holocene, triggered by climatic changes on the island (e.g. Oppedal et al., 2018; Berg et al., 2019). Although such fluctuations are unlikely to have had a significant effect on trough-wide terrigenous sediment distribution due to their restriction within the fjords (Bentley et al., 2007; Hodgson et al., 2014a; Graham et al., 2017; Lešić et al., 2022), they probably still controlled sediment delivery to the inner and mid-shelf, specifically in JTS. Additionally, glacier front fluctuations could have triggered in-situ fluctuations in primary production and, accordingly, the magnitude of the biogenic fraction of the sediment, specifically if meltwater served as a possible fertilisation agent (e.g. Arrigo et al., 2017), enhancing sedimentation rates during times of high primary production.

#### 6.5.2.1.3. Primary productivity

Changes in biogenic content are indeed represented by the frequent diatom layers in Unit A, which indicate somewhat regular switches between intervals with high (diatom layers) and low primary productivity (silty mud; see section 6.4.2). These could, incidentally, also explain the stronger acoustic stratification of Unit A in comparison to the overlying units B-D, where distinctly visible diatom layers are absent and sediment therefore might contain a larger fraction of terrigenous muds. Although these fluctuations could be related to glacier front oscillations, the presence of diatom layers in Unit A is presumed to be related to regular (predominantly siliceous) phytoplankton blooms (cf. Domack et al., 2006; Leventer et al., 2006; Graham et al., 2017). Consequently, their absence in Units B-D, i.e. sometime after 8.5 and 7.7 cal ka BP in KHT and JT, respectively, implies either a sudden cessation of such blooms, e.g. due to reduced meltwater input and/or wind-induced mixing of the water column (Leventer et al., 2006), or a potential “dilution” of the biogenic sediment due to increased sediment input from the island. As sedimentation rates at PS133/2\_17-13 in central KHT actually decrease across the upper boundary of Unit A (Table 6.3), and therefore do not indicate dilution in Units B-D, we conclude that the change in deposition that defines the A-B

unit boundary must have been associated with a change in regime that caused phytoplankton blooms to stop. This, in turn, was likely provoked by climatic factors (see also section 6.5.3 below).

#### 6.5.2.1.4. Shelf circulation

Given the dynamic behaviour of most meltwater streams and ocean currents, it would be conceivable that locations of sediment accumulation also vary both spatially and temporally. Indeed, variable configuration of meltwater streams and associated deposition has been documented in glacimarine settings, including fjords and continental shelves, where ocean currents additionally affect sediment distribution (e.g. Dunbar et al., 1985; Kehrl et al., 2011). Immediately after the LLGM, for instance, the establishment of a new current regime on a recently exposed continental shelf and an associated change in the depositional conditions would make sense; in fact, a similar scenario has been postulated for DT (Fig. 6.1b), where the progressive intrusion of (warmer) currents onto the shelf after the LLGM likely created a cavity beneath the stagnant ice margin, causing it to disintegrate rather rapidly from within (Lešić et al., 2022). Accordingly, retreating ice in KHTS after the LLGM could have successively exposed the shelf while simultaneously shifting any sedimentation hotspots, generated from localised meltwater flows at the ice margin, from the outer shelf towards the coast. This is in accordance with the general trough-fill architecture that shows a shift to more island-proximal sedimentation with the onset of Unit B, although the Holocene ages of the latter are at odds with such an interpretation. Nevertheless, on a wide and exposed shelf, such as that around SG, ocean currents are bound to play an important role also during the Holocene, where most tidewater glaciers were inferred to have fluctuated only within their respective fjords (Bentley et al., 2007; Hodgson et al., 2014a; Graham et al., 2017; Bakke et al., 2021; Lešić et al., 2022). Fluvial energy of potential meltwater streams was therefore likely decreased, making room for the more intensive pervasion of a complex system of ocean currents onto the inner shelf.

The SG continental shelf is indeed influenced by a number of different cross- and along shelf current directions, as well as wind and open-ocean currents that, as of today, impact different areas to variable degrees (Meredith et al., 2003; Meredith et al., 2005; Matano et al., 2020; Combes et al., 2023). The complexity is exacerbated by a seabed characterised by deep troughs, numerous bedrock highs and several shoals, that may further affect and direct such currents (Matano et al., 2020; Combes et al., 2023). This is especially conceivable for KHTS,



where a modern SACCF branch intrudes onto the continental shelf and is associated with peak along-shelf transport (Matano et al., 2020; Combes et al., 2023). Accordingly, the narrow bottleneck morphology of west JT with its along-shelf west-east orientation may have focused shelf currents flowing eastwards into the trough, thus actively preventing westward migration of island-runoff after <8.5/7.7 cal ka BP. This would then force intensified in-situ accumulation in central and east JT, which would account for an eastward thickening of trough-fill sequences in JTS (Fig. 6.4). Similarly, the same SACCF-related circulation might explain limited transport of sediment into central KHT on the mid-shelf and, consequently, to southern KHT, around <8.5/7.7 cal ka BP, as this current branch is also associated with reduced cross-shelf exchange (Matano et al., 2020).

#### 6.5.2.1.5. Bottom-currents

Aside from the general shelf circulation, the presence of moat-drift systems within AF2 along the western flank of KHT indicates active bottom-currents during the Holocene (Fig. 6.5 b-e). In shallower waters, such as the SG continental shelf, bottom-currents are generated and influenced by a variety of factors, such as wind, tides, and thermohaline gradients, all of which vary seasonally and make shallow-water bottom-currents less steady compared to those in deep water (Anderson et al., 1984; Verdicchio and Trincardi, 2008). This is of particular relevance for SG, where shelf waters are generally less than 400 m deep. Moreover, SG is not only subject to changes in local factors, such as meltwater and island run-off, but is also exposed to changes in wind and temperature across the Southern Ocean, making its shelf a likely target for complex bottom-current formation. Aside from the strength of existing bottom-currents, sediment supply is the other main contributor to moat development (Wilckens et al., 2023). While strong currents might lead to erosion when sediment supply is low, depending on the sediment properties, high sediment supply can lead to aggradation within moats even at relatively high current speeds (Wilckens et al., 2023). In central KHT, bottom-currents cause spatial differences in sediment deposition, creating moats in the deepest areas along the (north)-western trough flank (Fig. 6.5b,c), where currents are therefore inferred to be the strongest, while the adjacent areas undergo preferential deposition due to decreasing currents (cf. Wilckens et al., 2023). Although resolving bottom-current speeds around SG would go beyond the scope of this paper, the aggradation within the moat-drift system deposits in Unit A identified in section 6.4.1, as well as the relatively

high sedimentation rates on the inner and mid-shelf in Unit A (Table 6.3), imply periods of elevated sediment supply into the moat-drift system (Fig. 6.5b,c).

### 6.5.3. Temporal variability in sediment deposition

In addition to the spatial variability in sediment deposition, the presence of the three individual unit boundaries within AF2 suggest a temporal component to basin-fill sedimentation, which, based on coeval unit boundaries, likely affected the entire trough system. Accordingly, we identify three main changes in Holocene depositional environments, occurring (i) around <8.5/7.7 cal ka BP, when the diatom-rich silty muds of Unit A were replaced by the diatom-poor silty muds of Unit B, (ii) around 4.1-3.9 cal ka BP, when silty muds of Unit C succeeded Unit B, and (iii) around 2.6-2.1 cal ka BP, when accumulation of the most recent Unit D began (Fig. 6.7). Interestingly, these transitions are, albeit slightly offset temporally, also roughly simultaneous to larger-scale Holocene climate variability reported from the Antarctic Peninsula (Bentley et al., 2009) and the South Shetland Islands (Heredia Barión et al., 2023a; Heredia Barión et al., 2023b), suggesting comparability between there and SG.

#### 6.5.3.1. *Transition from Unit A to Unit B (<8.5/7.7 cal ka BP)*

The change from the relatively uniform Unit A (thickness generally between 8 and 35 m in both KHT and JT, max. 48 m in KHT, Table 6.1) to the unevenly distributed Unit B (thickness variable between max. 8.5 m in KHT and >27 m in JT Table 6.1) shows that a trough-wide mechanism around <8.5/7.7 cal ka BP started to 'trap' sediment within JT, forcing less material transport into KHT. In this context 'trapping' refers to sediment being held back in JT and its tributaries, though not necessarily by physical barriers. Trapping was accompanied by a switch to more basin-confined deposition and a change in primary production from a period of frequent and intensive phytoplankton blooms to one where diatoms seem to have been negligible for sedimentation. Indeed, this time period coincides with the end of the dry and warm Holocene Thermal Maximum (HTM; Ciais et al., 1992; Masson et al., 2000; Masson-Delmotte et al., 2004; Bentley et al., 2009), which occurred at the same time as a SHW minimum (Moreno et al., 2018; Moreno et al., 2021), and might have fostered relatively calm depositional conditions around SG. The latter would have been associated with limited wind-induced mixing of the water column and are in accordance with the strong acoustic stratification of Unit A (Figs. 6.4, 6.5), which probably represents the intercalation of

terrigenous muds and diatom layers. Because depositional conditions must have been homogeneous and calm enough to enable not only relatively uniform, trough system-wide sedimentation, but also the establishment of highly regular acoustic stratification and the rapid deposition of diatom oozes, we suggest that shelf currents were either relatively weak or absent during deposition of Unit A, while bottom-currents were at least active enough to form moat-drift systems (Fig. 6.5c). Diatom blooms could have developed from seasonal discharge of meltwater from relatively proximal glacier margins acting as a fertiliser (cf. Matano et al., 2020 and references therein). Albeit not proven for shelf environments, primary production in fjords is stimulated by glacial meltwater discharge (Arrigo et al., 2017), which is likely also the source of the enhanced terrigenous input inferred for Unit A. Although the HTM lasted only until ~9.5 cal ka BP in Antarctica (Ciais et al., 1992; Masson et al., 2000; Masson-Delmotte et al., 2004; Bentley et al., 2009) and is heterogeneous among Antarctic records due to their individual deglaciation history (Xiao et al., 2016), this warm period prevailed significantly longer on SG, where it lasted until <8.5/7.7 cal ka BP (e.g. Berg et al., 2019), thus matching the radiocarbon ages of the A-B unit boundary in KHTS (Table 6.2).

The shift from the warm HTM to generally colder conditions, as reported for SG's north-eastern side and Antarctica (e.g. Rosqvist and Schuber, 2003; Oppedal et al., 2018; Berg et al., 2019), is implied by a strong acoustic reflector marking the A-B unit boundary, as well as the absence of diatom bloom deposits and a less distinct stratification in Unit B. The simultaneous onset of significant sediment trapping in central and east JT, though likely reinforced by the narrow bottleneck morphology of west JT, might have been related to an increase in east-west directed currents around this time, probably resulting from a change in the strength or position of the SACCF that, considering the modern SACCF intrusion into KHTS (Matano et al., 2020; Combes et al., 2023), might have intruded onto the continental shelf and into KHTS as early as <8.5 cal ka BP. Such a change would be intricately coupled to a change in the SHW (cf. Gille, 2014; Liao and Chao, 2017; Yamazaki et al., 2021), leading us to suggest that wind strength increased during this cooling. Accordingly, mixing in the water column would have increased, thus inhibiting the occurrence of frequent and intensive diatom-blooms (Leventer et al., 2006). Indeed, SG experienced a strengthening of the SHW over the course of the mid-Holocene (Zwier et al., 2021) and has been proven to be very sensitive to wind stress in both the terrestrial and the marine realm (Matano et al., 2020; van der Bilt et al., 2022). This would explain the significant change in depositional environments and the inferred reconfiguration

in shelf circulation around <8.5/7.7 cal ka BP. The latter is also in accordance with lithofacies from outer DT (Fig. 6.1b), where high sand content and abrupt low sedimentation rates (10 cm ka<sup>-1</sup>) after 10.4 cal ka BP were interpreted to be the result of enhanced current activity on the outer shelf (Lešić et al., 2022), and thus supports the theory that a similar current regime developed in KHTS.

A reconfiguration in shelf circulation and an associated change in bottom-currents are also indicated by the evidence for local erosion in several locations of KHTS. These include changes within the moat-drift system across the A-B unit boundary in central KHT, where truncated reflectors within the moat (inset 1 in Fig. 6.1c) along the (north-)western flank, as well as along the western trough flank (inset in Fig. 6.5e), suggest partial erosion of Unit A and imply sudden changes in either the sediment supply, the sediment properties, the bottom-current strength, or a combination of the three. Furthermore, erosion by truncated reflectors can also be observed in central JT and west KHT (Figs. 6.4 b,c, 6.7a), where they are associated with a stratigraphic unconformity. The occurrence of depositional hiatuses at the core sites of GeoB22057-1 and GeoB22058-1 in JT (Fig. 6.7a), as well as in PS133/2\_17-13 in west KHT (Fig. 6.7b), may mark additional erosional events, but could also just represent gaps in sedimentation. Indeed, it is unclear from our data (i) how many erosional events occurred, (ii) when specifically they occurred, (iii) how long they lasted, and (iv) whether sedimentation took place in between. Although in a glacial trough setting, such as KHTS, erosional events could be related to gravity flows, e.g. turbidity currents, which have often been reported to be responsible for reworking sediment on glacimarine continental shelves (e.g. Anderson et al., 1984; Kuvaas and Leitchenkov, 1992; Michels et al., 2001; Kuvaas et al., 2005), we would expect to see other evidence of gravity-flow activity, such as slumps, in the form of acoustically transparent and lenticular sediment bodies, or turbidite-characteristic lithologies in the sub-bottom profiles and sediment cores (Lešić et al., in prep.). Although these occur locally as transparent bodies between bathymetric highs in west JT (Fig. A.1), their absence within east JT, central JT and central KHT and the tributaries, leads us to favour a change in bottom-currents as the erosive agent. If bottom-currents travelled along the, for this region preferred, direction from west to east (Matano et al., 2020; Combes et al., 2023), and increased in strength after the HTM, such currents, when entering JTS from the west, would then have become sufficiently focused in west JT to not only remove the top parts of Unit A, but also to prevent any subsequent deposition by keeping particles in suspension. Such particles would

then have been forced back towards the east, where the widening funnel-shaped trough morphology of central JT would have decreased kinetic energy of the currents and thus led to the accumulation of the gradually thickening sediment packages of Units B and C (Fig. 6.8a). Bottom-currents as the responsible agent for the unconformities in KHTS are also supported by Graham et al. (2017), who interpreted an unconformity on the north-eastern shelf to derive from similar mechanisms.

A rather substantial and long-term subsequent change in bottom-current dynamics after the end of the HTM is further implied by the development of a smaller moat-drift system onto the truncated reflectors within the already existing moat-drift system along Profile 3 (Fig. 6.5c). Throughout the development of Unit B-D, this smaller moat-drift system migrates laterally towards the (north-) western trough flank, which is typical for moat-drift systems along bathymetric contours (Wilckens et al., 2023) and might represent more stable conditions after <8.5/7.7 cal ka BP.

#### 6.5.3.2. *Transition from Unit B to Unit C (~4 cal ka BP)*

Cool and windy conditions with associated strength in bottom-currents, possibly related to a spatial and/or temporal change in the SACCF and its associated branches, persisted until ~4 cal ka BP, when the onset of the Holocene Hypsithermal marked the transition to a recurring warm period. Although having a similar lithology, small differences in acoustic properties as well as a pronounced boundary reflector between Units B and C suggest a slight shift in the sedimentary processes or their magnitude, albeit much smaller than the change around <8.5/7.7 cal ka BP. Our data therefore do not allow for an analysis of the exact changes and their magnitude at this point, but the lithological signature from this time period will be further investigated in Lešić et al. (in prep.).

Assuming that the erosion and hiatus in central JT after 7.7 cal ka BP was, in fact, caused by intensifying bottom-currents, the hiatus between ~3.9 and 2.6 cal ka BP in GeoB22057-1 further east would suggest a brief period of even stronger bottom-currents entering JT from the west. These currents must then have been strong enough to reach as far as central JT, where they prevented the deposition of Unit C at the GeoB22057-1 site (Fig. 6.7a). However, a further current strengthening during a transition to warmer climate may seem counter-intuitive. Alternatively, the hiatus could also be a result of rather stable bottom-current conditions and relief-fill, resulting in a bypass area around GeoB22057-1, while sediments

were held back in the deeper basins of east JT. This is also indicated by the pinch-out of Unit C towards GeoB22057-1 (Figs. 6.4b,c, 6.7a).

6.5.3.3. *Onset of trough-wide sediment draping (~2.6-2.1 cal ka BP)*

The strong bottom reflector, R1, of Unit D can be traced across our data throughout the entire JTS and central KHT (Figs. 6.4b-c, 6.5b-e) and therefore suggests that another KHTS-wide change in depositional environments occurred between 2.6 and 2.1 cal ka BP, which also marks the largest change since <8.5/7.7 cal ka BP. The draping, homogeneous character of Unit D covering all underlying units, alongside its very uniform thickness distribution, are indicative of relatively calm, open-marine conditions. A similar drape has also been reported from a sedimentary record in Cumberland Bay (Fig. 6.1b), dating the onset of sedimentation onto a bathymetrically exposed moraine to 2.2 cal ka BP (Graham et al., 2017). This suggests that the calmer depositional conditions might have regional significance across the marine realm around SG.

Calmer conditions are also implied by the fact that deposition of Unit D started at 2.6 cal ka BP in central JT, which suggests a shift in bottom-current strength, causing the currents entering JT from the west to no longer reach the central parts, thus allowing for the deposition of Unit D at the core site of GeoB22057-1. At the core site of GeoB22058-1 at the western end of central JT, Unit D started to accumulate slightly later, at ~2.1 cal ka BP, which implies that around that time bottom-current strength may have not necessarily abated in general across the shelf, but possibly became more homogeneous and less focused. Both events roughly coincide with studies from specifically the terrestrial regions of NE SG, which documented a substantial change from warmer to colder and more humid conditions around 2.6-2.2 cal ka BP (Rosqvist and Schuber, 2003; van der Putten et al., 2004; van der Putten et al., 2009), i.e. more or less exactly around the time we observe the change in sedimentation from Unit C to D (Fig. 6.8). This time period was associated with a change to “negative SAM-like conditions” (Strother et al., 2015; Zwier et al., 2021; van der Bilt et al., 2022). The SAM refers to the Southern Annular Mode, which describes modern variability in the latitudinal position and strength of the SHW around Antarctica over timescales of tens of years (Gong and Wang, 1998, 1999; Lee et al., 2019; Fogt and Marshall, 2020; Wright et al., 2022). Such variability is induced by changing air pressure over the Southern Ocean and leads to either a poleward contraction of the SHW core belt associated with low air pressure and increased winds over the Antarctic

continent (positive-phase SAM), or an expansion of the SHW belt towards the north, associated with low air pressure and increased winds over lower latitudes (negative-phase SAM; Gong and Wang, 1999; Sallée et al., 2008; Lee et al., 2019; van der Bilt et al., 2022). Indeed, SG was reported to have experienced a general increase of the Westerlies and related evaporation around this time (Strother et al., 2015; Zwier et al., 2021; van der Bilt et al., 2022). Although such a strengthening in wind seems to be at odds with an observation of more homogeneous depositional conditions and potentially less focussed bottom-currents, since the SHW are a key driver of the ACC (Orsi et al., 1995), they may have caused a shift in the latitudinal position of mean ACC transport or associated frontal positions (Meredith et al., 2004; Meredith and Hogg, 2006; Sallée et al., 2008; Gille, 2014) rather than affecting current strength itself. Indeed, such a shift was postulated in section 6.5.3.1 also for the transition from warmer to cooler conditions around  $<8.5/7.7$  cal ka BP and could mean that the main currents were redirected or simply less focused, affecting KHTS less. This might then satisfactorily explain why currents appear to have been less focussed in west and central JT after 2.6 cal ka BP.

## 6.6. Conclusions

Sub-bottom profiler data, complemented by bathymetric data and selected radiocarbon ages, show that a thick sequence of basin-fill sediments accumulated in KHTS throughout the Holocene. Notable differences in spatial and temporal distribution of the basin-fills further imply that there is a complex interplay of factors influencing Holocene sedimentation in KHTS. These include trough morphology and associated accommodation space, the sediment sources, shelf circulation, bottom-currents, as well as sediment supply from land and primary productivity.

The most significant transitions in the depositional environments in KHTS are marked by distinct reflectors between acoustic sub-units and occurred simultaneous to SG Holocene climate fluctuations between warmer to cooler phases. The dry and warm Holocene thermal maximum prior to  $<8.5/7.7$  cal ka BP marks a calm depositional environment with seemingly regular siliceous phytoplankton blooms due to increased meltwater input and strong stratification of the water column. The end of this period is associated with a change to enhanced trapping of sediment on the inner shelf and more basin-confined sedimentation, which were probably accompanied by a shift in the position of the SACCF, leading to a

reconfiguration of shelf circulation. Erosion related to focused bottom-currents in western KHT and central JT is evident from truncated reflectors of Units A and B. The subsequent deposition of Unit B, likely lacking diatom layers, suggests cooler and windier conditions, which persisted until the onset of deposition of Unit C, dated to ~4 cal ka BP. This transition likely marks the beginning of a recurring warmer period, the Holocene Hypsithermal, and could have been associated with a local strengthening in bottom-currents through the narrow west JT, as implied by a depositional hiatus in GeoB22057-1. The onset of deposition of Unit D's homogeneous sediment drape was dated to around 2.6 cal ka BP and thus coincides with the onset of cooler climate and strong winds in the region. As this time period also coincides with the first sediment deposition on top of eroded portions in central JT and central KHT, it is likely that another change in SACCF position impacted shelf circulation, resulting in redirected or less focussed currents in KHTS.

## **Acknowledgements**

This publication was funded by the "Deutsche Forschungsgemeinschaft" (DFG) within the priority program SPP 1158 "Antarctic Research with comparative investigations in Arctic ice areas" by the grants KU 683/18-1, BO 1049/23-1, and DO 705/4-1. We thank the captains and crews, as well as the chief scientists from RV Meteor cruise M134 and RV Polarstern cruise PS133/2 (Grant No. AWI\_PS133/2\_01 and AWI\_PS133/2\_02) (Alfred-Wegener-Institut Helmholtz-Zentrum für Polar und Meeresforschung, 2017). We acknowledge further financial support from the Helmholtz Association (Alfred Wegener Institute Helmholtz Centre for Polar and Marine Research) and are grateful to Miriam Römer for organising the funding for participation in the Polarstern cruise via the MARUM Incentive Funds Initiative. Further, we thank the AWI repository for providing gravity core PS133/2\_17-13. Additionally, we thank C. Gebhardt, J. Klages, J. Wollenburg, V. Schumacher, S. Wiebe, M. Seebeck and P. Daub from Alfred Wegener Institute, Helmholtz Centre for Polar and Marine Research in Bremerhaven, for their support. Further, we thank M. Römer and N. Römer-Stange for support with SMT The Kingdom Suite and C. Ferreira for the processing of bathymetric data. All figures in this publication were created using QGIS 3.22.10 and Adobe Illustrator 2022/2023.





## 7. Manuscript IV: Climate-driven Holocene sedimentation in King Haakon Trough System, sub-Antarctic South Georgia

In preparation for submission

Lešić, Nina-Marie<sup>1,2</sup> ([nlesic@marum.de](mailto:nlesic@marum.de)); Streuff, Katharina Teresa<sup>1</sup> ([kstreuff@marum.de](mailto:kstreuff@marum.de)); Titschack, Jürgen<sup>1</sup> ([jtitschack@marum.de](mailto:jtitschack@marum.de)); von Dobeneck, Tilo<sup>1</sup> ([dobeneck@uni-bremen.de](mailto:dobeneck@uni-bremen.de)); Kuhn, Gerhard<sup>1,2</sup> ([ge\\_ku@uni-bremen.de](mailto:ge_ku@uni-bremen.de)); Bohrmann, Gerhard<sup>1</sup> ([gbohrmann@marum.de](mailto:gbohrmann@marum.de))

*1 MARUM, Centre for Marine Environmental Sciences, and Faculty of Geosciences, University of Bremen (UoB), Klagenfurter Str., 28359 Bremen; Germany*

*2 Alfred Wegener Institute (AWI), Helmholtz Centre for Polar and Marine Research, Am Alten Hafens 26, 27568 Bremerhaven, Germany*

Corresponding author: Lešić, Nina-Marie ([nlesic@marum.de](mailto:nlesic@marum.de))

### **Abstract**

The sub-Antarctic microcontinent South Georgia is located in the Atlantic sector of the Southern Ocean and is situated within the core belt of the Southern Westerlies and between oceanographic fronts of the Antarctic Circumpolar current. It is thus very sensitive to the variability of these systems in the context of Southern Hemisphere climate change. After the last glacial maximum South Georgia underwent a superordinate ice retreat and experienced mostly minor glacier fluctuations on land and within the fjords during the Holocene, while the continental shelf was exposed to a complex system of ocean currents. Multi-proxy data and radiocarbon age models from four gravity cores, taken in King Haakon Trough System on the south-western continental shelf, reveal that trough sediments have not only recorded Holocene climate change on South Georgia, but also roughly reflect those in Patagonia and the Antarctic Peninsula. They provide evidence that at least three major transitions between warmer and cooler climate phases occurred since 10.8 cal ka BP, which were each associated with increased bottom-current activity in the trough system. Our record is the first evidence for small-scale climate fluctuations on the South Georgia shelf during the Holocene.

## 7.1. Introduction

(Glaci-)marine sediments on continental shelves in higher latitudes are subject to a multitude of factors that influence their depositional environments. These include shelf morphology, terrestrial run-off tied to glacier dynamics and associated meltwater, iceberg rafting, primary production and, by association, sea-ice, as well as shelf currents, all of which are known to vary, at least to some degree, seasonally, locally and regionally (e.g. Anderson et al., 1983; Anderson et al., 1984; Murphy et al., 2013; Matano et al., 2020). Accordingly, sedimentary archives in these regions tend to be highly complex, thus impeding the reconstruction of past climate. This is especially true for climatically dynamic areas, such as the Southern Ocean, where several large-scale climate systems affect the entire Southern Hemisphere, and, to some extent, also global climate (Strother et al., 2015; Wu et al., 2021; Wright et al., 2022).

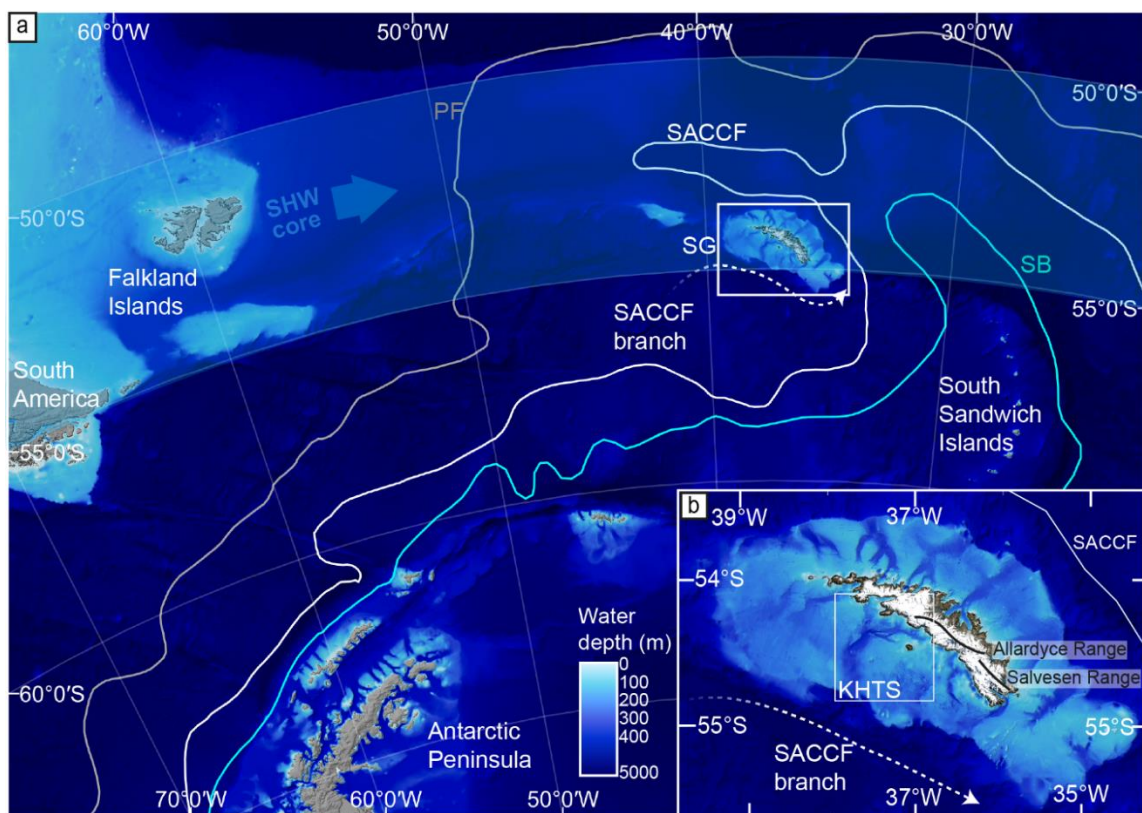


Fig. 7.1: a) Location of South Georgia in the Southern Ocean with respect to the Southern Hemisphere Westerly Wind core belt (SHW core), the Falkland Islands, the Antarctic Peninsula and the South Sandwich Islands, as well as the three oceanographic Antarctic Circumpolar Current (ACC) fronts. PF = Polar Front, SACCF= Southern Antarctic Circumpolar Current Front, SB = Southern Boundary of the Antarctic Circumpolar Currents. Frontal positions adapted after Orsi et al. (1995). b) South Georgia and its continental shelf area with an adjacent SACCF branch adapted after Matano et al. (2020). The study area of King Haakon Trough System (KHTS) is indicated by a white rectangle. DEM information for the ocean and shelf areas is based on GEBCO Compilation Group (2023), and Hogg et al. (2016); (2017). Bathymetric data within KHTS is based on data from cruise M134 (Bohrmann et al., 2017), while the map information for SG island is derived from Landsat imagery from South Georgia GIS (2023). (EPSG: 3762)

There are only few glaciated landmasses in the sub-Antarctic that reflect the maritime climate of the Southern Ocean without much influence from large continents nearby (cf. Bentley et al., 2007; Hodgson et al., 2014a; Hodgson et al., 2014b), but the Atlantic sector of the Southern Ocean hosts the microcontinent of South Georgia (SG), which is located within the core belt of the Southern Hemisphere Westerlies (SHW; 50 - 55°S; Lamy et al., 2010) and between two Antarctic Circumpolar Current fronts (ACC), the Polar Front (PF) and the Southern Antarctic Circumpolar Current Front (SACCF, Fig. 1; Orsi et al., 1995; Thorpe et al., 2002; Orsi and Harris, 2019). These atmospheric and oceanographic systems are intricately linked with the climate of the Southern Hemisphere and therefore make SG a prime target to study past climate evolution. Especially the sediments trapped in the deeply incised glacial troughs on the continental shelf around the island are of interest in this context, because they should archive climate variability and resulting environmental conditions at a high temporal resolution.

Despite SG's suitability to investigate regional climate in the context of large-scale Southern Hemisphere climate variability, the majority of present studies only cover a specific terrestrial and near-coastal sector of north-eastern SG (e.g. Clapperton et al., 1989b; Rosqvist and Schuber, 2003; van der Putten et al., 2009; Oppedal et al., 2018; Berg et al., 2019; Bakke et al., 2021; Zwier et al., 2021; van der Bilt et al., 2022), presumably because of this region's comparatively advanced deglaciation since the beginning of the Holocene, and according accessibility of large, ice-free areas (van der Putten and Verbruggen, 2005; Graham et al., 2017; Oppedal et al., 2018; Xia et al., 2020). Data from offshore SG, in turn, rather focus on ice extent and associated long-term climatic changes connected to the (Local) Last Glacial Maximum and the Antarctic Cold Reversal (ACR) than the Holocene (Graham et al., 2017; Lešić et al., 2022). Although a recent study by Lešić et al. (subm.) from King Haakon Trough System (KHTS; Fig. 7.1b, see also Lešić et al. (subm.) and Bohrmann et al. (2017) for unofficial nomenclature) focused on trough system-wide changes in Holocene sedimentation on SG's south-western continental shelf, data on the small-scale variability of depositional environments and climate remains scarce, particularly in the marine realm off the southern SG coast (Barrow, 1983b; Strother et al., 2015; Lešić et al., 2022).

In order to be able to decipher regional from local climate signals and to better understand the climatic evolution of SG and the Southern Hemisphere, more studies are needed documenting local depositional environments, especially from marine records. This study

provides one such piece of the puzzle, as it presents the first highly-resolved Holocene marine-lithological dataset from the inner and mid-continental shelf southwest of SG. It complements a recent study by Lešić et al. (submitted), documenting trough-wide depositional environments on the basis of hydroacoustic data in the King Haakon Trough System, by identifying millennial-scale Holocene climate variability in four sediment cores from the same glacial cross-shelf trough. The results are compared with climate fluctuations reconstructed from terrestrial data in north-eastern SG and will show how the latter translate to the lithologies of the marine realm. The four cores comprise the majority of the Holocene sediment succession, thereby recording trough sedimentation since 10.8 cal ka BP. They show that the majority of lithological horizons correspond not only to specific Holocene climate events reconstructed from north-eastern SG, but also to similar climate phases documented from around Antarctica. Our data therefore suggest that climatic changes observed in the sedimentary record of KHTS are of regional importance, affecting not only both sides of SG, but also the entire Southern Hemisphere.

## 7.2. Study area

### 7.2.1. Physiographic setting

SG (54-55°S, 35.5-38°W) is a partially glaciated, isolated microcontinent in the Atlantic sector of the sub-Antarctic (Dalziel et al., 2021) that is located within the main atmospheric and oceanographic systems driving Southern Hemisphere climate, the SHW and ACC (e.g. Moreno et al., 2018; Bakke et al., 2021; Yamazaki et al., 2021). Accordingly, changes in strength and/or position of either of these systems directly influence precipitation and temperature distribution on the island, as well as current configuration on SG's continental shelf (Strother et al., 2015; Matano et al., 2020; Bakke et al., 2021; Combes et al., 2023). SG is approximately 170 km long and 35 km wide and features the ~NW-SE-striking Allardyce mountain range, which rises to >2000 m and serves as an orographic barrier to the modern precipitation regime (Gordon et al., 2008; Cook et al., 2010; Farías-Barahona et al., 2020). The resulting precipitation gradient leads to drier conditions on the north-eastern side of the island and is probably related to the west winds that bring moisture to the south-western side of the island and, in turn, trigger regular warm and dry föhn winds, particularly affecting the lee (north-eastern) side of the mountains. These west winds hence regulate local temperature, moisture supply and snowfall on both sides of the mountains (Xia et al., 2020 and references therein),

which leads to a contemporary division of SG into a more or less ice-free north-eastern side and a still strongly glaciated south-western side (Gordon et al., 2008; Cook et al., 2010; Farías-Barahona et al., 2020). The mountain range still hosts several ice fields, from which glaciers move rapidly towards the coast, where many of them terminate as tidewater glaciers in bays and fjords (Gordon et al., 2008).

The many bays and fjords around SG's coast often merge seaward to form deeply incised cross-shelf trough systems (Graham et al., 2008) that mostly extend all the way to the edge of the large continental shelf (~30-100 km wide from coast to shelf edge) and likely formed during or prior to the Local Last Glacial Maximum (>30 ka BP) (LLGM; Graham et al., 2017; Lešić et al., 2022). One of these is the King Haakon Trough System (KHTS; Fig. 7.1b), which is located on the west wind-exposed and precipitation-rich south-western side of SG and, like many other troughs in the region, acts as a trap for thick sedimentary sequences (cf. Graham et al., 2008; Römer et al., 2014; Graham et al., 2017). Lešić et al. (subm.) first defined KHTS as a large composite system composed of (i) the large N-S-orientated King Haakon Trough (KHT; Fig. 7.2b) that extends southward of King Haakon Bay (Fig. 7.2a), and (ii) the Jacobsen Trough System (JTS), an additional smaller E-W-striking tributary system joining KHT from the east (Fig. 7.2a). JTS includes the larger Jacobsen and Annenkov Troughs (JT and AT, respectively), as well as their respective tributaries and bays (Fig. 7.2a). Water depths within the trough valleys and their tributaries vary between 200 and 400 m (based on the extent mapped in our data). KHTS is still influenced by several tidewater glaciers, whose fronts are currently aligned with the present coastline but keep retreating rather dramatically (Gordon et al., 2008; Cook et al., 2010; Graham et al., 2017). Recent work by Lešić et al. (subm.) and Streuff et al. (in prep.) revealed that, although a large ice stream must have drained through KHTS at some point in the past, the trough system has likely been free of grounded ice already before the start of the Holocene. Since the ungrounding of glacial ice and its retreat into the fjords, where glaciers have been fluctuating during the Holocene (Clapperton et al., 1989b; Bentley et al., 2007; Hodgson et al., 2014a; Graham et al., 2017; Bakke et al., 2021), KHTS has been fully exposed to shelf currents and water intrusions from the open ocean (cf. Matano et al., 2020; Combes et al., 2023), suggesting that the contemporary depositional environment is distal glacimarine to hemipelagic. The isolated position of SG, i.e. the large distance to other landmasses (Fig. 7.1a), further suggests that, with the exception of volcanic ash reported in Diamond Bog (north of Diamond Lake, Fig. 7.2; Oppedal et al., 2018) and scarce dust input

(Strother et al., 2015; Foster et al., 2016), most of the terrigenous material trapped in SG's glacial troughs is supplied by the island itself.

#### 7.2.2. Previous work

Previous research with focus on the Holocene climate on SG, to our knowledge, does not only comprise moraine mapping and further geomorphological approaches on the north-eastern side of SG (Clapperton, 1971; Clapperton and Sugden, 1980; Clapperton et al., 1989a; Clapperton et al., 1989b; Bentley et al., 2007; White et al., 2017; Oppedal et al., 2018; Bakke et al., 2021), but also palynological studies (Barrow, 1978, 1983b, 1983a; van der Putten et al., 2012; Strother et al., 2015) around King Edward Cove, Barff Peninsula (Fig. 7.1a), Cumberland Bay West (CBW; Fig. 2c) and Annenkov Island, as well as peat core analysis at Kanin Point, Diamond Bog and on Tønsberg Peninsula (van der Putten et al., 2004; van der Putten et al., 2009; van der Putten et al., 2012; Oppedal et al., 2018; Xia et al., 2020). Additionally, lake/lagoonal sediment cores from a series of water bodies between Stromness Bay and Barff Peninsula (Fig. 2a,c; Clapperton et al., 1989b; Birnie, 1990; Wasell, 1993; Rosqvist et al., 1999; Rosqvist and Schuber, 2003; van der Putten and Verbruggen, 2005; Oppedal et al., 2018; Berg et al., 2019; Bakke et al., 2021; Zwier et al., 2021; van der Bilt et al., 2022) and on Annenkov Island (Fan Lake, Fig. 2a; Strother et al., 2015) have been used for climate reconstruction, including biochemical proxies for quantitative temperature reconstruction (Foster et al., 2016). Compiled, these records allowed for a robust reconstruction of Holocene climate and its transitions between cooler, windier and warmer, calmer phases for SG island itself (Lešić et al., *subm.*). The most important phases are (i) the dry, and warm Holocene Thermal Maximum (HTM) before 7 ka BP, (ii) the subsequent cooler, windier climate due to strengthening SHW with associated cirque glacier re-advances around 7 ka BP and ~4.5 ka BP (Rosqvist et al., 1999; Rosqvist and Schuber, 2003; Oppedal et al., 2018; Berg et al., 2019; Bakke et al., 2021; Zwier et al., 2021), (iii) a recurring warm phase starting shortly before 4 ka BP, the so-called Holocene Hypsithermal (Clapperton et al., 1989a; Clapperton et al., 1989b; Rosqvist and Schuber, 2003; Foster et al., 2016; Oppedal et al., 2018; Berg et al., 2019; Xia et al., 2020) that might have peaked at ~2.6 cal ka BP on Annenkov Island (Foster et al., 2016) and (iv) a substantial change after the Hypsithermal to colder and more humid conditions during a Neoglacial (*cf.* Heredia Barión et al., 2023a) as soon as 2.75 cal ka BP (Birnie, 1990; Strother et al., 2015) with associated substantial glacier re-advances around 2 ka BP (*e.g.*

Rosqvist and Schuber, 2003; Oppedal et al., 2018). This most recent change to colder and wetter temperatures might have been linked to recurrent strengthening of the SHW on SG before 2 ka BP (van der Putten et al., 2004; van der Putten et al., 2009; Strother et al., 2015; Berg et al., 2019; Zwier et al., 2021; van der Bilt et al., 2022).

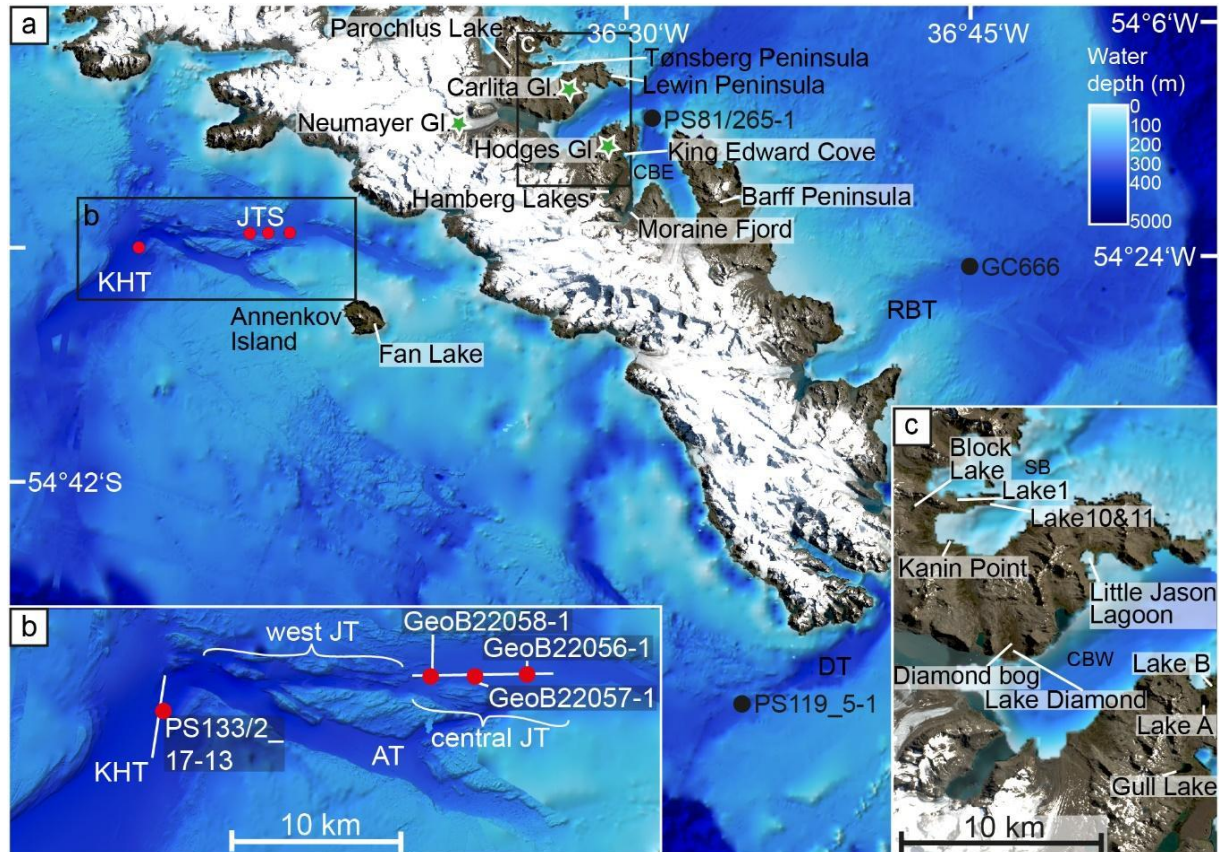


Fig. 7.2 a) overview of paleoclimate record locations on SG island and its continental shelf, as well as Annenkov Island from the literature described in section 7.2.2. Investigated glaciers and associated moraines are indicated with green stars, while gravity cores from the shelf are depicted with black dots. Red dots show the locations of this study's gravity cores. b) Inset of the northern part of KHTS, including King Haakon Trough (KHT), Annenkov Trough (AT) and the core location of PS133/2\_17-13 within in red, as well as, west JT and central JT, where the locations of the gravity cores GeoB22058-1, GeoB22057-1 and GeoB22056-1 are indicated in red. The orientation of two Parasound Profiles that cut the core locations in both troughs are indicated by white lines. c) a zoom in to the Lewin Peninsula and its surroundings, including Cumberland bay West (CBW), show the locations of paleoclimate records taken from bogs and lakes that were not resolved in subset a. DEM information for shelf is based on bathymetric data from M134 (Bohrmann et al., 2017) and Hogg et al. (2016);(2017). Map information for SG island is derived from Landsat imagery from South Georgia GIS (accessed 2023). (EPSG: 3762)

The Holocene SG climate development is more or less comparable to the Antarctic Peninsula, the Shetland Islands, (Bentley et al., 2009; Heredia Barión et al., 2023a) and Patagonia (Moreno et al., 2018; McCulloch et al., 2020), suggesting that the results from terrestrial records can be attributed to a larger scale and should therefore, though maybe to a different



extent, be detected on the south-western side of SG as well (Strother et al., 2015; Foster et al., 2016).

However, Holocene climate and/or depositional environment reconstruction in the marine realm of SG is very limited to near-shore sediment core investigations in Little Jason Lagoon (Berg et al., 2019), to the fjord outlet of Cumberland Bay East (CBE; core PS81/265-1, Fig. 7.2a; Graham et al., 2017), the north-eastern mid-continental shelf in the Royal Bay Trough (RBT; core GC666, Fig. 7.2a; Graham et al., 2017) and the Drygalski Trough (DT; core PS119\_5-1; Fig. 7.2a; Lešić et al., 2022), which represents the only published sedimentary record from the marine environment on the southern SG shelf to our knowledge. The shelf archives are not highly resolved and therefore limit Holocene climate reconstruction.

A recent study by Lešić et al. (subm.) investigated the Holocene sedimentation in KHTS based on hydroacoustic data and focused on the spatial and temporal variability of local and regional-scale sediment deposition. While trough system-wide strong reflectors between acoustic units in the sub-bottom profiler data indicated several notable changes in sedimentation over the course of the Holocene, the most important ones related to two main Holocene climate events around 8 and 2.6-2.1 cal ka BP that might be connected to changes in the SHW and the SACCF and represent transitions from warmer to cooler climates (Lešić et al., subm.). The dataset also revealed a relatively complex current regime and implied multiple further local-scale changes throughout the past ~10 ka that might relate to bottom- and/or turbidity currents.

### 7.3. Methods

Three of the four presented gravity cores, GeoB22056-1, GeoB22057-1 and GeoB22058-1, were taken in 2017 from Jacobsen Trough on R/V Meteor cruise M134 (Fig. 2b; Bohrmann et al., 2017). They were recovered with a 12 m-long barrel from approximately 270 m water depth and recovered 722 cm, 879 cm, and 941 cm, respectively. Gravity core PS133/2\_17-13, which is 895 cm-long, was taken in 2022 on R/V Polarstern cruise PS133/2 from a water depth of 344 m in King Haakon Trough, also using a 12 m-long core barrel (Kasten, 2023). Onboard both vessels, all cores were cut into 1 m-long sections, logged for magnetic susceptibility with Multi-Sensor Core Loggers (MSCL) and Bartington 140 mm magnetic susceptibility loop sensors, split and visually described for the identification of lithofacies (von Dobeneck, 2020a,

b, c; Kasten, 2023). The visible carbonatic material close to the surface of both PS133/2\_17-13 split core-halves was also extracted for radiocarbon dating. The cores GeoB22056-1, GeoB22057-1 and GeoB22058-1 were sampled and analysed upon return at the Faculty of Geosciences of the University of Bremen (UoB). Based on sub-bottom profiler data suggesting an unconformity at selected depth intervals, the respective archive halves of the sediment cores GeoB22057-1 (279-579 cm) and GeoB22058-1 (340 – 541 cm) and PS133/2\_17-13 (191-391 cm) were scanned using a Philips Brilliance iCT Elite 256 computer tomograph (CT) at the hospital Klinikum Bremen-Mitte. High-density clasts  $> \sim 1$  mm, open bioturbation traces and pores (air- or water-filled), as well as the matrix sediment were identified. Additionally, the obtained X-ray attenuation of the matrix sediment (measured in Hounsfield Units (HU)) is used as a proxy for dry bulk density (DBD). The whole method is described in detail in the Appendix in C1.1.

Two sample sets were taken from the working halves of all GeoB cores at  $\sim 10$ -cm intervals: 1)  $\sim 8$  ml of sediment (extracted with 1.5-cm syringes), and 2)  $\sim 1$  cm-thick sediment slabs ( $\sim 48.5$  ml) with a depth error of  $\pm 1$  cm. Water content was determined on the syringe samples, which were weighed and then freeze-dried. They were ground and measured for i) density with AWI-based Micromeritics AccuPyc II 1340 gas pycnometers, for ii) total carbon (TC) and (iii) total organic carbon (TOC) measurements, determined with a UoB-based Elementar Vario EL III through combustion and carbon-specific infrared wavelength absorption. TOC percentage results were corrected using a sample-specific factor, which represents the pre-analysis removal of the carbonate fraction. This factor was also used to calculate the carbonate content. Sediment dry bulk density (DBD) was calculated from water content and the measured dry density considering the salt correction (Kuhn, 2013; Wang et al., 2021). Following the leaching method after Müller and Schneider (1993), 15 syringe samples from the GeoB cores were further analysed for biogenic silica ( $bSiO_2$ , Fig. C.1, Table C.3), which is translated into biogenic opal by applying a factor of 100/90, accounting for 10% bound water within biogenic opal. For grainsize analysis, the sediment slabs were dispersed with demineralised water and sieved through 2 mm and 63  $\mu m$  meshes (mud  $< 63 \mu m$ , sand 63  $\mu m$  - 2 mm, and gravel  $> 2$  mm). Note that the samples were not treated prior to remove organic compounds. The weight fraction of grains larger than 2 mm is here defined as ice-rafted debris (IRD). The gravel and sand fractions were dried in a heating cabinet at 50°C, while the fractions  $< 63 \mu m$  were freeze-dried. On selected samples, the mud fraction was further

divided into silt (2 - 63 $\mu$ m) and clay (<2mm), according to the Atterberg method (Müller, 1967). Results from grain size analysis of the fine fraction (FF, defined as grains <63 $\mu$ m) will be presented throughout this manuscript as wt% clay or silt, and include mean values for each unit. Table 7.1 summarises the sedimentary characteristics for the established lithological units, the data itself is provided in the Appendix C (Table C.1-C.3). Note that analyses for physical and chemical properties were only carried out on the GeoB cores, so in the following, the according lithological facies parameters are only representative for sediments from central JT.

Fragments of bryozoans, gastropods and bivalves were picked directly from the cores, while benthic foraminifera were extracted from the sieved sand and gravel fraction. This material was collected at up to ten conspicuous horizons per core, inspected under a microscope for leaching, visible authigenic carbonate overgrowth, and/or brown discoloration and was, if dirty, cleaned with deionised water, before being sent for Accelerator Mass Spectrometry (AMS)  $^{14}$ C dating as CO<sub>2</sub> samples at the MICADAS laboratory at AWI (Mollenhauer et al., 2021). Lab errors range between  $\pm 0.036 - 0.108$  ka. Radiocarbon age calibration was carried out with the IntCal20 calibration curve (Reimer et al., 2020) in PaleoDataView (Langner and Mulitza, 2019), using modelled Marine Reservoir Ages (MRAs) with a temporal resolution of 0.05 ka, that are based on three simulations (Butzin et al., 2019, 2020; Heaton et al., 2020). Their median absolute deviations (MAD) lie within the laboratory error and are therefore neglected. Radiocarbon ages are displayed in Tables 7.2 and 7.3 (see section 7.4 below) and Table C.4. They serve as the basis for age model calculation and the determination of linear sedimentation rates. Age models (scripts in C1.2 adapted from De Vleeschouwer and Zeeden, 2021) were calculated with R (R Core Team, 2021; R Studio Team, 2021) and 'Bchron' after Haslett and Parnell (2008) and provide ages with a 2.5 % Lower Confidence Level and a 97.5 % Upper Confidence Level for significant unit boundaries (Table C.5). The refined ages were used for the calculation of linear sedimentation rates. Note that despite unknown penetration depths, a certain degree of core compression is expected for all cores, as similar inner trough sediments from Drygalski Trough taken during PS119 (Bohrmann, 2019) have shown 16 % core compression on average for gravity coring (Lešić, unpublished data). Calculated sedimentation rates are therefore considered to have a compression-related error, which is not included in the data. All ages discussed in the text and tables are presented as calibrated kiloyears before present (cal ka BP).

## 7.4. Results and Interpretation

### 7.4.1. Depositional units

#### 7.4.1.1. *Lithology*

The four sediment cores from JT and KHT all recovered generally stratified, diatom-bearing silt-dominated dark greenish grey (Munsell soil colour chart: GLEY 1 4/10Y) mud, partly intercalated with more sandy intervals or olive-coloured (5Y 4/3) flocculate layers, which are interpreted as diatom ooze (Figs. 7.3-7.6). The mud has generally low gravel (<2 wt%) and sand contents (0.16-47.41 wt%), which are only elevated in thin intervals (Table 7.1, Table C.1). The magnetic susceptibility in all cores is generally below  $\text{Kappa} \cdot 1000 \times 10^{-6}$  SI units but peaks where sand and gravel contents are elevated (von Dobeneck, 2020a, b, c), while WC exceeds 40 wt% and bSiO<sub>2</sub> values 15 wt% are fairly high throughout the JT cores, with an exception in a sand-rich layer in GeoB22056-1 (Fig. 7.6) that shows exceptionally low magnetic susceptibility (von Dobeneck, 2020a, b, c). The high WC is reflected in relatively low DBD values, which are usually elevated in siltier sections and, especially, in sand-richer layers (Figs. 7.4-7.6). Therefore, DBD appears to work as a grainsize proxy for the sediment matrix. TOC and carbonate are both low throughout all cores but behave opposingly within sand-rich layers, which contain very little TOC but elevated amounts of carbonate (Figs. 7.4-7.6).

The pattern of lithological variations along the core can be correlated with the CT scans (Fig. 7.7, Figs. C.2-C.4). This correlation shows 5-12cm thick layers with elevated sand and gravel (IRD, see section 7.3) content that exhibit elevated dry bulk density (DBD) and magnetic susceptibility above sharp, undulating lower contacts (Fig. 7.7) and partly deformed underlying, less dense, sediments (Fig.7a). Within these layers, the DBD decreases towards the top, which is gradual. These sharp lower contacts, together with changes in linear sedimentation across them, suggest that the mud need to be differentiated into four separate depositional units, Units A-D, and, in turn, make the sandy layers unit boundaries. They generally contain lower bSiO<sub>2</sub> (Fig. C.1) than the rest of the respective core, and contain little TOC (Figs. 7.4-7.6).

The units themselves mostly differ in the abundance of distinct diatom-ooze layers, which, in turn, affect DBD and WC, the grainsize distribution of the fine fraction (FF), the magnetic susceptibility and degree of bioturbation. Thus, the following sections focus on these parameters. Unit-specific value ranges and arithmetic means for all used parameters are

presented in Table 7.1 and the detailed list of lithological data is available in the Appendix (Tables C.1 and C.2).

*Table 7.1: Lithological characteristics of Units A-D (Dtotal) averages and in different sediment cores) with physical properties (WC = water content, DBD = dry-bulk density), total organic carbon (TOC), carbonate, bioturbation, Magnetic susceptibility (MS) and grain sizes. Samples with an error >10wt% in grain size are excluded from the calculation. Negative values for Carbonate are excluded. Note that the MS data for the GeoB cores are published on PANGAEA by von Dobeneck, (2020a, b, c). MS data for PS133/2\_17-13 was submitted to PANGAEA by Pormann and Gebhardt (subm.)*

Unit	A	B	C	Dtotal	D (17-13)	D (58-1)	D (57-1)	D(56-1)
WC (wt%)	Mean=59.1 Min=45.3 Max=70.6	Mean=50.2 Min=45 Max=54	-	Mean=53.3 Min=22.9 Max=69.7	-	-		
DBD (gcm <sup>-3</sup> )	Mean=0.56 Min=0.36 Max=0.84	Mean=0.73 Min=0.65 Max=0.85	-	Mean=0.67 Min=0.38 Max=1.52	-	-		
MS (Kappa* 10 <sup>-6</sup> SI units)	Min=29.5 Max=109.7	Min=60.8 Max=303.3	-	Min=73.9 Max=921.6	Min=73.9 Max=182.6	Min=86.7 Max=403	Min=170.1 Max=547.4	Min=22 5.6 Max=92 1.6
Clay in FF (wt%)	Mean=50 Min=35.8 Max=62.8	Mean=39.3 Min=31.8 Max=47.6	-	Mean=37.85 Min=1.4 Max=48	-	Mean=39.8 Min=30.38 Max=48	Mean=37.42 Min=28.07 Max=44.05	Mean=37.48 Min=1.4 Max=45.93
Silt in FF (wt%)	Mean =50 Min=37.2 Max=64.2	Mean=60.7 Min=52.4 Max=68.2	-	Mean=62.15 Min=52 Max=98.6	-	Mean=60.2 Min=52 Max=69.6 2	Mean=62.57 Min=56 Max=71.93	Mean=6 2.52 Min=54. 07 Max=98. 6
Sand (wt%)	Mean=1.24 Min=0.35 Max=9	Mean=1.8 Min=0.3 Max=6	-	Mean=1.81 Min=0.16 Max=47.41	-	-		
Gravel (wt%)	Mean=0.06 Min=0 Max=1.31	Mean= 0.11 Min =0 Max =1.6	-	Mean=0.04 Min=0 Max=1.42	-	-		
TOC (wt%)	Mean=0.65 Min=0.05 Max=1.02	Mean=0.69 Min=0.45 Max=0.84	-	Mean=0.67 Min=0.06 Max=0.93	-	-		
Carbonate (wt%)	Mean=0.9 Min=0.16 Max=3.5	Mean=0.89 Min=0.09 Max=5.97	-	Mean=0.66 Min=0.01 Max=5.4	-	-		
Open Bioturbation	Minor, mostly horizontal	Moderate, Small vertical and horizontal burros	Minor	Moderate, Longer vertical burrows	-	-		

**Unit A** occurs in two of the cores from KHTS, from 895 to 305 cm in PS133/2\_17\_13 (Fig. 7.3) and from 941 to 412 cm in GeoB22058-1 (Fig. 7.4). The mud is visually homogeneous with a minor degree of, mostly horizontal, open bioturbation. Out of all Units, it has the highest clay content in the fine fraction (FF) with a mean value of 50wt% and a maximum of 62.8wt% (Table 7.1). It also has the highest water content (Fig. 7.4) with 59.1wt% (Table 7.1), the highest bSiO<sub>2</sub> (Fig. C.1) and the lowest magnetic susceptibility (Table 7.1, Fig. 7.4). It contains frequent, intercalated mm to cm-thick diatom-ooze layers (Fig. 7.4). In PS133/2\_17-13 and GeoB22058-1, these layers are cm-spaced and dominate whole sections of Unit A, intercalated with tens of cm-thick clayey-mud layers (Fig. 7.3, 4, C.2, C.4). Salty pore water content (WC) and dry bulk density (DBD) oscillate between low and high values (Fig. 7.4), which mirror the cyclicity of the two intercalated lithologies, diatom-bearing silty mud and diatom ooze. Lower DBD and higher WC are characteristic of the diatom-ooze layers, whereas higher DBD and lower WC are associated with the mud intervals. Carbonate and TOC are generally very low, but also fluctuate more or less synchronously with the diatom-ooze layers (Fig. 7.4). The sand and IRD contents are low but increase in the upper 20 cm of Unit A (Figs. 7.4, C.2).

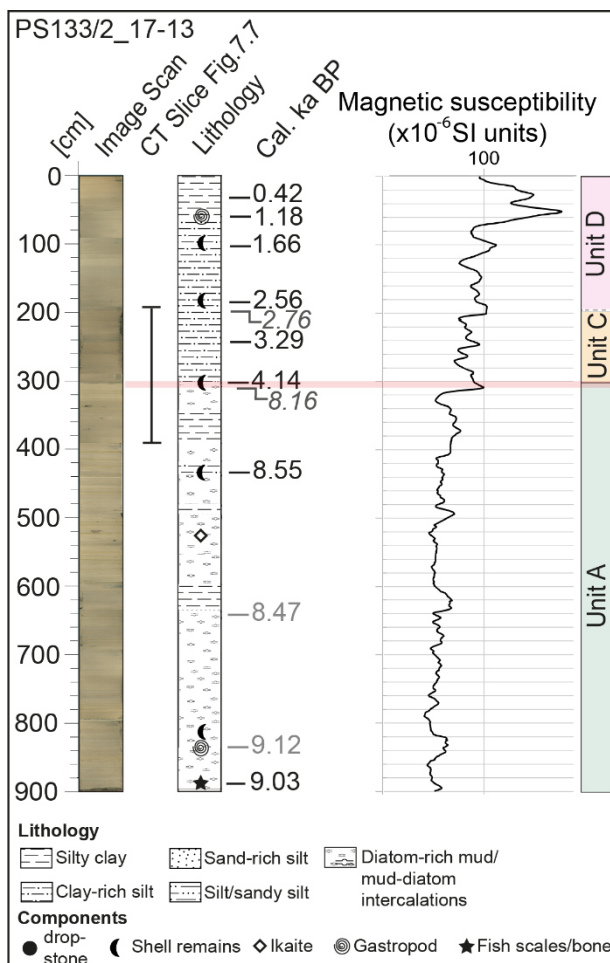


Fig. 7.3: Results of the lithological analyses from gravity core PS133/2\_17-13 with image scans, CT slice interval (length and depth position of CT slice), lithology log, radiocarbon dates, magnetic susceptibility, and facies log. The age model with age anchors and linear sedimentation rates based on calibrated and modelled radiocarbon ages are shown in Fig. 7.8, the latter are presented in greyscale and italic font. The hiatus between Units A and C is indicated in red.

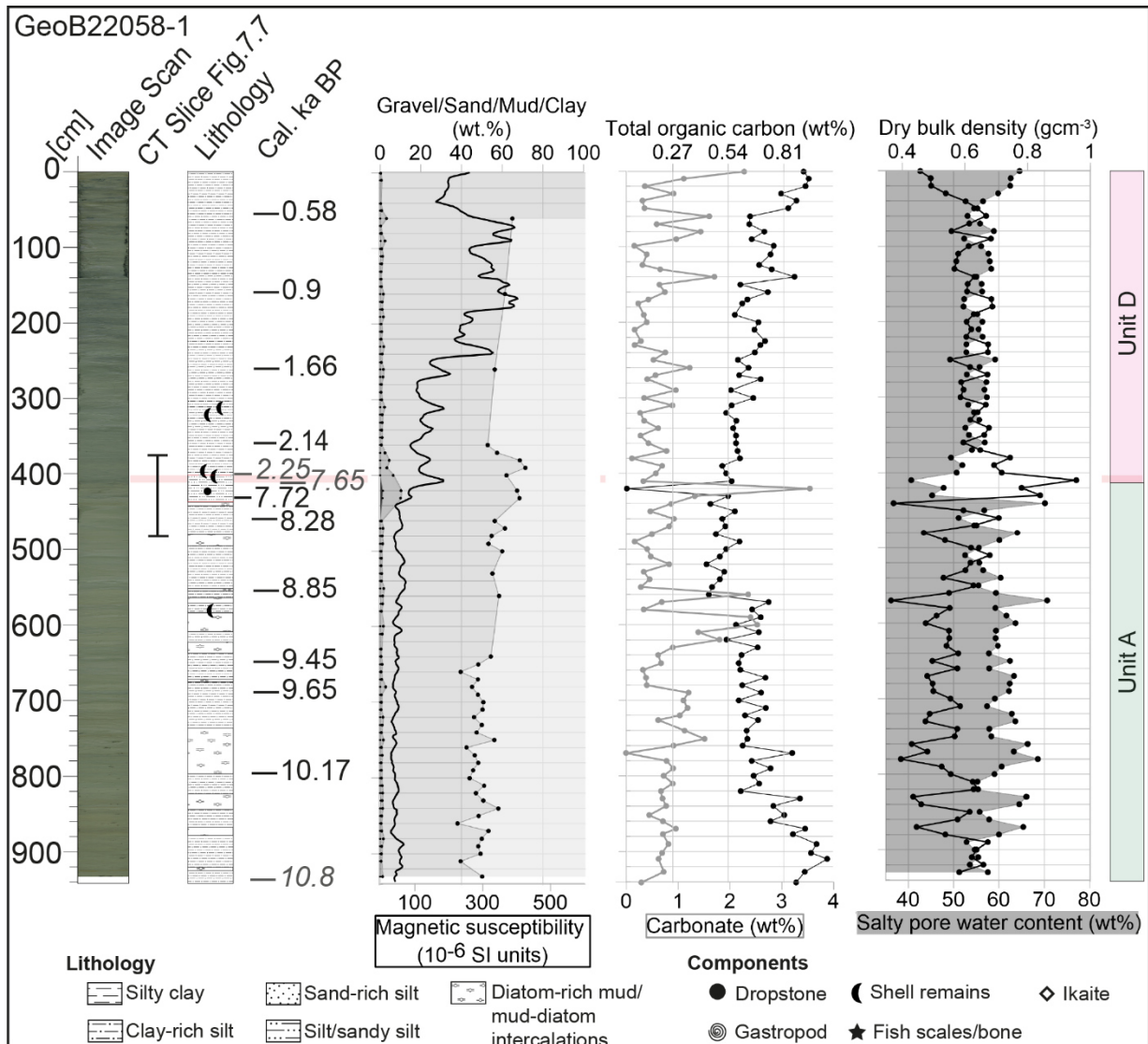


Fig. 7.4: Results of the lithological analyses from gravity core GeoB22058-1, with image scans, CT slice interval, lithology log, calibrated radiocarbon ages, grain size distribution, MS displayed as a curve without points after von Dobeneck (2020c), TOC (gray), carbonate (black line with points), and physical properties. Radiocarbon ages in greyscale italic font are ages inferred from the age model for the upper and lower side of the unit boundary. For the grainsizes, note that mud includes silt and clay and that the plot is cumulative for gravel, sand and mud. This plot is overlain, where available, by the clay content within the Fine Fraction (light grey shading). The hiatus between Units A and D is indicated in red.

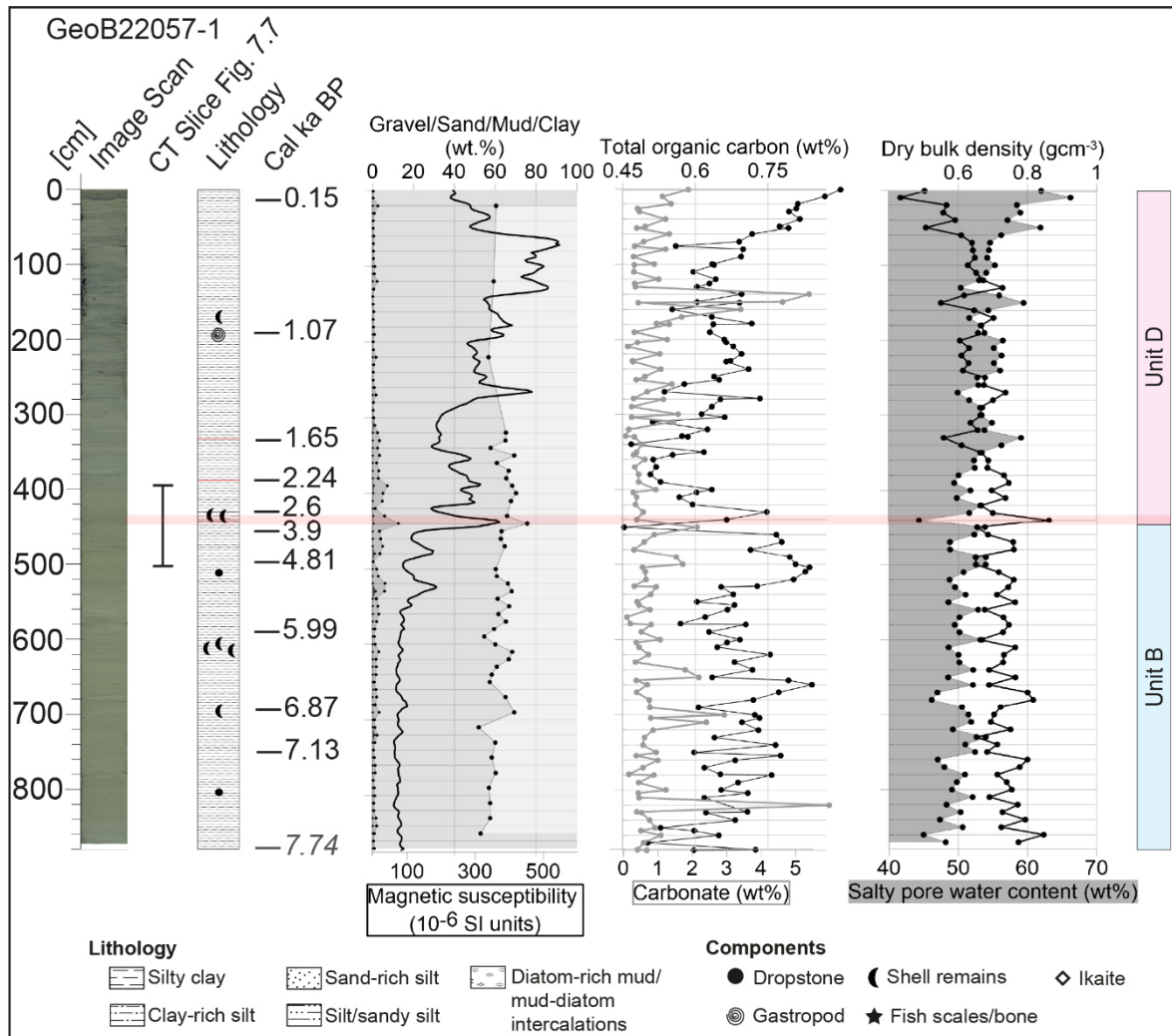


Fig. 7.5: Lithological analyses from gravity core GeoB22057-1, including two lithological units (B and D, coloured blue and red, respectively), calibrated radiocarbon ages, grain size distribution, MS after von Dobeneck (2020b) TOC (gray), carbonate (black) and physical properties. Image scans, lithology log and radiocarbon ages are shown for reference. Ages in greyscale italic font are ages inferred from the age model. The length and depth position of the CT scan slice across the unit boundary is indicated between the image scan and lithology log. For the grainsizes, note that mud includes silt and clay and that the plot is cumulative for gravel, sand and mud. This plot is overlain, where available, by the clay content within the Fine Fraction (light grey shading). The hiatus between Units B and D is indicated in red.

**Unit B** was recovered only by GeoB22057-1 (Fig. 7.5), which contains 434 cm of Unit B, ranging from 879 – 445 cm core depth (Fig. 7.7). Unit B is faintly stratified without distinct diatom-ooze layers and a moderate degree of open bioturbation with small vertical and horizontal burrows (Fig. 7.7) and overall more homogenous WC and DBD values compared to Unit A. In turn, it features, with 60.7wt%, a significantly higher silt content in the FF, which very slightly increases towards the Unit top. It shows slightly higher magnetic susceptibility, but significantly lower WC (50wt%) and slightly higher DBD values (Table 7.1), which correlate with the, compared to Unit A, elevated DBD-proxy in the CT scans.



**Unit C** is only present in PS133/2\_17-13 from KHT at a core depth between 305 and 197 cm (Abb. 3) and is weakly laminated to massive. Crude manual analysis of the grain size during visual logging suggested a silty clay. The DBD, inferred from the CT scan (Fig. 7.7a) is higher than in Unit A and slightly lower than for Unit B. Like Unit B, diatom-ooze layers are absent. The CT scan slice shows bioturbation within the unit with only little open bioturbation but many filled burrows. At the lower boundary, Unit C filled a burrow (Fig. 7.7a). Several fossil remains could be observed in Unit C, as well as occasional lone dropstones (Figs. 7.7; C.4).

**Unit D** was sampled by all four cores in KHTS (central JT = GeoB22058-1, GeoB22057-1, GeoB22056-1; northern KHT = PS133/2\_17-13) and is the uppermost depositional unit in KHTS. In the cores, Unit D is between 197 cm (PS133/2\_17-13) and >722 cm thick, meaning that GeoB22056-1 has presumably not penetrated the lower contact (Figs. 7.3-7.6, 7.9). Unit D has the highest degree of open bioturbation, especially above 340 cm (Fig. C.3), with longer vertical burrows than any other Unit, and black streaks and mottles in the upper 100 – 200 cm core depth (Figs. 7.3-7.6). According to CT data, Unit D is especially affected by bioturbation in GeoB22057-1 above 345 cm, where vertical burrows are more frequent and longer (Fig. C.3). Out of all units, Unit D has the highest magnetic susceptibility, which decreases from GeoB22056-1 to PS133/2\_17-13, i.e. from east to west (Fig. 7.2b), along with the silt content (Figs. 7.4-7.6). Along Unit D in all cores, WC lies between Unit A and B with 53wt% but has a large range due to low values in a thick sand layer in GeoB22056-1 (665 - 654 cm), along with the clay content within the FF that drops to its minimum (Table 7.1, Fig. 7.6), while DBD shows opposing behaviour (Fig. 7.6, Table 7.1). WC, and with it TOC, increases in Unit D towards the core tops, while DBD decreases (Figs. 7.4-7.6). This is in accordance with PS133/2\_17-13, which features a soupy texture in its uppermost 25 cm. Unit D in GeoB22056-1 includes a distinct sand- and silt-rich layer with sharp lower and upper boundary and exceptionally low clay content in the FF (1.4 wt%).

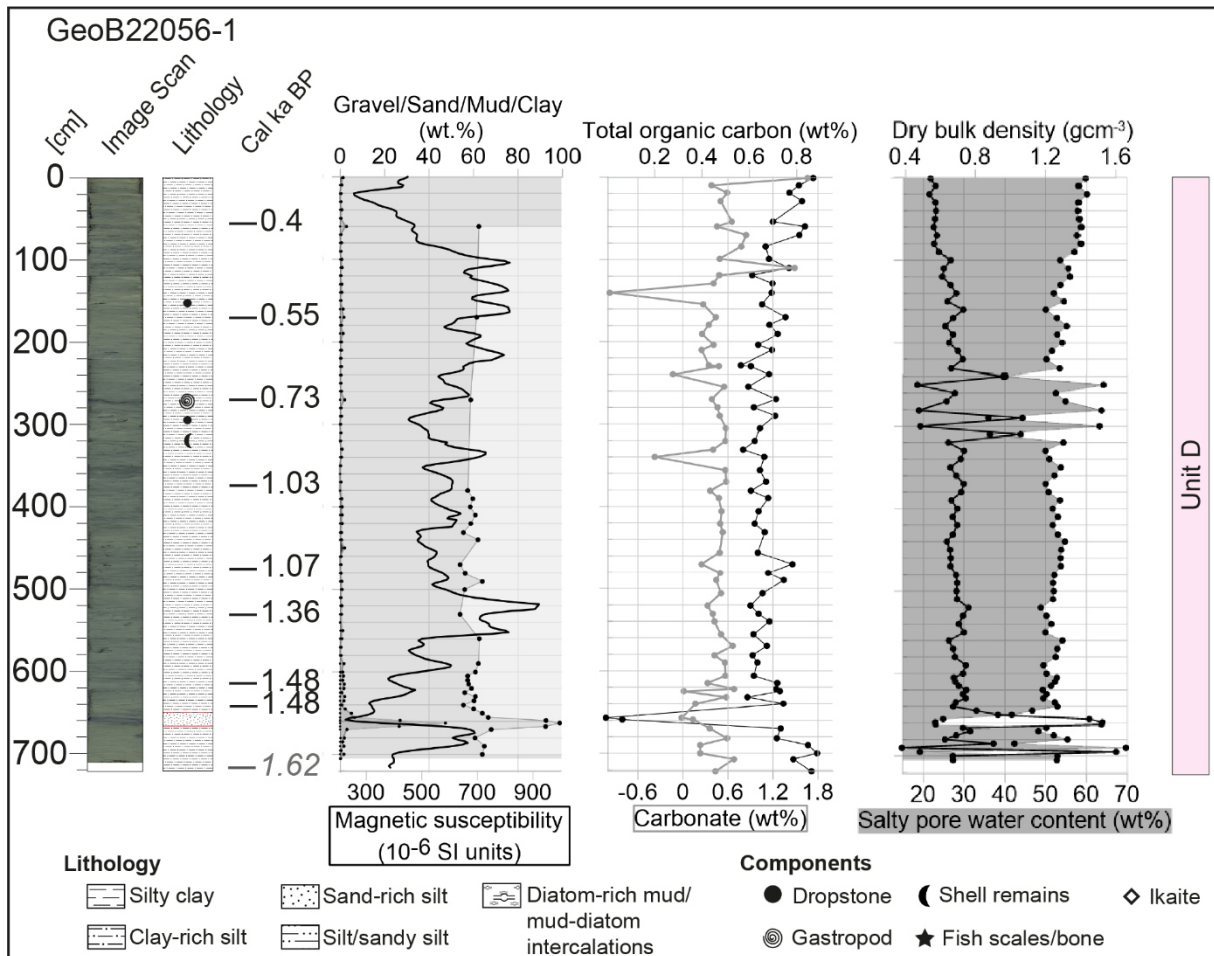


Fig. 7.6: Lithological analyses from gravity core GeoB22056-1, including lithological unit A, coloured red, as well as calibrated radiocarbon ages, grainsize distribution, MS after von Dobeneck (2020a), TOC, carbonate and physical properties. Image scans, lithology log and radiocarbon ages are shown for reference. Ages in greyscale italic font are ages inferred from the age model. For the grainsizes, note that mud includes silt and clay and that the plot is cumulative for gravel, sand and mud. This plot is overlain, where available, by the clay content within the Fine Fraction (light grey shading).

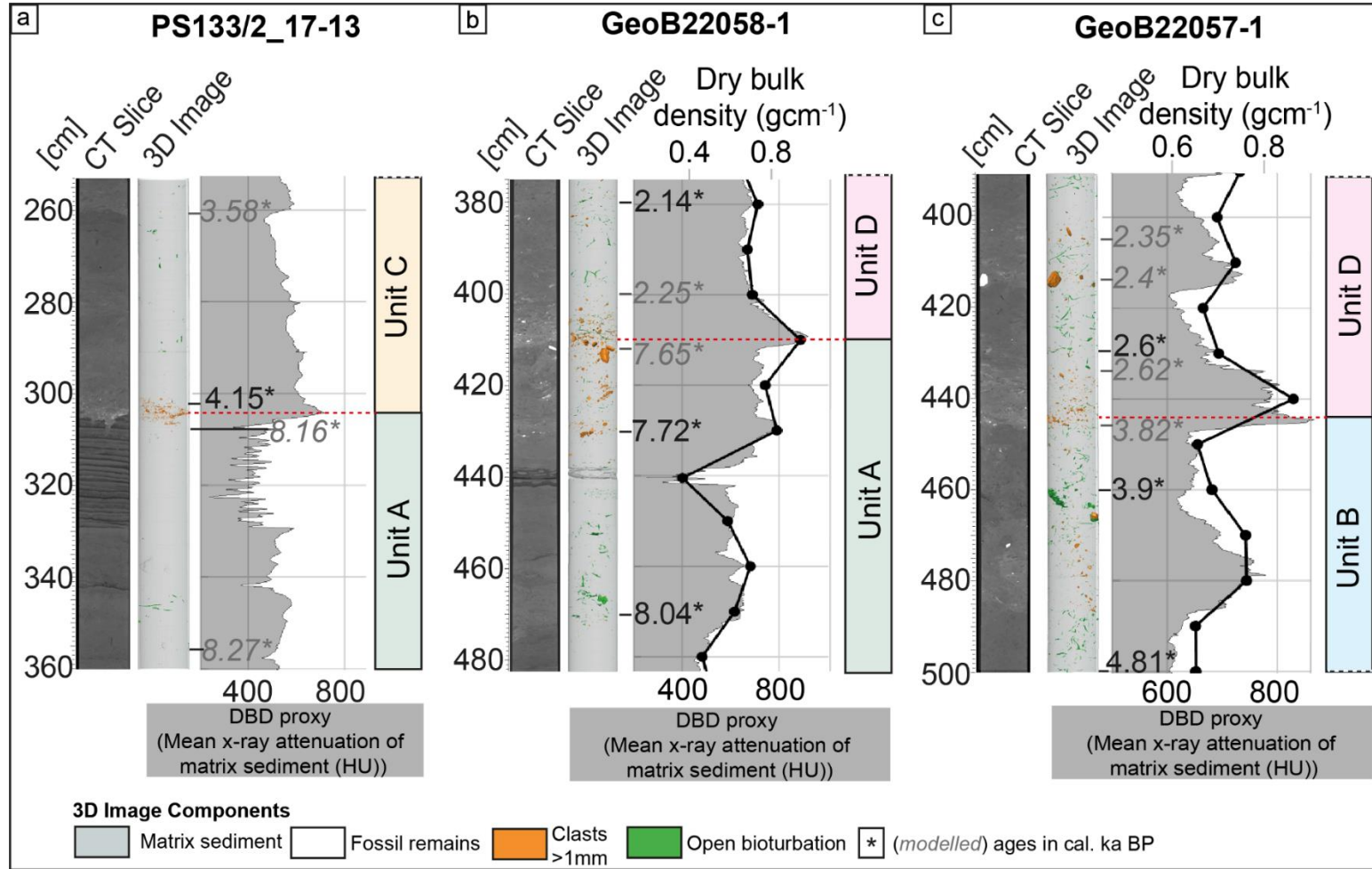


Fig. 7.7 CT scan Slice for the cores PS133/2\_17-13 (KHT), GeoB22058-1 (central JT) and GeoB22057-1 (central JT) in KHTS from west to east, along with their 3 D image interpretation with matrix sediment (grey), embedded fossil remains (white), clasts (orange) and open bioturbation (air or water filled, green). The mean x-ray attenuation of the matrix sediment can be used as a proxy for the WBD and is plotted together with the dry bulk density derived from the core samples (where available). Important calibrated radiocarbon ages are indicated in black, while ages derived from the age models are depicted in greyscale italic font. For overview, the respective lithological units are indicated on the right-hand side of each core. Unit boundaries are indicated by a red dashed line.

7.4.1.2. *Sediment ages*

**Unit A** deposition was placed between >10.8 and 7.65 cal ka BP in GeoB22058-1 and between ~9.03 and 8.16 cal ka BP in PS133/2\_17-13 (Figs. 7.3, 7.4) and, hence, is attributed to the early- to mid-Holocene (Walker et al., 2009). The age models of both cores (Figs. 7.8, 7.9) show a significant decrease of sedimentation rates (Table 7.3) in the uppermost 4 m towards the Unit top and thereby imply decreasing sedimentation towards the mid-Holocene in KHTS, with higher sedimentation rates in KHT (PS133/2\_17-13).

**Unit B** deposition was dated to the period between 7.74 and 3.82 cal ka BP in GeoB22057-1 (Fig. 7.5; Table 7.2), which conforms to the mid- to late Holocene (Walker et al., 2009) and means that Unit B was deposited over a period of ~4 ka. In PS133/2\_17-13 (Fig. 7.3), this time period is associated with a hiatus between >8 and 4.14 cal ka BP, which explains the absence of Unit B in this core. Sedimentation rates in Unit B consecutively decrease from 220 cmka<sup>-1</sup> to 54 cmka<sup>-1</sup> at the unit top (Table. 7.3).

**Unit C** in KHT was deposited between 4.14 and 2.76 cal ka BP, with relatively constant sedimentation rates of around 70-80 cmka<sup>-1</sup> (Fig. 7.3, Fig. 7.8), which means that Unit C was deposited for ~1.4 ka. This time period fits well to the age gap in GeoB22057-1 that is attributed to the depositional time frame for Unit C in JT. The Unit boundary between A and C in PS133/2\_17-13 is also characterised by a fourfold decrease in sedimentation rates from ~320 to 79 cm ka<sup>-1</sup> (Fig. 7.8), which is in accordance with a temporary break in sedimentation due to the non-deposition of Unit B.

**Unit D** deposition started around 2.76 cal ka BP in KHT (PS133/2\_17-13) and between 2.62 (GeoB22057-1) and 2.25 cal ka BP (GeoB22058-1) in central JT (Table 7.2; Figs. 7.8, 7.9). The sand rich layer was dated to >1.48 cal ka BP (Tab. 1; Fig.9) and is therefore significantly younger than the lower Unit D contact, suggesting that GeoB22056-1 did not penetrate the Unit boundary C-D. The sedimentation rates within Unit D decrease from east (JT) to west (KHT) by a factor of ten (Table 7.3, Fig. 7.9).

Table 7.2: Conventional radiocarbon ages and calibrated weighted mean ages (ca.1 ka BP) discussed in the text. \*"Mollusc" refers to gastropod and bivalve (fragments). For a complete overview of calibration and age ranges, see Table C.4 in Annex C

Sample details			Conventional radiocarbon ages		IntCal20 calibration	Lab Code
Gravity core	Depth (cm)	Carbonate source	Age (14C ka BP)	Age error (ka)	Weighted mean (cal. ka BP)	
GeoB22056-1	60	Bryozoa	1.386	±0.059	0.404	AWI 6164.1.1
GeoB22056-1	170	Bryozoa	1.55	±0.064	0.548	AWI 6165.1.1
GeoB22056-1	270	*Mollusc	1.72	±0.06	0.731	AWI 4451.1.1
GeoB22056-1	380	Bryozoa	2.05	±0.059	1.031	AWI 6166.1.1
GeoB22056-1	490	*Mollusc	2.096	±0.063	1.073	AWI 4452.1.1
GeoB22056-1	530	*Mollusc	2.353	±0.062	1.364	AWI 4453.1.1
GeoB22056-1	620	*Mollusc	2.502	±0.06	1.481	AWI 4454.1.1
GeoB22056-1	645	*Mollusc	2.504	±0.06	1.483	AWI 4455.1.1
GeoB22057-1	20	*Mollusc	1.241	±0.061	0.15	AWI 6167.1.1
GeoB22057-1	192	*Mollusc	2.097	±0.062	1.072	AWI 9972.1.1
GeoB22057-1	340	*Mollusc	2.6	±0.066	1.645	AWI 4456.1.1
GeoB22057-1	390	*Mollusc	3.116	±0.066	2.238	AWI 4457.1.1
GeoB22057-1	430	*Mollusc	3.403	±0.066	2.598	AWI 4458.1.1
GeoB22057-1	460	*Mollusc	4.443	±0.067	3.899	AWI 4459.1.1
GeoB22057-1	500	*Mollusc	5.15	±0.069	4.814	AWI 4460.1.1
GeoB22057-1	590	*Mollusc	6.226	±0.108	5.991	AWI 4461.1.1
GeoB22057-1	610	*Mollusc	6.076	±0.074	5.891	AWI 4462.1.1
GeoB22057-1	694	*Mollusc	7.013	±0.078	6.874	AWI 9973.1.1
GeoB22057-1	750	*Mollusc	7.285	±0.079	7.129	AWI 4463.1.1
GeoB22058-1	60	*Mollusc	1.608	±0.06	0.584	AWI 4464.1.1
GeoB22058-1	160	Bryozoa	1.938	±0.074	0.9	AWI 6169.1.1
GeoB22058-1	260	*Mollusc	2.618	±0.065	1.658	AWI 6170.1.1
GeoB22058-1	380	Bryozoa	2.983	±0.062	2.143	AWI 6171.1.1
GeoB22058-1	430	Benthic Foram	7.879	±0.087	7.718	AWI 4465.1.1
GeoB22058-1	470	Benthic Foram	8.516	±0.09	8.276	AWI 4466.1.1
GeoB22058-1	560	*Mollusc	8.95	±0.083	8.849	AWI 4467.1.1
GeoB22058-1	650	Benthic Foram	9.345	±0.09	9.446	AWI 4468.1.1
GeoB22058-1	690	*Mollusc	9.441	±0.09	9.646	AWI 4469.1.1
GeoB22058-1	800	Benthic Foram	9.896	±0.09	10.167	AWI 4470.1.1
PS133/2_17-13	30	*Mollusc	1.423	±0.056	0.422	AWI 10471.1.1
PS133/2_17-13	60.5	*Mollusc	2.222	±0.059	1.182	AWI 10472.1.1
PS133/2_17-13	101	*Mollusc	2.624	±0.059	1.66	AWI 10473.1.1
PS133/2_17-13	183.5	*Mollusc	3.323	±0.062	2.557	AWI 10474.1.1
PS133/2_17-13	236	*Mollusc	3.967	±0.063	3.294	AWI 10475.1.1
PS133/2_17-13	303.5	*Mollusc	4.65	±0.073	4.144	AWI 10476.1.1
PS133/2_17-13	434	Benthic Foram	8.696	±0.084	8.511	AWI 10477.1.1
PS133/2_17-13	636.5	*Mollusc	8.652	±0.082	8.486	AWI 10478.1.1
PS133/2_17-13	834.5	*Mollusc	9.092	±0.085	9.119	AWI 10479.1.2
PS133/2_17-13	885.5	Fish scale	9.038	±0.036	9.028	AWI 10480.1.1

7.4.1.3. *Correlation with acoustic facies*

Correlation of the cores with the acoustic data shows that all depositional Units can be correlated with the respective acoustic Units A-D, and the boundary layers with strong reflectors, which are described in Lešić et al. (subm.).

**Unit A**, sampled by GeoB22058-1 and PS133/2\_17-13, correlates with the upper portions of acoustic Unit (Lešić et al., subm.). The contacts between depositional Unit A and its overlying Unit D at 412 cm in GeoB22058-1 and at 305 cm in PS133/2\_17-13, boundary between A and C, approximately correlate with the transition from acoustic Unit A to its overlying Units in the sub-bottom profiler data (Figs. 7.8, 7.9), respectively. In JT, the acoustic data shows truncated reflectors at the boundary A to D (Fig. 7.8).

**Unit B**, sampled by GeoB22057-1, correlates with acoustic Unit B (Fig. 7.9) (Lešić et al., subm.). The contact between lithological Unit B and its overlying Unit D at 446 cm in GeoB22057-1 approximately correlates with the transition from acoustic Unit B to its overlying acoustic Unit D in the sub-bottom profiler data at the core location (Fig. 7.9) (Lešić et al., subm.). In KHT however, depositional Unit B was not sampled by PS133/2\_17-13, which is in accordance with the acoustic data, featuring a pinch-out of acoustic Unit B from northern and southern directions towards the core location of PS133/2\_17-13 (Fig.8).

**Unit C** was sampled only in KHT, where it correlated with acoustic Unit C. In JT, however, the absence of the depositional Unit C can be explained by the pinch-out of acoustic Unit C towards the west and the core location GeoB22057-1.

**Unit D**, sampled by all cores, can be correlated with acoustic Unit D, which drapes both KHT and JT and represents the upper part of an unconformity (Lešić et al., subm.).

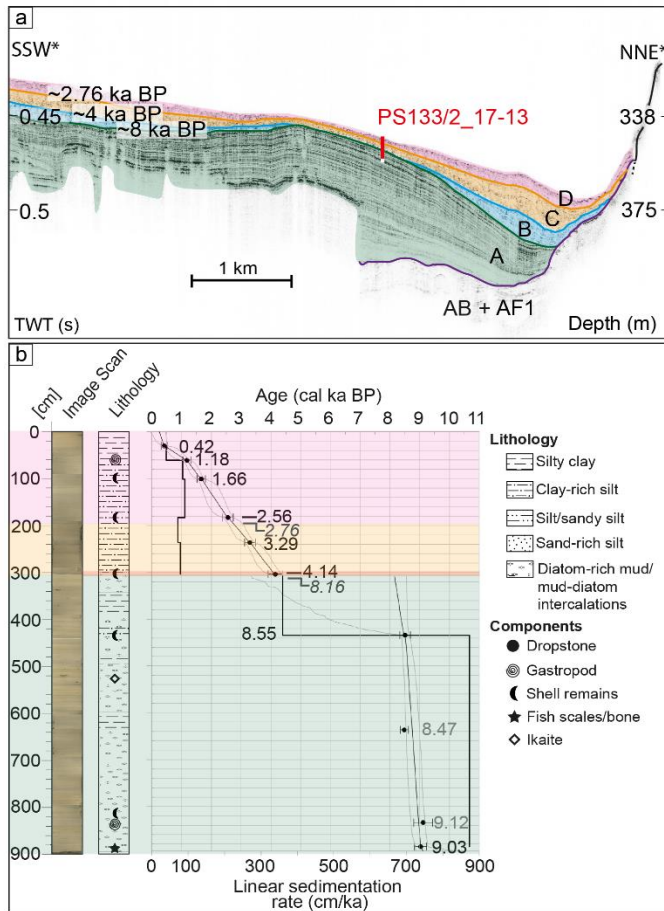


Fig. 7.8 correlation of acoustic data at the core location and the lithological results. a) the core location and length of PS133/2\_17-13 with regard to the acoustic subsurface data along the Profile indicated in Fig. 7.2b. The Units of LF1 are coloured according to acoustic units from AF-1 in Lešić et al. (subm.). Note that the length is indicated in red and potential core compression of 16% in white b) the results of PS133/2\_17-13 coloured in green for Unit A, in yellow for Unit C and in red for Unit D.

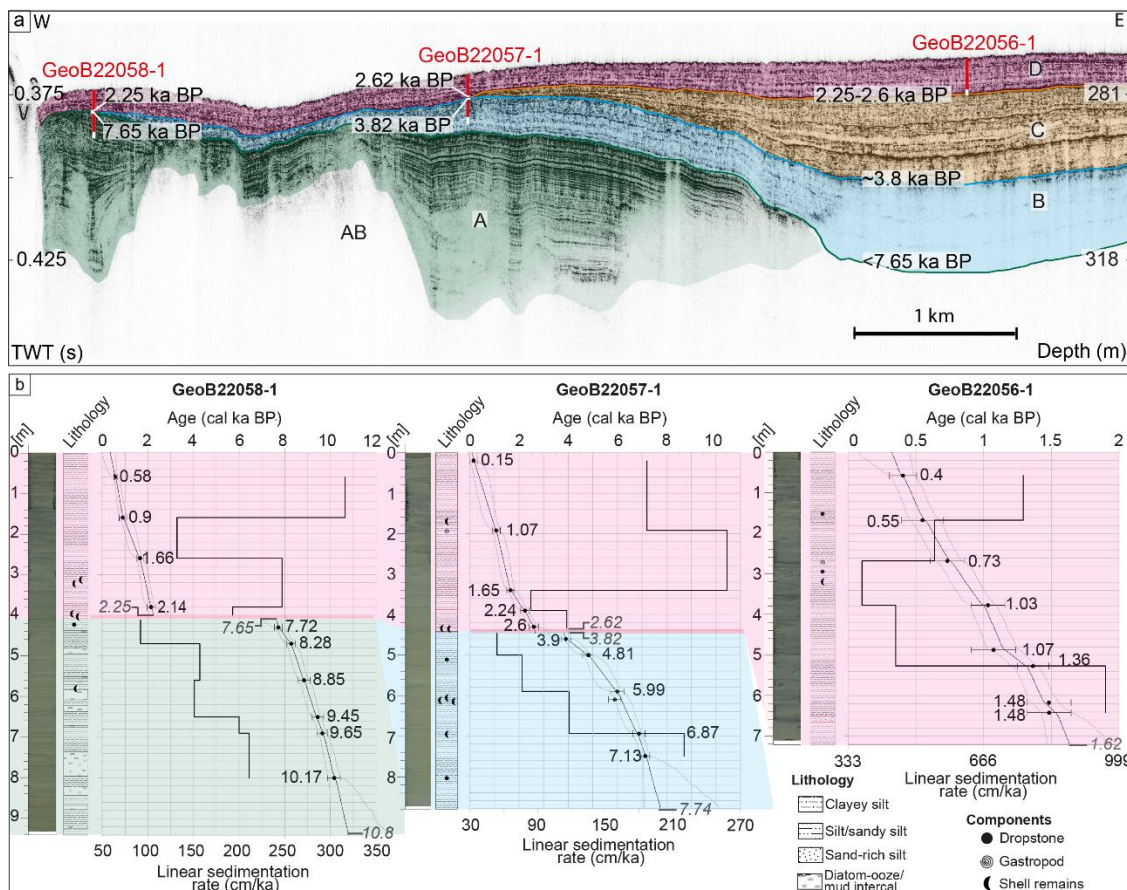


Fig. 7.9: correlation of a) acoustic data from the Profile in JT in Fig. 7.2b with b) the GeoB cores and their age models and linear sedimentation rates

Manuscript IV: Climate-driven Holocene sedimentation in King Haakon Trough System, sub-Antarctic South Georgia

Table 7.3: Linear sedimentation rates of cores GeoB22056-1, GeoB22057-1, GeoB22058-1, PS133/2\_17-13 calculated between dated and modelled lithological boundaries, the latter are indicated\*.

Core	Depth range (cm)	Thickness (cm)	Age range (ka)	Time period (ka)	Sedimentation rate (cm ka <sup>-1</sup> )	Unit
GeoB22056-1	60 – 170	110	0.404 – 0.548	0.144	764	D
GeoB22056-1	170 – 270	100	0.548 – 0.731	0.183	546	D
GeoB22056-1	270 – 380	110	0.731 – 1.031	0.3	367	D
GeoB22056-1	380 – 530	150	1.031 – 1.364	0.333	450	D
GeoB22056-1	530 – 645	115	1.364 – 1.483	0.119	966	D
GeoB22057-1	20 – 192	172	0.15 – 1.131	0.922	187	D
GeoB22057-1	192 – 340	148	1.072 – 1.645	0.573	258	D
GeoB22057-1	340 – 390	50	1.645 – 2.238	0.593	84	D
GeoB22057-1	390 – 434*	44	2.238 – 2.619	0.381	116	D
GeoB22057-1	446* – 500	54	3.815 – 4.814	0.999	54	B
GeoB22057-1	500 – 610	90	4.814 – 5.991	1.177	76	B
GeoB22057-1	610 – 694	104	5.991 – 6.874	0.883	118	B
GeoB22057-1	694 – 750	56	6.874 – 7.129	0.255	220	B
GeoB22058-1	60 – 160	100	0.584 – 0.9	0.316	316	D
GeoB22058-1	160 – 260	100	0.9 – 1.658	0.758	132	D
GeoB22058-1	260 – 380	120	1.658 – 2.143	0.485	247	D
GeoB22058-1	380 – 400*	20	2.143 – 2.247	0.1035	193	D
GeoB22058-1	412* – 470	58	7.645 – 8.276	0.631	92	A
GeoB22058-1	470 – 560	90	8.276 – 8.849	0.573	157	A
GeoB22058-1	560 – 650	90	8.49 – 9.446	0.597	151	A
GeoB22058-1	650 – 690	40	9.446 – 9.646	0.2	200	A
GeoB22058-1	690 – 800	110	9.646 – 10.167	0.521	211	A
PS133/2_17-13	30 – 60.5	30.5	0.422 – 1.182	0.76	40	D
PS133/2_17-13	60.5 – 101	40.5	1.182 – 1.659	0.477	85	D
PS133/2_17-13	101 – 197*	96	1.659 – 2.76*	1.101	87	D
PS133/2_17-13	197* – 236	39	2.76 – 3.294	0.534	73	C
PS133/2_17-13	236 – 303.5	67.5	3.294 – 4.144	0.85	79	C
PS133/2_17-13	308* – 434	126	8.161 – 8.511	0.35	359	A
PS133/2_17-13	434 – 885.5	451.5	8.511 – 9.028	0.517	837	A



#### 7.4.2. Interpretation

Based on the homogeneous nature and the predominantly muddy grain sizes of the diatom-bearing mud with scarce sand and gravel content, we interpret the entirety Unit A-D as marine sediment, deposited from mostly hemipelagic sedimentation in a glacier-distal to marine setting.

The magnetic susceptibility seems characteristic for each Unit, being highest in Unit D and very low in Unit A and B, potentially reflecting slight differences in sediment composition, e.g. the silt content and biogenic components. However, Units A and B could have been subjected to iron mineral reduction. This is a diagenetic process and can be caused by e.g. anaerobic oxidation of methane and/or oxidation of organic sediment compounds by bacteria, resulting in low magnetic susceptibility compared to the iron content in affected sediment (cf. Funk et al., 2004; Riedinger et al., 2005; Bohrmann et al., 2017; Kars et al., 2018). A strong variability of iron/magnetic susceptibility ratios along the cores, decreasing strongly across the Unit boundaries A-D and B-D in JT (Lešić, unpublished data), indicate that Unit A and B might indeed be affected (cf. Funk et al., 2004). Obliteration of the acoustic signal by gas was proposed for the correlated acoustic units, especially Unit A, in Lešić et al. (subm.), and could explain the reduction. Thus, magnetic susceptibility is excluded from further interpretations that concern differences between the Unit specific depositional conditions with respect to climate variability. Note that in Unit C and D, which do not seem to be affected internal, magnetic susceptibility fluctuations could still be a lithological signal.

Unit A's high clay content and the frequent diatom-ooze layers within, along-side high  $bSiO_2$  values, suggest that Unit A was likely deposited in a bio-productive and relatively calm environment that did not only foster high primary productivity, especially in the form of phytoplankton blooms, but also enabled the deposition of these well-defined layers (Fig. 7.7a,b). The cyclic occurrence of the diatom-ooze layers in both GeoB22058-1 and PS133/2\_17-13 is reminiscent of varves (Schimmelmann et al., 2016) and could be related to oscillations between periods with a high concentration of nutrients in and stronger stratification of the water column due to meltwater input and periods where the shelf waters were depleted or well mixed (cf. Leventer et al., 2006). This could be seasonal variations, e.g. in shelf currents (Combes et al., 2023), transporting nutrient-rich waters to the core sites, in wind strength, in (meltwater-) runoff from South Georgia (river, glaciers) or seasonal sea-ice

acting as fertilisers before 8.16/7.65 cal ka BP (cf. Arrigo et al., 2017; Matano et al., 2020). The excellent preservation might be connected to high sedimentation rates in Unit A, especially in KHT ( $873 \text{ cmka}^{-1}$ ), that inhibited most bioturbation (see e.g. Ó Cofaigh and Dowdeswell, 2001). Decreasing TOC values and sedimentation rates, as well as less frequent sections with high abundance of diatom-ooze layers towards the Unit top and the increase in sand and IRD, suggest changing environmental conditions in KHTS towards the mid-Holocene.

The lack of diatom-ooze layers in Unit B could be either attributed to the absence of large seasonal diatom blooms after  $\sim 7.7$  cal. ka BP or depositional conditions that did not allow them to deposit, e.g. lower sedimentation rates. Still, fairly high bSiO<sub>2</sub> values and sedimentation rates suggest that diatoms were indeed incorporated within the sediment, albeit not as distinct diatom-ooze layers, suggesting that the blooms were either absent or ooze-layers not preserved due to bioturbation. Decreasing sedimentation rates and the very slight increase in silt towards the Unit top indicate that depositional conditions changed successively, either due to decreasing sediment supply or increasing current strength, and might have enabled enhanced bioturbation. However, albeit the higher silt content throughout Unit B, in comparison with Unit A (Table 7.1), the silt and sand content do not increase significantly towards the Unit top, suggesting that the sediment supply to the core location dominated this change. Still, central KHT and central JT likely hosted dynamic depositional environments, which is further supported by the non-deposition of Unit B at the core location of PS133/2\_17-13 (Fig. 7.3, 7.8).

The higher DBD in Unit C, compared to Unit A, indicates a higher content of coarser grainsizes in Unit C, assuming DBD works as a proxy for grainsize distribution (see section 7.4). The absence of diatom-ooze layers and the spatial variability of deposition, including the non-deposition at and west of GeoB22057-1 (Fig. 7.9), indicate that the environmental and depositional conditions might have been more comparable to Unit B than Unit A and remained dynamic until 2.76-2.1 cal ka BP, in KHT and JT respectively (Lešić et al., *subm.*). The almost massive internal structure, as well as the more frequent occurrence of fragmented fossil remains, rather than whole shells, could indicate periodic influence of sediment reworking, potentially related to bioturbation or turbidites.

In Unit D, the general absence of distinct diatom-rich layers suggests that large seasonal-diatom blooms were absent, although the relatively high bSiO<sub>2</sub> content shows that the

background deposition of diatoms was fairly constant throughout the Holocene. High WC and low DBD in between 200-400 cm in GeoB22056-1 might also stem from elevated diatom-content, supporting background primary production or smaller blooms.

While Unit D is quite uniformly present at all core locations, suggesting that environmental conditions might have been less dynamic towards the end of the Holocene than during mid-Holocene, local differences in sedimentation occurred in central JT, e.g. leading to the deposition of a sand- and silt-rich layer before 1.48 cal ka BP (665 - 654 cm; GeoB22056-1). The exceptionally low clay content in this layer indicates that either the current strength must have been really high, keeping the clay fraction in suspension, or that this is a proximal deposit of some kind of gravity flow coming from the trough flanks (cf. Anderson et al., 1984 and references therein; Streuff et al., 2017a). However, the sharp upper boundary does not support an e.g. turbiditic origin (Bouma, 1962). Further, the east-west decrease in silt and magnetic susceptibility might indicate a transport direction of the meltwater-derived sediment to the west, with coarser particles being deposited closer to their source and higher clay content in more distal locations (Dowdeswell et al., 2015). This is supported by the decreasing sedimentation rates from east to west that suggest an increasing distance from the source.

The undulating bases of all boundary layers (Fig. 7.7a-c), together with the abrupt increase in DBD and clasts >1mm (Fig. 7.4-7), and the deformation of diatom-ooze layers at the unit boundary of A to C in PS133/2\_17-13, indicate erosional contacts. This is supported by the correlated strong reflectors throughout KHTS and top-eroded acoustic layers (Lešić et al., *subm.*). While correlation with acoustic data indicates that this erosion was minimal at the core locations PS133/2\_17-13 and GeoB22057-1, and jumps in their respective age models can be associated with non-deposition, cut-off reflectors at the core location GeoB22058-1 rather suggests a larger degree of erosion, which was even resolved by the sub-bottom profiler (Lešić et al., *subm.*). The gradual decrease of DBD (Fig. 7.7) in the sediment above the erosional surfaces in the CT scans, alongside the decrease in sand, evident from the grainsize analysis, imply a gradual change in the grainsize distribution of the matrix sediment towards smaller grain sizes and indicate a fining-upward pattern.

## 7.5. Discussion

### 7.5.1. Timing of Holocene changes in KHTS and their temporal relation to regional climate records

Radiocarbon dating at lithological boundaries and subsequent age modelling along the cores in KHTS have shown that, based on changes in lithology, environmental conditions changed sustainably for periods of several ka on multiple occasions during the Holocene. Despite the dynamic depositional conditions in KHTS during the Holocene (Lešić et al., *subm.*), indicated by the uneven distribution of sediment in the trough basins that lead to hiatuses, the radiocarbon ages at the unit boundaries show that switches in sedimentation, leading to the deposition of the boundary layers and subsequently different units, occurred relatively simultaneously throughout KHTS. Consequently, Unit A is the oldest sampled lithological unit and was deposited before 8.16 and 7.67 cal ka BP in central KHT and central JT, respectively, while the overlying Unit B was deposited subsequently until ~4.1 and 3.8 cal ka BP in central KHT and central JT, respectively. Unit C was subsequently deposited until 2.76 – 2.25 cal ka BP. Thus, the onset of Unit D deposition was dated to ~2.76-2.25 cal ka BP. The calibrated and modelled ages for the unit boundaries show only a slight offset between the troughs, e.g. the variable onset of Unit D deposition throughout KHTS between 2.76-2.25 cal ka BP. The small offset of ~0.5 ka between Unit D onsets, and the even smaller offset for Unit C (~0.3 ka), shows that our age control is good, as they are only marginally larger or even smaller than the uncertainty for each calibrated radiocarbon date (Table C.4) and could therefore be an effect of sampling and availability of datable components, radiocarbon dating and calibrating itself instead of difference in timing between the troughs. This artefact could be caused by e.g. the influence of terrestrial material and freshwater, consequential difficulties in estimating the marine reservoir effect for SG (Butzin et al., 2019; Berg et al., 2020; Butzin et al., 2020; Heaton et al., 2020) and/or methane seepage and potential authigenic carbonate overgrowth on the individual biogenic carbonate particles, which is difficult to identify under the microscope and can lead to systematically older ages, causing jumps in age models (Wollenburg et al., 2023). In our record, however, the few reverse ages lie within sections of high sedimentation rates and within the analytical error (Figs. 7.8, 7.9, Table 7.1) and all larger jumps in our temporal records correlate with abrupt changes in lithology, non-deposition or indicators for some degree of erosion. Thus, we consider the age models to be reliable.

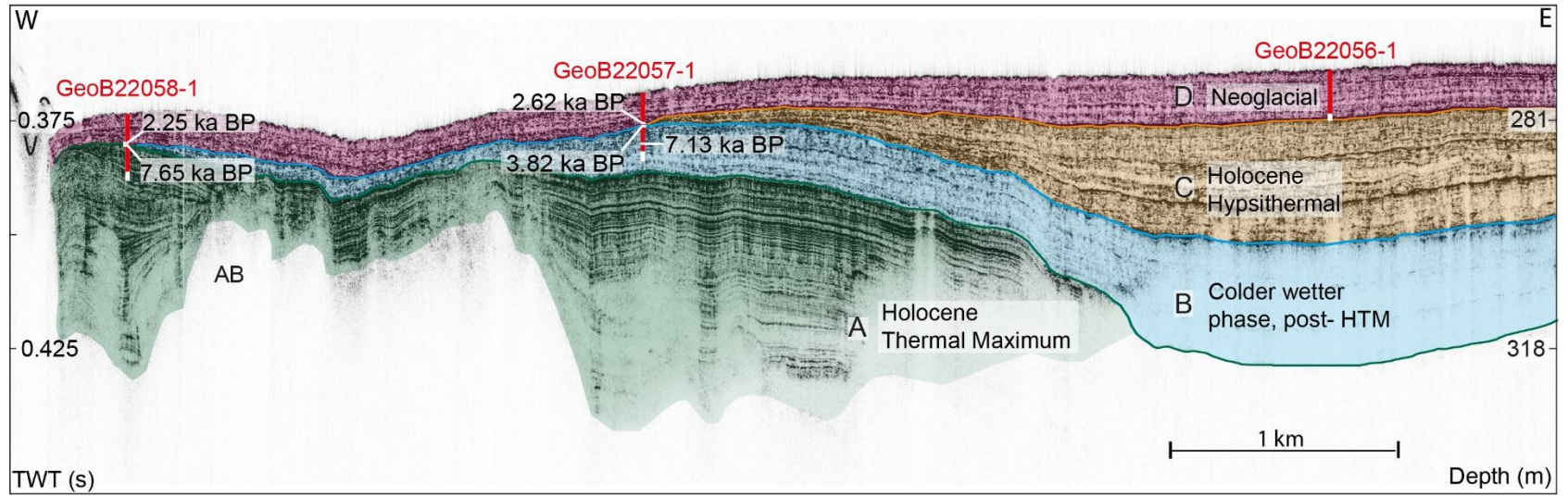


Fig. 7.10: Correlation of lithological units A-D (A=green, B = blue, C= yellow, D= pink), inferred from the cores and their ages, with the acoustic units (Lešić et al., subm.), including the ages above and below their respective unit boundaries. According to the time periods of Unit A-D, Holocene climate phases are correlated: A to the Holocene Thermal Maximum, B to the subsequent colder and wetter post-HTM phase, C to the Holocene Hypsithermal and D to the subsequent Neoglacial.

Despite the solid age models, the top Unit A in JT and KHT, and hence the base of Unit B, is difficult to determine, considering that Unit A in JT is affected by erosion, which was extensive enough to have been resolved by acoustic data (Fig. 7.9) (Lešić et al., *subm.*) and the unit boundary between Unit A and B has not been sampled. The modelled radiocarbon age of 7.67 cal ka BP in GeoB22058-1 lies directly below the erosional contact to Unit D and thus only provides the information that the erosional process started sometime after 7.67 cal ka BP. However, the oldest radiocarbon age in Unit B of 7.13 cal ka BP (GeoB22057-1) narrows down the timing for the Unit boundary between Unit A and B in JT, which can be observed in the sub-bottom profiler data (Fig. 7.9) (Lešić et al., *subm.*), to between 7.65 and 7.13 cal ka BP. In central KHT, it is even more difficult to determine the end of Unit A deposition. Although the sub-bottom profile did not resolve erosion at its top (Fig. 7.8) (Lešić et al., *subm.*), Unit B was not deposited at the core site and the top age of Unit A was extrapolated over 130 cm towards the unit top, which leads to higher uncertainty for the age 8.16 cal ka BP than all other ages in this study (Fig. 7.8a, Table C.5). Hence, the top of Unit A in PS133/2\_17-13 could also be younger than the modelled age of 8.16 cal ka BP, indicating that the offset between central KHT and central JT, regarding the top of Unit A, might be an artefact of calibration and modelling as well, and does not necessarily mean that the timing in both troughs was different. However, given the large trough system and the nature of sedimentary systems, which can prograde and retrograde, a small difference in timing would not be surprising and also cannot be excluded on the basis of our data (*cf.* Lešić et al., *subm.*).

Following this, the depositional Units A to D, along with their transitions, have been deposited not only quite synchronously within KHTS, but also to the four major Holocene climate phases around South Georgia and the Antarctic Peninsula (Fig. 7.10), which are i) the warm Holocene Thermal Maximum (HTM) that ended around  $7.2 \pm 0.4$  cal ka BP on SG island, considerably later than on the Antarctic Peninsula (Rosqvist et al., 1999; Rosqvist and Schuber, 2003; Bentley et al., 2009; Oppedal et al., 2018; Zwier et al., 2021), that correlates with Unit A, ii) the subsequent colder and wetter phase, which correlates with the overlying Unit B, or the corresponding hiatuses in GeoB22058-1 and PS133/2\_17-13, iii) the warmer and dryer Holocene Hypsithermal that started around  $4 \pm 0.4$  cal ka BP (Rosqvist and Schuber, 2003; Foster et al., 2016; Oppedal et al., 2018; Xia et al., 2020) and corresponds to Unit C, or its corresponding hiatuses in GeoB220581 and GeoB22057-1 and iv) the Neoglacial, which started around  $2 \pm 0.7$  cal ka BP and is synchronous with Unit D (Clapperton et al., 1989a;

Clapperton et al., 1989b; Strother et al., 2015; Foster et al., 2016; Oppedal et al., 2018; Zwier et al., 2021; van der Bilt et al., 2022; Heredia Barión et al., 2023a).

## 7.5.2. Holocene climate reflected in the lithologies of the marine realm in KHTS – central JT

### 7.5.2.1. *Depositional Units*

The distal glacial-marine to hemipelagic sediments from KHTS, deposited since at least 10.8 cal ka BP (Table C.5), support the previous reconstructions that ice-free conditions prevailed on the shelf during the Holocene (Clapperton et al., 1989b; Bentley et al., 2007; Hodgson et al., 2014a; Graham et al., 2017; Lešić et al., 2022) and are therefore in accordance with Holocene shelf records from Royal Bay Trough (CG666 in RBT; Fig. 7.2a; Graham et al., 2017) and Drygalski Trough (PS119\_5-1 in DT; Fig. 7.2a; Lešić et al., 2022) that show open-marine conditions for the continental shelf for the entire Holocene. To our knowledge, however, our record from KHTS, albeit affected by hiatuses, features the highest temporal resolution for Holocene depositional variability on the entire continental shelf so far. Indeed, detailed information on the timing of Holocene depositional changes lack from other marine records on the continental shelf, although variable sand content in the upper 200 cm of both GC666 and PS119\_5-1 suggest that the Holocene depositional system might have changed repeatedly at the core locations in both RBT and DT (Fig. 7.2a). Scarce radiocarbon dates and low sedimentation rates within the Holocene succession of GC666 and PS119\_5-1, respectively, likely to their more distal position on the mid- and outer shelf, hinder precise age estimations of the sandy intervals within, although a rough assignment to the Holocene (for GC666, see Table C.5) is possible (Lešić et al., 2022). In DT, the sand layers were tentatively connected with a temporally variable current regime, which is in accordance with interpretations made for KHTS based on sub-bottom profiles (Lešić et al., *subm.*). Based on the higher temporal resolution of our lithological record in KHTS, a more in-depth interpretation of depositional conditions and their relation to Holocene climate is possible.

Despite the generally homogeneous character of the Holocene KHTS sediments, the slight decrease of silt within the FF of Unit D from east to west indicates slight spatial differences in deposition (Table 7.1). This could be caused by different current regimes at the core locations, keeping more clay in suspension in the east. However, it could also be a sediment source effect, depositing more clay, which stays in suspension longer, further away from the source

than the silt, in turn, enhancing silt content closer to the sediment source. Indeed, this would be in accordance with the geometry of JT, which is fed from the east (Fig. 7.2) (Lešić et al., *subm.*).

Still, these spatial differences in lithology within JT are rather minor and considerably smaller than the difference between the sampled Units A, B and D. Therefore, we consider differences in lithology between all Units within JT to rather reflect temporal changes in the depositional environment than only spatial variability, even if not all units were sampled by each core (Table 7.1, Figs. 7.8, 7.9).

### ***Holocene Thermal Maximum (Unit A)***

Generally, the diatom-rich sediment with distinct diatom-ooze layers in Unit A fits the characteristics for warm and dry conditions during the HTM, which might trigger, *inter alia*, accelerated melting of glacial ice in the fjords and onshore, leading to enhanced sediment-laden meltwater input into the shelf waters and fertilising them (*cf.* Matano et al., 2020). Indeed, the HTM on SG island is connected to glacier retreat in both cirque and tidewater glaciers (Bakke et al., 2021), implying enhanced meltwater input into the fjords. Also, the high clay content in Unit A, indicative of relatively low energetic depositional conditions, fits into the warm and calmer HTM climate that coincided with a minimum of the SHW (Moreno et al., 2018) and relatively evenly distributed sediments in KHTS (Lešić et al., *submitted*). Albeit occurring in Unit A in GeoB22058-1, there is no significant IRD content recorded for Unit A in neither the samples nor the CT scans that could indicate frequent iceberg melting/rafting, especially in PS133/2\_17-13, where IRD within Unit A seems absent. However, the high sedimentation rates in Unit A, another indicator for increased terrigenous and/or biogenic sediment input into the trough, might have diluted such iceberg rafting signals. This dilution effect for Unit A is supported by the increase of IRD towards the unit top in GeoB2058-1 (Fig. 7.7), which correlates with a sudden drop in sedimentation rates around 8.28 cal ka BP, indicating that IRD content and sedimentation rates are connected in KHTS. Still, enhanced IRD content towards the unit top might still represent stronger iceberg activity towards the end of this warmer period during the Holocene. Along with decreasing sedimentation rates towards the unit top, the increasing sand content, as well as less frequent occurrence of diatom-ooze layers, suggest a gradual change of the environmental and depositional conditions towards stronger currents and potentially less fertilisation in KHTS after 8.28 cal ka



BP before an abrupt change after 7.67 cal ka BP, leading to erosion and the deposition of a different unit with different properties.

The interbedding with diatom-ooze is analogous to Royal Bay Trough (Graham et al., 2017), where a similar lithology was linked to the meltwater input from an ice margin during deglaciation after the Local Last Glacial Maximum (LLGM; Clark et al., 2009) and deposited until after ~13 cal ka BP (recalibrated after Graham et al., 2017; Table C.4), associated with the Antarctic Cold Reversal (ACR; 14.5 - 12.8 ka BP; Jouzel et al., 1995; Zech et al., 2007; Moreno et al., 2009; García et al., 2012; Jomelli et al., 2014; Stansell et al., 2015; Pedro et al., 2016; Graham et al., 2017; Stewart et al., 2021; Reynhout et al., 2022). Thus, there seems to be a temporal offset between the north-eastern shelf and the south-western shelf, which has already been suggested due to the precipitation and temperature gradients across the mountain ranges (Gordon et al., 2008; Cook et al., 2010) and faster retreat rates for the north-eastern side (Cook et al., 2010). Consequently, the ice margin close to RBT might have already retreated faster towards the coast after the ACR than in KHTS. However, this offset comprises ~5 ka and seems rather large to be solely attributed to an orographically provoked precipitation and temperature gradient across the island. Indeed, this change in sedimentation is associated with truncated reflectors at the unit boundary in both RBT and KHTS (Graham et al., 2017; Lešić et al., submitted), associated with (bottom-)currents. Thus, the complex configuration of oceanographic fronts around SG (Fig. 7.1a), especially the SACCF, might have influenced the water masses on the north-eastern and south-western shelf differently during the Holocene. In fact, it not only directly borders the continental shelf of SG, but intrudes it locally, e.g. at KHTS (Fig. 7.1b), (Matano et al., 2020; Combes et al., 2023), and likely meridionally shifted during the post LGM-deglaciation and the subsequent Holocene interglacial (cf. Verleye and Louwye, 2010; Ai et al., 2023), possibly altering the current configuration on the shelf several times throughout the Holocene (Lešić et al., subm.). This could explain why the highly bio-productive environment with frequent diatom-blooms was already replaced by a less productive environment around 13 cal ka BP in RBT, while conditions stayed favourable for diatom blooms and their deposition until the mid-Holocene between – 8 and 7 cal ka BP.

This timing of its HTM makes SG, and with it KHTS, reminiscent of the HTM timing in Patagonia, which was associated with a dry climate in southern-most Patagonia due to a long-term

poleward contraction of the SHW until 7.05 cal ka BP (McCulloch et al., 2020). In contrast, the HTM on the Antarctic Peninsula ceased already around 9.5 cal ka BP (Bentley et al., 2009). This seems odd, given the fact that SG likely hosted an extensive ice cap during its LLGM, rather indicating a comparability with the Antarctic Peninsula and West Antarctica than Patagonia, where the most extensive ice extent occurred during earlier Quaternary glaciations (Graham et al., 2008; Barlow et al., 2016; Graham et al., 2017; Lešić et al., 2022). However, southernmost Patagonia and SG both lie at the same latitudes and within the modern core belt of the SHW, while the Antarctic Peninsula and West Antarctica lie considerably more south (Fig. 7.1a) and would experience stronger winds during a poleward contraction of the Westerlies (cf. Lee et al., 2019; Fogt and Marshall, 2020). Therefore, and given the fact that Holocene climate in Patagonia and the SG area seems to be largely connected to variability of the SHW (Gilli et al., 2005; Strother et al., 2015; Moreno et al., 2018; McCulloch et al., 2020; Zwier et al., 2021; van der Bilt et al., 2022), it makes sense that the timing climatic changes in these regions correlates.

#### ***Post-HTM, colder and windier climate (Unit B)***

The post-HTM phase during the mid-Holocene is connected with colder, wetter climate and stronger winds around SG (Berg et al., 2019; Zwier et al., 2021) and in southernmost Patagonia (Gilli et al., 2005; Moreno et al., 2018; McCulloch et al., 2020), as well as repeated cirque glacier advances (Oppedal et al., 2018; Berg et al., 2019; Bakke et al., 2021). In our record, absent large diatom blooms fit to windier conditions, which would have, at least on the luv side of SG, increased the mixing of the water column, thus possibly inhibiting large blooms (cf. Leventer et al., 2006). However, the absence of diatom-ooze layers throughout Unit B could also be caused by bioturbation, which is stronger in Unit B than Unit A and might have homogenised the sediment. Still, this would imply that potential diatom ooze-layers were subsequently mixes into the surrounding sediment and should enhance the bSiO<sub>2</sub> content of it. However, this is not observed in our bSiO<sub>2</sub> records (Fig. C.1), that show lower bSiO<sub>2</sub> content in the Units B-D compared to Unit A, where the samples were taken from the muddy intervals. Also, complete homogenisation of the Units B-D might cause reverse ages along our record, which are not observed. This, in turn, rather suggests that primary production was indeed lower during the post-HTM period.

In RBT (Fig. 7.2a), a similar lithology with high diatom content but absent diatom-ooze layers overlies a unit with diatomaceous ooze-rich layers, indicating a similar, albeit older, switch from a highly productive to a less productive hemipelagic shelf environment, that was connected to decreasing glacier influence (Graham et al., 2017). For the shift in productivity across the A-B unit boundary after 7.65 cal ka BP in KHTS, this could mean decreased meltwater input into the JT and seems to align with terrestrial records that report glacier re-advances and a lowering of the equilibrium line altitude that are likely connected to a mid-Holocene cooling subsequent to the HTM (e.g. White et al., 2017; Oppedal et al., 2018; Berg et al., 2019), indicating that the sediments in KHTS archived this climatic change.

The increase in silt content in Unit B compared to Unit A by 10wt% suggests that the dynamics within the water column were different than during the HTM, either featuring more locally focused or generally enhanced currents within JT. Indeed, a changing current regime across the unit boundary A to B was also suggested by Lešić et al. (submitted).

#### ***Holocene Hypsithermal (Unit C)***

Unit C within central JT and KHT, based on the respective hiatuses in GeoB22057-1 and GeoB22058-1 and the correlation with acoustic data (Fig. 7.8), indicates a dynamic depositional environment, although deposited during the warmer Holocene Hypsithermal (e.g. Strother et al., 2015), for which we would have expected slightly calmer conditions than during the prior windier period. Unfortunately, Unit C was not sampled in central JT, and thus cannot provide further information on grain size there. However, it has a higher DBD than Unit A (Fig. 7.7), inferred from the x-ray attenuation of its matrix, in turn indicating a different grain size distribution, potentially with more silt than in Unit A, which supports different environmental conditions in KHTS than during the preceding warm period, the HTM. It also does not feature distinct diatom-ooze layers and therefore seems more similar Unit B than Unit A, which is supported by its acoustic signal, that shows weaker stratification than Unit A in both troughs (Lešić et al., subm.). Further, no increase in IRD is evident from the CT scan Slice from PS133/2\_17-13 (Fig. 7.7, Fig C. 4), which seems odd for a potentially warmer and meltwater-richer period with associated increased iceberg calving. Also, a potential dilution of IRD input can be excluded, given the rather low sedimentation rates within Unit C (Table 7.3). Still, warm phases, if associated with increased precipitation, do not necessarily mean glacial recession, especially for marine-terminating glaciers (Bentley et al., 2007). However,

records from Fan Lake (Fig. 7.2a), indicate that the Hypsithermal was not only warm on the south-western side of the mountain ranges, but also relatively dry, contradicting the sustenance of marine-terminating glaciers by higher precipitation on this side of the island (Strother et al., 2015). On the other hand, the accuracy of the age model of the Fan Lake record has been questioned, making it possible that the Hypsithermal might not have been as warm as previously thought (Xia et al., 2020) or that the Holocene Hypsithermal might not have had a similar effect on the marine depositional and environmental conditions in KHTS than the HTM, although another poleward shift of the SHW has been suggested for the Hypsithermal (Moreno et al., 2018; Heredia Barión et al., 2023a). This could be feasible, given that not all marine records around the Antarctic Peninsula have recorded the Hypsithermal, while others do show enhanced primary production, meltwater and even the collapse of the Prince Gustav Channel Ice Shelf during the Hypsithermal (Bentley et al., 2009).

### ***Neoglacial (Unit D)***

The more even distribution of the overlying Unit D, which is indicated by its presence in all cores, their correlation to the acoustic data, and a similar thickness across KHTS first reported by Lešić et al. (submitted), suggests a second large change in depositional environment that enabled trough-wide sedimentation between 2.76 and 2.25 cal ka BP. This correlates large change in climate was indeed proposed for the start of the Neoglacial around 2.75 cal ka BP (Birnie, 1990; Strother et al., 2015), associated with (substantial) glacier re-advances (Rosqvist and Schuber, 2003; Oppedal et al., 2018; Bakke et al., 2021) and a strengthening of the SHW on SG before 2 ka BP (van der Putten et al., 2004; van der Putten et al., 2009; Strother et al., 2015; Berg et al., 2019; Zwier et al., 2021; van der Bilt et al., 2022), which could have been translated into a shift of the dependent SACCF front or the main transport within the ACC and caused a change in (bottom-)current configuration (Lešić et al., submitted). On a trough-system wide scale, based on the even distribution of Unit D, this change was correlated with not necessarily weaker, but less focused shelf currents (Lešić et al., submitted). This is indeed reflected by the grain sizes of the FF in Unit D (Table 7.1), which features the highest silt content among all units.

This change is also roughly simultaneous to the onset of marine sedimentation of similar lithology at the core site of PS81/265-1 (Graham et al., 2017) on a moraine ridge at 2.23 cal ka BP (Fig. 7.2a). This implies that deposition in Cumberland Bay (CB; Fig. 7.2) was restricted to

basins before 2.23 cal ka BP and only commenced on bathymetric elevations in CB, when conditions also changed to widespread sedimentation in KHTS. Hence, the onset of even and widespread deposition could have been simultaneous on both sides of the island, supporting rather regional-wide shifts in temperature and current regimes.

Although Unit D appears to rather weakly stratified based on its acoustic signature, especially in KHT (Lešić et al., submitted), its physical and chemical properties, along with the magnetic susceptibility and grain sizes, vary, especially in GeoB22056-1, where the last 1.5 cal ka BP are highly resolved (Fig. 7.6, Fig. 7.9). Interestingly, the sand-rich layer in GeoB22056-1, dated to before 1.48 cal ka BP, can be correlated with another, albeit weakly developed, undulating surface with an upward increase in WBD in GeoB22057-1 (Fig. C. 4), which was dated to 1.6 cal ka BP. While the changes within Unit D were not resolved by acoustic data (Lešić et al., submitted), this switch is roughly coeval to the transition from the Little Ice Age to the Medieval Climate Anomaly around 1.5-1.4 ka BP (Heredia Barión et al., 2023a and references therein), indicating that island-proximal sedimentation in KHTS, where Unit D successions are thick, might have resolved small-scale climate changes.

#### 7.5.2.2. *Unit Boundaries*

While the lithological units show internal variability and slight differences in depositional conditions between warm and cooler climate phases on SG, the respective 5-12 cm thick boundary layers are equally synchronous within KHTS and coeval to the shifts between the climate periods. Along with their erosional bases, they feature the largest difference in lithology along all cores with regard to grain size distribution and physical properties with the highest content in sand and gravel and the lowest content in TOC, indicating the occurrence of events. They also correlate with continuous strong reflectors in the entire KHTS (Lešić et al., submitted), implying that they are present not only in the sampled cores but throughout KHTS and that the inferred events must have affected the entire KHTS. The only exception in our data is the boundary between Unit A and D in GeoB22058-1, which features truncated reflectors (Lešić et al., submitted). A similar strong unit boundary with truncated reflectors can be observed in RBT (Graham et al., 2017), where, similar to our records, sand content abruptly increases above the contact in CG666 as well, while organic carbon and opal are depleted. Both Graham et al. (2017) and Lešić et al. (submitted) proposed changes in (bottom-)current configuration as a possible cause for this kind of boundary.

The gradual increase in sand and IRD towards the Top of Units A and B in JT (Figs. 7.4, 7.5), and the simultaneous gradual decrease in sedimentation rates in both units and troughs (Figs. 7.8, 7.9) support this interpretation, indicating a continuous increase in current strength in both Units towards the end of their respective climate periods already. The overlying erosional bases of the boundaries (Fig. 7.7) implies a following abrupt increase in current strength at the seafloor, which caused erosion. In the CT scans, the erosion is especially evident at the boundary between Unit A and C, where diatom-ooze layers are cut off irregularly (Fig. 7.7a). Abrupt changes, in fact, have been identified in southern-most Patagonia for several rapid climate change events due to shifts in the SHW (McCulloch et al., 2020). Thus, the corresponding oceanographic system, the ACC, might react equally fast. Above the erosional surface, subsequent preferential deposition of sand and gravel is evident and could be caused by high current speeds. This is similar for all unit boundaries associated with hiatuses that correlate with one or more depositional units, e.g. the boundary between Unit A and C in PS133/2\_17-13, between A and D in GeoB22058-1 and the boundary between Unit B and D in GeoB22057-1 (Fig. 7.7). This indicates that these hiatuses could be caused by winnowing that lasted for up to several ka and is supported by the acoustic data that shows pinch-outs of the respective units towards the core location, where they are absent (Figs. 7.8, 7.9). Further, the boundary between Unit C and D in PS133/2\_17-13 supports this theory, as it is the only boundary not affected by a depositional hiatus and lacks the enrichment of IRD, despite featuring the characteristic undulating surface and the accompanying increase in DBD (Fig. C.4). The fining up signature within and above the hiatus-affected boundaries, which can be inferred from the upward decreasing DBD record of the CT scan (Fig. 7.7), implies a subsequent decrease in currents with the deposition onset of the subsequent Unit.

Still, the erosional bases, increased contents of IRD and sand, inferred from the component analysis and DBD-proxy of the CT scan, respectively, is reminiscent of turbidites, along with the fining-upward trend (Bouma, 1962). They are common in glacial marine environments (Anderson et al., 1984; Streuff et al., 2017b) and might be triggered by slope instability due to e.g. bottom-currents (cf. Laberg and Camerlenghi, 2008) or earthquakes (Talling, 2021). Both options seem feasible, given the steep trough flanks and spatial variation in deposition and erosion (Streuff et al., in prep.; Lešić et al., *subm.*) and the post-glacial isostatic adjustment (GIA) of the SG microcontinent (Barlow et al., 2016). However, the only reasonable cause to trigger trough system-wide turbidites during the Holocene would be post-glacial earthquakes

due to GIA (e.g. cf. Steffen and Wu, 2011). Indeed, relative sea level changes have occurred during the Holocene on the SG microcontinent, e.g. around 8 cal ka BP, as archived in the marine record in Little Jason Lagoon (Fig. 7.2c), which shows a distinct lithological boundary at 8 ( $\pm$  0.8) cal ka BP (Barlow et al., 2016; Berg et al., 2019). However, this boundary was connected to a transition from freshwater to marine conditions and a rise of relative sea level of several meters, driven by postglacial eustatic sea level rise that outpaced glacio-isostatic uplift of SG (Berg et al., 2019; Barlow et al., 2016), rather than an abrupt uplift event. Still, we cannot rule out such events due to the continuous GIA of South Georgia (Barlow et al., 2016), but find it unlikely that they were synchronous to interglacial climate changes between warmer and colder periods and provoked the spatial variability of sediment deposition in the deep troughs, which was investigated by Lešić et al. (subm.). Further, if the boundary layers were turbiditic deposits, we would expect less consistent radiocarbon ages results, or even reverse ages, above the erosional contact, as turbidites should carry older material. Hence, we propose that the boundary layers between the units are the result of an abrupt trough system-wide increase of current speed during the transition between warmer and cooler climate periods that caused partial erosion. Depending on the current dynamics during the warmer/cooler phase and the exposure of the location to present bottom-currents, we propose subsequent winnowing, which continued until the environmental conditions changed again due to following climate transitions that altered the current-configuration in KHTS.

## 7.6. Conclusion

The lithologies and age models of the investigated cores show that KHTS, as a depositional environment, has been very sensitively reacting to Holocene climate change. It has recorded at least four Holocene phases as four lithological units and, hence, three transitions between warmer and cooler climate phases since 10.8 cal ka BP. These include the change from the Holocene Thermal Maximum to the subsequent cooler and windier phase between 7-8 cal ka BP, which was accompanied by a distinct change in primary production, the transition to the Holocene Hypsithermal around 4 cal ka BP and the most recent cooling of the Neoglacial between 2.76 and 2.25 cal ka BP. The climate transitions correlate with the unit boundaries, which were likely caused by bottom-currents that caused erosion and winnowing due to abrupt changes in current activity in the entire trough system. We conclude that, in addition to climate-driven lithology changes, KHTS might have experienced enhanced bottom-currents

during the transitions from warmer to cooler phases and vice versa, implying that the oceanographic setting of the shelf waters in KHTS was likely affected by Holocene climate variability. Thus, our findings do not only confirm that Holocene climate variability was archived in the sediments on the continental shelf, but also support a previous investigation of KHTS that, based on acoustic data, that suggests changing current configuration on the shelf due to changes in the SACCF (Lešić et al., *subm.*).

## **Acknowledgements**

This study was funded by the “Deutsche Forschungsgemeinschaft” (DFG) in the framework of the priority program SPP 1158 "Antarctic Research with comparative investigations in Arctic ice areas" by the grants BO 1049/23-1, KU 683/18-1 and DO 705/4-1. We thank the captains, chief scientists and crews from RV *Polarstern* cruise PS133/2 (Grant No. AWI\_PS133/2\_01 and AWI\_PS133/2\_02) (Alfred-Wegener-Institut Helmholtz-Zentrum für Polar und Meeresforschung, 2017) and RV *Meteor* cruise M134, as well as the AWI repository for access to gravity core PS133/2\_17-13. We acknowledge further financial support from the Helmholtz Association (Alfred Wegener Institute Helmholtz Centre for Polar and Marine Research) and are grateful to Miriam Römer for organising the funding for participation in the *Polarstern* cruise via the MARUM Incentive Funds Initiative. Cores GeoB22056-1, 57-1 and 58-1 have been provided by the GeoB Core Repository at the MARUM - Centre for Marine Environmental Sciences, University of Bremen, Germany. Gesundheit Nord GmbH - Klinikum Bremen Mitte, Prof. Dr. Arne-Jörn Lemke and Christian Timann are gratefully acknowledged for performing and supporting the CT measurements. Further, we thank M. Seebeck, V. Schumacher, S. Wiebe, P. Daub and C. Gebhardt from Alfred Wegener Institute, Helmholtz Centre for Polar and Marine Research in Bremerhaven, for support with coring, core and sample processing, as well as J. Klages and J. Wollenburg for scientific guidance. We thank D. Flenner and all student helpers for their contribution to this study and J. Malnati for her laboratory support at University of Bremen. All figures in this publication were created using QGIS 3.22.10 and Adobe Illustrator 2022/2023 , plots were made in Grapher by Golden Software..



## 8. Concluding remarks and perspectives

This thesis integrates the lithological data and radiocarbon ages of five sediment cores with landform mapping and the analysis of sub-bottom profiles from two fjord- and trough systems on the south-western shelf, Drygalski Fjord System (DFS) and King Haakon Trough System (KHTS). The aim is to assess South Georgia's response to the major climate changes since the last glaciation (Fig. 8.1) and the glacial history of DFS and KHTS. The investigations (Chapters 4-6) show that trough formation on the southern shelf, based on their orientations, is likely connected to faults and shear zones that might have provided structural weaknesses explored by glacial ice (cf. Graham et al., 2008). Radiocarbon dating shows that the sampled glaci-marine to hemipelagic sediments in these troughs, depending on their proximity to the island, have recorded the last 1.5 to 24.5 cal ka BP. Island-proximal sediment cores from within the cross-shelf troughs are rather high-resolution records and excellently archive the more recent Holocene climate signals. This is due to the high sedimentation rates on the inner shelf that enables the deposition of thick sediment successions (Chapters 6 and 7). In contrast, the outer shelf areas are characterised by thin marine deposits due to low sedimentation rates (Chapters 4 and 5), and gravity cores from there are therefore better suited to investigate the LLGM and subsequent long-term changes as they can more easily penetrate these older successions (Chapter 4). Therefore, South Georgia's shelf sediments are not only excellent to study the past evolution of the South Georgia Ice Cap (SGIC) since at least the last glacial, but have also recorded climate-dependent changes in the depositional environments during the subsequent deglaciation and the Holocene. In Drygalski Trough (DT), the results show that the outer trough and the adjacent shelf areas were covered by glacial ice before 30 ka BP. Subsequently, the ice thinned and created a subglacial cavity with restricted access to the ocean. Around 17.5 cal ka BP (Fig. 8.1), ice retreated from the mid-shelf towards the island (Chapter 4). This indicates a shelf-wide ice extent during an early Local Last Glacial Maximum in the area around DT (Fig. 8.1). While this timeline was established with radiocarbon dating of the respective lithofacies, a similar approach in KHTS is not possible. The oldest obtained radiocarbon age in KHTS on the mid-shelf is 10.2 cal ka BP and no gravity core, to our knowledge, was retrieved from the outer trough thus far. Still, landform mapping and sub-bottom profiler data yielded evidence for grounded ice on the shelf in KHTS, directly underlying (glaci-)marine to hemipelagic through fill on the mid-shelf. The respective onset of trough fill sedimentation was extrapolated to be max. 30 ka old. While this is only an

approximation, it still suggests that the entire (glaci-)marine trough fill could be of post-LLGM origin (Chapter 5).

This does not only align with our findings in DT, but also indicates that the LLGM could have eroded potential previous trough fills and might have extended all the way to the shelf edge and at least to the mid-shelf. However, multiple generations of glacial deposits and landforms on the outer shelf of KHTS indicate repeated extensive glaciation with grounded ice within the trough system. Thus, although a LLGM glaciation all the way to the shelf edge in KHTS is feasible, we cannot exclude that the recessional moraines at the shelf edge (Fig. 8.1) stem from the retreating ice cap of the, e.g., penultimate glacial.

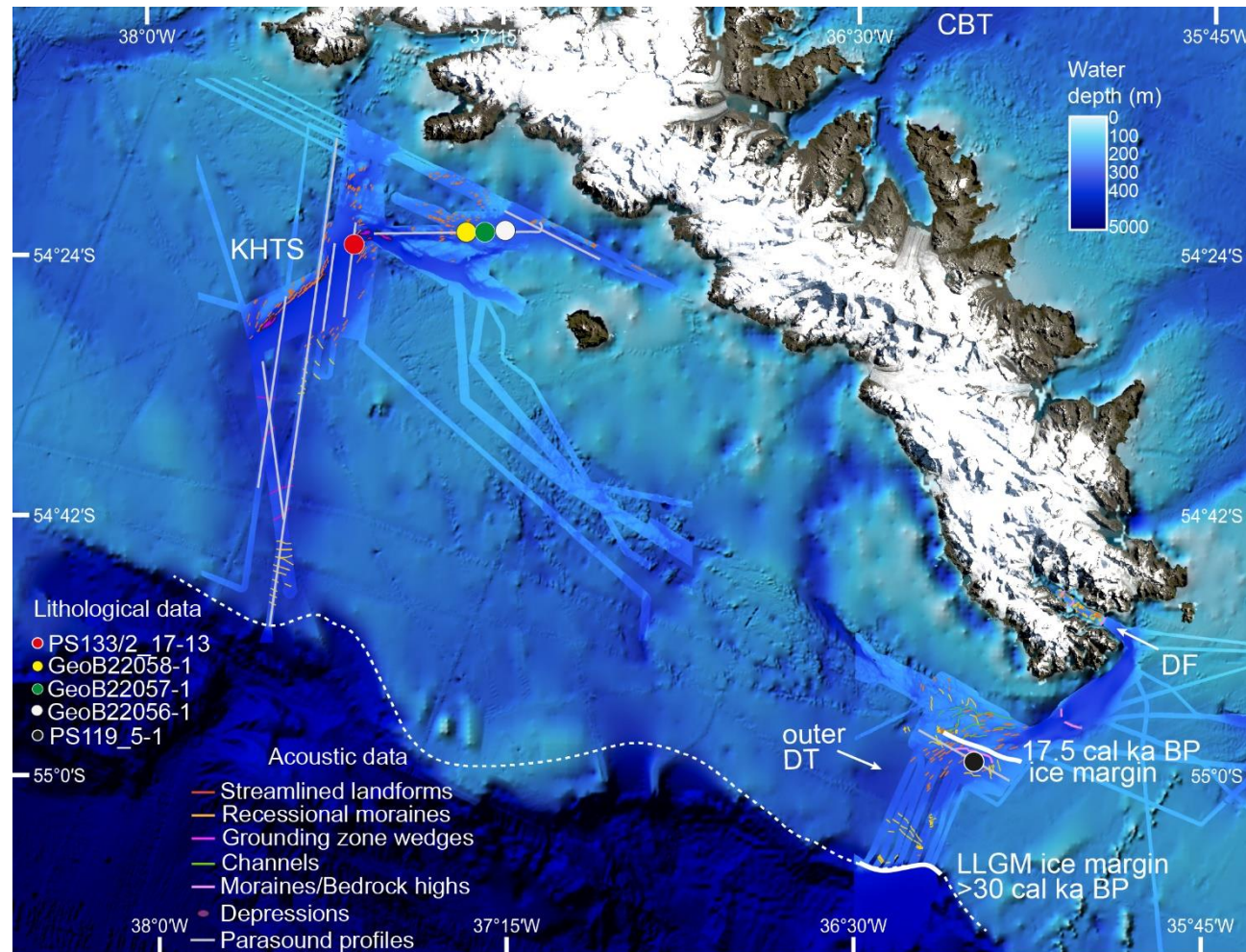


Fig. 8.1: The map shows the data used in this thesis, including gravity cores (coloured dots), the Parasound profiles (light grey lines), and the landforms mapped in the bathymetric data, which are highlighted. and the mapped landforms in King Haakon Trough System (KHTS) and Drygalski Fjord System, including Drygalski Fjord (DF) and the outer Drygalski Trough (DT). The thick white (dotted) lines indicate suggested ice extents. CBT = Cumberland Bay Trough. DEM information for the ocean and shelf areas is based on GEBCO Compilation Group (2023), Hogg et al. (2016); (2017), and bathymetry data from PS81, M134 and PS119 (Bohrmann, 2013; Bohrmann et al., 2017; Bohrmann, 2019). Map information for SG island is derived from Landsat imagery from South Georgia GIS (2023) (EPSG: 3762)

Ultimately, this thesis not only provides the important evidence that the LLGM ice extent on South Georgia was relatively early and extensive in DT, but also indicates that large parts of the south-western continental shelf were influenced by it.

A large ice extent on the southwestern shelf would suggest that the South Georgia LLGM extent was rather more comparable to the Antarctic Peninsula and the West Antarctic Ice Sheet than Patagonia, as the latter experienced its most extensive ice-extents during earlier glaciations (e.g. Barlow et al., 2016). Whether this can be extrapolated to the whole South Georgia shelf, however, is unclear. While landforms on the shallow areas around both troughs are indicators for grounded ice and do not seem to have been overridden or buried, we cannot reliably assign them to a specific glaciation. Furthermore, dated evidence is lacking to support a shelf-wide glaciation during the LLGM on the north-eastern shelf, although similar geomorphological features are present on the north-eastern shelf (Graham et al., 2008; Graham et al., 2017). This makes shelf-wide assumptions difficult. Indeed, it is known that the mountain ranges on the island serve as orographic barriers and likely influence microclimate. Consequently, precipitation difference between both sides could have potentially provoked different LLGM ice extents on the opposite sides of the mountains (cf. Gordon et al., 2008; Cook et al., 2010; Farías-Barahona et al., 2020).

Therefore, radiocarbon dating on gravity cores from the outermost shelf areas should be performed to reconstruct the ice extent, e.g. on the north-eastern side, where postglacial sedimentation might be as scarce as on the outermost shelf on the south-western side of the island (Graham et al., 2008). For this approach, Cumberland Bay Trough would be a suitable area, as it features morainal ridges close to the shelf edge (Fig. 3.3). Since it drains large parts of the remaining SGIC, it should also reflect past major ice-extent changes (Fig. 8.1).

Ice-extent changes during the post-LLGM deglaciation in DT are easily detectable in the stacked sediment facies via differences in grainsize distribution, IRD content, TOC and DBD content. This includes the retreat from the mid-shelf around 17.5 cal ka BP, only minor iceberg influence after 15 cal ka BP and enhanced terrigenous input due to a re-advance into DFS during the ACR. For the following interglacial, however, it is rather difficult to detect the comparably smaller-scale climate changes and associated ice-extent changes in the outer trough. This is due to the large distance to the ice margin, which fluctuated within the fjord (Lešić et al., 2022). However, these ice-distal environments in both KHST and DT recorded

changes in depositional and environmental conditions. In KHTS, due to the high temporal resolution, this could be associated with an intruding SACCF branch and (dependent) shelf circulation, bottom currents and climate-controlled island-runoff. These change synchronously with terrestrial records of climate transitions between warmer (calmer) and cooler (windier) periods from South Georgia island and other SH areas. The major transitions around South Georgia were recorded during transitions from warmer to colder climate, such as the end of the Holocene Thermal Maximum and the Holocene Hypsithermal. We hence correlate the Holocene changes in the depositional system of KHTS and DT with South Georgia's response to SH climate fluctuations.

Consequently, our data show the sensitivity of South Georgia's continental shelf environments and solidify their association with SH climate. The island's position near one of the SH's most important and very sensitive climate drivers, the ACC, apparently leads to a rapid response to climate variability. This might be due to the SACCF front, which, today, borders and locally intrudes the shelf (Matano et al., 2020; Combes et al., 2023). Given the apparently early LLGM on South Georgia, which could have occurred as early as 30 cal ka BP, an early response to minor climate fluctuations seems reasonable.

Investigations in island-proximal areas of other troughs around South Georgia should be carried out to elucidate if the detailed record of Holocene climate transitions in KHTS is an exception on the shelf due to the rather local intrusion of the SACCF (cf. Matano et al., 2020; Combes et al., 2023), or can also be detected elsewhere on the shelf.

After considering all key results from this thesis, the shelf sediments are an excellent location to study both short- and long-term maritime climate fluctuations in the South Atlantic sector of the sub-Antarctic, especially due to the influence of the ACC. Hence, South Georgia also provides, quite easily accessible due to the shallow shelf waters, sedimentary climate records that can benchmark e.g. sub-Antarctic ice cap behaviour since the LLGM. These paleodata could be used to test future modelling approaches, that are needed to understand and reliably predict the consequences of current climate change.

## 9. Acknowledgements

First, a reminiscent journey: If someone told my 10-year-old me – or even my 20-year-old me – that one day I would write and hand in a dissertation in natural sciences, both would not have believed them – likely along with all my teachers. While always eager to learn, I never believed in my strength when it came to STEM, and deciding to go and try out Geosciences at the University of Tübingen was based on the love for fossils that I collected since I was a child and fascinating late-night documentaries I watched with my father. However, I quickly realised how far one can get if one is driven by natural curiosity.

My first expedition on *RV Polarstern* made it clear to me, however, that my near academic future would revolve more around climate. This was the beginning of my PhD journey – and before I want to thank the people who supported me since starting to work on my doctoral thesis, I want to thank all the people that paved parts of the way that got me there:

My parents, who took me outside to hike and hunt for pyrite and local fossils in Swabia. My friends and chosen family members Lisa Heinz, Alice Mahlbacher and Joëlle Kubeneck, who taught me true and unconditional friendship and how much fun field trips and shared interests are. Prof. Dr. Marcus Nowak, as he guided me through my first experiences in research and planted the seed for my aspiration to pursue a career in research – encouraging me to think about PhD programs in the first place. The members of the Marine Geology section at the Alfred-Wegener-Institute, Helmholtz Centre for Marine and Polar Science in Bremerhaven (AWI), who made it possible for me to work with marine sediments for the first time in my life. Simon Dreutter, who trusted me and my abilities when I did not trust them myself - and proved me wrong. All the fellow researches and crew onboard *RV Polarstern* during my four expeditions, who accompanied me during my first spectacular experiences in marine sciences.

The PhD was, up until now, the most difficult journey I embarked on. It was sabotaged by the pandemic right from the start and thus demanded my entire energy, self-motivation and stamina. Therefore, I want to sincerely thank everybody that supported me along the way.

To my supervisors Prof. Dr. Gerhard Bohrmann and Dr. Gerhard Kuhn, as well as Prof. Dr. Tilo von Dobeneck, I want to express my gratefulness for the opportunity to work on this thesis and their scientific guidance as my thesis committee. My sincerest thanks also go to Prof. Dr. Sabine Kasten for the support and opportunity to collect samples on cruise PS133/2 (Grant No. AWI\_PS133/2\_0).

I want to thank Dr. Katharina Streuff, who has been member of the thesis committee, a reliable constant, incredible support and teacher throughout the past years until the very end. I am very grateful for our collaboration and for all the fancy new words in my vocabulary. I also thank all further collaborators, Dr. Jürgen Titschack, Darjan Gande, Alina Ivanova and Simon Pormann, who enriched my thesis.

I am very grateful for the excellent support in the laboratories at AWI and University of Bremen, especially Catalina Gebhardt, Valéa Schumacher, Susanne Wiebe, Pascal Daub, Michael Seebeck, Brit Kockisch, Marco Klann, Jens Matthiesen and Janice Malnati.

For the scientific discussions and supervision at the AWI, I want to thank Johann Klages, whose door was always open for me.

Further, I want to thank all my colleagues and office mates at both AWI and University of Bremen for the welcoming and friendly environment, especially Yi-Ting Tseng, Mechthild Doll and Victoria Kürzinger for their kindness, understanding and encouraging words and all the shared laughs.

Last, but not least, I want to thank Eva Leitschuh, Maja, Johannes and Jaro Konopatzki, as well as Nils Rose, who were my home far away from home.

This thesis was funded by the “Deutsche Forschungsgemeinschaft” (DFG) in the framework of the priority program SPP 1158 "Antarctic Research with comparative investigations in Arctic ice areas" by the grants BO 1049/23-1, KU 683/18-1 and DO 705/4-1. Additional funds for the acquisition of PS133/2 data stem from Grant No. AWI\_PS133/2\_01 and AWI\_PS133/2\_02 (Alfred-Wegener-Institut Helmholtz-Zentrum für Polar und Meeresforschung, 2017). I acknowledge further financial support from the Helmholtz Association (Alfred Wegener Institute Helmholtz Centre for Polar and Marine Research) and am thankful for the funding of my participation, organised by Miriam Römer, in this Polarstern cruise, via the MARUM Incentive Funds Initiative.

## 10. References

- Abram, N.J., Mulvaney, R., Vimeux, F., Phipps, S.J., Turner, J., England, M.H., 2014. Evolution of the Southern Annular Mode during the past millennium. *Nature Climate Change* 4, 564-569.
- Ai, X.E., Thöle, L.M., Auderset, A., Schmitt, M., Moretti, S., Studer, A.S., Michel, E., Wegmann, M., Mazaud, A., Bijl, P.K., 2023. Meridional migration of the Antarctic Circumpolar Current over the last glacial cycle. In *Goldschmidt Lyon*
- Åkesson, H., Nisancioglu, K.H., Nick, F.M., 2018. Impact of fjord geometry on grounding line stability. *Frontiers in Earth Science*, 71.
- Alfred-Wegener-Institut Helmholtz-Zentrum für Polar- und Meeresforschung (2017) Polar Research and Supply Vessel POLARSTERN Operated by the Alfred-Wegener-Institute. *Journal of large-scale research facilities*, 3, A119. <http://dx.doi.org/10.17815/jlsrf-3-163>.
- Alley, R., Holschuh, N., MacAyeal, D., Parizek, B., Zoet, L., Riverman, K., Muto, A., Christianson, K., Clyne, E., Anandakrishnan, S., Stevens, N., GHOST Collaboration, 2021. Bedforms of Thwaites Glacier, West Antarctica: Character and Origin. *Journal of Geophysical Research: Earth Surface* 126, e2021JF006339.
- Alley, R.B., 1993. In search of ice-stream sticky spots. *Journal of Glaciology* 39, 447-454.
- Alve, E., 1995. Benthic foraminiferal distribution and recolonization of formerly anoxic environments in Drammensfjord, southern Norway. *Marine Micropaleontology* 25, 169-186.
- Anandakrishnan, S., Alley, R.B., 1994. Ice Stream C, Antarctica, sticky spots detected by microearthquake monitoring. *Annals of Glaciology* 20, 183-186.
- Anandakrishnan, S., Blankenship, D., Alley, R., Stoffa, P., 1998. Influence of subglacial geology on the position of a West Antarctic ice stream from seismic observations. *Nature* 394, 62-65.
- Andersen, H.V., 1952. *Buccella*, a new genus of the rotalid foraminifera. *Journal of the Washington Academy of Sciences* 42, 143-151.
- Anderson, J., Brake, C., Domack, E., Myers, N., Singer, J., 1983. Sedimentary dynamics of the Antarctic continental shelf. *Antarctic Earth Science*, 387-389.
- Anderson, J., Kurtz, D., Domack, E., Balshaw, K., 1980. Glacial and glacial marine sediments of the Antarctic continental shelf. *The Journal of Geology* 88, 399-414.
- Anderson, J.B., 1975. Ecology and distribution of foraminifera in the Weddell Sea of Antarctica. *Micropaleontology*, 69-96.
- Anderson, J.B., Brake, C.F., Myers, N.C., 1984. Sedimentation on the Ross Sea continental shelf, Antarctica. *Marine Geology* 57, 295-333.
- Andreassen, K., Laberg, J.S., Vorren, T.O., 2008. Seafloor geomorphology of the SW Barents Sea and its glaci-dynamic implications. *Geomorphology* 97, 157-177.
- Andreassen, K., Winsborrow, M.C., Bjarnadóttir, L.R., Rüther, D.C., 2014. Ice stream retreat dynamics inferred from an assemblage of landforms in the northern Barents Sea. *Quaternary Science Reviews* 92, 246-257.
- Andresen, C.S., McCarthy, D.J., Valdemar Dylmer, C., Seidenkrantz, M.-S., Kuijpers, A., Lloyd, J.M., 2010. Interaction between subsurface ocean waters and calving of the Jakobshavn Isbræ during the late Holocene. *The Holocene* 21, 211-224.
- Arndt, J.E., Forwick, M., 2016. Deep-water iceberg ploughmarks on Hovgaard Ridge, Fram Strait, Atlas of submarine glacial landforms: Modern, Quaternary and ancient. *Geological Society London, Memoirs*, pp. 285-286.
- Arndt, J.E., Jokat, W., Dorschel, B., 2017. The last glaciation and deglaciation of the Northeast Greenland continental shelf revealed by hydro-acoustic data. *Quaternary Science Reviews* 160, 45-56.
- Arndt, J.E., Jokat, W., Dorschel, B., Myklebust, R., Dowdeswell, J.A., Evans, J., 2015. A new bathymetry of the Northeast Greenland continental shelf: Constraints on glacial and other processes. *Geochemistry, Geophysics, Geosystems* 16, 3733-3753.



## References

---

- Arrigo, K.R., van Dijken, G.L., Castelao, R.M., Luo, H., Rennermalm, Å.K., Tedesco, M., Mote, T.L., Oliver, H., Yager, P.L., 2017. Melting glaciers stimulate large summer phytoplankton blooms in southwest Greenland waters. *Geophysical Research Letters* 44, 6278-6285.
- Bakke, J., Paasche, Ø., Schaefer, J.M., Timmermann, A., 2021. Long-term demise of sub-Antarctic glaciers modulated by the Southern Hemisphere Westerlies. *Scientific Reports* 11, 1–10.
- Bamber, J., 2021. Chapter 8 - Land ice: indicator, and integrator, of climate change, in: Letcher, T.M. (Ed.), *Climate Change (Third Edition)*. Elsevier, pp. 141-156.
- Barlow, N.L.M., Bentley, M.J., Spada, G., Evans, D.J.A., Hansom, J.D., Brader, M.D., White, D.A., Zander, A., Berg, S., 2016. Testing models of ice cap extent, South Georgia, sub-Antarctic. *Quaternary Science Reviews* 154, 157–168.
- Barnes, D.K.A., Sands, C.J., Hogg, O.T., Robinson, B.J.O., Downey, R.V., Smith, J.A., 2016. Biodiversity signature of the Last Glacial Maximum at South Georgia, Southern Ocean. *Journal of Biogeography* 43, 2391–2399.
- Barnes, P.W., Lien, R., 1988. Icebergs rework shelf sediments to 500 m off Antarctica. *Geology* 16, 1130-1133.
- Barrow, C., 1978. Postglacial pollen diagrams from south Georgia (sub-Antarctic) and West Falkland island (South Atlantic). *Journal of Biogeography*, 251-274.
- Barrow, C., 1983a. Palynological studies in South Georgia: III. Three profiles from near King Edward Cove, Cumberland East Bay. *British Antarctic Survey Bulletin* 58, 43-60.
- Barrow, C., 1983b. Palynological studies in south Georgia: IV. Profiles from Barff peninsula and Annenkov island. *British Antarctic Survey Bulletin* 58, 61-70.
- Bart, P.J., Krogmeier, B.J., Bart, M.P., Tulaczyk, S., 2017. The paradox of a long grounding during West Antarctic Ice Sheet retreat in Ross Sea. *Scientific Reports* 7, 1-8.
- Bartels-Rausch, T., 2013. Ten things we need to know about ice and snow. *Nature* 494, 27-29.
- Bartoli, G., Sarnthein, M., Weinelt, M., Erlenkeuser, H., Garbe-Schönberg, D., Lea, D., 2005. Final closure of Panama and the onset of northern hemisphere glaciation. *Earth and Planetary Science Letters* 237, 33-44.
- Batchelor, C.L., Dowdeswell, J.A., 2015. Ice-sheet grounding-zone wedges (GZWs) on high-latitude continental margins. *Marine Geology* 363, 65–92.
- Beaver, D.G., Kent, D.V., Dalziel, I.W., 2022. Paleomagnetic constraints from South Georgia on the tectonic reconstruction of the Early Cretaceous Rocas Verdes marginal basin system of southernmost South America. *Tectonics* 41, e2021TC006990.
- Bentley, M., Evans, D., Fogwill, C., Hansom, J., Sugden, D., Kubik, P., 2007. Glacial geomorphology and chronology of deglaciation, South Georgia, sub-Antarctic. *Quaternary Science Reviews* 26, 644–677.
- Bentley, M.J., Hodgson, D., Smith, J., Cofaigh, C., Domack, E., Larter, R., Roberts, S., Brachfeld, S., Leventer, A., Hjort, C., Hillenbrand, C.D., Evans, J., 2009. Mechanisms of Holocene palaeoenvironmental change in the Antarctic Peninsula region. *The Holocene* 19, 51-69.
- Berg, S., Jivcov, S., Kusch, S., Kuhn, G., Wacker, L., Rethemeyer, J., 2020. Compound-specific radiocarbon analysis of (Sub-)Antarctic coastal marine sediments - potential and challenges for chronologies. *Paleoceanography and Paleoclimatology*, e2020PA003890.
- Berg, S., White, D.A., Jivcov, S., Melles, M., Leng, M.J., Rethemeyer, J., Allen, C., Perren, B., Bennike, O., Viehberg, F., 2019. Holocene glacier fluctuations and environmental changes in subantarctic South Georgia inferred from a sediment record from a coastal inlet. *Quaternary Research* 91, 132–148.
- Berger, A., 1988. Milankovitch theory and climate. *Reviews of Geophysics* 26, 624-657.
- Birnie, J., 1990. Holocene environmental change in South Georgia: Evidence from lake sediments. *Journal of Quaternary Science* 5, 171-187.
- Boex, J., Fogwill, C., Harrison, S., Glasser, N., Hein, A., Schnabel, C., Xu, S., 2013. Rapid thinning of the late Pleistocene Patagonian Ice Sheet followed migration of the Southern Westerlies. *Scientific Reports* 3, 1-6.
- Bohrmann, G., 2013. The expedition of the research vessel “Polarstern” to the Antarctic in 2013 (ANT-XXIX/4), *Berichte zur Polar- und Meeresforschung = Reports on Polar and Marine*

## References

---

- Research. Alfred-Wegener-Institut, Helmholtz-Zentrum für Polar- und Meeresforschung, pp. 1-145.
- Bohrmann, G., 2019. The expedition PS119 of the research vessel POLARSTERN to Eastern Scotia Sea in 2019, *Berichte zur Polar- und Meeresforschung = Reports on Polar and Marine Research*. Alfred-Wegener-Institut, Helmholtz-Zentrum für Polar- und Meeresforschung, Bremerhaven, Germany, pp. 1-236.
- Bohrmann, G., Aromokeye, A.D., Bihler, V., Dehning, K., Dohrmann, I., Gentz, T., Grahs, M., Hogg, O., Hüttich, D., Kasten, S., Kirschenmann, E., Lange, M., Leymann, T., Linse, K., Loher, M., Malnati, J., Mau, S., Mickoleit, A., Nowald, N., Pape, T., Reuter, C., Rohleder, C., Römer, M., Sahling, H., Stange, N., Torres, M., Vittori, V., von Dobeneck, T., von Neuhoff, H., Weinrebe, W., Wintersteller, P., 2017. R/V METEOR Cruise Report M134, Emissions of Free Gas from Cross-Shelf Troughs of South Georgia: Distribution, Quantification, and Sources for Methane Ebullition Sites in Sub-Antarctic Waters, Port Stanley (Falkland Islands) - Punta Arenas (Chile), 16 January - 18 February 2017, *Berichte aus dem MARUM und dem Fachbereich Geowissenschaften der Universität Bremen*. MARUM–Zentrum für Marine Umweltwissenschaften, Fachbereich Geowissenschaften, Universität Bremen, pp. 1-220.
- Boulton, G., 1986. Push-moraines and glacier-contact fans in marine and terrestrial environments. *Sedimentology* 33, 677-698.
- Bouma, A.H., 1962. Sedimentology of some flysch deposits. A graphic approach to facies interpretation 168.
- Bova, S., Rosenthal, Y., Liu, Z., Godad, S.P., Yan, M., 2021. Seasonal origin of the thermal maxima at the Holocene and the last interglacial. *Nature* 589, 548-553.
- Bradwell, T., Stoker, M.S., Golledge, N.R., Wilson, C.K., Merritt, J.W., Long, D., Everest, J.D., Hestvik, O.B., Stevenson, A.G., Hubbard, A.L., Finlayson, A.G., Mathers, H.E., 2008. The northern sector of the last British Ice Sheet: maximum extent and demise. *Earth-Science Reviews* 88, 207-226.
- Brady, H., 1881. Notes on some of the reticularian Rhizopoda of the " Challenger " Expedition. Part III. 1. Classification. 2. Further notes on new species. 3. Note on Biloculina mud. *Quarterly Journal of Microscopical Science, new series* 21, 31-71.
- Bressan, A., Constantin, A., 2019. The deflection angle of surface ocean currents from the wind direction. *Journal of Geophysical Research: Oceans* 124, 7412-7420.
- Breuer, B., Lange, M., Blindow, N., 2006. Sensitivity studies on model modifications to assess the dynamics of a temperate ice cap, such as that on King George Island, Antarctica. *Journal of Glaciology* 52, 235-247.
- Brouard, E., Lajeunesse, P., 2017. Maximum extent and decay of the Laurentide Ice Sheet in Western Baffin Bay during the Last glacial episode. *Scientific Reports* 7, 10711.
- Butzin, M., Heaton, T.J., Köhler, P., Lohmann, G., 2019. Marine radiocarbon reservoir ages simulated for IntCal20, link to model results in NetCDF format, Supplement to: Butzin, M et al. (2020): A short note on marine reservoir age simulations used in IntCal20. *Radiocarbon*, 1-7, <https://doi.org/10.1017/RDC.2020.9>. PANGAEA.
- Butzin, M., Heaton, T.J., Köhler, P., Lohmann, G., 2020. A short note on marine reservoir age simulations used in IntCal20. *Radiocarbon*, 865-871.
- Camerlenghi, A., Rebesco, M., Accettella, D., 2016. Storfjorden trough-mouth fan, barents sea margin. *Memoirs* 46, 371-372.
- Caress, D., Chayes, D., 2017. MB-System: Mapping the Seafloor, <https://www.mbari.org/products/>, pp. research-software/mb-system.
- Carter, A., Curtis, M., Schwanethal, J., 2014. Cenozoic tectonic history of the South Georgia microcontinent and potential as a barrier to Pacific-Atlantic through flow. *Geology* 42, 299-302.
- Carter, A., Riley, T.R., Hillenbrand, C.-D., Rittner, M., 2017. Widespread Antarctic glaciation during the late Eocene. *Earth and Planetary Science Letters* 458, 49-57.

## References

---

- Ciais, P., Petit, J., Jouzel, J., Lorius, C., Barkov, N., Lipenkov, V., Nicolaiev, V., 1992. Evidence for an early Holocene climatic optimum in the Antarctic deep ice-core record. *Climate Dynamics* 6, 169-177.
- Clapperton, C.M., Sugden, D., Pelto, M., 1989a. Relationship of land terminating and fjord glaciers to Holocene climatic change, South Georgia, Antarctica, *Glacier Fluctuations and Climatic Change*. Springer, pp. 57-75.
- Clapperton, C.M., 1971. Geomorphology of the Stromness Bay-Cumberland Bay area, South Georgia. British Antarctic Survey.
- Clapperton, C.M., 1990. Quaternary glaciations in the Southern Ocean and Antarctic Peninsula area. *Quaternary Science Reviews* 9, 229-252.
- Clapperton, C.M., Sugden, D., Birnie, R., Hanson, J., Thom, G., 1978. Glacier fluctuations in South Georgia and comparison with other island groups in the Scotia Sea, in: Bakker, E.M.V.Z. (Ed.), *Antarctic glacial history and world palaeoenvironments*. Balkema, Rotterdam, pp. 98-104.
- Clapperton, C.M., Sugden, D.E., 1980. Geomorphology of the St Andrews Bay-Royal Bay area, South Georgia, Sheet 1. BAS Misc. Cambridge, British Antarctic Survey.
- Clapperton, C.M., Sugden, D.E., Birnie, J., Wilson, M.J., 1989b. Late-glacial and Holocene glacier fluctuations and environmental change on South Georgia, Southern Ocean. *Quaternary Research* 31, 210-228.
- Clark, C.D., Hughes, A.L., Greenwood, S.L., Jordan, C., Sejrup, H.P., 2012. Pattern and timing of retreat of the last British-Irish Ice Sheet. *Quaternary Science Reviews* 44, 112-146.
- Clark, P.U., Alley, R.B., Keigwin, L.D., Licciardi, J.M., Johnsen, S.J., Wang, H., 1996. Origin of the first global meltwater pulse following the last glacial maximum. *Paleoceanography* 11, 563-577.
- Clark, P.U., Dyke, A.S., Shakun, J.D., Carlson, A.E., Clark, J., Wohlfarth, B., Mitrovica, J.X., Hostetler, S.W., McCabe, A.M., 2009. The Last Glacial Maximum. *Science* 325, 710-714.
- Clark, P.U., Mix, A.C., 2002. Ice sheets and sea level of the Last Glacial Maximum. *Quaternary Science Reviews* 21, 1-7.
- Combes, V., Matano, R., Meredith, M., Young, E., 2023. Variability of the shelf circulation around South Georgia, Southern Ocean. *Journal of Geophysical Research: Oceans*, e2022JC019257.
- Cook, A.J., Poncet, S., Cooper, A.P.R., Herbert, D.J., Christie, D., 2010. Glacier retreat on South Georgia and implications for the spread of rats. *Antarctic Science* 22, 255-263.
- Cowan, E.A., Powell, R.D., Anderson, J.B., Ashley, G.M., 1991. Ice-proximal sediment accumulation rates in a temperate glacial fjord, southeastern Alaska, Glacial marine sedimentation; Paleoclimatic significance. *Geological Society of America*, pp. 61-73.
- Curtis, M.L., 2007. Main Andean sinistral shear along the Cooper Bay Dislocation zone, south Georgia?, in: Cooper, A.K., Raymond, C.R., Team, I.E. (Eds.), *Antarctica: a keystone in a changing world*. Online proceedings of the 10th International Symposium on Antarctic Earth Sciences. U.S. Geological Survey and National Academies Press, santa barbara, California, p. 4pp.
- Curtis, M.L., 2011. Geological Map of South Georgia (1:250 000 scale), BAS GEOMAP 2 Series, Sheet 4. British Antarctic Survey, Cambridge, UK.
- Dalziel, I.W., Macdonald, D.I., Stone, P., Storey, B.C., 2021. South Georgia microcontinent: Displaced fragment of the southernmost Andes. *Earth-Science Reviews* 220, 103671.
- Darvill, C.M., Bentley, M.J., Stokes, C.R., Hein, A.S., Rodés, Á., 2015. Extensive MIS 3 glaciation in southernmost Patagonia revealed by cosmogenic nuclide dating of outwash sediments. *Earth and Planetary Science Letters* 429, 157-169.
- Davis, W.J., 2023. Mass extinctions and their relationship with atmospheric carbon dioxide concentration: Implications for Earth's future. *Earth's Future* 11, e2022EF003336.
- Denis, D., Crosta, X., Zaragosi, S., Romero, O., Martin, B., Mas, V., 2006. Seasonal and subseasonal climate changes recorded in laminated diatom ooze sediments, Adelie Land, East Antarctica. *The Holocene* 16, 1137-1147.

## References

---

- De Vleeschouwer, D., Zeeden, C., 2021. Age Models and Geochronology: An Introduction to Different Age-depth Modelling Approaches. Zenodo. <https://doi.org/10.5281/zenodo.4749027>
- Dickens, W., Kuhn, G., Leng, M., Graham, A.G., Dowdeswell, J., Meredith, M., Hillenbrand, C.-D., Hodgson, D., Roberts, S., Sloane, H., Smith, J.A., 2019. Enhanced glacial discharge from the eastern Antarctic Peninsula since the 1700s associated with a positive Southern Annular Mode. *Scientific Reports* 9, 14606.
- Dickens, W.A., Graham, A.G., Smith, J.A., Dowdeswell, J.A., Larter, R.D., Hillenbrand, C.D., Trathan, P.N., Arndt, J.E., Kuhn, G., 2014. A new bathymetric compilation for the South Orkney Islands region, Antarctic Peninsula (49–39 W to 64–59 S): Insights into the glacial development of the continental shelf. *Geochemistry, Geophysics, Geosystems* 15, 2494-2514.
- Diekmann, B., Kuhn, G., Rachold, V., Abelmann, A., Brathauer, U., Fütterer, D.K., Gersonde, R., Grobe, H., 2000. Terrigenous sediment supply in the Scotia Sea (Southern Ocean): response to Late Quaternary ice dynamics in Patagonia and on the Antarctic Peninsula. *Palaeogeography, Palaeoclimatology, Palaeoecology* 162, 357-387.
- Domack, E., Amblas, D., Gilbert, R., Brachfeld, S., Camerlenghi, A., Rebesco, M., Canals, M., Urgeles, R., 2006. Subglacial morphology and glacial evolution of the Palmer deep outlet system, Antarctic Peninsula. *Geomorphology* 75, 125-142.
- Domack, E.W., 1990. Laminated terrigenous sediments from the Antarctic Peninsula: the role of subglacial and marine processes. Geological Society, London, Special Publications 53, 91-103.
- Domack, E.W., Powell, R., 2018. Modern Glaciomarine Environments and Sediments: An Antarctic Perspective, in: Menzies, J., van de Meer, J.J.M. (Eds.), *Past Glacial Environments*, 2 ed. Elsevier, Waltham, MA, USA, pp. 181–272.
- Dorschel, B., Hehemann, L., Viquerat, S., Warnke, F., Dreutter, S., Schulze Tenberge, Y., Accettella, D., An, L., Barrios, F., Bazhenova, E.A., Black, J., Bohoyo, F., Davey, C., de Santis, L., Escutia Dotti, C., Fremand, A.C., Fretwell, P.T., Gales, J.A., Gao, J., Gasperini, L., Greenbaum, J.S., Henderson Jencks, J., Hogan, K.A., Hong, J.K., Jakobsson, M., Jensen, L., Kool, J., Larin, S., Larter, R.D., Leitchenkov, G.L., Loubrieu, B., Mackay, K., Mayer, L., Millan, R., Morlighem, M., Navidad, F., Nitsche, F.-O., Nogi, Y., Pertuisot, C., Post, A.L., Pritchard, H.D., Purser, A., Rebesco, M., Rignot, E., Roberts, J.L., Rovere, M., Ryzhov, I., Sauli, C., Schmitt, T., Silvano, A., Smith, J.E., Snaith, H., Tate, A.J., Tinto, K., Vandenbossche, P., Weatherall, P., Wintersteller, P., Yang, C., Zhang, T., Arndt, J.E., 2022. The International Bathymetric Chart of the Southern Ocean Version 2 (IBCSO v2). PANGAEA.
- Dowdeswell, J., Bamber, J., 2007. Keel depths of modern Antarctic icebergs and implications for sea-floor scouring in the geological record. *Marine Geology* 243, 120-131.
- Dowdeswell, J., Cofaigh, C.Ó., Noormets, R., Larter, R.D., Hillenbrand, C.-D., Benetti, S., Evans, J., Pudsey, C., 2008a. A major trough-mouth fan on the continental margin of the Bellingshausen Sea, West Antarctica: the Belgica Fan. *Marine Geology* 252, 129-140.
- Dowdeswell, J., Cofaigh, C.Ó., Pudsey, C., 2004. Continental slope morphology and sedimentary processes at the mouth of an Antarctic palaeo-ice stream. *Marine Geology* 204, 203-214.
- Dowdeswell, J., Ottesen, D., Evans, J., Cofaigh, C., Anderson, J., 2008b. Submarine glacial landforms and rates of ice-stream collapse. *Geology* 36, 819-822.
- Dowdeswell, J., Ottesen, D., Rise, L., 2016a. Landforms characteristic of inter-ice stream settings on the Norwegian and Svalbard continental margins. Geological Society, London, *Memoirs* 46, 437-444.
- Dowdeswell, J., Vásquez, M., 2013. Submarine landforms in the fjords of southern Chile: implications for glaciomarine processes and sedimentation in a mild glacier-influenced environment. *Quaternary Science Reviews* 64, 1-19.
- Dowdeswell, J.A., Canals, M., Jakobsson, M., Todd, B.J., Dowdeswell, E.K., Hogan, K.A., 2016b. The variety and distribution of submarine glacial landforms and implications for ice-sheet reconstruction. Geological Society, London, *Memoirs* 46, 519-552.

## References

---

- Dowdeswell, J.A., Forsberg, C.F., 1992. The size and frequency of icebergs and bergy bits derived from tidewater glaciers in Kongsfjorden, northwest Spitsbergen. *Polar Research* 11, 81-91.
- Dowdeswell, J.A., Hogan, K.A., Arnold, N.S., Mugford, R.I., Wells, M., Hirst, J.P.P., Decalf, C., 2015. Sediment-rich meltwater plumes and ice-proximal fans at the margins of modern and ancient tidewater glaciers: Observations and modelling. *Sedimentology* 62, 1665-1692.
- Dowdeswell, J.A., Jakobsson, M., Hogan, K.A., O'Regan, M., Backman, J., Evans, J., Hell, B., Löwemark, L., Marcussen, C., Noormets, R., Cofaigh, C.Ó., Sellén, E., Sölvsten, M., 2010. High-resolution geophysical observations of the Yermak Plateau and northern Svalbard margin: implications for ice-sheet grounding and deep-keeled icebergs. *Quaternary Science Reviews* 29, 3518-3531.
- Dowdeswell, J.A., Ottesen, D., Bellec, V.K., 2020. The changing extent of marine-terminating glaciers and ice caps in northeastern Svalbard since the 'Little Ice Age' from marine-geophysical records. *The Holocene* 30, 389-401.
- Dowdeswell, J.A., Ottesen, D., Rise, L., Craig, J., 2007. Identification and preservation of landforms diagnostic of past ice-sheet activity on continental shelves from three-dimensional seismic evidence. *Geology* 35, 359-362.
- Dowdeswell, J.A., Villinger, H., Whittington, R.J., Marienfeld, P., 1993. Iceberg scouring in Scoresby Sund and on the East Greenland continental shelf. *Marine Geology* 111, 37-53.
- Dunbar, R.B., Anderson, J.B., Domack, E.W., Jacobs, S.S., 1985. Oceanographic influences on sedimentation along the Antarctic continental shelf. *Oceanology of the Antarctic Continental Shelf* 43, 291-312.
- Ehlers, J., Gibbard, P.L., Hughes, P.D., 2018. Quaternary glaciations and chronology, Past glacial environments. Elsevier, pp. 77-101.
- Elverhøi, A., Hooke, R.L., Solheim, A., 1998. Late Cenozoic erosion and sediment yield from the Svalbard–Barents Sea region: implications for understanding erosion of glacierized basins. *Quaternary Science Reviews* 17, 209-241.
- Elverhøi, A., Lønne, Ø., Seland, R., 1983. Glaciomarine sedimentation in a modern fjord environment, Spitsbergen. *Polar Research* 1, 127-150.
- Evans, D.J.A., Phillips, E.R., Hiemstra, J.F., Auton, C.A., 2006a. Subglacial till: Formation, sedimentary characteristics and classification. *Earth-Science Reviews* 78, 115–176.
- Evans, J., Dowdeswell, J.A., Cofaigh, C.Ó., 2004. Late Quaternary submarine bedforms and ice-sheet flow in Gerlache Strait and on the adjacent continental shelf, Antarctic Peninsula. *Journal of Quaternary Science* 19, 397-407.
- Evans, J., Dowdeswell, J.A., Cofaigh, C.Ó., Benham, T.J., Anderson, J.B., 2006b. Extent and dynamics of the West Antarctic Ice Sheet on the outer continental shelf of Pine Island Bay during the last glaciation. *Marine Geology* 230, 53-72.
- Evans, J., Ó Cofaigh, C., Dowdeswell, J.A., Wadhams, P., 2009. Marine geophysical evidence for former expansion and flow of the Greenland Ice Sheet across the north-east Greenland continental shelf. *Journal of Quaternary Science: Published for the Quaternary Research Association* 24, 279-293.
- Evans, J., Pudsey, C., 2002. Sedimentation associated with Antarctic Peninsula ice shelves: implications for palaeoenvironmental reconstructions of glaciomarine sediments. *Journal of the Geological Society* 159, 233-237.
- Evans, J., Pudsey, C.J., ÓCofaigh, C., Morris, P., Domack, E., 2005. Late Quaternary glacial history, flow dynamics and sedimentation along the eastern margin of the Antarctic Peninsula Ice Sheet. *Quaternary Science Reviews* 24, 741-774.
- Eyles, N., Eyles, C.H., Miall, A.D., 1983. Lithofacies types and vertical profile models; an alternative approach to the description and environmental interpretation of glacial diamict and diamictite sequences. *Sedimentology* 30, 393–410.
- Eyring, V., Gillett, N., Achutarao, K., Barimalala, R., Barreiro Parrillo, M., Bellouin, N., Cassou, C., Durack, P., Kosaka, Y., McGregor, S., Min, S., Morgenstern, O., 2021. Human influence on the climate system. In *climate change 2021: the physical science basis. Contribution of*

## References

---

- working group i to the sixth assessment report of the intergovernmental panel on climate change. IPCC Sixth Assessment Report.
- Farías-Barahona, D., Sommer, C., Sauter, T., Bannister, D., Seehaus, T., Malz, P., Casassa, G., Mayewski, P., Turton, J., Braun, M., 2020. Detailed quantification of glacier elevation and mass changes in South Georgia. *Environmental Research Letters* 15.
- Ferrari, R., Jansen, M.F., Adkins, J.F., Burke, A., Stewart, A.L., Thompson, A.F., 2014. Antarctic sea ice control on ocean circulation in present and glacial climates. *Proceedings of the National Academy of Sciences* 111, 8753-8758.
- Flenner, D., 2019. Deglacial sediment variability and unconformity of Jacobsen Trough, South Georgia - New insight into the marine deposition history, FB05, Department of Geosciences. University of Bremen.
- Fogt, R.L., Marshall, G.J., 2020. The Southern Annular Mode: variability, trends, and climate impacts across the Southern Hemisphere. *Wiley Interdisciplinary Reviews: Climate Change* 11, e652.
- Forwick, M., Vorren, T.O., 2011. Stratigraphy and deglaciation of the Isfjorden area, Spitsbergen. *Norwegian Journal of Geology* 90, 163-179.
- Forwick, M., Vorren, T.O., Hald, M., Korsun, S., Roh, Y., Vogt, C., Yoo, K.-C., 2010. Spatial and temporal influence of glaciers and rivers on the sedimentary environment in Sassenfjorden and Tempelfjorden, Spitsbergen. *Geological Society, London, Special Publications* 344, 163-193.
- Foster, L.C., Pearson, E.J., Juggins, S., Hodgson, D.A., Saunders, K.M., Verleyen, E., Roberts, S., 2016. Development of a regional glycerol dialkyl glycerol tetraether (GDGT)-temperature calibration for Antarctic and sub-Antarctic lakes. *Earth and Planetary Science Letters* 433, 370-379.
- Frakes, L.A., 1966. Geologic setting of South Georgia island. *Geological Society of America Bulletin* 77, 1463-1468.
- Frakes, L.A., Francis, J.E., Syktus, J.I., 1992. *Climate modes of the Phanerozoic*. Cambridge University Press, Cambridge.
- Freire, F., Gyllencreutz, R., Greenwood, S.L., Mayer, L., Egilsson, A., Thorsteinsson, T., Jakobsson, M., 2015. High resolution mapping of offshore and onshore glaciogenic features in metamorphic bedrock terrain, Melville Bay, northwestern Greenland. *Geomorphology* 250, 29-40.
- Funk, J., Von Dobeneck, T., Reitz, A., 2004. Integrated rock magnetic and geochemical quantification of redoxomorphic iron mineral diagenesis in Late Quaternary sediments from the Equatorial Atlantic, The South Atlantic in the Late Quaternary: Reconstruction of material budgets and current systems. *Springer*, pp. 237-260.
- Fyke, J., Sergienko, O., Löfverström, M., Price, S., Lenaerts, J.T., 2018. An overview of interactions and feedbacks between ice sheets and the Earth system. *Reviews of Geophysics* 56, 361-408.
- García, J.L., Kaplan, M.R., Hall, B.L., Schaefer, J.M., Vega, R.M., Schwartz, R., Finkel, R., 2012. Glacier expansion in southern Patagonia throughout the Antarctic cold reversal. *Geology* 40, 859-862.
- GEBCO Compilation Group, 2023. GEBCO 2023 Grid.
- Geprägs, P., Torres, M.E., Mau, S., Kasten, S., Römer, M., Bohrmann, G., 2016. Carbon cycling fed by methane seepage at the shallow Cumberland Bay, South Georgia, sub-Antarctic. *Geochemistry, Geophysics, Geosystems* 17, 1401-1418.
- Gerrish, L., 2020. Vector polygons of the Sub-Antarctic coastline (1.0) [Data set], UK Polar Data Centre, Natural Environment Research Council, UK Research & Innovation.
- Gerrish, L., Ireland, L., Fretwell, P., Cooper, P., 2023. High resolution vector polygons of the Antarctic coastline (7.7) [Data set]. UK Polar Data Centre, Natural Environment Research Council, UK Research & Innovation.
- Gersonde, R., Crosta, X., Abelmann, A., Armand, L., 2005. Sea-surface temperature and sea ice distribution of the Southern Ocean at the EPILOG Last Glacial Maximum—a circum-

## References

---

- Antarctic view based on siliceous microfossil records. *Quaternary Science Reviews* 24, 869-896.
- Gibbard, P., Cohen, K.M., 2008. Global chronostratigraphical correlation table for the last 2.7 million years. *Episodes Journal of International Geoscience* 31, 243-247.
- Gille, S.T., 2014. Meridional displacement of the Antarctic circumpolar current. *Philosophical Transactions of the Royal Society A: Mathematical, Physical and Engineering Sciences* 372, 20130273.
- Gille, S.T., McKee, D.C., Martinson, D.G., 2016. Temporal changes in the Antarctic circumpolar current: Implications for the Antarctic continental shelves. *Oceanography* 29, 96-105.
- Gilli, A., Ariztegui, D., Anselmetti, F.S., McKenzie, J.A., Markgraf, V., Hajdas, I., McCulloch, R.D., 2005. Mid-Holocene strengthening of the southern westerlies in South America—sedimentological evidences from Lago Cardiel, Argentina (49 S). *Global and Planetary Change* 49, 75-93.
- Goldner, A., Herold, N., Huber, M., 2014. Antarctic glaciation caused ocean circulation changes at the Eocene–Oligocene transition. *Nature* 511, 574-577.
- Gong, D., Wang, S., 1998. Antarctic oscillation: concept and applications. *Chinese Science Bulletin* 43, 734-738.
- Gong, D., Wang, S., 1999. Definition of Antarctic oscillation index. *Geophysical Research Letters* 26, 459-462.
- Gordon, J.E., Haynes, V.M., Hubbard, A., 2008. Recent glacier changes and climate trends on South Georgia. *Global and Planetary Change* 60, 72–84.
- Graham, A.G.C., Fretwell, P.T., Larter, R.D., Hodgson, D.A., Wilson, C.K., Tate, A.J., Morris, P., 2008. A new bathymetric compilation highlighting extensive paleo-ice sheet drainage on the continental shelf, South Georgia, sub-Antarctica. *Geochemistry, Geophysics, Geosystems* 9.
- Graham, A.G.C., Hodgson, D.A., 2016. Terminal moraines in the fjord basins of sub-Antarctic South Georgia. *Geological Society, London, Memoirs* 46, 67-68.
- Graham, A.G.C., Kuhn, G., Meisel, O., Hillenbrand, C.-D., Hodgson, D.A., Ehrmann, W., Wacker, L., Wintersteller, P., Dos Santos Ferreira, C., Römer, M., White, D., Bohrmann, G., 2017. Major advance of South Georgia glaciers during the Antarctic Cold Reversal following extensive sub-Antarctic glaciation. *Nature Communications* 8, 14798.
- Graham, A.G.C., Larter, R.D., Gohl, K., Hillenbrand, C.-D., Smith, J.A., Kuhn, G., 2009. Bedform signature of a West Antarctic palaeo-ice stream reveals a multi-temporal record of flow and substrate control. *Quaternary Science Reviews* 28, 2774-2793.
- Greenbaum, J., Blankenship, D., Young, D., Richter, T., Roberts, J., Aitken, A., Legresy, B., Schroeder, D., Warner, R., Van Ommen, T., Siegert, M.J., 2015. Ocean access to a cavity beneath Totten Glacier in East Antarctica. *Nature Geoscience* 8, 294-298.
- Greenwood, S.L., Clason, C.C., Helanow, C., Margold, M., 2016. Theoretical, contemporary observational and palaeo-perspectives on ice sheet hydrology: processes and products. *Earth-Science Reviews* 155, 1-27.
- Greenwood, S.L., Kleman, J., 2010. Glacial landforms of extreme size in the Keewatin sector of the Laurentide Ice Sheet. *Quaternary Science Reviews* 29, 1894-1910.
- Hagemann, J., 2023. Subantarctic Pacific biomarker-based upper ocean temperature and Patagonian Ice Sheet dynamics during the past 160,000 years, Faculty of Geosciences. University of Bremen.
- Haslett, J., Parnell, A., 2008. A simple monotone process with application to radiocarbon-dated depth chronologies. *Journal of the Royal Statistical Society: Series C (Applied Statistics)* 57, 399–418.
- Hass, H.C., Kuhn, G., Monien, P., Brumsack, H.-J., Forwick, M., 2010. Climate fluctuations during the past two millennia as recorded in sediments from Maxwell Bay, South Shetland Islands, West Antarctica. *Geological Society, London, Special Publications* 344, 243–260.

## References

---

- Hayashi, T., Yamanaka, T., Hikasa, Y., Sato, M., Kuwahara, Y., Ohno, M., 2020. Latest Pliocene Northern Hemisphere glaciation amplified by intensified Atlantic meridional overturning circulation. *Communications Earth & Environment* 1, 25.
- Hays, J.D., Lozano, J.A., Shackleton, N., Irving, G., 1976. Reconstruction of the Atlantic and western Indian Ocean sectors of the 18,000 BP Antarctic Ocean, in: R.M., C., Hays, J.D. (Eds.), *Investigation of Late Quaternary Paleoceanography and Paleoclimatology*.
- Heaton, T., Bard, E., Ramsey, C.B., Butzin, M., Hatte, C., Hughen, K., Köhler, P., Reimer, P., 2022. A Response to Community Questions on the Marine20 Radiocarbon Age Calibration Curve: Marine Reservoir Ages and the Calibration of 14C samples from the Oceans. *Radiocarbon*, 1-27.
- Heaton, T.J., Köhler, P., Butzin, M., Bard, E., Reimer, R.W., Austin, W.E.N., Bronk Ramsey, C., Grootes, P.M., Hughen, K.A., Kromer, B., Reimer, P.J., Adkins, J., Burke, A., Cook, M.S., Olsen, J., Skinner, L.C., 2020. Marine20—The Marine Radiocarbon Age Calibration Curve (0–55,000 cal BP). *Radiocarbon* 62, 779-820.
- Heredia Barión, P., Roberts, S.J., Spiegel, C., Binnie, S.A., Wacker, L., Davies, J., Gabriel, I., Jones, V.J., Blockley, S., Pearson, E.J., Foster, L., Davies, S., Roland, T.P., Hocking, E.P., Bentley, M.J., Hodgson, D.A., Hayward, C.L., McCulloch, R.D., Strelin, J.A., Kuhn, G., 2023a. Holocene deglaciation and glacier readvances on the Fildes Peninsula and King George Island (Isla 25 de Mayo), South Shetland Islands, NW Antarctic Peninsula. *The Holocene*, 09596836231157059.
- Heredia Barión, P.A., Strelin, J.A., Roberts, S.J., Spiegel, C., Wacker, L., Niedermann, S., Bentley, M.J., Pearson, E.J., Czalbowski, N.T.M., Davies, S.J., Schnetger, B., Grosjean, M., Arcusa, S., Perren, B., Hocking, E.P., Kuhn, G., 2023b. The impact of Holocene deglaciation and glacial dynamics on the landscapes and geomorphology of Potter Peninsula, King George Island (Isla 25 Mayo), NW Antarctic Peninsula. *Frontiers in Earth Science* 10, 1073075.
- Hillenbrand, C.-D., Larter, R.D., Dowdeswell, J., Ehrmann, W., Cofaigh, C.Ó., Benetti, S., Graham, A.G., Grobe, H., 2010. The sedimentary legacy of a palaeo-ice stream on the shelf of the southern Bellingshausen Sea: Clues to West Antarctic glacial history during the Late Quaternary. *Quaternary Science Reviews* 29, 2741-2763.
- Hillenbrand, C.-D., Smith, J.A., Hodell, D.A., Greaves, M., Poole, C.R., Kender, S., Williams, M., Andersen, T.J., Jernas, P.E., Elderfield, H., Klages, J.P., Roberts, S.J., Gohl, K., Larter, R.D., Kuhn, G., 2017. West Antarctic Ice Sheet retreat driven by Holocene warm water incursions. *Nature* 547, 43-48.
- Hodgson, D.A., Graham, A.G.C., Griffiths, H.J., Roberts, S.J., Cofaigh, C.Ó., Bentley, M.J., Evans, D.J.A., 2014a. Glacial history of sub-Antarctic South Georgia based on the submarine geomorphology of its fjords. *Quaternary Science Reviews* 89, 129–147.
- Hodgson, D.A., Graham, A.G.C., Roberts, S.J., Bentley, M.J., Cofaigh, C.Ó., Verleyen, E., Vyverman, W., Jomelli, V., Favier, V., Brunstein, D., Verfaillie, D., Colhoun, E.A., Saunders, K.M., Selkirk, P.M., Mackintosh, A., Hedding, D.W., Nel, W., Hall, K., McGlone, M.S., van der Putten, N., Dickens, W.A., Smith, J.A., 2014b. Terrestrial and submarine evidence for the extent and timing of the Last Glacial Maximum and the onset of deglaciation on the maritime-Antarctic and sub-Antarctic islands. *Quaternary Science Reviews* 100, 137–158.
- Hogan, K.A., Dix, J.K., Lloyd, J.M., Long, A.J., Cotterill, C.J., 2011. Seismic stratigraphy records the deglacial history of Jakobshavn Isbræ, West Greenland. *Journal of Quaternary Science* 26, 757–766.
- Hogan, K.A., Ó Cofaigh, C., Jennings, A.E., Dowdeswell, J.A., Hiemstra, J.F., 2016. Deglaciation of a major palaeo-ice stream in Disko Trough, West Greenland. *Quaternary Science Reviews* 147, 5–26.
- Hogg, O., Huvenne, V., Griffiths, H., Dorschel, B., Linse, K., 2017. A Bathymetric Compilation of South Georgia, 1985-2015.
- Hogg, O.T., Huvenne, V.A., Griffiths, H.J., Dorschel, B., Linse, K., 2016. Landscape mapping at sub-Antarctic South Georgia provides a protocol for underpinning large-scale marine protected areas. *Scientific Reports* 6, 1-15.



## References

---

- Holland, D.M., Thomas, R.H., De Young, B., Ribergaard, M.H., Lyberth, B., 2008. Acceleration of Jakobshavn Isbræ triggered by warm subsurface ocean waters. *Nature Geoscience* 1, 659-664.
- Hughes, A.L., Gyllencreutz, R., Lohne, Ø.S., Mangerud, J., Svendsen, J.I., 2016. The last Eurasian ice sheets—a chronological database and time-slice reconstruction, DATED-1. *Boreas* 45, 1-45.
- Hunter, L.E., Powell, R.D., Smith, G.W., 1996. Facies architecture and grounding-line fan processes of morainal banks during the deglaciation of coastal Maine. *Geological Society of America Bulletin* 108, 1022-1038.
- Inman, D.L., Nordstrom, C.E., Flick, R.E., 1976. Currents in submarine canyons: An air-sea-land interaction. *Annual review of fluid mechanics* 8, 275-310.
- Ishman, S.E., Domack, E.W., 1994. Oceanographic controls on benthic foraminifers from the Bellingshausen margin of the Antarctic Peninsula. *Marine Micropaleontology* 24, 119-155.
- Ishman, S.E., Szymcek, P., 2003. Foraminiferal Distributions in the Former Larsen-A Ice Shelf and Prince Gustav Channel Refion, Eastern Antarctic Peninsula Margin: A Baseline for Holocene Paleoenvironmental Change, *Antarctic Peninsula Climate Variability: Historical and Paleoenvironmental Perspectives*, pp. 239-260.
- Jomelli, V., Favier, V., Vuille, M., Braucher, R., Martin, L., Blard, P.-H., Colose, C., Brunstein, D., He, F., Khodri, M., Bourlès, D.L., Leanni, L., Rinterknecht, V., Grancher, D., Francou, B., Ceballos, J.L., Fonseca, H., Liu, Z., Otto-Bliesner, B.L., 2014. A major advance of tropical Andean glaciers during the Antarctic cold reversal. *Nature* 513, 224-228.
- Jomelli, V., Mokadem, F., Schimmelpfennig, I., Chapron, E., Rinterknecht, V., Favier, V., Verfaillie, D., Brunstein, D., Legentil, C., Michel, E., Swingedouw, D., Jaouen, A., Aumaitre, G., Bourlès, D.L., Keddadouche, K., 2017. Sub-Antarctic glacier extensions in the Kerguelen region (49 S, Indian Ocean) over the past 24,000 years constrained by <sup>36</sup>Cl moraine dating. *Quaternary Science Reviews* 162, 128-144.
- Jouzel, J., Vaikmae, R., Petit, J., Martin, M., Duclos, Y., Stievenard, M., Lorius, C., Toots, M., Mélières, M., Burckle, L., Barkov, N., Kotlyakov, V.M., 1995. The two-step shape and timing of the last deglaciation in Antarctica. *Climate Dynamics* 11, 151-161.
- Jovane, L., Coccioni, R., Marsili, A., Acton, G., Koeberl, C., Montanari, A., 2009. The late Eocene greenhouse-icehouse transition: Observations from the Massignano global stratotype section and point (GSSP). *Geol. Soc. Am., Special Paper* 452, 149-168.
- Kaplan, M., Fogwill, C., Sugden, D., Hulton, N., Kubik, P., Freeman, S., 2008. Southern Patagonian glacial chronology for the Last Glacial period and implications for Southern Ocean climate. *Quaternary Science Reviews* 27, 284-294.
- Kars, M., Musgrave, R.J., Hoshino, T., Jonas, A.S., Bauersachs, T., Inagaki, F., Kodama, K., 2018. Magnetic mineral diagenesis in a high temperature and deep methanic zone in Izu rear arc marine sediments, Northwest Pacific Ocean. *Journal of Geophysical Research: Solid Earth* 123, 8331-8348.
- Karukäpp, R., 2004. Late-Glacial ice streams of the southeastern sector of the Scandinavian Ice Sheet and the asymmetry of its landforms. *Baltica* 17, 41-48.
- Kasten, S., 2023. The Expedition PS133/2 of the Research Vessel POLARSTERN to the Scotia Sea in 2022. *Berichte zur Polar-und Meeresforschung= Reports on polar and marine research* 775.
- Kehrl, L.M., Hawley, R.L., Powell, R.D., Brigham-Grette, J., 2011. Glacimarine sedimentation processes at Kronebreen and Kongsvegen, Svalbard. *Journal of Glaciology* 57, 841-847.
- Kellogg, T.B., Kellogg, D.E., 1988. Antarctic cryogenic sediments: biotic and inorganic facies of ice shelf and marine-based ice sheet environments. *Palaeogeography, Palaeoclimatology, Palaeoecology* 67, 51-74.
- Kempf, P., Forwick, M., Laberg, J.S., Vorren, T.O., 2013. Late Weichselian and Holocene sedimentary palaeoenvironment and glacial activity in the high-arctic van Keulenfjorden, Spitsbergen. *The Holocene* 23, 1607-1618.

- Kennett, J.P., 1977. Cenozoic evolution of Antarctic glaciation, the circum-Antarctic Ocean, and their impact on global paleoceanography. *Journal of Geophysical Research* 82, 3843-3860.
- Kilfeather, A.A., Cofaigh, C.Ó., Lloyd, J.M., Dowdeswell, J.A., Xu, S., Moreton, S.G., 2011. Ice-stream retreat and ice-shelf history in Marguerite Trough, Antarctic Peninsula: Sedimentological and foraminiferal signatures. *GSA Bulletin* 123, 997-1015.
- Kirkham, J.D., Hogan, K.A., Larter, R.D., Arnold, N.S., Ely, J.C., Clark, C.D., Self, E., Games, K., Huuse, M., Stewart, M.A., Ottesen, D., Dowdeswell, J.A., 2022. Tunnel valley formation beneath deglaciating mid-latitude ice sheets: Observations and modelling. *Quaternary Science Reviews*, 107680.
- Kirkham, J.D., Hogan, K.A., Larter, R.D., Arnold, N.S., Nitsche, F.O., Kuhn, G., Gohl, K., Anderson, J.B., Dowdeswell, J.A., 2020. Morphometry of bedrock meltwater channels on Antarctic inner continental shelves: Implications for channel development and subglacial hydrology. *Geomorphology* 370, 107369.
- Kirshner, A.E., Anderson, J.B., Jakobsson, M., O'Regan, M., Majewski, W., Nitsche, F.O., 2012. Post-LGM deglaciation in Pine Island Bay, West Antarctica. *Quaternary Science Reviews* 38, 11-26.
- Klages, J.P., Kuhn, G., Hillenbrand, C.-D., Graham, A.G., Smith, J.A., Larter, R.D., Gohl, K., Wacker, L., 2014. Retreat of the West Antarctic Ice Sheet from the western Amundsen Sea shelf at a pre-or early LGM stage. *Quaternary Science Reviews* 91, 1-15.
- Klages, J.P., Kuhn, G., Hillenbrand, C.-D., Graham, A.G.C., Smith, J.A., Larter, R.D., Gohl, K., 2013. First geomorphological record and glacial history of an inter-ice stream ridge on the West Antarctic continental shelf. *Quaternary Science Reviews* 61, 47-61.
- Kohfeld, K.E., Graham, R.M., de Boer, A.M., Sime, L.C., Wolff, E.W., Le Quéré, C., Bopp, L., 2013. Southern Hemisphere westerly wind changes during the Last Glacial Maximum: paleo-data synthesis. *Quaternary Science Reviews* 68, 76-95.
- Kuhn, G., 2013. Don't forget the salty soup: Calculations for bulk marine geochemistry and radionuclide geochronology. *Mineralogical Society of Great Britain and Ireland*.
- Kuhn, G., Hillenbrand, C.-D., Kasten, S., Smith, J.A., Nitsche, F.O., Frederichs, T., Wiers, S., Ehrmann, W., Klages, J.P., Mogollón, J.M., 2017. Evidence for a palaeo-subglacial lake on the Antarctic continental shelf. *Nature Communications* 8, 15591.
- Kuvaas, B., Kristoffersen, Y., Guseva, J., Leitchenkov, G., Gandjukhin, V., Løvås, O., Sand, M., Brekke, H., 2005. Interplay of turbidite and contourite deposition along the Cosmonaut Sea/Enderby Land margin, East Antarctica. *Marine Geology* 217, 143-159.
- Kuvaas, B., Leitchenkov, G., 1992. Glaciomarine turbidite and current controlled deposits in Prydz Bay, Antarctica. *Marine Geology* 108, 365-381.
- Laberg, J., Camerlenghi, A., 2008. The significance of contourites for submarine slope stability. *Developments in Sedimentology* 60, 537-556.
- Laberg, J., Vorren, T., 1995. Late Weichselian submarine debris flow deposits on the Bear Island Trough mouth fan. *Marine Geology* 127, 45-72.
- Lamy, F., Kilian, R., Arz, H.A., Francois, J.-P., Kaiser, J., Prange, M., Steinke, T., 2010. Holocene changes in the position and intensity of the southern westerly wind belt. *Nature Geoscience* 3, 695-699.
- Lang, N., Wolff, E.W., 2011. Interglacial and glacial variability from the last 800 ka in marine, ice and terrestrial archives. *Climate of the Past* 7, 361-380.
- Langner, M., Mulitza, S., 2019. Technical note: PaleoDataView – a software toolbox for the collection, homogenization and visualization of marine proxy data. *Clim. Past* 15, 2067-2072.
- Lee, D.Y., Petersen, M.R., Lin, W., 2019. The southern annular mode and southern ocean surface westerly winds in E3SM. *Earth and Space Science* 6, 2624-2643.
- Lepp, A.P., Simkins, L.M., Anderson, J.B., Clark, R.W., Wellner, J.S., Hillenbrand, C.-D., Smith, J.A., Lehrmann, A.A., Totten, R., Larter, R.D., Hogan, K.A., Nitsche, F.O., Graham, A.G.C., Wacker, L., 2022. Sedimentary signatures of persistent subglacial meltwater drainage from Thwaites Glacier, Antarctica. *Frontiers in Earth Science* 10.

## References

---

- Lešić, N.-M., Streuff, K.T., Bohrmann, G., Kuhn, G., 2022. Glacimarine sediments from outer Drygalski Trough, sub-Antarctic South Georgia—evidence for extensive glaciation during the Last Glacial Maximum. *Quaternary Science Reviews* 292, 107657.
- Lešić, N.-M., Streuff, K.T., Bohrmann, G., Kuhn, G., subm. Spatial and temporal variability in Holocene trough-fill sediments, King Haakon Trough System, sub-Antarctic South Georgia. *Quaternary Science Advances*.
- Lešić, N.-M., Streuff, K.T., Titschack, J., Von Dobeneck, T., Kuhn, G., Bohrmann, G., in prep. Climate-driven Holocene sedimentation in King Haakon Trough System, sub-Antarctic South Georgia
- Leventer, A., Domack, E., Pike, J., Stickley, C., Maddison, E., Brachfeld, S.A., Manley, P., McClennen, C., 2006. Marine sediment record from the East Antarctic margin reveals dynamics of ice sheet recession. *GSA TODAY*, 16(12), 4.
- Liau, J.-R., Chao, B.F., 2017. Variation of Antarctic circumpolar current and its intensification in relation to the southern annular mode detected in the time-variable gravity signals by GRACE satellite. *Earth, Planets and Space* 69, 1-9.
- Livermore, R., Hillenbrand, C.D., Meredith, M., Eagles, G., 2007. Drake Passage and Cenozoic climate: an open and shut case? *Geochemistry, Geophysics, Geosystems* 8.
- Lloyd, J.M., 2006. Late Holocene environmental change in Disko Bugt, west Greenland: interaction between climate, ocean circulation and Jakobshavn Isbrae. *Boreas* 35, 35-49.
- Lucchi, R.G., Pedrosa, M.T., Camerlenghi, A., Urgeles, R., De Mol, B., Rebesco, M., 2012. Recent submarine landslides on the continental slope of Storfjorden and Kveithola Trough-Mouth Fans (north west Barents Sea), *Submarine Mass Movements and Their Consequences: 5th International Symposium*. Springer, pp. 735-745.
- Lundqvist, J., 1981. Moraine morphology: terminological remarks and regional aspects. *Geografiska Annaler: Series A, Physical Geography* 63, 127-138.
- Macdonald, D.I.M., Storey, B.C., Thomson, J.W., 1987. South Georgia BAS GEOMAP Series, Sheet 1. British Antarctic Survey, Cambridge, p. 1:250000 Geological map and supplementary text 250063 pp.
- MacLean, B., Blasco, S., Bennett, R., Clarke, J.H., Patton, E., 2016. Crag-and-tail features, Amundsen Gulf, Canadian Arctic Archipelago, in: Dowdeswell, J.A., Canals, M., Jakobsson, M., Todd, B.J., Dowdeswell, E.K., Hogan, K.A. (Eds.), *Atlas of Submarine Glacial Landforms: Modern, Quaternary and Ancient*.
- Mair, B., 1987. The Geology of South Georgia: VI. Larsen Harbour Formation, Scientific reports. British Antarctic Survey.
- Masson-Delmotte, V., Stenni, B., Jouzel, J., 2004. Common millennial-scale variability of Antarctic and Southern Ocean temperatures during the past 5000 years reconstructed from the EPICA Dome C ice core. *The Holocene* 14, 145-151.
- Masson-Delmotte, V., Stenni, B., Pol, K., Braconnot, P., Cattani, O., Falourd, S., Kageyama, M., Jouzel, J., Landais, A., Minster, B., Barnola, J.M., Chappellaz, J., Krinner, G., Johnson, J., Röthlisberger, R., Hansen, J., Mikolajewicz, U., Otto-Bliesner, B., 2010. EPICA Dome C record of glacial and interglacial intensities. *Quaternary Science Reviews* 29, 113-128.
- Masson-Delmotte, V., Zhai, P., Pörtner, H.-O., Roberts, D., Skea, J., Shukla, P.R., Pirani, A., Moufouma-Okia, W., Péan, C., Pidcock, R., Connors, S., Matthews, J.B.R., Chen, Y., Zhou, X., Gomis, M.I., Lonnoy, E., Maycock, T., Tignor, M., Waterfield, T., 2022. Global Warming of 1.5 C: An IPCC special report on the impacts of global warming of 1.5 C above pre-industrial levels and related global greenhouse gas emission pathways, in the context of strengthening the global response to the threat of climate change, sustainable development, and efforts to eradicate poverty. Cambridge University Press, Cambridge, UK and New York, NY, USA, p. 616 pp.
- Masson, V., Vimeux, F., Jouzel, J., Morgan, V., Delmotte, M., Ciais, P., Hammer, C., Johnsen, S., Lipenkov, V.Y., Mosley-Thompson, E., Petit, J.-R., Steig, E.J., Stievenard, M., Vaikmae, R., 2000. Holocene climate variability in Antarctica based on 11 ice-core isotopic records. *Quaternary Research* 54, 348-358.

## References

---

- Matano, R.P., Combes, V., Young, E.F., Meredith, M.P., 2020. Modeling the Impact of Ocean Circulation on Chlorophyll Blooms Around South Georgia, Southern Ocean. *Journal of Geophysical Research: Oceans* 125, e2020JC016391.
- McCave, I., Crowhurst, S., Kuhn, G., Hillenbrand, C., Meredith, M., 2014. Minimal change in Antarctic Circumpolar Current flow speed between the last glacial and Holocene. *Nature Geoscience* 7, 113-116.
- McCulloch, R.D., Blaikie, J., Jacob, B., Mansilla, C.A., Morello, F., De Pol-Holz, R., San Román, M., Tisdall, E., Torres, J., 2020. Late glacial and Holocene climate variability, southernmost Patagonia. *Quaternary Science Reviews* 229, 106131.
- Meredith, M., Watkins, J., Murphy, E., Ward, P., Bone, D., Thorpe, S., Grant, S., Ladkin, R., 2003. Southern ACC Front to the northeast of South Georgia: Pathways, characteristics, and fluxes. *Journal of Geophysical Research: Oceans* 108.
- Meredith, M.P., Brandon, M.A., Murphy, E.J., Trathan, P.N., Thorpe, S.E., Bone, D.G., Chernyshkov, P.P., Sushin, V.A., 2005. Variability in hydrographic conditions to the east and northwest of South Georgia, 1996–2001. *Journal of Marine Systems* 53, 143-167.
- Meredith, M.P., Hogg, A.M., 2006. Circumpolar response of Southern Ocean eddy activity to a change in the Southern Annular Mode. *Geophysical Research Letters* 33.
- Meredith, M.P., Woodworth, P.L., Hughes, C.W., Stepanov, V., 2004. Changes in the ocean transport through Drake Passage during the 1980s and 1990s, forced by changes in the Southern Annular Mode. *Geophysical Research Letters* 31.
- Michels, K.H., Rogenhagen, J., Kuhn, G., 2001. Recognition of contour-current influence in mixed contourite-turbidite sequences of the western Weddell Sea, Antarctica. *Marine Geophysical Researches* 22, 465-485.
- Mollenhauer, G., Grotheer, H., Gentz, T., Bonk, E., Hefter, J., 2021. Standard operation procedures and performance of the MICADAS radiocarbon laboratory at Alfred Wegener Institute (AWI), Germany. *Nuclear Instruments and Methods in Physics Research Section B: Beam Interactions with Materials and Atoms* 496, 45-51.
- Moreno, P., Henríquez, W., Pesce, O., Henríquez, C., Fletcher, M., Garreaud, R., Villa-Martínez, R., 2021. An early Holocene westerly minimum in the southern mid-latitudes. *Quaternary Science Reviews* 251, 106730.
- Moreno, P., Kaplan, M., François, J., Villa-Martínez, R., Moy, C., Stern, C., Kubik, P., 2009. Renewed glacial activity during the Antarctic cold reversal and persistence of cold conditions until 11.5 ka in southwestern Patagonia. *Geology* 37, 375-378.
- Moreno, P., Vilanova, I., Villa-Martínez, R., Dunbar, R., Mucciarone, D., Kaplan, M., Garreaud, R., Rojas, M., Moy, C., Pol-Holz, D., Lambert, F., 2018. Onset and evolution of southern annular mode-like changes at centennial timescale. *Scientific Reports* 8, 1-9.
- Morlighem, M., Bondzio, J., Seroussi, H., Rignot, E., Larour, E., Humbert, A., Rebuffi, S., 2016. Modeling of Store Gletscher's calving dynamics, West Greenland, in response to ocean thermal forcing. *Geophysical Research Letters* 43, 2659-2666.
- Mörner, N.-A., Sylwan, C., 1989. Magnetostratigraphy of the Patagonian moraine sequence at Lago Buenos Aires. *Journal of South American Earth Sciences* 2, 385-389.
- Moros, M., Jensen, K.G., Kuijpers, A., 2006. Mid-to late-Holocene hydrological and climatic variability in Disko Bugt, central West Greenland. *The Holocene* 16, 357-367.
- Motyka, R.J., Hunter, L., Echelmeyer, K.A., Connor, C., 2003. Submarine melting at the terminus of a temperate tidewater glacier, LeConte Glacier, Alaska, USA. *Annals of Glaciology* 36, 57-65.
- Mudelsee, M., Raymo, M.E., 2005. Slow dynamics of the Northern Hemisphere glaciation. *Paleoceanography* 20.
- Müller, G., 1967. *Methods in sedimentary petrology*. E. Schweizerbart'sche Verlagsbuchhandlung (Nägele u. Obermiller).
- Müller, P.J., Schneider, R., 1993. An automated leaching method for the determination of opal in sediments and particulate matter. *Deep Sea Research Part I: Oceanographic Research Papers* 40, 425-444.

## References

---

- Murdmaa, I., Ivanova, E., Duplessy, J.-C., Levitan, M., Khusid, T., Bourtman, M., Alekhina, G., Alekseeva, T., Belousov, M., Serova, V., 2006. Facies system of the Eastern Barents Sea since the last glaciation to present. *Marine Geology* 230, 275-303.
- Murphy, E., Hofmann, E., Watkins, J., Johnston, N., Piñones, A., Ballerini, T., Hill, S., Trathan, P., Tarling, G., Cavanagh, R., Young, E.F., Thorpe, S.E., Fretwell, P., 2013. Comparison of the structure and function of Southern Ocean regional ecosystems: the Antarctic Peninsula and South Georgia. *Journal of Marine Systems* 109, 22-42.
- Nel, W., Hedding, D.W., Rudolph, E.M., 2023. The sub-Antarctic islands are increasingly warming in the 21st century. *Antarctic Science* 35, 124-126.
- Nicholls, K.W., Østerhus, S., Makinson, K., Gammelsrød, T., Fahrbach, E., 2009. Ice-ocean processes over the continental shelf of the southern Weddell Sea, Antarctica: A review. *Reviews of Geophysics* 47.
- Nienow, P., Sharp, M., Willis, I., 1998. Seasonal changes in the morphology of the subglacial drainage system, Haut Glacier d'Arolla, Switzerland. *Earth Surface Processes and Landforms* 23, 825-843.
- Nitsche, F.O., Gohl, K., Larter, R.D., Hillenbrand, C.-D., Kuhn, G., Smith, J., Jacobs, S., Anderson, J., Jakobsson, M., 2013. Paleo ice flow and subglacial meltwater dynamics in Pine Island Bay, West Antarctica. *The Cryosphere* 7, 249-262.
- Ó Cofaigh, C., 1996. Tunnel valley genesis. *Progress in physical geography* 20, 1-19.
- Ó Cofaigh, C., Andrews, J., Jennings, A., Dowdeswell, J., Hogan, K., Kilfeather, A., Sheldon, C., 2013. Glacimarine lithofacies, provenance and depositional processes on a West Greenland trough-mouth fan. *Journal of Quaternary Science* 28, 13-26.
- Ó Cofaigh, C., Dowdeswell, J.A., 2001. Laminated sediments in glacimarine environments: diagnostic criteria for their interpretation. *Quaternary Science Reviews* 20, 1411-1436.
- Ó Cofaigh, C., Dowdeswell, J.A., Allen, C.S., Hiemstra, J.F., Pudsey, C.J., Evans, J., Evans, D.J., 2005a. Flow dynamics and till genesis associated with a marine-based Antarctic palaeo-ice stream. *Quaternary Science Reviews* 24, 709-740.
- Ó Cofaigh, C., Dowdeswell, J.A., Evans, J., Kenyon, N.H., Taylor, J., Mienert, J., Wilken, M., 2004. Timing and significance of glacially influenced mass-wasting in the submarine channels of the Greenland Basin. *Marine Geology* 207, 39-54.
- Ó Cofaigh, C., Dowdeswell, J.A., Grobe, H., 2001. Holocene glacimarine sedimentation, inner Scoresby Sund, East Greenland: the influence of fast-flowing ice-sheet outlet glaciers. *Marine Geology* 175, 103-129.
- Ó Cofaigh, C., Evans, J., Dowdeswell, J.A., Larter, R.D., 2007. Till characteristics, genesis and transport beneath Antarctic paleo-ice streams. *Journal of Geophysical Research: Earth Surface* 112.
- Ó Cofaigh, C., Hogan, K., Dowdeswell, J., Streuff, K., 2016. Stratified glacimarine basin-fills in West Greenland fjords. *Geological Society, London, Memoirs* 46, 99-100.
- Ó Cofaigh, C., Larter, R.D., Dowdeswell, J.A., Hillenbrand, C.D., Pudsey, C.J., Evans, J., Morris, P., 2005b. Flow of the West Antarctic Ice Sheet on the continental margin of the Bellingshausen Sea at the Last Glacial Maximum. *Journal of Geophysical Research: Solid Earth* 110.
- Ó Cofaigh, C., Pudsey, C.J., Dowdeswell, J.A., Morris, P., 2002. Evolution of subglacial bedforms along a paleo-ice stream, Antarctic Peninsula continental shelf. *Geophysical Research Letters* 29, 41-1 - 41-4.
- Oppedal, L.T., Bakke, J., Paasche, Ø., Werner, J.P., van der Bilt, W.G.M., 2018. Cirque Glacier on South Georgia Shows Centennial Variability over the Last 7000 Years. *Frontiers in Earth Science* 6.
- Orsi, A.H., Harris, U., 2019. Fronts of the Antarctic Circumpolar Current - GIS data. Australian Antarctic Data Centre.
- Orsi, A.H., Whitworth, T., Nowlin, W.D., 1995. On the meridional extent and fronts of the Antarctic Circumpolar Current. *Deep Sea Research Part I: Oceanographic Research Papers* 42, 641-673.

- Ottesen, D., Dowdeswell, J., 2006. Assemblages of submarine landforms produced by tidewater glaciers in Svalbard. *Journal of Geophysical Research: Earth Surface* 111.
- Ottesen, D., Dowdeswell, J., Bellec, V., Bjarnadóttir, L., 2017. The geomorphic imprint of glacier surges into open-marine waters: examples from eastern Svalbard. *Marine Geology* 392, 1-29.
- Ottesen, D., Dowdeswell, J., Rise, L., 2005. Submarine landforms and the reconstruction of fast-flowing ice streams within a large Quaternary ice sheet: The 2500-km-long Norwegian-Svalbard margin (57–80 N). *Geological Society of America Bulletin* 117, 1033-1050.
- Ottesen, D., Dowdeswell, J.A., 2009. An inter-ice-stream glaciated margin: Submarine landforms and a geomorphic model based on marine-geophysical data from Svalbard. *Geological Society of America Bulletin* 121, 1647-1665.
- Ottesen, D., Dowdeswell, J.A., Landvik, J.Y., Mienert, J., 2007. Dynamics of the Late Weichselian ice sheet on Svalbard inferred from high-resolution sea-floor morphology. *Boreas* 36, 286-306.
- Past Interglacials Working Group of PAGES, 2016. Interglacials of the last 800,000 years. *Reviews of Geophysics* 54, 162-219.
- Patton, H., Andreassen, K., Bjarnadóttir, L.R., Dowdeswell, J.A., Winsborrow, M.C., Noormets, R., Polyak, L., Auriac, A., Hubbard, A., 2015. Geophysical constraints on the dynamics and retreat of the Barents Sea ice sheet as a paleobenchmark for models of marine ice sheet deglaciation. *Reviews of Geophysics* 53, 1051-1098.
- Pedro, J.B., Bostock, H.C., Bitz, C.M., He, F., Vandergoes, M.J., Steig, E.J., Chase, B.M., Krause, C.E., Rasmussen, S.O., Markle, B.R., Cortese, G., 2016. The spatial extent and dynamics of the Antarctic Cold Reversal. *Nature Geoscience* 9, 51–55.
- Peltier, C., Kaplan, M.R., Birkel, S.D., Soteres, R.L., Sagredo, E.A., Aravena, J.C., Araos, J., Moreno, P.I., Schwartz, R., Schaefer, J.M., 2021. The large MIS 4 and long MIS 2 glacier maxima on the southern tip of South America. *Quaternary Science Reviews* 262, 106858.
- Pieńkowski, A.J., England, J.H., Furze, M.F., Blasco, S., Mudie, P.J., MacLean, B., 2013. 11,000 yrs of environmental change in the Northwest Passage: A multiproxy core record from central Parry Channel, Canadian High Arctic. *Marine Geology* 341, 68-85.
- Pieńkowski, A.J., England, J.H., Furze, M.F., Marret, F., Eynaud, F., Vilks, G., MacLean, B., Blasco, S., Scourse, J.D., 2012. The deglacial to postglacial marine environments of SE Barrow Strait, Canadian Arctic Archipelago. *Boreas* 41, 141-179.
- Porrman, S., Gebhardt, C., subm. to PANGAEA. Physical properties of sediment core PS133/2\_17-13
- Post, A., O'Neel, S., Motyka, R.J., Streveler, G., 2011. A complex relationship between calving glaciers and climate. *Eos, Transactions American Geophysical Union* 92, 305-306.
- Powell, R.D., 1984. Glacimarine processes and inductive lithofacies modelling of ice shelf and tidewater glacier sediments based on Quaternary examples. *Marine Geology* 57, 1-52.
- Putnam, A.E., Denton, G.H., Schaefer, J.M., Barrell, D.J.A., Andersen, B.G., Finkel, R.C., Schwartz, R., Doughty, A.M., Kaplan, M.R., Schlüchter, C., 2010. Glacier advance in southern middle-latitudes during the Antarctic Cold Reversal. *Nature Geoscience* 3, 700–704.
- R Core Team, 2021. A language and environment for statistical computing.
- R Studio Team, 2021. RStudio: Integrated development environment for R. RStudio, PBC, Boston, MA.
- Rabassa, J., Coronato, A., Bujalesky, G., Salemme, M., Roig, C., Meglioli, A., Heusser, C., Gordillo, S., Roig, F., Borromei, A., Quattrocchio, M., 2000. Quaternary of Tierra del Fuego, southernmost South America: an updated review. *Quaternary International* 68, 217-240.
- Raymo, M.E., Ruddiman, W.F., 1992. Tectonic forcing of late Cenozoic climate. *Nature* 359, 117-122.
- Rebesco, M., Hernández-Molina, F.J., Van Rooij, D., Wåhlin, A., 2014. Contourites and associated sediments controlled by deep-water circulation processes: State-of-the-art and future considerations. *Marine Geology* 352, 111-154.

## References

---

- Reimer, P.J., Austin, W.E.N., Bard, E., Bayliss, A., Blackwell, P.G., Ramsey, C.B., Butzin, M., Cheng, H., Edwards, R.L., Friedrich, M., Grootes, P.M., Guilderson, T.P., Hajdas, I., Heaton, T.J., Hogg, A.G., Hughen, K.A., Kromer, B., Manning, S.W., Muscheler, R., Palmer, J.G., Pearson, C., van der Plicht, J., Reimer, R.W., Richards, D.A., Scott, E.M., Southon, J.R., Turney, C.S.M., Wacker, L., Adolphi, F., Büntgen, U., Capano, M., Fahrni, S.M., Fogtmann-Schulz, A., Friedrich, R., Köhler, P., Kudsk, S., Miyake, F., Olsen, J., Reinig, F., Sakamoto, M., Sookdeo, A., Talamo, S., 2020. The IntCal20 Northern Hemisphere Radiocarbon Age Calibration Curve (0–55 cal kBP). *Radiocarbon* 62, 725–757.
- Reynhout, S.A., Kaplan, M.R., Sagredo, E.A., Aravena, J.C., Soteres, R.L., Schwartz, R., Schaefer, J.M., 2022. Holocene glacier history of northeastern Cordillera Darwin, southernmost South America (55° S). *Quaternary Research* 105, 166–181.
- Riedinger, N., Pfeifer, K., Kasten, S., Garming, J.F.L., Vogt, C., Hensen, C., 2005. Diagenetic alteration of magnetic signals by anaerobic oxidation of methane related to a change in sedimentation rate. *Geochimica et Cosmochimica Acta* 69, 4117–4126.
- Römer, M., Torres, M., Kasten, S., Kuhn, G., Graham, A.G.C., Mau, S., Little, C.T.S., Linse, K., Pape, T., Geprägs, P., Fischer, D., Wintersteller, P., Marcon, Y., Rethemeyer, J., Bohrmann, G., 2014. First evidence of widespread active methane seepage in the Southern Ocean, off the sub-Antarctic island of South Georgia. *Earth and Planetary Science Letters* 403, 166–177.
- Rosqvist, G.C., Rietti-Shati, M., Shemesh, A., 1999. Late glacial to middle Holocene climatic record of lacustrine biogenic silica oxygen isotopes from a Southern Ocean island. *Geology* 27, 967.
- Rosqvist, G.C., Schuber, P., 2003. Millennial-scale climate changes on South Georgia, Southern Ocean. *Quaternary Research* 59, 470–475.
- Royer, D.L., 2006. CO<sub>2</sub>-forced climate thresholds during the Phanerozoic. *Geochimica et Cosmochimica Acta* 70, 5665–5675.
- Ruggieri, E., Herbert, T., Lawrence, K.T., Lawrence, C.E., 2009. Change point method for detecting regime shifts in paleoclimatic time series: application to  $\delta^{18}\text{O}$  time series of the Plio-Pleistocene. *Paleoceanography* 24.
- Ryan, J., Dowdeswell, J., Hogan, K., 2016. Three cross-shelf troughs on the continental shelf of SW Greenland from Olex data. *Atlas of Submarine Glacial Landforms: Modern, Quaternary Ancient* 46, 167–168.
- Rydningen, T.A., Vorren, T.O., Laberg, J.S., Kolstad, V., 2013. The marine-based NW Fennoscandian ice sheet: glacial and deglacial dynamics as reconstructed from submarine landforms. *Quaternary Science Reviews* 68, 126–141.
- Sallée, J.B., Speer, K., Morrow, R., 2008. Response of the Antarctic Circumpolar Current to Atmospheric Variability. *Journal of Climate* 21, 3020–3039.
- Scher, H.D., Martin, E.E., 2006. Timing and climatic consequences of the opening of Drake Passage. *Science* 312, 428–430.
- Schimmelmann, A., Lange, C.B., Schieber, J., Francus, P., Ojala, A.E., Zolitschka, B., 2016. Varves in marine sediments: A review. *Earth-Science Reviews* 159, 215–246.
- Schmieder, F., von Dobeneck, T., Bleil, U., 2000. The Mid-Pleistocene climate transition as documented in the deep South Atlantic Ocean: initiation, interim state and terminal event. *Earth and Planetary Science Letters* 179, 539–549.
- Seltzer, A.M., Ng, J., Aeschbach, W., Kipfer, R., Kulongoski, J.T., Severinghaus, J.P., Stute, M., 2021. Widespread six degrees Celsius cooling on land during the Last Glacial Maximum. *Nature* 593, 228–232.
- Seramur, K.C., Powell, R.D., Carlson, P.R., 1997. Evaluation of conditions along the grounding line of temperate marine glaciers: an example from Muir Inlet, Glacier Bay, Alaska. *Marine Geology* 140, 307–327.
- Sévellec, F., Fedorov, A.V., 2015. Unstable AMOC during glacial intervals and millennial variability: The role of mean sea ice extent. *Earth and Planetary Science Letters* 429, 60–68.

## References

---

- Sigman, D.M., Boyle, E.A., 2000. Glacial/interglacial variations in atmospheric carbon dioxide. *Nature* 407, 859-869.
- Sigman, D.M., Hain, M.P., Haug, G.H., 2010. The polar ocean and glacial cycles in atmospheric CO<sub>2</sub> concentration. *Nature* 466, 47-55.
- Sikes, E.L., Umling, N.E., Allen, K.A., Ninnemann, U.S., Robinson, R.S., Russell, J.L., Williams, T.J., 2023. Southern Ocean glacial conditions and their influence on deglacial events. *Nature Reviews Earth & Environment*, 1-17.
- Sime, L.C., Kohfeld, K.E., Le Quéré, C., Wolff, E.W., de Boer, A.M., Graham, R.M., Bopp, L., 2013. Southern Hemisphere westerly wind changes during the Last Glacial Maximum: model-data comparison. *Quaternary Science Reviews* 64, 104–120.
- Ślubowska-Woldengen, M., Rasmussen, T.L., Koc, N., Klitgaard-Kristensen, D., Nilsen, F., Solheim, A., 2007. Advection of Atlantic Water to the western and northern Svalbard shelf since 17,500 cal yr BP. *Quaternary Science Reviews* 26, 463-478.
- Smith, A.G., Pickering, K.T., 2003. Oceanic gateways as a critical factor to initiate icehouse Earth. *Journal of the Geological Society* 160, 337-340.
- Smith, J.A., Graham, A.G.C., Post, A.L., Hillenbrand, C.-D., Bart, P.J., Powell, R.D., 2019. The marine geological imprint of Antarctic ice shelves. *Nature Communications* 10.
- Smith, J.A., Hillenbrand, C.-D., Kuhn, G., Larter, R.D., Graham, A.G.C., Ehrmann, W., Moreton, S.G., Forwick, M., 2011. Deglacial history of the West Antarctic Ice Sheet in the western Amundsen Sea Embayment. *Quaternary Science Reviews* 30, 488–505.
- Sokolov, S., Rintoul, S.R., 2009. Circumpolar structure and distribution of the Antarctic Circumpolar Current fronts: 1. Mean circumpolar paths. *Journal of Geophysical Research: Oceans* 114.
- South Georgia GIS, 2023. SGGIS.
- Spagnolo, M., Clark, C.D., 2009. A geomorphological overview of glacial landforms on the Icelandic continental shelf. *Journal of Maps* 5, 37-52.
- Spagnolo, M., Clark, C.D., Ely, J.C., Stokes, C.R., Anderson, J.B., Andreassen, K., Graham, A.G., King, E.C., 2014. Size, shape and spatial arrangement of mega-scale glacial lineations from a large and diverse dataset. *Earth Surface Processes and Landforms* 39, 1432-1448.
- Stalling, D., Westerhoff, M., Hege, H.-C., 2005. Amira: A highly interactive system for visual data analysis. *The visualization handbook* 38, 749-767.
- Stansell, N.D., Rodbell, D.T., Licciardi, J.M., Sedlak, C.M., Schweinsberg, A.D., Huss, E.G., Delgado, G.M., Zimmerman, S.H., Finkel, R.C., 2015. Late glacial and Holocene glacier fluctuations at Nevado Huaguruncho in the eastern cordillera of the Peruvian Andes. *Geology* 43, 747-750.
- Steffen, H., Wu, P., 2011. Glacial isostatic adjustment in Fennoscandia—a review of data and modeling. *Journal of Geodynamics* 52, 169-204.
- Stephens, B.B., Keeling, R.F., 2000. The influence of Antarctic sea ice on glacial–interglacial CO<sub>2</sub> variations. *Nature* 404, 171-174.
- Stewart, F., Stoker, M., 1990. Problems associated with seismic facies analysis of diamicton-dominated, shelf glacigenic sequences. *Geo-Marine Letters* 10, 151-156.
- Stewart, J.A., Li, T., Spooner, P.T., Burke, A., Chen, T., Roberts, J., Rae, J.W., Peck, V., Kender, S., Liu, Q., Robinson, L.F., 2021. Productivity and dissolved oxygen controls on the Southern Ocean deep-sea benthos during the Antarctic Cold Reversal. *Paleoceanography and Paleoclimatology* 36, e2021PA004288.
- Stokes, C.R., Clark, C.D., 1999. Geomorphological criteria for identifying Pleistocene ice streams. *Annals of Glaciology* 28, 67-74.
- Stokes, C.R., Clark, C.D., 2002. Are long subglacial bedforms indicative of fast ice flow? *Boreas* 31, 239-249.
- Stone, P., 1974. Physiography of the north-east coast of South Georgia. *British Antarctic Survey Bulletin* 38, 17-36.



- Storey, B., Macdonald, D., 1984. Processes of formation and filling of a Mesozoic back-arc basin on the island of South Georgia. Geological Society, London, Special Publications 16, 207-218.
- Storey, B.C., 1983. The geology of South Georgia: V. Drygalski Fjord Complex, Scientific reports. British Antarctic Survey.
- Stow, D.A., Faugères, J.-C., Howe, J.A., Pudsey, C.J., Viana, A.R., 2002. Bottom currents, contourites and deep-sea sediment drifts: current state-of-the-art. Geological Society, London, Memoirs 22, 7-20.
- Streuff, K., Cofaigh, C.O., Hogan, K., Jennings, A., Lloyd, J.M., Noormets, R., Nielsen, T., Kuijpers, A., Dowdeswell, J.A., Weinrebe, W., 2017a. Seafloor geomorphology and glacial marine sedimentation associated with fast-flowing ice sheet outlet glaciers in Disko Bay, West Greenland. Quaternary Science Reviews 169, 206-230.
- Streuff, K., Cofaigh, C.O., Noormets, R., Lloyd, J.M., 2017b. Submarine landforms and glacial marine sedimentary processes in Lomfjorden, East Spitsbergen. Marine Geology 390, 51-71.
- Streuff, K., Forwick, M., Szczuciński, W., Andreassen, K., Ó Cofaigh, C., 2015. Submarine landform assemblages and sedimentary processes related to glacier surging in Kongsfjorden, Svalbard. arktos 1, 1-19.
- Streuff, K.T., Lešić, N.-M., Kuhn, G., Bohrmann, G., in prep. Glacial history of the King Haakon Trough System, sub-Antarctic South Georgia.
- Streuff, K.T., Ó Cofaigh, C., Wintersteller, P., 2022. GlaciDat—a GIS database of submarine glacial landforms and sediments in the Arctic. Boreas 51, 517-531.
- Strother, S.L., Salzmann, U., Roberts, S.J., Hodgson, D.A., Woodward, J., Van Nieuwenhuyze, W., Verleyen, E., Vyverman, W., Moreton, S.G., 2015. Changes in Holocene climate and the intensity of Southern Hemisphere Westerly Winds based on a high-resolution palynological record from sub-Antarctic South Georgia. The Holocene 25, 263–279.
- Sugden, D.E., Clapperton, C.M., 1977. The Maximum Ice Extent on Island Groups in the Scotia Sea, Antarctica. Quaternary Research 7, 268–282.
- Talling, P.J., 2021. Fidelity of turbidites as earthquake records. Nature Geoscience 14, 113-116.
- Taylor, J., Dowdeswell, J., Kenyon, N., Ó Cofaigh, C., 2002. Late Quaternary architecture of trough-mouth fans: debris flows and suspended sediments on the Norwegian margin. Geological Society, London, Special Publications 203, 55-71.
- Thorpe, S.E., Heywood, K.J., Brandon, M.A., Stevens, D.P., 2002. Variability of the southern Antarctic Circumpolar Current front north of South Georgia. Journal of Marine Systems 37, 87–105.
- Tierney, J.E., Zhu, J., King, J., Malevich, S.B., Hakim, G.J., Poulsen, C.J., 2020. Glacial cooling and climate sensitivity revisited. Nature 584, 569-573.
- Toggweiler, J.R., Russell, J.L., Carson, S.R., 2006. Midlatitude westerlies, atmospheric CO<sub>2</sub>, and climate change during the ice ages. Paleoclimatology 21.
- Turnbull, I., Craw, D., 1988. Relationships between the Cumberland Bay and Sandebugten Formations, South Georgia, and some tectonic implications. Journal of the Geological Society 145, 591-602.
- U.S. Department of State, O.o.t.G., 2013. Detailed World Polygons (LSIB), South America, 2013. U.S. Department of State. Humanitarian Information Unit, Washington, DC, US.
- U.S.G.S., 1981. U.S. Geographic Names Information System (GNIS), in: Survey, U.S.G. (Ed.). U.S. Geological Survey, Reston, VA.
- van der Bilt, W.G., D’Andrea, W.J., Oppedal, L.T., Bakke, J., Bjune, A.E., Zwier, M., 2022. Stable Southern Hemisphere westerly winds throughout the Holocene until intensification in the last two millennia. Communications Earth & Environment 3, 1-13.
- van der Putten, N., Stieperaere, H., Verbruggen, C., Ochyra, R., 2004. Holocene palaeoecology and climate history of South Georgia (sub-Antarctica) based on a macrofossil record of bryophytes and seeds. The Holocene 14, 382-392.

- van der Putten, N., Verbruggen, C., 2005. The onset of deglaciation of Cumberland Bay and Stromness Bay, South Georgia. *Antarctic Science* 17, 29-32.
- van der Putten, N., Verbruggen, C., Björck, S., de Beaulieu, J.-L., Barrow, C.J., Frenot, Y., 2012. Is palynology a credible climate proxy in the Subantarctic? *The Holocene* 22, 1113-1121.
- van der Putten, N., Verbruggen, C., Ochyra, R., Spassov, S., De Beaulieu, J.-L., De Dapper, M., Hus, J., Thouveny, N., 2009. Peat bank growth, Holocene palaeoecology and climate history of South Georgia (sub-Antarctica), based on a botanical macrofossil record. *Quaternary Science Reviews* 28, 65-79.
- van der Vegt, P., Janszen, A., Moscariello, A., 2012. Tunnel valleys: current knowledge and future perspectives. Geological Society, London, Special Publications 368, 75-97.
- Velichko, A., Kononov, Y.M., Faustova, M., 1997. The last glaciation of Earth: size and volume of ice-sheets. *Quaternary International* 41, 43-51.
- Verdicchio, G., Trincardi, F., 2008. Shallow-water contourites. *Developments in Sedimentology* 60, 409-433.
- Verleye, T.J., Louwye, S., 2010. Late Quaternary environmental changes and latitudinal shifts of the Antarctic Circumpolar Current as recorded by dinoflagellate cysts from offshore Chile (41 S). *Quaternary Science Reviews* 29, 1025-1039.
- Voigt, I., Chiessi, C.M., Prange, M., Mulitza, S., Groeneveld, J., Varma, V., Henrich, R., 2015. Holocene shifts of the southern westerlies across the South Atlantic. *Paleoceanography* 30, 39-51.
- von Dobeneck, T., 2020a. Susceptibility of sediment core Geob22056-1, In: von Dobeneck, T (2020): Susceptibility measured on 18 sediment cores from METEOR cruise M134/1. PANGAEA, <https://doi.org/10.1594/PANGAEA.914649>. PANGAEA.
- von Dobeneck, T., 2020b. Susceptibility of sediment core Geob22057-1, In: von Dobeneck, T (2020): Susceptibility measured on 18 sediment cores from METEOR cruise M134/1. PANGAEA, <https://doi.org/10.1594/PANGAEA.914649>. PANGAEA.
- von Dobeneck, T., 2020c. Susceptibility of sediment core Geob22058-1, In: von Dobeneck, T (2020): Susceptibility measured on 18 sediment cores from METEOR cruise M134/1. PANGAEA, <https://doi.org/10.1594/PANGAEA.914649>. PANGAEA.
- Walker, M., Johnsen, S., Rasmussen, S.O., Popp, T., Steffensen, J.P., Gibbard, P., Hoek, W., Lowe, J., Andrews, J., Björck, S., Cwynar, L.C., Hughen, K., Kershaw, P., Kromer, B., Litt, T., Lowe, D.J., Nakagawa, T., Newnham, R., Schwander, J., 2009. Formal definition and dating of the GSSP (Global Stratotype Section and Point) for the base of the Holocene using the Greenland NGRIP ice core, and selected auxiliary records. *Journal of Quaternary Science: Published for the Quaternary Research Association* 24, 3-17.
- Wang, R., Kuhn, G., Gong, X., Biskaborn, B.K., Gersonde, R., Lembke-Jene, L., Lohmann, G., Tiedemann, R., Diekmann, B., 2021. Deglacial land-ocean linkages at the Alaskan continental margin in the Bering Sea. *Frontiers in Earth Science* 9, 712415.
- Wasell, A., 1993. Diatom stratigraphy and evidence of Holocene environmental changes in selected lake basins in the Antarctic and South Georgia. Stockholm Univ., Dept. of Quaternary Research.
- Waugh, D.W., Banerjee, A., Fyfe, J.C., Polvani, L.M., 2020. Contrasting recent trends in Southern Hemisphere Westerlies across different ocean basins. *Geophysical Research Letters* 47, e2020GL088890.
- Weinans, E., Omta, A.W., van Voorn, G.A., van Nes, E.H., 2021. A potential feedback loop underlying glacial-interglacial cycles. *Climate Dynamics* 57, 523-535.
- White, D., Bennike, O., Melles, M., Berg, S., Binnie, S., 2017. Was South Georgia covered by an ice cap during the Last Glacial Maximum? Geological Society, London, Special Publications 461, 49-59.
- Wilckens, H., Schwenk, T., Lüdmann, T., Betzler, C., Zhang, W., Chen, J., Hernández-Molina, F.J., Lefebvre, A., Cattaneo, A., Spieß, V., Miramontes, E., 2023. Factors controlling the morphology and internal sediment architecture of moats and their associated contourite drifts. *Sedimentology* 70, 1472-1495.

- Wild, C.T., Alley, K.E., Muto, A., Truffer, M., Scambos, T.A., Pettit, E.C., 2022. Weakening of the pinning point buttressing Thwaites Glacier, West Antarctica. *The Cryosphere* 16, 397-417.
- Willeit, M., Calov, R., Talento, S., Greve, R., Bernaldes, J., Klemann, V., Bagge, M., Ganopolski, A., 2023. Glacial inception through rapid ice area increase driven by albedo and vegetation feedbacks. *EGUsphere* 2023, 1-41.
- Williamson, W.C., 1858. On the recent foraminifera of Great Britain. The Ray Society, London.
- Winkelmann, D., Jokat, W., Jensen, L., Schenke, H.-W., 2010. Submarine end moraines on the continental shelf off NE Greenland—Implications for Lateglacial dynamics. *Quaternary Science Reviews* 29, 1069-1077.
- Wollenburg, J.E., Matthiessen, J., Vogt, C., Nehrke, G., Grotheer, H., Wilhelms-Dick, D., Geibert, W., Mollenhauer, G., 2023. Omnipresent authigenic calcite distorts Arctic radiocarbon chronology. *Communications Earth & Environment* 4, 136.
- Wright, N.M., Krause, C.E., Phipps, S.J., Bosch, G., Abram, N.J., 2022. Influence of long-term changes in solar irradiance forcing on the Southern Annular Mode. *Climate of the Past* 18, 1509-1528.
- Wu, S., Lembke-Jene, L., Lamy, F., Arz, H.W., Nowaczyk, N., Xiao, W., Zhang, X., Hass, H.C., Titschack, J., Zheng, X., Liu, J., Dumm, L., Diekmann, B., Nürnberg, D., Tiedemann, R., Kuhn, G., 2021. Orbital- and millennial-scale Antarctic Circumpolar Current variability in Drake Passage over the past 140,000 years. *Nature Communications* 12, 1–9.
- Xia, Z., Oppedal, L.T., Van der Putten, N., Bakke, J., Yu, Z., 2020. Ecological response of a glacier-fed peatland to late Holocene climate and glacier changes on subantarctic South Georgia. *Quaternary Science Reviews* 250, 106679.
- Xiao, W., Esper, O., Gersonde, R., 2016. Last Glacial-Holocene climate variability in the Atlantic sector of the Southern Ocean. *Quaternary Science Reviews* 135, 115-137.
- Yamazaki, K., Aoki, S., Katsumata, K., Hirano, D., Nakayama, Y., 2021. Multidecadal poleward shift of the southern boundary of the Antarctic Circumpolar Current off East Antarctica. *Science Advances* 7, eabf8755.
- Zech, R., Kull, C., Kubik, P.W., Veit, H., 2007. Exposure dating of Late Glacial and pre-LGM moraines in the Cordón de Doña Rosa, Northern/Central Chile (~31° S). *Climate of the Past* 3, 1–14.
- Zhang, Q., Zhang, Y., Wu, Z., 2022. Multiple time scales of the southern annular mode. *Climate Dynamics*, 1-18.
- Zilliacus, H., 1989. Genesis of De Geer moraines in Finland. *Sedimentary Geology* 62, 309-317.
- Zwier, M., van der Bilt, W.G., de Stigter, H., Bjune, A.E., 2021. Pollen evidence of variations in Holocene climate and Southern Hemisphere Westerly Wind strength on sub-Antarctic South Georgia. *The Holocene* 32, 09596836211060495.

## 11. Appendices

### Appendix A for Chapter 5

#### Appendix A

Supporting Online Material for

#### **Glacimarine sediments from outer Drygalski Trough, sub-Antarctic South Georgia – evidence for extensive glaciation during the Last Glacial Maximum**

Lešić, Nina-Marie<sup>1,2</sup> (nlesic@marum.de); Streuff, Katharina Teresa<sup>2</sup> (kstreuff@marum.de); Bohrmann, Gerhard<sup>2</sup> (gbohrmann@marum.de); Kuhn, Gerhard<sup>1,2</sup> (gerhard.kuhn@awi.de)

*1 Alfred Wegener Institute (AWI), Helmholtz Centre for Polar and Marine Research, Am Alten Hafen 26, 27568 Bremerhaven, Germany*

*2 MARUM, Centre for Marine Environmental Sciences, and Faculty of Geosciences, University of Bremen (UoB), Klagenfurter Str., D-28334 Bremen*

available under the DOI <https://doi.org/10.1016/j.quascirev.2022.107657> under the license CC-BY-NC-ND 4.0: <https://creativecommons.org/licenses/by-nc-nd/4.0/legalcode.en>

#### A1. Methods

##### 1.1 Bchron age model code

```
rm(list = ls())
```

```
library(Bchron)
```

```
#####  
#####
```

```
# Let's take a look at the dataset.
```

```
#####  
#####
```

```
dates =  
matrix(c(0.01,0.55,0.85,1.35,1.85,2.55,3.35,4.515,5.30,6.15,8.16,0.131,1.146,2.295,5.2  
99,10.361,12.406,12.821,13.389,15.441,17.328,24.262,0.134,0.160,0.343,0.262,0.185,  
0.352,0.304,0.320,0.541,0.372,0.914), nrow = 11, ncol = 3)
```

```
# Bchron likes to work with whole numbers... so we convert kyr to yr
```

```
dates[,2] = dates[,2] * 1000
```

```
dates[,3] = dates[,3] * 1000
```

```
colnames(dates) <- c("Depth (m)", "Age (a)", "Uncertainty (2sigma, yr)")
```

```
dates = as.data.frame(dates)
```

```

plot(dates$`Age (a)`, dates$`Depth (m)`, ylim = c(8.22,0.01), xlim=c(0,25300),xaxs = "i",
yaxs = "i", col = "blue", pch = 19, xlab = "Age (a)", ylab = "Depth (m)")

for (j in 1:11) {segments(dates[j,2]-dates[j,3],dates[j,1],dates[j,2]+dates[j,3],dates[j,1],
col = "blue", lwd = 2)}

depths_i=seq(0,8.22,0.01)

#####
#####

# Bchron (for pleistocene and holocene)

#####
#####

#monte carlo simulations

output = Bchronology(
  ages = dates$`Age (a)`,
  ageSds = dates$`Uncertainty (2sigma, yr)`/2,
  positions = dates$`Depth (m)`,
  calCurves = rep("normal",11),
  predictPositions = depths_i)

ages_Bchron=matrix(data = NA, nrow = 823, ncol = 3)
colnames(ages_Bchron) <- c("2.5% CL", "Median Age", "97.5% CL")
for (k in 1:823){
  ages_Bchron[k,]=quantile(output$thetaPredict[,k], probs = c(0.025,0.5,0.975))}

dev.off()

plot(dates$`Age (a)`, dates$`Depth (m)`, ylim = c(8.22,0), xlim = c(0, 25300), yaxs = "i",
yaxs = "i", col = "blue", pch = 19, xlab = "Age (ka)", ylab = "Depth (m)")

for (j in 1:11)

points(ages_Bchron[,2], depths_i, col = "grey")

lines(ages_Bchron[,1], depths_i) # Upper confidence level

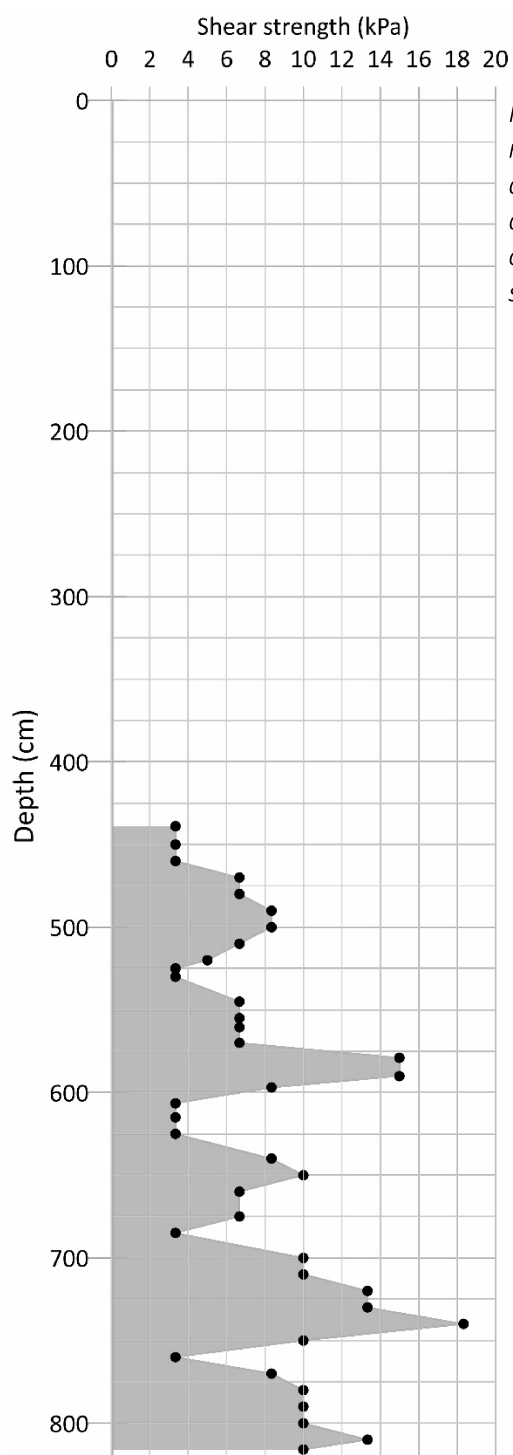
lines(ages_Bchron[,3], depths_i) # Lower confidence level

write.csv(ages_Bchron, "age_model_Bchron.csv", row.names = F)

```

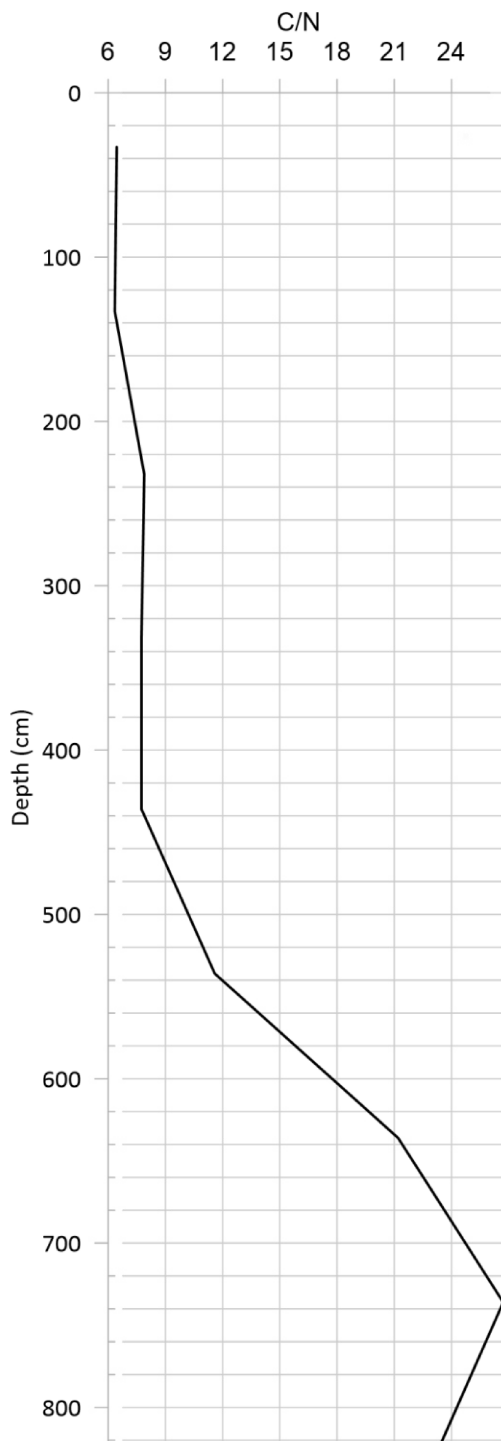
A2. Figures

A2.1 Shear strength measured in sediment core PS119\_5-1



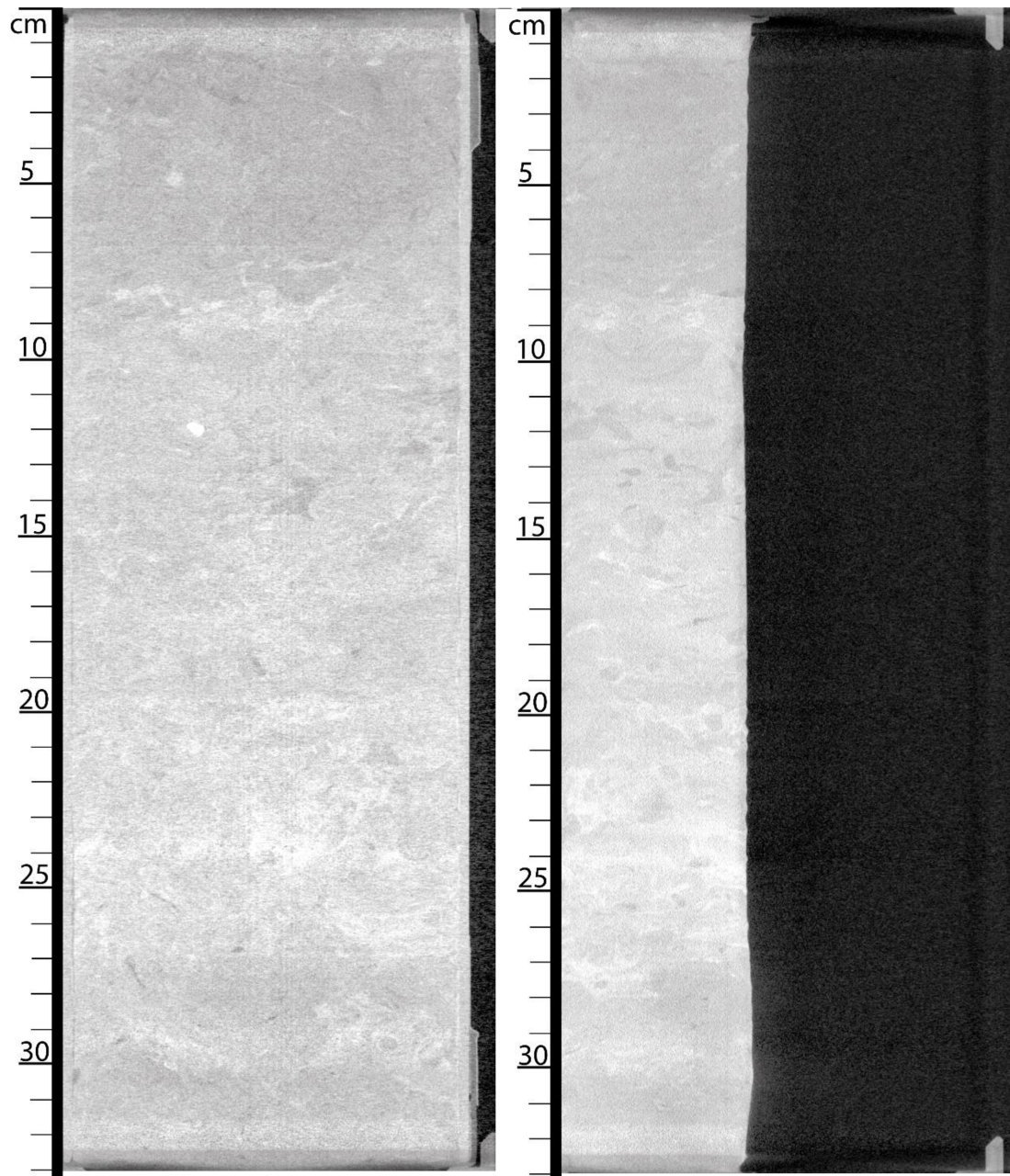
*Fig. A 1: Shear strength measurements were only measured in the diamictic section and shortly above. Measurements in the upper part of the core are not shown here; they were neglected after observation of apparent artefacts caused by grain size distribution.*

A2.2 TC/N ratio measured in sediment core PS119\_5-1



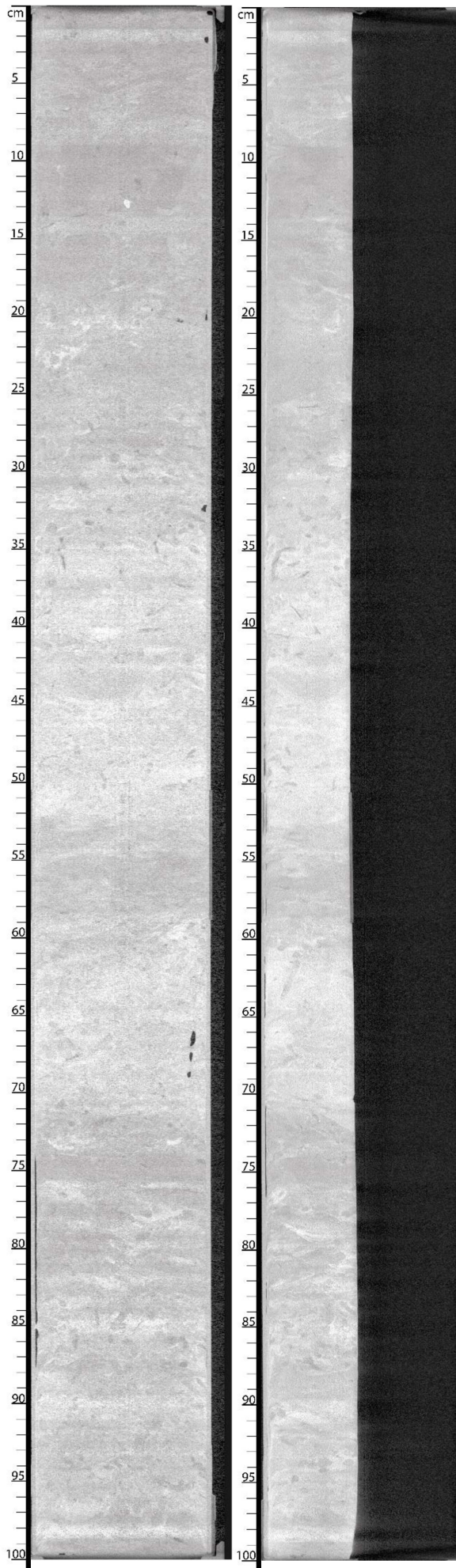
*Fig. A 2: TC/N data are based on several TC and TOC measurements along the core that were carried out to compare datasets from different analysis facilities. Together with the information on carbon, nitrogen data were collected on these few samples and give insight into the terrestrial fraction of the carbon signal. Measurements were carried out with an Elementar Vario EL III.*

A2.3 CT scan Slices from sediment core PS119\_5-1

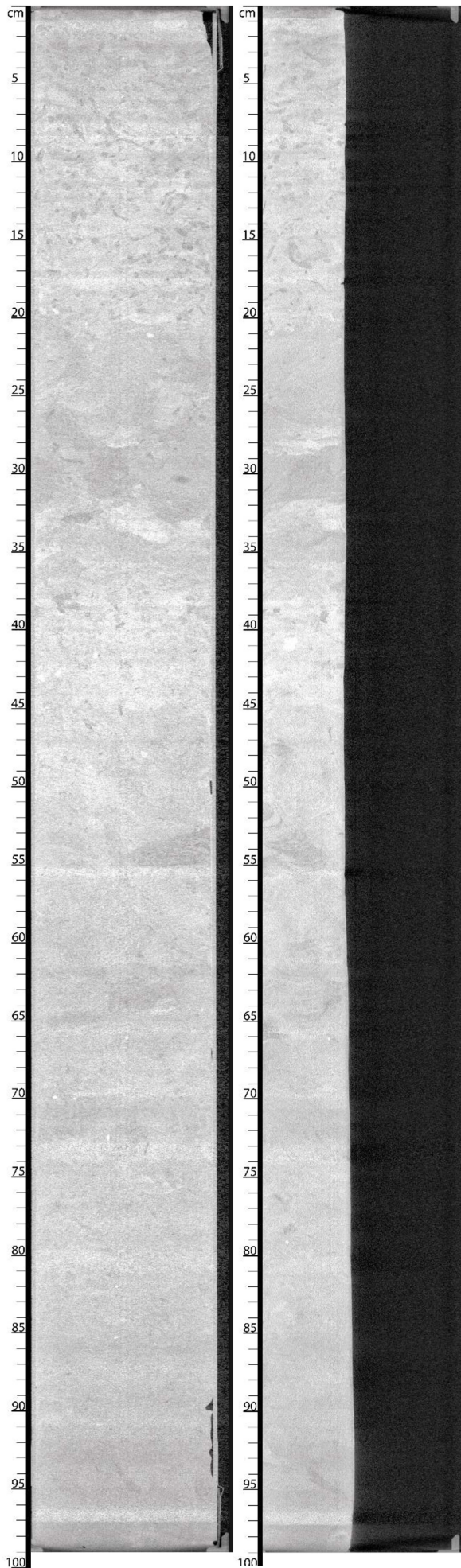


*Fig. A 3 CT Scan Slices Section 1 (33-0cm); Front view and side view through the core centre of PS119\_5-1.*

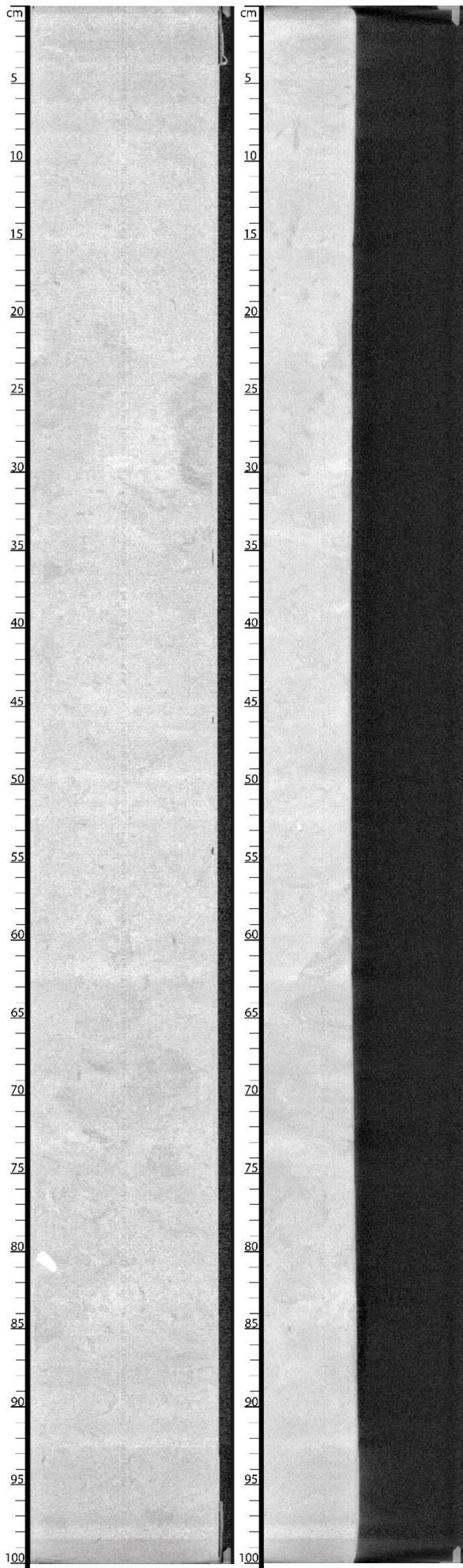




*Fig. A 4: CT Scan Slices Section 2 (133-33cm); Front view and side view through the core centre of PS119\_5-1.*

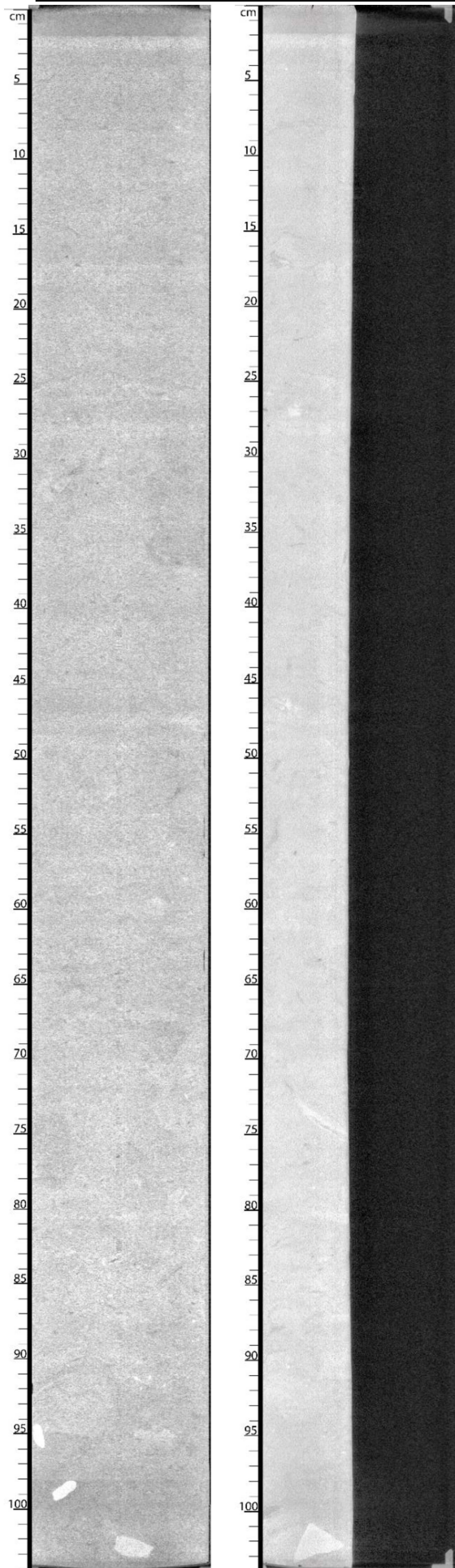


*Fig. A 5: CT Scan Slices Section 3 (232-133cm); Front view and side view through the core centre of PS119 5-1.*

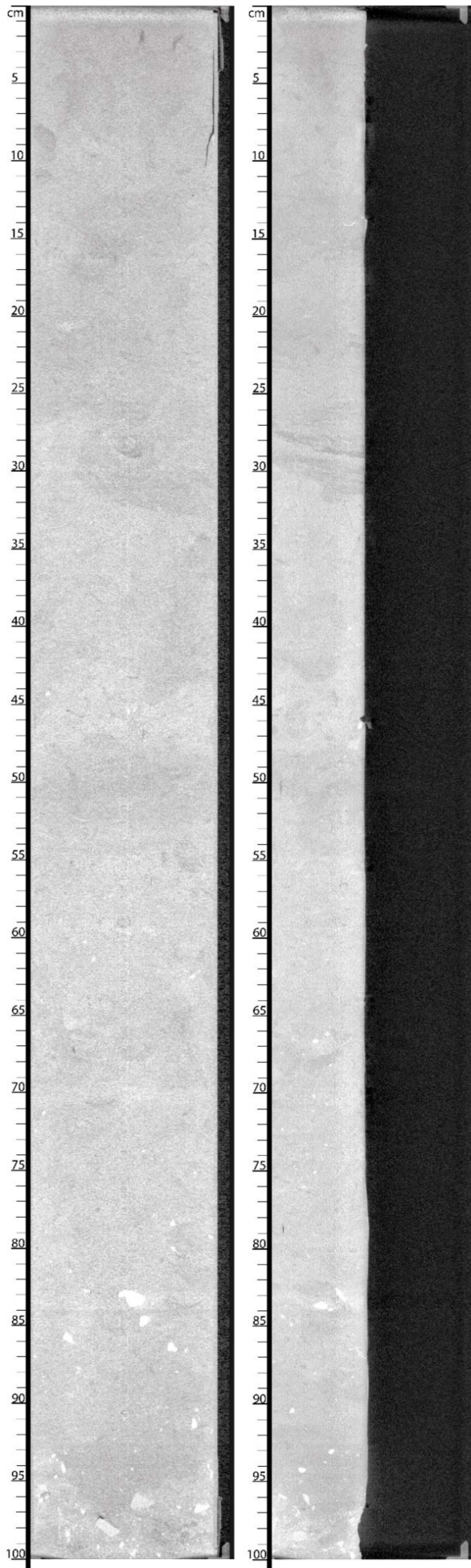


*Fig. A 6: CT Scan Slices Section 4 (332-232cm); Front view and side view through the core centre of PS119\_5-1.*

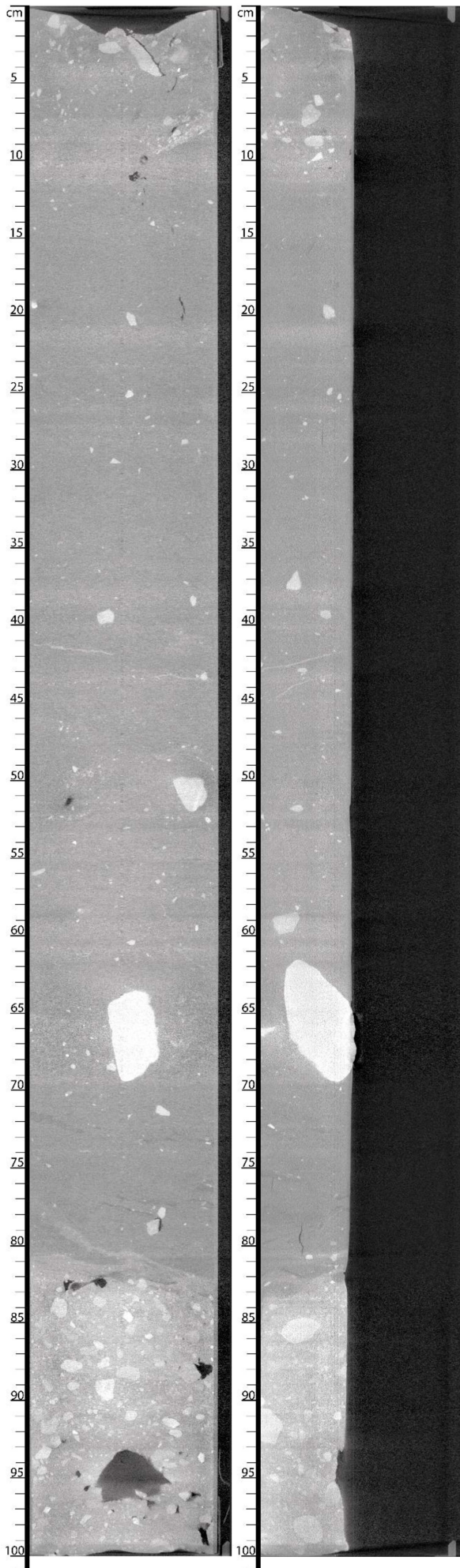
## Appendices



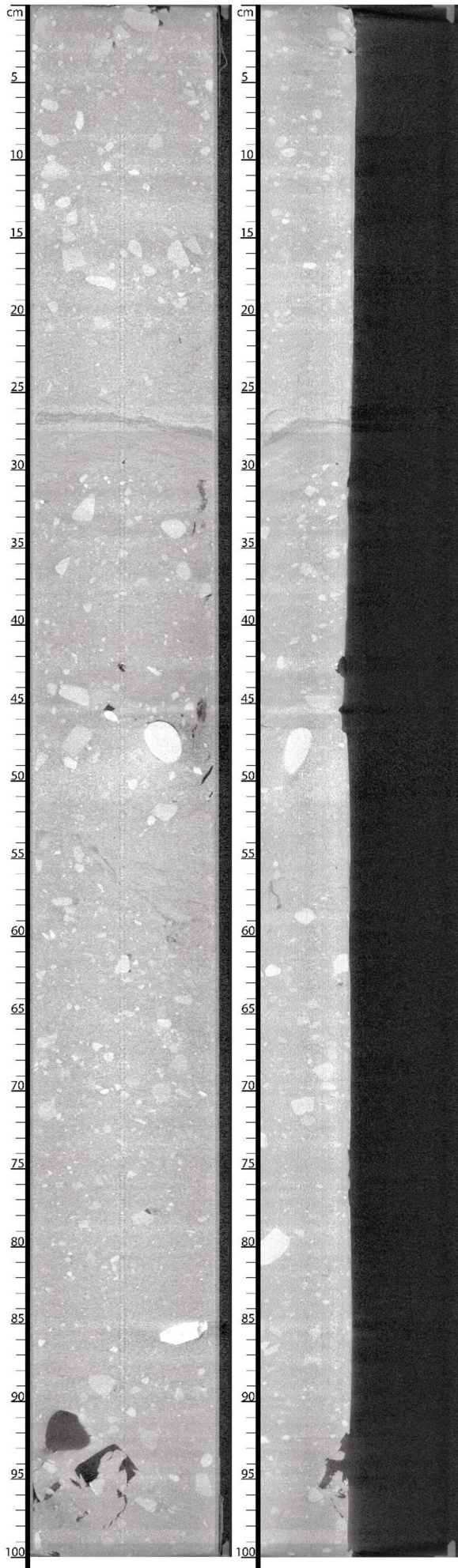
*Fig. A 7: CT Scan Slices Section 5 (436-332cm); Front view and side view through the core centre of PS119 5-1.*



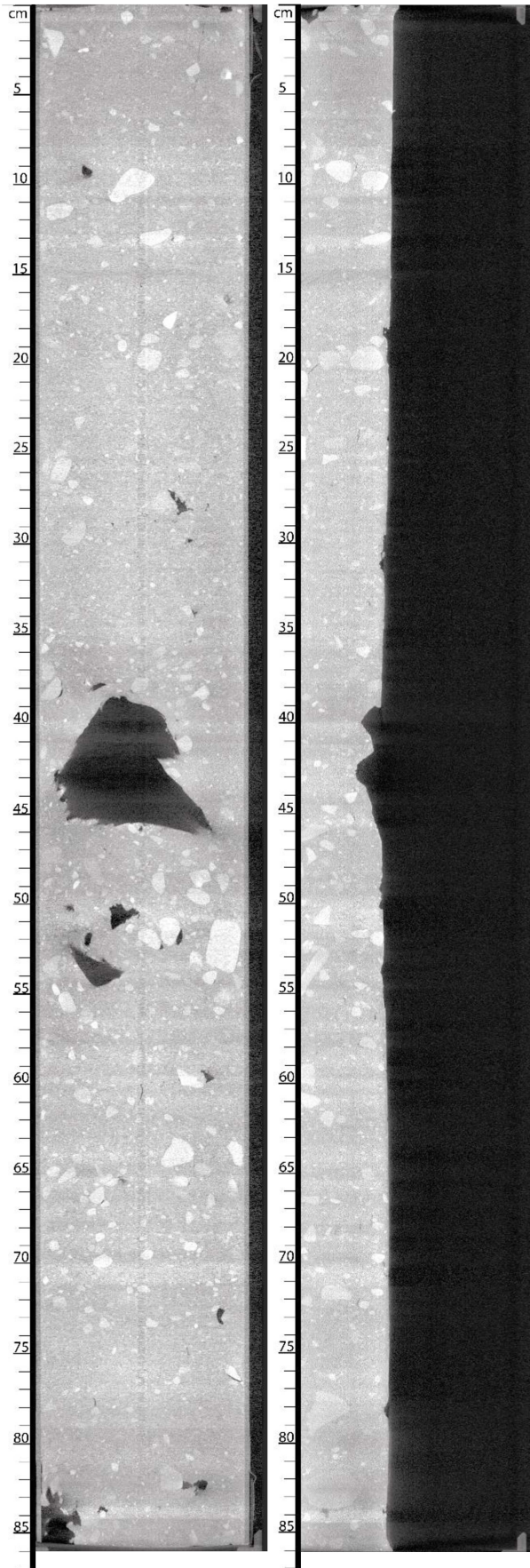
*Fig. A 8: CT Scan Slices Section 6 (536-436cm); Front view and side view through the core centre of PS119\_5-1.*



*Fig. A 9: CT Scan Slices Section 7 (636-536cm); Front view and side view through the core centre of PS119\_5-1.*



*Fig. A 10: CT Scan Slices Section 8 (736-636cm); Front view and side view through the core centre of PS119\_5-1.*



*Fig. A 11: CT Scan Slices Section 9 (822-736cm); Front view and side view through the core centre of PS119\_5-1.*



## A3. Tables

Table A. 1: Conventional radiocarbon ages and IntCal20 calibration results for this study (Reimer et al., 2020), including original and recalibrated ages for PS81/265-1 and GC666 (Graham et al., 2017). MRA are based on Butzin et al. (2019, 2020) and Heaton et al. (2020).

Sample details	Conventional radiocarbon ages					IntCal20 calibration					Lab Code
	Depth (cm)	Carbon source	$^{14}\text{C}/^{12}\text{C}$ ( $\times 10^{-12}$ )	Age ( $^{14}\text{C}$ ka BP)	Age error (ka)	MRA (ka)	MRA MAD (ka)	Min (cal ka BP)	Weighted mean (cal ka BP)	Max (cal ka BP)	
PS119_5-1	1	Benthic forams	1,0231 $\pm 0,75\%$	0.913	$\pm 0.07$ 2	0.9	<0.014	0.009	0.131	0.276	5705.1.1
PS119_5-1	55	Benthic forams	0,8478 $\pm 0,98\%$	2.190	$\pm 0.08$ 4	0.96	<0.014	0.973	1.146	1.292	6154.1.1
PS119_5-1	85	Benthic forams	0,7721 $\pm 0,90\%$	3.199	$\pm 0.08$ 5	0.91	<0.014	2.009	2.295	2.695	5706.1.1
PS119_5-1	135	Benthic forams	0,5698 $\pm 0,83\%$	5.515	$\pm 0.07$ 3	0.91	<0.014	5.046	5.299	5.569	6155.1.1
PS119_5-1	185	Benthic forams	0,3282 $\pm 1,04\%$	10.017	$\pm 0.09$	0.85	<0.014	10.19 7	10.361	10.56 6	6156.1.1
PS119_5-1	255	Benthic forams	0,2489 $\pm 1,20\%$	12.263	$\pm 0.10$ 3	1.77	0.78	12.00 4	12.406	12.70 8	6157.1.1
PS119_5-1	335	Gastropod	0,2478 $\pm 1,58\%$	12.590	$\pm 0.15$ 4	1.76	0.77	12.49	12.821	13.09 7	5707.1.1
PS119_5-1	451.5	Gastropod	0,2262 $\pm 1,64\%$	13.365	$\pm 0.16$ 3	1.85	0.768	13.10 6	13.389	13.74 6	5708.1.1
PS119_5-1	530	Benthic forams	0,1915 $\pm 1,74\%$	14.854	$\pm 0.17$ 9	1.95	0.772	14.91 9	15.441	16.00 1	5709.1.1
PS119_5-1	615	Shell fragments	0,1560 $\pm 1,50\%$	15.897	$\pm 0.12$ 4	1.66	0.765	17.03 3	17.328	17.77 7	6160.1.1
PS119_5-1	625	Carbonate fragments	0,0076 $\pm 8,87\%$	>37.90 8	-	-	-	-	-	-	5710.1.1
PS119_5-1	625	Benthic forams	0,0121 $\pm 7,45\%$	>37.90 8	-	-	-	-	-	-	5711.1.1
PS119_5-1	816	Mixed forams	0,0807 $\pm 2,83\%$	22.192	$\pm 0.35$ 9	2.08	0.702	23.34 6	24.262	25.17 3	5713.1.1
PS119_5-1	816	Carbonate fragments	0,0099 $\pm 8,25\%$	>37.90 8	-	-	-	-	-	-	5712.1.1
Graham et al. (2017)		<i>IntCal20 calibration (Marine13 calibration)</i>									<i>Lab Code</i>
PS81/265-1	251-254	Benthic forams	-	12.59	$\pm 0.04$	1.74	0.77	12.73 2	12.778 (13.344)	12.83 4	BETA-444223

								(13.19 5)		(13.49 1)	
PS81/265- 1	305. 5	Gastropod	-	13.85	±0.04	1.86	0.77	13.79 (14.85 7)	13.902 (15.174)	14.02 3 (15.43 2)	BETA- 40296 1
GC666	388	Gastropod	-	11.926	±0.08	1.77	0.77	11.34 9 (12.55 7)	11.75 (12.712)	12.41 9 (12.91 2)	ETH- 51518 .1
GC666	510	Shell fragments	-	13.301	±0.13 5	1.79	0.77	13.11 7 (13.73 4)	13.375 (14.145)	13.73 (14.79 9)	ETH- 51520
GC666	815	Benthic forams	-	13.572	±0.21 1	1.88	0.77	13.17 8 (13.91 8)	13.581 (14.628)	14.02 7 (15.32 1)	ETH- 51522

Table A. 2: PS119\_5-1 Grainsize data, shear strength, \*refers to the net dry weight of the sample

Core	depth (m)	Gravel fraction (counts/10cm <sup>-3</sup> )	Gravel (wt%)	Sand fraction (wt%)	Fine fraction (wt%)	Error occurred in the sieving process (wt%)*	Shear strength (kPa)
PS119-5-1	0.01	0	0.08	13.05	86.88	9	NN
PS119-5-1	0.08	0.21	0.07	10.64	89.29	4	NN
PS119-5-1	0.15	0	0	11.05	88.95	4	NN
PS119-5-1	0.25	0	0	19.31	80.69	2	NN
PS119-5-1	0.35	0	0	11.39	88.61	2	NN
PS119-5-1	0.45	0	0	7.4	92.6	3	NN
PS119-5-1	0.55	0.21	0.05	11.16	88.79	4	NN
PS119-5-1	0.65	0	0	19.18	80.82	2	NN
PS119-5-1	0.75	0.21	0.05	22.53	77.41	5	NN
PS119-5-1	0.85	0	0	29.61	70.39	5	NN
PS119-5-1	0.95	0	0	26.66	73.34	4	NN
PS119-5-1	1.05	0.41	0.1	22.87	77.03	2	NN
PS119-5-1	1.15	0.62	0.06	31.93	68.01	1	NN
PS119-5-1	1.25	0	0	36.29	63.71	1	NN
PS119-5-1	1.35	0.41	0.03	41.41	58.56	2	NN
PS119-5-1	1.45	0.21	0.02	32.23	67.75	1	NN
PS119-5-1	1.55	1.24	0.67	22.66	76.67	2	NN
PS119-5-1	1.65	0.21	0.13	27.3	72.57	5	NN
PS119-5-1	1.75	1.44	0.41	52.31	47.28	1	NN

Appendix A for Chapter 5

Core	depth (m)	Gravel fraction (counts/10cm <sup>-3</sup> )	Gravel (wt%)	Sand fraction (wt%)	Fine fraction (wt%)	Error occurred in the sieving process (wt%)*	Shear strength (kPa)
PS119-5-1	1.85	0.62	0.14	49.01	50.86	4	NN
PS119-5-1	1.95	0.62	0.05	32.05	67.9	2	NN
PS119-5-1	2.05	0	0	23.64	76.36	1	NN
PS119-5-1	2.15	0	0	23.86	76.14	1	NN
PS119-5-1	2.25	0.21	0.02	17.11	82.87	1	NN
PS119-5-1	2.35	0.21	0.07	18.84	81.08	2	NN
PS119-5-1	2.45	0.21	0.02	12.54	87.45	4	NN
PS119-5-1	2.55	0	0.04	17.24	82.73	5	NN
PS119-5-1	2.65	0	0	14.73	85.27	1	NN
PS119-5-1	2.75	0	0	14.06	85.94	1	NN
PS119-5-1	2.85	0	0	15.29	84.71	2	NN
PS119-5-1	2.95	0	0	14.66	85.34	5	NN
PS119-5-1	3.05	0	0	12.02	87.98	1	NN
PS119-5-1	3.15	0.21	0.02	14.22	85.76	2	NN
PS119-5-1	3.25	0	0	11.57	88.43	1	NN
PS119-5-1	3.35	0	0.05	11.92	88.03	1	NN
PS119-5-1	3.45	0.21	0.03	11.83	88.14	1	NN
PS119-5-1	3.55	0	0	13.74	86.26	2	NN
PS119-5-1	3.65	0.21	0.09	10.83	89.08	1	NN
PS119-5-1	3.75	0	0	11.08	88.92	1	NN
PS119-5-1	3.85	0	0	12.24	87.76	0	NN
PS119-5-1	3.95	0	0	12.84	87.16	1	NN
PS119-5-1	4.05	0	0	24.56	75.44	2	NN
PS119-5-1	4.15	1.03	0.65	30.92	68.43	6	NN
PS119-5-1	4.25	0	0	23.67	76.33	2	NN
PS119-5-1	4.35	0.21	0.16	19.41	80.43	2	NN
PS119-5-1	4.39	0	0	17.91	82.09	2	3
PS119-5-1	4.5	0.21	0.02	17.51	82.48	2	3
PS119-5-1	4.6	0	0	18.93	81.07	2	3
PS119-5-1	4.7	0	0	23.22	76.78	2	7
PS119-5-1	4.8	0.21	0.01	27.6	72.39	2	7
PS119-5-1	4.9	0	0	28.8	71.2	2	8
PS119-5-1	5	0	0	24.32	75.68	2	8
PS119-5-1	5.1	0.82	0.28	29.81	69.91	4	7
PS119-5-1	5.2	1.85	0.53	24.46	75.01	2	5
PS119-5-1	5.25	2.27	1.37	18.17	80.45	2	3
PS119-5-1	5.3	8.86	3.41	30.65	65.95	6	3
PS119-5-1	5.45	9.47	5.01	11.84	83.16	6	7
PS119-5-1	5.55	1.85	0.69	3.14	96.17	2	7
PS119-5-1	5.605	6.8	2.25	5.64	92.11	2	7
PS119-5-1	5.7	1.85	0.64	2.61	96.75	2	7
PS119-5-1	5.8	1.85	0.51	3.85	95.64	1	15

Appendix A for Chapter 5

Core	depth (m)	Gravel fraction (counts/10cm <sup>-3</sup> )	Gravel (wt%)	Sand fraction (wt%)	Fine fraction (wt%)	Error occurred in the sieving process (wt%)*	Shear strength (kPa)
PS119-5-1	5.9	5.56	1.98	6.8	91.22	1	15
PS119-5-1	5.97	3.91	1.2	7.39	91.42	2	8
PS119-5-1	6	2.47	5.42	5.1	89.48	1	0
PS119-5-1	6.065	1.85	1.02	5.05	93.93	1	3
PS119-5-1	6.1	0.21	0.04	2.89	97.07	1	0
PS119-5-1	6.15	3.3	2.09	25.48	72.43	6	3
PS119-5-1	6.25	33.16	28.93	45.17	25.91	3	3
PS119-5-1	6.4	41.61	17.12	57.93	24.94	3	8
PS119-5-1	6.5	25.75	10.5	55.01	34.49	1	10
PS119-5-1	6.6	33.16	10.1	68.14	21.76	1	7
PS119-5-1	6.645	6.39	1.02	70.27	28.71	3	NN
PS119-5-1	6.75	27.6	10.16	46.02	43.83	1	7
PS119-5-1	6.85	24.1	9.66	53.35	37	1	3
PS119-5-1	6.9	23.69	8.6	62.4	29	3	NN
PS119-5-1	7	31.31	12.5	48.78	38.72	1	10
PS119-5-1	7.1	29.87	11.62	43.67	44.71	1	10
PS119-5-1	7.2	28.63	7.91	47.47	44.61	5	13
PS119-5-1	7.3	19.57	18.19	40.33	41.48	0	13
PS119-5-1	7.4	30.28	9.31	46.79	43.9	1	18
PS119-5-1	7.5	45.73	10.6	58.61	30.79	1	10
PS119-5-1	7.6	107.72	14.82	59.6	25.58	2	3
PS119-5-1	7.7	64.06	16.05	59.73	24.22	0	8
PS119-5-1	7.8	42.02	11.46	45.76	42.78	2	10
PS119-5-1	7.9	78.27	20	44.26	35.75	1	10
PS119-5-1	8	69	20.92	47.35	31.73	0	10
PS119-5-1	8.1	25.13	6.52	61.55	31.93	1	13
PS119-5-1	8.16	21.63	14.51	48.21	37.28	7	10
PS119-5-1	8.2	20.6	27.84	42.29	29.87	0	NN

Table A.3: PS119\_5-1 Chemical properties

Core	depth (m)	TC (wt%)	TOC (wt%)	Carbonate content (wt%)	bSiO2 (wt%)
PS119_5-1	0.01	0.87	0.69	1.52	20.83
PS119_5-1	0.08	0.68	0.56	0.97	NN
PS119_5-1	0.15	0.65	0.58	0.59	NN
PS119_5-1	0.25	0.52	0.45	0.55	NN
PS119_5-1	0.35	0.59	0.53	0.49	NN
PS119_5-1	0.45	0.64	0.54	0.85	NN
PS119_5-1	0.55	0.63	0.57	0.47	NN
PS119_5-1	0.65	0.53	0.48	0.46	NN
PS119_5-1	0.75	0.46	0.36	0.83	NN
PS119_5-1	0.85	0.49	0.42	0.58	NN

Appendix A for Chapter 5

Core	depth (m)	TC (wt%)	TOC (wt%)	Carbonate content (wt%)	bSiO2 (wt%)
PS119_5-1	0.95	0.45	0.39	0.52	NN
PS119_5-1	1.05	0.5	0.44	0.48	11.29
PS119_5-1	1.15	0.56	0.47	0.76	NN
PS119_5-1	1.25	0.51	0.46	0.41	NN
PS119_5-1	1.35	0.44	0.38	0.48	NN
PS119_5-1	1.45	0.44	0.43	0.13	NN
PS119_5-1	1.55	0.55	0.46	0.69	10.62
PS119_5-1	1.65	0.56	0.47	0.71	NN
PS119_5-1	1.75	0.41	0.37	0.32	NN
PS119_5-1	1.85	0.47	0.39	0.64	NN
PS119_5-1	1.95	0.57	0.54	0.3	NN
PS119_5-1	2.05	0.58	0.5	0.64	9.55
PS119_5-1	2.15	0.51	0.38	1.07	NN
PS119_5-1	2.25	0.56	0.47	0.69	NN
PS119_5-1	2.35	0.55	0.46	0.77	NN
PS119_5-1	2.45	0.57	0.49	0.67	NN
PS119_5-1	2.55	0.56	0.49	0.64	12.67
PS119_5-1	2.65	0.55	0.5	0.42	NN
PS119_5-1	2.75	0.6	0.52	0.64	NN
PS119_5-1	2.85	0.57	0.48	0.73	NN
PS119_5-1	2.95	0.55	0.49	0.54	NN
PS119_5-1	3.05	0.63	0.56	0.55	14.23
PS119_5-1	3.15	0.57	0.48	0.77	NN
PS119_5-1	3.25	0.62	0.54	0.67	NN
PS119_5-1	3.35	0.61	0.51	0.86	NN
PS119_5-1	3.45	0.63	0.54	0.75	NN
PS119_5-1	3.55	0.66	0.57	0.82	11.1
PS119_5-1	3.65	0.65	0.56	0.74	NN
PS119_5-1	3.75	0.65	0.56	0.8	NN
PS119_5-1	3.85	0.63	0.53	0.84	NN
PS119_5-1	3.95	0.64	0.55	0.74	NN
PS119_5-1	4.05	0.59	0.5	0.73	11.42
PS119_5-1	4.15	0.62	0.5	0.99	NN
PS119_5-1	4.25	0.63	0.55	0.64	NN
PS119_5-1	4.35	0.64	0.57	0.63	NN
PS119_5-1	4.39	0.66	0.59	0.62	NN
PS119_5-1	4.5	0.68	0.56	1.01	11.43
PS119_5-1	4.6	0.66	0.53	1.11	NN
PS119_5-1	4.7	0.63	0.52	0.9	NN
PS119_5-1	4.8	0.59	0.49	0.87	NN
PS119_5-1	4.9	0.56	0.46	0.82	NN
PS119_5-1	5	0.61	0.48	1.14	7.37
PS119_5-1	5.1	0.57	0.47	0.8	NN
PS119_5-1	5.2	0.61	0.5	0.96	NN

Appendix A for Chapter 5

Core	depth (m)	TC (wt%)	TOC (wt%)	Carbonate content (wt%)	bSiO <sub>2</sub> (wt%)
PS119_5-1	5.25	0.61	0.47	1.17	NN
PS119_5-1	5.3	0.63	0.44	1.61	4.74
PS119_5-1	5.45	0.73	0.52	1.7	NN
PS119_5-1	5.55	0.73	0.56	1.4	10.55
PS119_5-1	5.605	0.69	0.54	1.22	NN
PS119_5-1	5.7	0.73	0.56	1.4	NN
PS119_5-1	5.79	0.73	0.54	1.56	NN
PS119_5-1	5.9	0.73	0.54	1.55	NN
PS119_5-1	5.97	0.7	0.5	1.71	NN
PS119_5-1	6	0.72	0.53	1.54	NN
PS119_5-1	6.065	0.76	0.55	1.75	NN
PS119_5-1	6.1	0.71	0.49	1.84	2.38
PS119_5-1	6.15	0.71	0.51	1.72	NN
PS119_5-1	6.25	0.54	0.23	2.54	1.02
PS119_5-1	6.4	0.49	0.23	2.2	NN
PS119_5-1	6.5	0.52	0.24	2.31	NN
PS119_5-1	6.6	0.41	0.22	1.61	NN
PS119_5-1	6.645	0.44	0.21	1.96	NN
PS119_5-1	6.75	0.51	0.31	1.71	2.69
PS119_5-1	6.85	0.49	0.27	1.91	NN
PS119_5-1	6.9	0.47	0.24	1.89	NN
PS119_5-1	7	0.51	0.24	2.26	NN
PS119_5-1	7.1	0.58	0.32	2.21	NN
PS119_5-1	7.2	0.6	0.35	2.12	NN
PS119_5-1	7.3	0.58	0.24	2.86	NN
PS119_5-1	7.4	0.47	0.25	1.86	2.15
PS119_5-1	7.5	0.47	0.26	1.73	NN
PS119_5-1	7.6	0.5	0.27	1.93	NN
PS119_5-1	7.7	0.64	0.25	3.27	NN
PS119_5-1	7.8	0.56	0.28	2.35	1.38
PS119_5-1	7.9	0.57	0.27	2.49	NN
PS119_5-1	8	0.54	0.26	2.39	NN
PS119_5-1	8.1	0.57	0.26	2.63	0.81
PS119_5-1	8.16	0.51	0.25	2.21	NN
PS119_5-1	8.2	0.49	0.28	1.82	NN

Table A.4: PS119\_5-1 Physical properties

Core	depth (m)	Water content (wt%)	Salt corrected water content (wt%)	pycnometer density (gcm <sup>-3</sup> )	Wet Bulk Density (WBD) (gcm <sup>-3</sup> )	Porosity (P) (vol%)	grain density (GD) (gcm <sup>-3</sup> )	dry bulk density (DBD) (gcm <sup>-3</sup> )
PS119_5-1	0.010	50.10	51.90	2.559	1.44	73.13	2.58	0.69
PS119_5-1	0.080	44.40	46.00	2.642	1.53	68.90	2.66	0.83

Appendix A for Chapter 5

Core	depth (m)	Water content (wt%)	Salt corrected water content (wt%)	pycnometer density (gcm-3)	Wet Bulk Density (WBD) (gcm-3)	Porosity (P) (vol%)	grain density (GD) (gcm-3)	dry bulk density (DBD) (gcm-3)
PS119_5-1	0.150	43.30	44.90	2.619	1.54	67.73	2.64	0.85
PS119_5-1	0.250	35.40	36.70	2.699	1.69	60.57	2.72	1.07
PS119_5-1	0.350	37.50	38.90	2.664	1.65	62.48	2.68	1.01
PS119_5-1	0.450	43.50	45.10	2.331	1.48	65.24	2.34	0.81
PS119_5-1	0.550	41.10	42.60	2.601	1.57	65.47	2.62	0.90
PS119_5-1	0.650	35.80	37.10	2.680	1.68	60.80	2.70	1.06
PS119_5-1	0.750	29.70	30.80	2.723	1.81	54.33	2.74	1.25
PS119_5-1	0.850	31.70	32.80	2.722	1.77	56.62	2.74	1.19
PS119_5-1	0.950	32.00	33.20	2.703	1.75	56.83	2.72	1.17
PS119_5-1	1.050	31.60	32.70	2.680	1.76	56.11	2.69	1.18
PS119_5-1	1.150	34.60	35.80	2.639	1.69	59.13	2.65	1.08
PS119_5-1	1.250	31.50	32.70	2.680	1.76	56.07	2.69	1.18
PS119_5-1	1.350	29.10	30.10	2.697	1.81	53.30	2.71	1.27
PS119_5-1	1.450	29.70	30.80	2.702	1.80	54.09	2.71	1.25
PS119_5-1	1.550	34.90	36.20	2.669	1.69	59.76	2.68	1.08
PS119_5-1	1.650	36.00	37.30	2.676	1.67	61.00	2.69	1.05
PS119_5-1	1.750	26.30	27.30	2.738	1.88	50.15	2.75	1.37
PS119_5-1	1.850	29.70	30.80	2.681	1.79	53.90	2.69	1.24
PS119_5-1	1.950	35.70	37.00	2.628	1.67	60.21	2.64	1.05
PS119_5-1	2.050	33.70	34.90	2.637	1.71	58.10	2.65	1.11
PS119_5-1	2.150	32.30	33.40	2.649	1.73	56.61	2.66	1.15
PS119_5-1	2.250	33.60	34.80	2.619	1.70	57.87	2.63	1.11
PS119_5-1	2.350	33.90	35.20	2.622	1.70	58.24	2.63	1.10
PS119_5-1	2.450	35.00	36.30	2.619	1.68	59.39	2.63	1.07
PS119_5-1	2.550	37.90	39.30	2.586	1.62	62.17	2.60	0.98
PS119_5-1	2.650	34.80	36.00	2.606	1.68	59.01	2.62	1.07
PS119_5-1	2.750	35.60	36.90	2.606	1.66	59.96	2.62	1.05
PS119_5-1	2.850	35.20	36.50	2.623	1.67	59.68	2.64	1.06
PS119_5-1	2.950	36.30	37.60	2.574	1.64	60.35	2.59	1.03
PS119_5-1	3.050	42.50	44.00	2.578	1.55	66.59	2.59	0.87
PS119_5-1	3.150	36.20	37.50	2.611	1.66	60.57	2.62	1.03
PS119_5-1	3.250	37.80	39.20	2.620	1.63	62.37	2.63	0.99
PS119_5-1	3.350	36.00	37.30	2.586	1.65	60.13	2.60	1.04
PS119_5-1	3.450	38.30	39.70	2.583	1.61	62.53	2.60	0.97
PS119_5-1	3.550	39.40	40.80	2.574	1.59	63.57	2.59	0.94
PS119_5-1	3.650	37.90	39.30	2.604	1.62	62.35	2.62	0.99
PS119_5-1	3.750	39.10	40.50	2.551	1.59	63.03	2.56	0.95
PS119_5-1	3.850	38.10	39.50	2.582	1.62	62.31	2.60	0.98
PS119_5-1	3.950	39.30	40.70	2.585	1.60	63.55	2.60	0.95
PS119_5-1	4.050	33.80	35.00	2.631	1.70	58.17	2.64	1.11
PS119_5-1	4.150	37.00	38.40	2.597	1.64	61.35	2.61	1.01
PS119_5-1	4.250	37.70	39.10	2.586	1.62	61.98	2.60	0.99

Appendix A for Chapter 5

Core	depth (m)	Water content (wt%)	Salt corrected water content (wt%)	pycnometer density (gcm <sup>-3</sup> )	Wet Bulk Density (WBD) (gcm <sup>-3</sup> )	Porosity (P) (vol%)	grain density (GD) (gcm <sup>-3</sup> )	dry bulk density (DBD) (gcm <sup>-3</sup> )
PS119_5-1	4.350	35.60	36.90	2.604	1.66	59.88	2.62	1.05
PS119_5-1	4.390	36.70	38.00	2.609	1.65	61.12	2.62	1.02
PS119_5-1	4.500	42.30	43.90	2.542	1.54	66.11	2.56	0.87
PS119_5-1	4.600	37.10	38.40	2.600	1.64	61.43	2.61	1.01
PS119_5-1	4.700	34.70	35.90	2.616	1.68	58.99	2.63	1.08
PS119_5-1	4.800	32.70	33.90	2.643	1.72	57.11	2.66	1.14
PS119_5-1	4.900	32.40	33.60	2.639	1.73	56.66	2.65	1.15
PS119_5-1	5.000	34.30	35.50	2.611	1.69	58.54	2.62	1.09
PS119_5-1	5.100	32.40	33.60	2.629	1.73	56.61	2.64	1.15
PS119_5-1	5.200	34.30	35.60	2.638	1.69	58.83	2.65	1.09
PS119_5-1	5.250	32.90	34.10	2.622	1.71	57.10	2.63	1.13
PS119_5-1	5.300	30.30	31.40	2.640	1.77	54.28	2.65	1.21
PS119_5-1	5.450	38.40	39.80	2.627	1.62	63.05	2.64	0.98
PS119_5-1	5.550	42.40	44.00	2.585	1.55	66.60	2.60	0.87
PS119_5-1	5.605	42.80	44.40	2.591	1.55	67.04	2.61	0.86
PS119_5-1	5.700	38.80	40.20	2.612	1.61	63.30	2.63	0.96
PS119_5-1	5.790	39.30	40.70	2.631	1.61	63.99	2.65	0.95
PS119_5-1	5.900	38.10	39.50	2.592	1.62	62.46	2.61	0.98
PS119_5-1	5.970	38.30	39.70	2.616	1.62	62.83	2.63	0.98
PS119_5-1	6.000	40.80	42.30	2.635	1.59	65.52	2.65	0.91
PS119_5-1	6.065	45.40	47.10	2.590	1.51	69.39	2.61	0.80
PS119_5-1	6.100	48.70	50.50	2.623	1.47	72.50	2.65	0.73
PS119_5-1	6.150	44.90	46.60	2.647	1.53	69.42	2.67	0.82
PS119_5-1	6.250	19.00	19.70	2.762	2.07	39.90	2.77	1.66
PS119_5-1	6.400	15.50	16.10	2.717	2.15	33.75	2.72	1.80
PS119_5-1	6.500	16.40	17.00	2.726	2.13	35.33	2.73	1.77
PS119_5-1	6.600	15.20	15.80	2.728	2.16	33.33	2.73	1.82
PS119_5-1	6.645	18.10	18.80	2.733	2.08	38.25	2.74	1.69
PS119_5-1	6.750	19.40	20.10	2.717	2.04	40.05	2.72	1.63
PS119_5-1	6.850	17.10	17.70	2.775	2.13	36.87	2.78	1.76
PS119_5-1	6.900	17.60	18.20	2.708	2.09	37.14	2.71	1.71
PS119_5-1	7.000	18.40	19.00	2.769	2.09	38.91	2.78	1.70
PS119_5-1	7.100	20.00	20.70	2.699	2.02	40.78	2.71	1.60
PS119_5-1	7.200	19.90	20.60	2.711	2.03	40.83	2.72	1.61
PS119_5-1	7.300	18.00	18.60	2.724	2.08	37.92	2.73	1.69
PS119_5-1	7.400	17.10	17.70	2.756	2.12	36.70	2.76	1.75
PS119_5-1	7.500	15.80	16.40	2.708	2.14	34.14	2.71	1.79
PS119_5-1	7.600	15.90	16.50	2.729	2.14	34.57	2.73	1.79
PS119_5-1	7.700	15.00	15.60	2.739	2.17	33.10	2.74	1.84
PS119_5-1	7.800	18.70	19.40	2.709	2.06	38.92	2.72	1.66
PS119_5-1	7.900	18.10	18.80	2.713	2.08	38.02	2.72	1.69
PS119_5-1	8.000	16.50	17.10	2.723	2.12	35.53	2.73	1.76



Appendix A for Chapter 5

---

Core	depth (m)	Water content (wt%)	Salt corrected water content (wt%)	pycnometer density ( $\text{gcm}^{-3}$ )	Wet Bulk Density (WBD) ( $\text{gcm}^{-3}$ )	Porosity (P) (vol%)	grain density (GD) ( $\text{gcm}^{-3}$ )	dry bulk density (DBD) ( $\text{gcm}^{-3}$ )
PS119_5-1	8.100	15.70	16.30	2.735	2.15	34.27	2.74	1.80
PS119_5-1	8.160	14.90	15.40	2.770	2.20	33.04	2.78	1.86
PS119_5-1	8.160	16.00	16.60	2.723	2.14	34.63	2.73	1.78
PS119_5-1	8.200	15.20	15.80	2.737	2.17	33.39	2.74	1.83

## Appendix B for Chapter 6

### Appendix B

Supporting Online Material for

### Spatial and temporal variability in Holocene trough-fill sediments, King Haakon Trough System, sub-Antarctic South Georgia

Lešić, Nina-Marie<sup>1,2</sup> (nlesic@marum.de); Streuff, Katharina Teresa<sup>1</sup> (kstreuff@marum.de); Bohrmann, Gerhard<sup>1</sup> (gbohrmann@marum.de); Kuhn, Gerhard<sup>1,2</sup> (ge\_ku@uni-bremen.de)

<sup>1</sup> MARUM, Centre for Marine Environmental Sciences, and Faculty of Geosciences, University of Bremen (UoB), Klagenfurter Str.2-4, 28359 Bremen

<sup>2</sup> Alfred Wegener Institute (AWI), Helmholtz Centre for Polar and Marine Research, Am Alten Hafen 26, 27568 Bremerhaven, Germany

#### B1. Figures

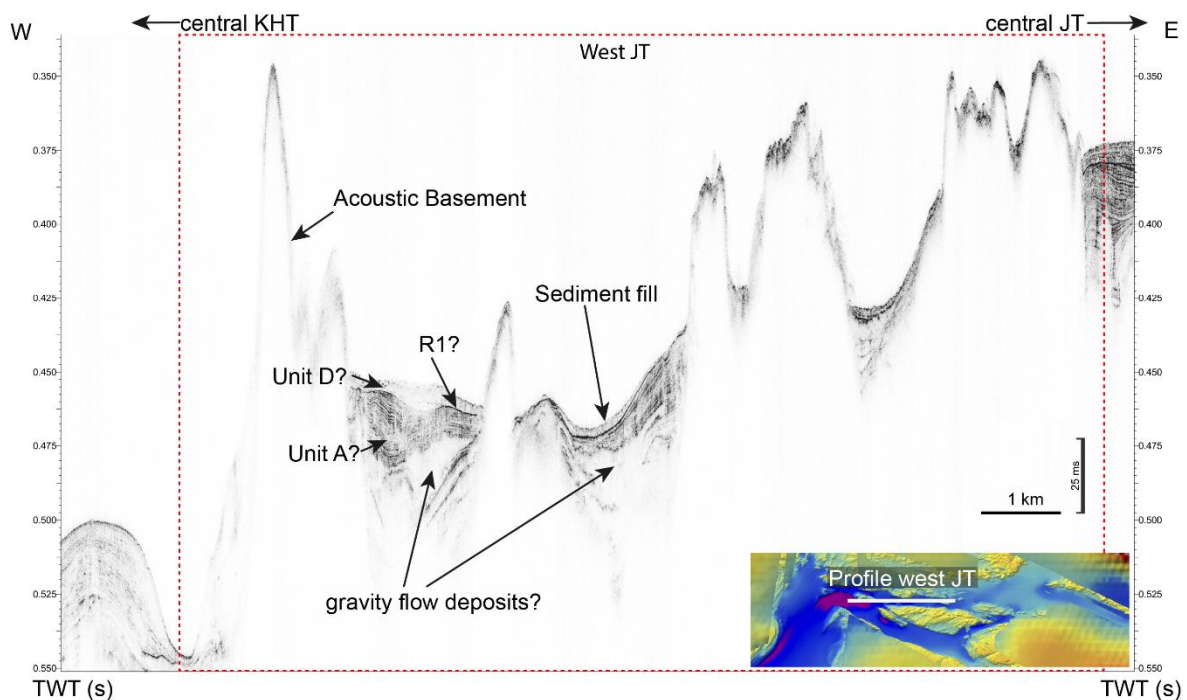


Fig. B. 1: Acoustic Profile through west JT. The red dashed line frames west JT with central JT to the east and central KHT to the west. The position of the Profile is indicated by the white line in the inset in the lower right corner. The KHTS typical acoustic units are difficult to identify due to obscured signals and an incorporated, transparent facies. However, the strongest reflector is reminiscent of R1 (Figure 4)

## Appendix C for Chapter 7

### Appendix C

Supporting Online Material for

#### Climate-driven Holocene sedimentation in King Haakon Trough System, sub-Antarctic South Georgia

Lešić, Nina-Marie<sup>1,2</sup> (nlesic@marum.de); Streuff, Katharina Teresa<sup>1</sup> (kstreuff@marum.de); Titschack, Jürgen<sup>1</sup> (jtitschack@marum.de); von Dobeneck, Tilo<sup>1</sup> (dobeneck@uni-bremen.de); Kuhn, Gerhard<sup>1</sup> (ge\_ku@uni-bremen.de); Bohrmann, Gerhard<sup>1</sup> (gbohrmann@marum.de)

<sup>1</sup> MARUM, Centre for Marine Environmental Sciences, and Faculty of Geosciences, University of Bremen (UoB), Klagenfurter Str., D-28334 Bremen

<sup>2</sup> Alfred Wegener Institute (AWI), Helmholtz Centre for Polar and Marine Research, Am Alten Hafen 26, 27568 Bremerhaven, Germany

#### C1. Methods

##### C1.1 CT tomograph

The computer tomograph at the hospital ‘Klinikum Bremen-Mitte’, a Philips Brilliance iCT Elite 256 computer tomograph (CT) device, was operated with a current of 300 mA and an X-ray source voltage of 120 kV. The resulting CT image stacks feature a physical resolution of 0.293 mm in the x and y directions and 0.625 mm resolution in the z direction (collimation; 0.3 mm reconstruction interval). For Image reconstruction, the filtered Back Projection (fBP) mode and a bone kernel (YB (Enhanced)) was used. Data processing was carried out with the ZIB edition of the Amira software (version 2022.05; Stalling et al., 2005). In the process, CT scans of the core sections were merged and cropped to remove the core liners and exclude the outermost ~2 mm of sediment. With the *Segmentation Editor*, utilising the marker-based watershed algorithm, the following constituents were segmented and categorised: Open bioturbation traces and pores (air- or water-filled), high-density clasts >~1 mm, as well as the matrix sediment and fossil remains. The respective markers were set by thresholding. With the *ContourTreeSegmentation* module (persistence mode: adaptive; persistent values: 0.05), individual clasts were identified and separated. To obtain the X-ray attenuation of the sediment matrix and its standard deviation (measured in Hounsfield Unit (HU)), which is used as a dry bulk density (DBD) proxy, we used the *Material Statistics* module (statistic per slice and label), but only after reducing the matrix sediment label by two voxels to avoid potential marginal effects.

##### C1.2 Age model codes for RSuite

## C1.2.1 GeoB22058-1

## C1.2.1.1 Upper part (Unit D)

```

rm(list = ls())
library(Bchron)

#####
#####
# Let's take a look at the dataset.
#####
#####
dates = matrix(c(0.6,1.6,2.6,3.8,0.584,0.9,1.658,2.143,0.071,0.161,0.143,0.184), nrow = 4, ncol = 3)
# Bchron likes to work with whole numbers... so we convert kyr to yr
dates[,2] = dates[,2] * 1000
dates[,3] = dates[,3] * 1000
colnames(dates) <- c("Depth (m)", "Age (a)", "Uncertainty (2sigma, yr)")
dates = as.data.frame(dates)
plot(dates$`Age (a)`, dates$`Depth (m)`, ylim = c(4,0.01), xlim=c(0,12000),xaxs = "i", yaxs = "i", col =
"blue", pch = 19, xlab = "Age (a)", ylab = "Depth (m)")
for (j in 1:4){segments(dates[j,2]-dates[j,3],dates[j,1],dates[j,2]+dates[j,3],dates[j,1], col = "blue", lwd
= 2)}
depths_i=seq(0,4,0.01)

#####
#####
# Bchron (for pleistocene and holocene)
#####
#####
#monte carlo simulations
output = Bchronology(
  ages = dates$`Age (a)`,
  ageSds = dates$`Uncertainty (2sigma, yr)`,/2,
  positions = dates$`Depth (m)`,
  calCurves = rep("normal",4),
  predictPositions = depths_i)

ages_Bchron=matrix(data = NA, nrow = 401, ncol = 3)
colnames(ages_Bchron) <- c("2.5% CL", "Median Age", "97.5% CL")
for (k in 1:401){
  ages_Bchron[k,]=quantile(output$thetaPredict[,k], probs = c(0.025,0.5,0.975))}

dev.off()
plot(dates$`Age (a)`, dates$`Depth (m)`, ylim = c(4,0), xlim = c(0,12000), yaxs = "i", yaxs = "i", col =
"blue", pch = 19, xlab = "Age (ka)", ylab = "Depth (m)")
for (j in 1:4){segments(dates[j,2]-dates[j,3],dates[j,1],dates[j,2]+dates[j,3],dates[j,1], col = "blue", lwd
= 2)}
points(ages_Bchron[,2], depths_i, col = "grey")
lines(ages_Bchron[,1], depths_i) # Upper confidence level
lines(ages_Bchron[,3], depths_i) # Lower confidence level

write.csv(ages_Bchron, "age_model_Bchron_GeoB22058-1_upperpart.csv", row.names = F)

```

## C1.2.1.2 Lower part (Unit A)

```

rm(list = ls())
library(Bchron)

#####
#####
# Let's take a look at the dataset.
#####
#####
dates =
matrix(c(4.3,4.7,5.6,6.5,6.9,8,7.718,8.276,8.849,9.446,9.646,10.167,0.1735,0.1945,0.259,0.257,0.217
5,0.294), nrow = 6, ncol = 3)
# Bchron likes to work with whole numbers... so we convert kyr to yr
dates[,2] = dates[,2] * 1000
dates[,3] = dates[,3] * 1000
colnames(dates) <- c("Depth (m)", "Age (a)", "Uncertainty (2sigma, yr)")
dates = as.data.frame(dates)
plot(dates$`Age (a)`, dates$`Depth (m)`, ylim = c(9.41,0.01), xlim=c(0,12000),xaxs = "i", yaxs = "i", col
= "blue", pch = 19, xlab = "Age (a)", ylab = "Depth (m)")
for (j in 1:6){segments(dates[j,2]-dates[j,3],dates[j,1],dates[j,2]+dates[j,3],dates[j,1], col = "blue", lwd
= 2)}
depths_i=seq(4.12,9.41,0.01)

#####
#####
# Bchron (for pleistocene and holocene)
#####
#####
#monte carlo simulations
output = Bchronology(
  ages = dates$`Age (a)`,
  ageSds = dates$`Uncertainty (2sigma, yr)`/2,
  positions = dates$`Depth (m)`,
  calCurves = rep("normal",6),
  predictPositions = depths_i)

ages_Bchron=matrix(data = NA, nrow = 530, ncol = 3)
colnames(ages_Bchron) <- c("2.5% CL", "Median Age", "97.5% CL")
for (k in 1:530){
  ages_Bchron[k,]=quantile(output$thetaPredict[,k], probs = c(0.025,0.5,0.975))}

dev.off()
plot(dates$`Age (a)`, dates$`Depth (m)`, ylim = c(9.41,4.12), xlim = c(0,12000), yaxs = "i", yaxs = "i", col
= "blue", pch = 19, xlab = "Age (ka)", ylab = "Depth (m)")
for (j in 1:6){segments(dates[j,2]-dates[j,3],dates[j,1],dates[j,2]+dates[j,3],dates[j,1], col = "blue", lwd
= 2)}
points(ages_Bchron[,2], depths_i, col = "grey")
lines(ages_Bchron[,1], depths_i) # Upper confidence level
lines(ages_Bchron[,3], depths_i) # Lower confidence level

```

```
write.csv(ages_Bchron, "age_model_Bchron_GeoB22058-1_lowerpart.csv", row.names = F)
```

## C1.2.2 GeoB22057-1

### C1.2.2.1 Upper part (Unit D)

```
rm(list = ls())
library(Bchron)

#####
#####
# Let's take a look at the dataset.
#####
#####
dates = matrix(c(0.2,1.92,3.4,3.9,4.3,0.15,1.072,1.645,2.238,2.598,0.149,0.164,0.161,0.175,0.1925),
nrow = 5, ncol = 3)
# Bchron likes to work with whole numbers... so we convert kyr to yr
dates[,2] = dates[,2] * 1000
dates[,3] = dates[,3] * 1000
colnames(dates) <- c("Depth (m)", "Age (a)", "Uncertainty (2sigma, yr)")
dates = as.data.frame(dates)
plot(dates$`Age (a)`, dates$`Depth (m)`, ylim = c(8.79,0.01), xlim=c(0,9000),xaxs = "i", yaxs = "i", col =
"blue", pch = 19, xlab = "Age (a)", ylab = "Depth (m)")
for (j in 1:5){segments(dates[j,2]-dates[j,3],dates[j,1],dates[j,2]+dates[j,3],dates[j,1], col = "blue", lwd
= 2)}
depths_i=seq(0,4.46,0.01)

#####
#####
# Bchron (for pleistocene and holocene)
#####
#####
#monte carlo simulations
output = Bchronology(
  ages = dates$`Age (a)`,
  ageSds = dates$`Uncertainty (2sigma, yr)`/2,
  positions = dates$`Depth (m)`,
  calCurves = rep("normal",5),
  predictPositions = depths_i)

ages_Bchron=matrix(data = NA, nrow = 447, ncol = 3)
colnames(ages_Bchron) <- c("2.5% CL", "Median Age", "97.5% CL")
for (k in 1:447){
  ages_Bchron[k,]=quantile(output$thetaPredict[,k], probs = c(0.025,0.5,0.975))}

dev.off()
plot(dates$`Age (a)`, dates$`Depth (m)`, ylim = c(8.79,0), xlim = c(0,9000), yaxs = "i", yaxs = "i", col =
"blue", pch = 19, xlab = "Age (ka)", ylab = "Depth (m)")
for (j in 1:5){segments(dates[j,2]-dates[j,3],dates[j,1],dates[j,2]+dates[j,3],dates[j,1], col = "blue", lwd
= 2)}
points(ages_Bchron[,2], depths_i, col = "grey")
```

```
lines(ages_Bchron[,1], depths_i) # Upper confidence level
lines(ages_Bchron[,3], depths_i) # Lower confidence level

write.csv(ages_Bchron, "age_model_Bchron_GeoB22057-1_upperpart.csv", row.names = F)
```

## C.1.2.2.1 Lower part (Unit B)

```
rm(list = ls())
library(Bchron)

#####
#####
# Let's take a look at the dataset.
#####
#####
dates = matrix(c(4.6,5,5.9,6.94,7.5,3.899,4.814,5.991,6.874,7.129,0.1935,0.229,0.274,0.243,0.1875),
nrow = 5, ncol = 3)
# Bchron likes to work with whole numbers... so we convert kyr to yr
dates[,2] = dates[,2] * 1000
dates[,3] = dates[,3] * 1000
colnames(dates) <- c("Depth (m)", "Age (a)", "Uncertainty (2sigma, yr)")
dates = as.data.frame(dates)
plot(dates$`Age (a)`, dates$`Depth (m)`, ylim = c(8.79,0.01), xlim=c(0,9000),xaxs = "i", yaxs = "i", col =
"blue", pch = 19, xlab = "Age (a)", ylab = "Depth (m)")
for (j in 1:5){segments(dates[j,2]-dates[j,3],dates[j,1],dates[j,2]+dates[j,3],dates[j,1], col = "blue", lwd
= 2)}
depths_i=seq(4.46,8.79,0.01)

#####
#####
# Bchron (for pleistocene and holocene)
#####
#####
#monte carlo simulations
output = Bchronology(
  ages = dates$`Age (a)`,
  ageSds = dates$`Uncertainty (2sigma, yr)`,/2,
  positions = dates$`Depth (m)`,
  calCurves = rep("normal",5),
  predictPositions = depths_i)

ages_Bchron=matrix(data = NA, nrow = 434, ncol = 3)
colnames(ages_Bchron) <- c("2.5% CL", "Median Age", "97.5% CL")
for (k in 1:434){
  ages_Bchron[k,]=quantile(output$thetaPredict[,k], probs = c(0.025,0.5,0.975))}

dev.off()
plot(dates$`Age (a)`, dates$`Depth (m)`, ylim = c(8.79,0), xlim = c(0,9000), yaxs = "i", yaxs = "i", col =
"blue", pch = 19, xlab = "Age (ka)", ylab = "Depth (m)")
for (j in 1:5){segments(dates[j,2]-dates[j,3],dates[j,1],dates[j,2]+dates[j,3],dates[j,1], col = "blue", lwd
= 2)}
points(ages_Bchron[,2], depths_i, col = "grey")
```

```
lines(ages_Bchron[,1], depths_i) # Upper confidence level
lines(ages_Bchron[,3], depths_i) # Lower confidence level

write.csv(ages_Bchron, "age_model_Bchron_GeoB22057-1_lowerpart.csv", row.names = F)
```

## C1.2.3 GeoB22056-1

```
rm(list = ls())
library(Bchron)

#####
#####
# Let's take a look at the dataset.
#####
#####
dates
matrix(c(0.6,1.7,2.7,3.8,4.9,5.3,6.2,6.45,0.404,0.548,0.731,1.031,1.073,1.364,1.481,1.483,0.1
,0.1555,0.1250,0.1250,0.1646,0.1145,0.1635,0.1615), nrow = 8, ncol = 3)
# Bchron likes to work with whole numbers... so we convert kyr to yr
dates[,2] = dates[,2] * 1000
dates[,3] = dates[,3] * 1000
colnames(dates) <- c("Depth (m)", "Age (a)", "Uncertainty (2sigma, yr)")
dates = as.data.frame(dates)
plot(dates$`Age (a)`, dates$`Depth (m)`, ylim = c(7.22,0.01), xlim=c(0,3000),xaxs = "i", yaxs =
"i", col = "blue", pch = 19, xlab = "Age (a)", ylab = "Depth (m)")
for (j in 1:8){segments(dates[j,2]-dates[j,3],dates[j,1],dates[j,2]+dates[j,3],dates[j,1], col =
"blue", lwd = 2)}
depths_i=seq(0,7.22,0.01)

#####
#####
# Bchron (for pleistocene and holocene)
#####
#####
#monte carlo simulations
output = Bchronology(
  ages = dates$`Age (a)`,
  ageSds = dates$`Uncertainty (2sigma, yr)`,/2,
  positions = dates$`Depth (m)`,
  calCurves = rep("normal",8),
  predictPositions = depths_i)

ages_Bchron=matrix(data = NA, nrow = 723, ncol = 3)
colnames(ages_Bchron) <- c("2.5% CL", "Median Age", "97.5% CL")
for (k in 1:723){
  ages_Bchron[k,]=quantile(output$thetaPredict[,k], probs = c(0.025,0.5,0.975))}

dev.off()
```



```

plot(dates$`Age (a)`, dates$`Depth (m)`, ylim = c(7.22,0), xlim = c(0,3000), xaxs = "i", yaxs = "i",
col = "blue", pch = 19, xlab = "Age (ka)", ylab = "Depth (m)")
for (j in 1:8){segments(dates[j,2]-dates[j,3],dates[j,1],dates[j,2]+dates[j,3],dates[j,1], col =
"blue", lwd = 2)}
points(ages_Bchron[,2], depths_i, col = "grey")
lines(ages_Bchron[,1], depths_i) # Upper confidence level
lines(ages_Bchron[,3], depths_i) # Lower confidence level

write.csv(ages_Bchron, "age_model_Bchron_GeoB22056-1.csv", row.names = F)

```

### C1.2.3 PS133/2\_17-13

#### C1.2.3.1 Upper part (Unit C+D)

```

rm(list = ls())
library(Bchron)

#####
#####
# Let's take a look at the dataset.
#####
#####
dates
matrix(c(0.30,0.605,1.01,1.83,2.36,3.035,0.422,1.182,1.659,2.557,3.294,4.144,0.102,0.141,0.141,0.1
79,0.182,0.239), nrow = 6, ncol = 3)
# Bchron likes to work with whole numbers... so we convert kyr to yr
dates[,2] = dates[,2] * 1000
dates[,3] = dates[,3] * 1000
colnames(dates) <- c("Depth (m)", "Age (a)", "Uncertainty (2sigma, yr)")
dates = as.data.frame(dates)
plot(dates$`Age (a)`, dates$`Depth (m)`, ylim = c(3.04,0.01), xlim=c(0,5000),xaxs = "i", yaxs = "i", col =
"blue", pch = 19, xlab = "Age (a)", ylab = "Depth (m)")
for (j in 1:6){segments(dates[j,2]-dates[j,3],dates[j,1],dates[j,2]+dates[j,3],dates[j,1], col = "blue", lwd
= 2)}
depths_i=seq(0,3.04,0.01)

#####
#####
# Bchron (for pleistocene and holocene)
#####
#####
#monte carlo simulations
output = Bchronology(
  ages = dates$`Age (a)`,
  ageSds = dates$`Uncertainty (2sigma, yr)`/2,
  positions = dates$`Depth (m)`,
  calCurves = rep("normal",6),
  predictPositions = depths_i)

ages_Bchron=matrix(data = NA, nrow = 305, ncol = 3)

```

```

colnames(ages_Bchron) <- c("2.5% CL", "Median Age", "97.5% CL")
for (k in 1:305){
  ages_Bchron[k,]=quantile(output$thetaPredict[,k], probs = c(0.025,0.5,0.975))}

dev.off()
plot(dates$`Age (a)`, dates$`Depth (m)`, ylim = c(3.04,0), xlim = c(0,5000), xaxs = "i", yaxs = "i", col =
"blue", pch = 19, xlab = "Age (ka)", ylab = "Depth (m)")
for (j in 1:6){segments(dates[j,2]-dates[j,3],dates[j,1],dates[j,2]+dates[j,3],dates[j,1], col = "blue", lwd
= 2)}
points(ages_Bchron[,2], depths_i, col = "grey")
lines(ages_Bchron[,1], depths_i) # Upper confidence level
lines(ages_Bchron[,3], depths_i) # Lower confidence level

write.csv(ages_Bchron, "age_model_Bchron_PS133-2_17-13_upperpart.csv", row.names = F)

```

### C1.2.3.2 Lower part (Unit A)

```

rm(list = ls())
library(Bchron)

#####
#####
# Let's take a look at the dataset.
#####
#####
dates = matrix(c(4.34,8.855,8.511,9.028,0.137,0.202), nrow = 2, ncol = 3)
# Bchron likes to work with whole numbers... so we convert kyr to yr
dates[,2] = dates[,2] * 1000
dates[,3] = dates[,3] * 1000
colnames(dates) <- c("Depth (m)", "Age (a)", "Uncertainty (2sigma, yr)")
dates = as.data.frame(dates)
plot(dates$`Age (a)`, dates$`Depth (m)`, ylim = c(8.95,0.01), xlim=c(3500,12000),xaxs = "i", yaxs = "i",
col = "blue", pch = 19, xlab = "Age (a)", ylab = "Depth (m)")
for (j in 1:2){segments(dates[j,2]-dates[j,3],dates[j,1],dates[j,2]+dates[j,3],dates[j,1], col = "blue", lwd
= 2)}
depths_i=seq(3.08,8.95,0.01)

#####
#####
# Bchron (for pleistocene and holocene)
#####
#####
#monte carlo simulations
output = Bchronology(
  ages = dates$`Age (a)`,
  ageSds = dates$`Uncertainty (2sigma, yr)`/2,
  positions = dates$`Depth (m)`,
  calCurves = rep("normal",2),
  predictPositions = depths_i)

ages_Bchron=matrix(data = NA, nrow = 588, ncol = 3)

```

```

colnames(ages_Bchron) <- c("2.5% CL", "Median Age", "97.5% CL")
for (k in 1:588){
  ages_Bchron[k,]=quantile(output$thetaPredict[,k], probs = c(0.025,0.5,0.975))}

dev.off()
plot(dates$`Age (a)`, dates$`Depth (m)`, ylim = c(8.95,3.08), xlim = c(3500,12000), xaxs = "i", yaxs = "i",
col = "blue", pch = 19, xlab = "Age (ka)", ylab = "Depth (m)")
for (j in 1:2){segments(dates[j,2]-dates[j,3],dates[j,1],dates[j,2]+dates[j,3],dates[j,1], col = "blue", lwd
= 2)}
points(ages_Bchron[,2], depths_i, col = "grey")
lines(ages_Bchron[,1], depths_i) # Upper confidence level
lines(ages_Bchron[,3], depths_i) # Lower confidence level

write.csv(ages_Bchron, "age_model_Bchron_PS133-2_17-13_lowerpart.csv", row.names = F)

```

## C1.1.4 GC666

```

rm(list = ls())
library(Bchron)

#####
#####
# Let's take a look at the dataset.
#####
#####
dates = matrix(c(0,3.88,131,11750,133.5,212), nrow = 2, ncol = 3)
colnames(dates) <- c("Depth (m)", "Age (a)", "Uncertainty (2sigma, yr)")
dates = as.data.frame(dates)
plot(dates$`Age (a)`, dates$`Depth (m)`, ylim = c(3.88,0.01), xlim=c(0,12000),xaxs = "i", yaxs = "i", col
= "blue", pch = 19, xlab = "Age (a)", ylab = "Depth (m)")
for (j in 1:2){segments(dates[j,2]-dates[j,3],dates[j,1],dates[j,2]+dates[j,3],dates[j,1], col = "blue", lwd
= 2)}
depths_i=seq(0,3.88,0.01)

#####
#####
# Bchron (for pleistocene and holocene)
#####
#####
#monte carlo simulations
output = Bchronology(
  ages = dates$`Age (a)`,
  ageSds = dates$`Uncertainty (2sigma, yr)`/2,
  positions = dates$`Depth (m)`,
  calCurves = rep("normal",2),
  predictPositions = depths_i)

ages_Bchron=matrix(data = NA, nrow = 389, ncol = 3)
colnames(ages_Bchron) <- c("2.5% CL", "Median Age", "97.5% CL")
for (k in 1:389){
  ages_Bchron[k,]=quantile(output$thetaPredict[,k], probs = c(0.025,0.5,0.975))}

```

```

dev.off()
plot(dates$`Age (a)` , dates$`Depth (m)` , ylim = c(3.88,0), xlim = c(3500,12000), xaxs = "i", yaxs = "i",
col = "blue", pch = 19, xlab = "Age (ka)", ylab = "Depth (m)")
for (j in 1:2){segments(dates[j,2]-dates[j,3],dates[j,1],dates[j,2]+dates[j,3],dates[j,1], col = "blue", lwd
= 2)}
points(ages_Bchron[2], depths_i, col = "grey")
lines(ages_Bchron[1], depths_i) # Upper confidence level
lines(ages_Bchron[3], depths_i) # Lower confidence level

write.csv(ages_Bchron, "age_model_Bchron_JR257_GC666_2.csv", row.names = F)

```

## C2. Figures

### C2.1 Biogenic silica

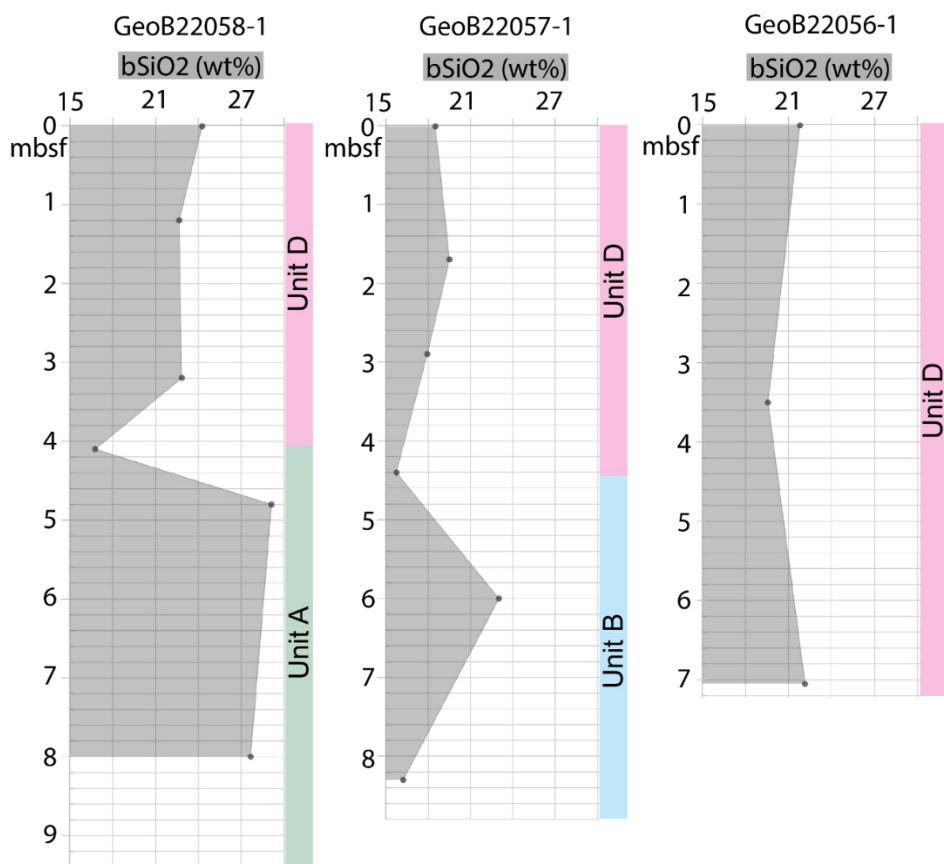


Fig. C.1: Biogenic silica (bSiO<sub>2</sub>) values for Jacobsen Trough cores within the assigned Unit wint wt%. Note that this is not equivalent to biogenic opal. To assess biogenic opal, a factor of 100/90 has to be applied, which accounts for 19% bound water within the biogenic opal (Müller and Schneider, 1993)

### C2.2 CT scan Slices

C2.2.1 GeoB22058-1

**GeoB22058-1**

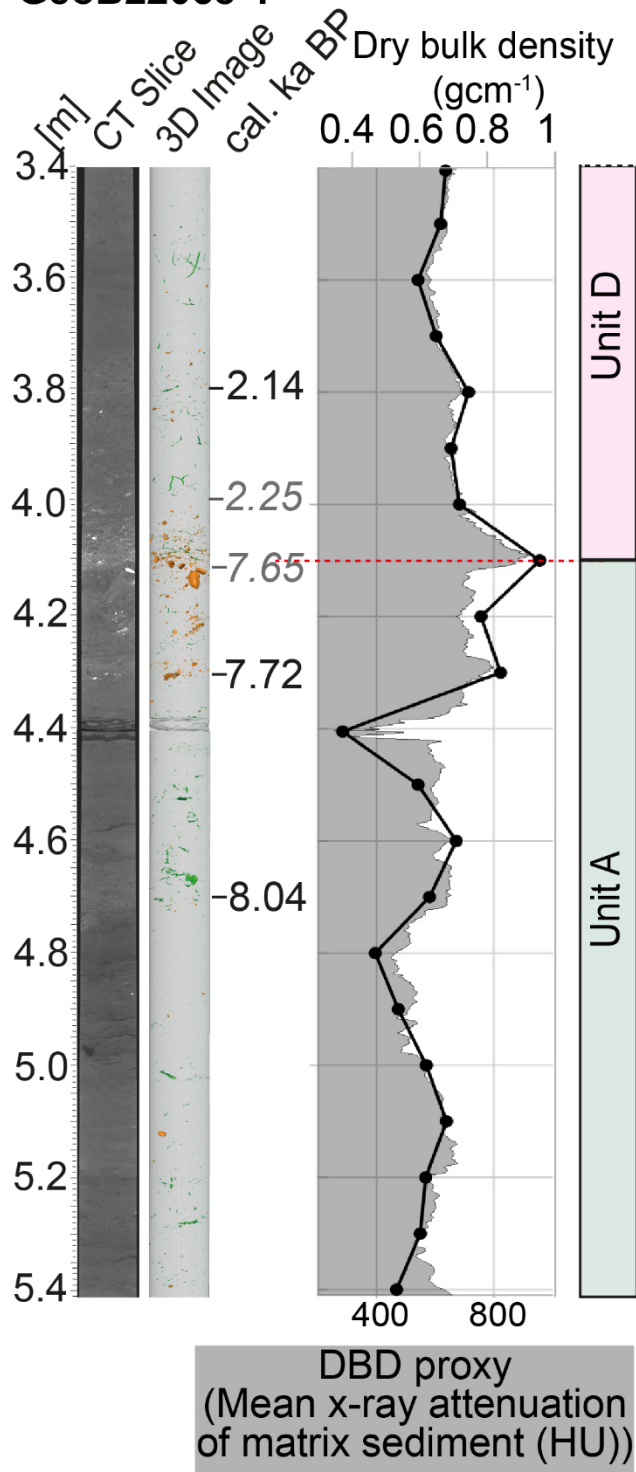
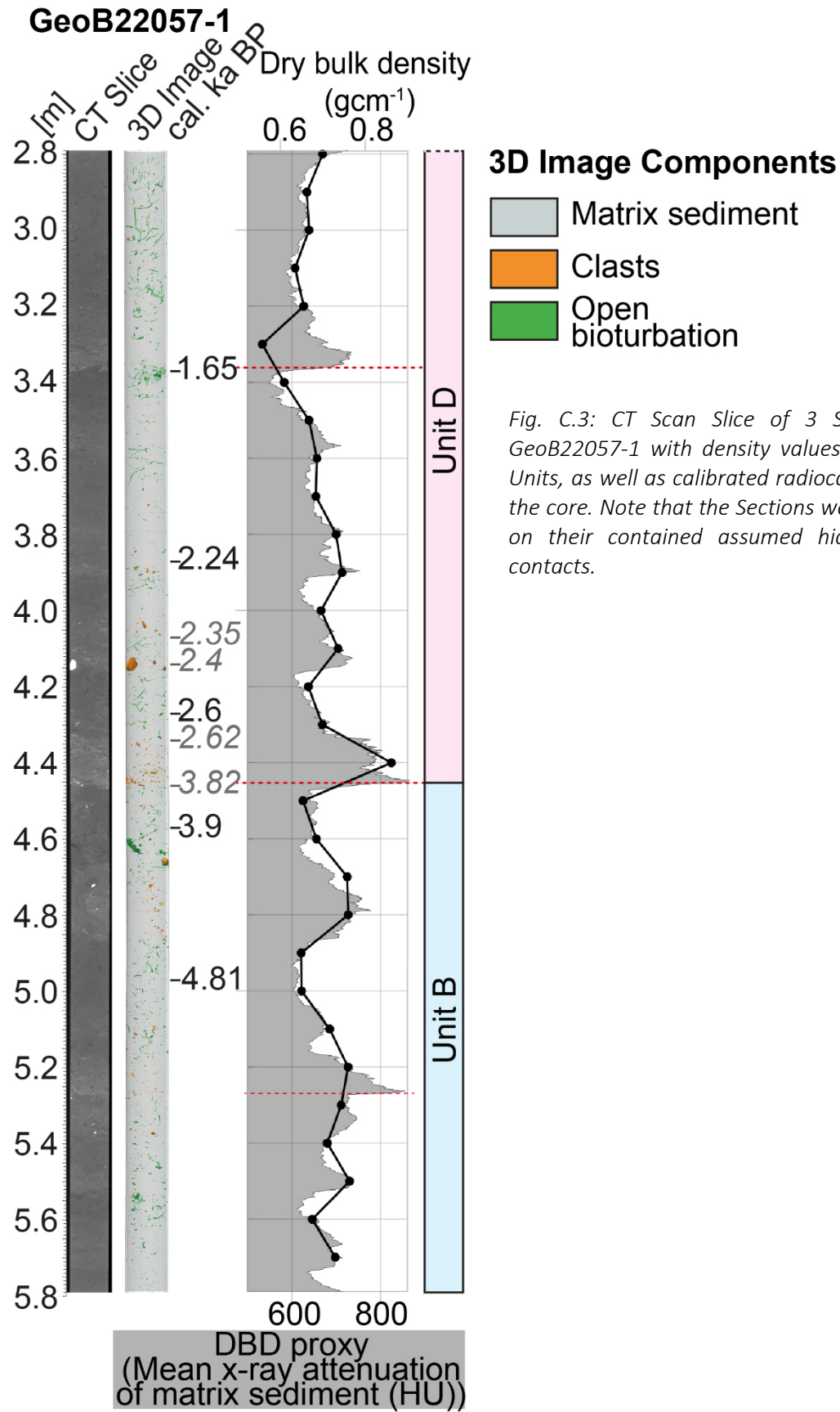


Fig. C.2: CT Scan Slice of 2 Sections of core GeoB22058-1 with density values and interpreted Units, as well as calibrated radiocarbon ages along the core. Note that the Sections were chosen based on their contained assumed hiatuses and Unit contacts.

**3D Image Components**

- Matrix sediment
- Open bioturbation
- Clasts

C2.2.2 GeoB22057-1



C2.2.3 PS133/2\_17-13

**PS133/2\_17-13**

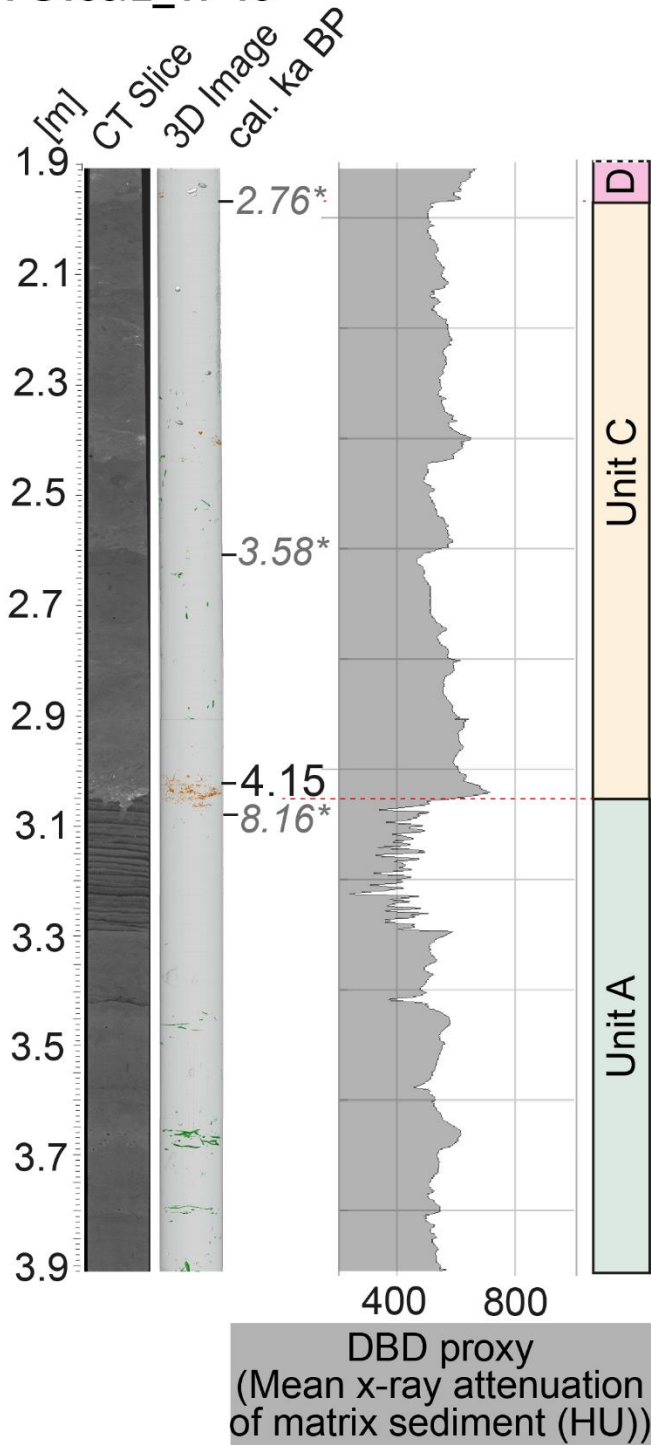


Fig. C.4: CT Scan Slice of PS133/2\_17-13 with density values and interpreted Units, as well as calibrated radiocarbon ages along the core. Note that the Sections were chosen based on their contained assumed hiatuses and Unit contacts.

**3D Image Components**

- Matrix sediment
- Open bioturbation
- Clasts
- Fossil remains

## C3. Tables

Table C.1: Lithological data from the cores GeoB22056-1, GeoB22057-1, GeoB22058-1, Note that FF refers to the fine fraction and includes all grainsizes <63 $\mu$ m, E\* refers to error (wt%) that occurs during grainsize analysis. Positive values mean sample loss, negative values mean sample gain (due to e.g. water). All samples with errors that exceed 10wt% were excluded from interpretation.

Sample details		Grainsize distribution (wt%)						Physical properties (density in (gcm <sup>-3</sup> ))			
Core (GeoB)	Depth (cm)	Gravel	Sand	Mud (FF)	Clay in FF	Silt in FF	E*	Salty WC (wt%)	Corr. Pycnometer. density	DBD	WBD
22056-1	1	0.790	0.559	98.651	NN	NN	5.4	59.710	2.495	0.542	1.346
22056-1	10	0	0.728	99.272	NN	NN	1.3	58.094	2.514	0.572	1.365
22056-1	20	0	0.259	99.741	NN	NN	2.8	60.045	2.493	0.536	1.342
22056-1	30	0	0.348	99.652	NN	NN	4.3	58.070	2.486	0.571	1.362
22056-1	40	0	0.827	99.173	NN	NN	3.0	57.937	2.501	0.574	1.365
22056-1	50	0	0.434	99.566	NN	NN	2.5	58.289	2.513	0.569	1.363
22056-1	60	0	2.785	97.215	38.257	61.743	10.8	58.754	2.517	0.560	1.359
22056-1	70	0	0.329	99.671	NN	NN	2.8	57.739	2.523	0.579	1.370
22056-1	80	0	0.509	99.491	NN	NN	3.1	58.679	2.535	0.563	1.362
22056-1	90	0	0.293	99.707	NN	NN	3.8	57.158	2.527	0.590	1.377
22056-1	100	0.032	0.789	99.180	NN	NN	1.7	53.584	2.550	0.660	1.421
22056-1	110	0.123	0.717	99.160	NN	NN	3.0	55.655	2.537	0.619	1.395
22056-1	120	0	0.364	99.636	NN	NN	4.3	56.081	2.530	0.610	1.390
22056-1	130	0	0.814	99.186	NN	NN	3.9	53.661	2.545	0.658	1.419
22056-1	140	0	0.776	99.224	NN	NN	3.3	52.024	2.553	0.691	1.440
22056-1	150	0	0.372	99.628	NN	NN	4.1	54.563	2.537	0.640	1.408
22056-1	160	0	1.250	98.750	NN	NN	1.4	50.056	2.553	0.731	1.464
22056-1	170	0	1.623	98.377	38.829	61.171	5.5	52.819	2.540	0.674	1.429
22056-1	180	0	0.618	99.382	NN	NN	3.8	55.216	2.535	0.627	1.400
22056-1	190	0	1.330	98.670	NN	NN	1.9	52.892	2.547	0.673	1.429
22056-1	200	0	0.557	99.443	NN	NN	3.4	54.126	2.551	0.649	1.415
22056-1	210	0.057	0.472	99.471	NN	NN	2.8	51.574	2.558	0.700	1.446
22056-1	220	0	0.382	99.618	NN	NN	2.2	50.214	2.555	0.728	1.463
22056-1	230	0	0.512	99.488	NN	NN	1.2	53.483	2.548	0.661	1.422
22056-1	240	0	0.444	99.556	NN	NN	2.3	40.149	2.557	0.958	1.600
22056-1	250	0.036	0.377	99.587	NN	NN	4.0	64.182	2.560	0.468	1.308
22056-1	260	0.027	0.530	99.442	NN	NN	3.4	52.502	2.570	0.683	1.437
22056-1	270	0	2.032	97.968	41.778	58.222	4.9	54.869	2.561	0.635	1.408
22056-1	280	0.044	0.390	99.566	NN	NN	2.8	63.693	2.564	0.477	1.313
22056-1	290	0	0.512	99.488	NN	NN	2.2	35.944	2.565	1.068	1.668
22056-1	300	0	0.235	99.765	NN	NN	3.9	63.216	2.572	0.485	1.319
22056-1	310	0.097	0.299	99.604	NN	NN	1.6	36.325	2.560	1.057	1.660
22056-1	320	0	0.214	99.786	NN	NN	4.3	54.341	2.556	0.645	1.413
22056-1	330	0.271	0.564	99.165	NN	NN	1.9	49.968	2.573	0.735	1.469
22056-1	340	0.044	0.512	99.444	NN	NN	3.1	50.898	2.578	0.716	1.458
22056-1	350	0	0.252	99.748	NN	NN	3.3	53.714	2.546	0.657	1.419
22056-1	360	0	NN	100.000	NN	NN	3.6	52.137	2.571	0.690	1.441
22056-1	370	0	0.287	99.713	NN	NN	3.1	49.992	2.559	0.733	1.466
22056-1	380	0	NN	100.000	42.093	57.907	7.0	50.701	2.564	0.719	1.458
22056-1	390	0	0.794	99.206	40.159	59.841	5.4	53.504	2.571	0.663	1.425
22056-1	400	0	0.907	99.093	41.358	58.642	5.1	51.730	2.558	0.697	1.444
22056-1	410	0	0.914	99.086	39.049	60.951	5.4	53.026	2.551	0.671	1.428



Appendix C for Chapter 7

Core (GeoB)	Depth (cm)	Gravel	Sand	Mud (FF)	Clay in FF	Silt in FF	E*	Salty WC (wt%)	Corr. Pycno-meter. density	DBD	WBD
22056-1	420	0	0.834	99.166	41.107	58.893	4.8	51.746	2.551	0.696	1.443
22056-1	431	0	0.460	99.540	44.299	55.701	5.5	53.009	2.558	0.671	1.429
22056-1	440	0	0.494	99.506	37.729	62.271	16.0	54.716	2.541	0.637	1.407
22056-1	450	1.417	0.626	97.957	NN	NN	3.1	53.819	2.550	0.655	1.418
22056-1	460	0	0.293	99.707	NN	NN	3.7	53.671	2.571	0.659	1.423
22056-1	470	0	0.343	99.657	45.747	54.253	6.9	53.723	2.551	0.657	1.420
22056-1	480.5	0	0.434	99.566	43.566	56.434	5.2	52.120	2.553	0.689	1.439
22056-1	490	0	0.773	99.227	35.939	64.061	16.1	51.827	2.572	0.696	1.445
22056-1	500	0.366	0.471	99.162	43.962	56.038	4.8	51.994	2.558	0.692	1.441
22056-1	510	0	0.436	99.564	NN	NN	2.6	51.814	2.560	0.696	1.444
22056-1	520	0.188	0.632	99.180	NN	NN	3.3	48.824	2.583	0.760	1.485
22056-1	530	0	0.577	99.423	45.929	54.071	-4.7	50.201	2.554	0.728	1.463
22056-1	540	0	NN	NN	NN	NN	4.3	51.416	2.568	0.704	1.450
22056-1	550	0.077	0.954	98.969	NN	NN	1.3	49.944	2.559	0.734	1.467
22056-1	560	0	0.743	99.257	37.312	62.688	15.7	54.123	2.528	0.648	1.411
22056-1	570	0	0.369	99.631	NN	NN	4.5	52.861	2.545	0.674	1.429
22056-1	580	0	0.339	99.661	NN	NN	2.3	52.455	2.562	0.683	1.436
22056-1	590	0	1.667	98.333	37.935	62.065	6.2	49.475	2.571	0.745	1.475
22056-1	600	0	1.037	98.963	39.124	60.876	5.0	50.222	2.559	0.728	1.463
22056-1	605	0	1.447	98.553	42.851	57.149	6.3	52.754	2.556	0.676	1.432
22056-1	610	0	1.143	98.857	42.624	57.376	6.2	52.255	2.542	0.685	1.436
22056-1	615	0	1.813	98.187	42.481	57.519	5.2	51.316	2.544	0.705	1.447
22056-1	620	0	1.624	98.376	41.136	58.864	6.2	49.307	2.564	0.748	1.476
22056-1	625	0	0.786	99.214	43.810	56.190	5.4	50.217	2.554	0.728	1.462
22056-1	630	0	2.102	97.898	39.544	60.456	5.5	49.449	2.555	0.744	1.472
22056-1	635	0	1.623	98.377	39.937	60.063	4.0	52.236	2.559	0.687	1.438
22056-1	640	0	0.798	99.202	44.440	55.560	5.7	52.903	2.556	0.673	1.430
22056-1	645	0	2.292	97.708	40.408	59.592	6.0	46.714	2.582	0.806	1.513
22056-1	650	0	4.986	95.014	37.492	62.508	5.6	41.663	2.612	0.928	1.590
22056-1	655	0	6.522	93.478	35.240	64.760	4.8	24.816	2.709	1.449	1.927
22056-1	659	0	26.987	73.013	9.579	90.421	1.4	22.943	2.730	1.525	1.979
22056-1	662	0	47.409	52.591	1.402	98.598	2.9	23.020	2.721	1.519	1.973
22056-1	666	0	26.517	73.483	9.816	90.184	3.0	50.161	2.541	0.728	1.461
22056-1	670	0	3.024	96.976	32.511	67.489	6.0	48.245	2.557	0.770	1.488
22056-1	675	NN	NN	NN	NN	NN	NN	51.983	2.530	0.690	1.437
22056-1	680	0.134	1.696	98.170	59.357	38.813	-5.6	55.346	2.544	0.625	1.400
22056-1	685	0	1.066	98.934	NN	NN	22.6	42.360	2.548	0.903	1.566
22056-1	690	0.033	1.626	98.341	63.755	34.586	-19.5	69.664	2.515	0.380	1.252
22056-1	695	0	0.388	99.612	NN	NN	7.0	19.124	2.539	1.602	1.981
22056-1	700	0	1.742	98.258	62.582	35.676	2.2	52.882	2.521	0.671	1.425
22056-1	705	0	0.201	99.799	NN	NN	2.7	52.750	2.507	0.673	1.424
22057-1	1	0	0.179	99.821	NN	NN	6.8	61.981	2.477	0.502	1.321
22057-1	10	0	0.225	99.775	NN	NN	3.6	66.225	2.479	0.432	1.280
22057-1	20	0	2.649	97.351	40.691	59.309	8.0	58.474	2.518	0.565	1.362
22057-1	30	0	0.758	99.242	NN	NN	4.8	58.973	2.506	0.556	1.355
22057-1	40	0	0.168	99.832	NN	NN	5.0	57.123	2.525	0.591	1.377
22057-1	50	0	0.221	99.779	NN	NN	5.4	61.884	2.523	0.506	1.327

Appendix C for Chapter 7

Core (GeoB)	Depth (cm)	Gravel	Sand	Mud (FF)	Clay in FF	Silt in FF	E*	Salty WC (wt%)	Corr. Pycno-meter. density	DBD	WBD
22057-1	60	0	0.684	99.316	NN	NN	4.8	56.203	2.525	0.608	1.387
22057-1	70	0	0.520	99.480	NN	NN	3.4	54.605	2.540	0.639	1.408
22057-1	80	0	0.479	99.521	NN	NN	4.3	54.441	2.533	0.642	1.408
22057-1	90	0	0.541	99.459	NN	NN	3.5	54.195	2.550	0.648	1.414
22057-1	100	0	0.946	99.054	NN	NN	3.2	55.292	2.561	0.627	1.403
22057-1	110	0	0.768	99.232	NN	NN	3.6	54.049	2.562	0.651	1.417
22057-1	120	0	2.115	97.885	41.735	58.265	5.3	52.998	2.562	0.672	1.430
22057-1	130	0	0.696	99.304	NN	NN	3.0	50.356	2.583	0.728	1.465
22057-1	140	0	0.157	99.843	NN	NN	4.5	55.911	2.576	0.616	1.398
22057-1	150	0	0.269	99.731	NN	NN	4.3	59.431	2.540	0.549	1.354
22057-1	160	0.180	0.370	99.450	NN	NN	3.5	54.343	2.562	0.646	1.414
22057-1	170	0	0.349	99.651	NN	NN	2.8	51.584	2.572	0.701	1.448
22057-1	180	0	0.525	99.475	NN	NN	3.8	53.261	2.547	0.666	1.424
22057-1	190	0	0.854	99.146	NN	NN	3.1	52.853	2.567	0.675	1.432
22057-1	200	0	0.209	99.791	NN	NN	4.1	56.437	2.536	0.604	1.386
22057-1	210	0	0.429	99.571	NN	NN	3.4	55.139	2.572	0.631	1.406
22057-1	220	0	1.662	98.338	44.045	55.955	7.6	56.257	2.561	0.609	1.392
22057-1	230	0	0.622	99.378	NN	NN	3.7	55.156	2.556	0.629	1.404
22057-1	240	0	0.286	99.714	NN	NN	4.0	56.038	2.563	0.613	1.395
22057-1	250	0	0.319	99.681	NN	NN	3.9	52.762	2.562	0.677	1.432
22057-1	260	0	0.832	99.168	NN	NN	3.8	52.901	2.554	0.673	1.430
22057-1	270	0.128	1.464	98.408	NN	NN	3.0	49.906	2.573	0.736	1.469
22057-1	280	0	0.397	99.603	NN	NN	3.0	51.578	2.552	0.700	1.445
22057-1	290	0	0.292	99.708	NN	NN	2.6	53.457	2.558	0.663	1.424
22057-1	300	0	0.591	99.409	NN	NN	3.5	53.206	2.555	0.667	1.426
22057-1	310	0.764	0.355	98.882	NN	NN	3.6	54.870	2.554	0.635	1.407
22057-1	320	0	2.331	97.669	35.648	64.352	12.7	53.792	2.547	0.655	1.418
22057-1	330	0	3.421	96.579	36.237	63.763	5.3	59.070	2.570	0.557	1.362
22057-1	340	0	2.285	97.715	43.352	56.648	6.7	56.225	2.553	0.609	1.391
22057-1	350	0	3.264	96.736	31.742	68.258	14.4	53.201	2.557	0.668	1.427
22057-1	360	0	2.028	97.972	39.994	60.006	5.7	52.280	2.561	0.686	1.438
22057-1	370	0	3.009	96.991	34.467	65.533	10.1	52.388	2.558	0.684	1.436
22057-1	380	0	2.720	97.280	35.633	64.367	5.5	50.036	2.551	0.732	1.464
22057-1	390	0.562	6.714	92.724	34.289	65.711	15.5	49.409	2.561	0.746	1.474
22057-1	400	0.339	4.778	94.883	31.465	68.535	7.2	51.757	2.550	0.696	1.443
22057-1	410	0.037	4.617	95.346	33.996	66.004	5.8	49.787	2.543	0.736	1.466
22057-1	420	0.044	1.239	98.717	NN	NN	2.9	53.187	2.530	0.666	1.423
22057-1	430	0.320	5.471	94.209	36.454	63.546	6.9	51.589	2.548	0.699	1.445
22057-1	440	0.358	12.28	87.367	28.067	71.933	6.3	44.314	2.591	0.862	1.547
22057-1	450	0	3.420	96.580	38.348	61.652	6.7	53.839	2.536	0.654	1.416
22057-1	460	0	4.000	96.000	38.814	61.186	7.0	52.290	2.546	0.685	1.436
22057-1	470	0	4.839	95.161	37.146	62.854	5.7	48.786	2.549	0.758	1.480
22057-1	480	0.961	2.597	96.442	NN	NN	2.6	48.805	2.578	0.760	1.484
22057-1	490	0	0.349	99.651	NN	NN	3.0	53.969	2.513	0.649	1.411
22057-1	500	0	2.083	97.917	40.632	59.368	7.8	53.942	2.516	0.650	1.412
22057-1	510	0	2.738	97.262	40.348	59.652	6.3	50.743	2.543	0.716	1.454
22057-1	520	0	6.008	93.992	36.040	63.960	6.4	48.733	2.559	0.760	1.482
22057-1	530	1.571	4.194	94.235	33.804	66.196	6.2	49.521	2.564	0.743	1.473
22057-1	540	0	1.758	98.242	39.526	60.474	5.9	51.037	2.550	0.711	1.452
22057-1	550	0	2.617	97.383	34.182	65.818	6.0	48.564	2.560	0.763	1.484

Appendix C for Chapter 7

Core (GeoB)	Depth (cm)	Gravel	Sand	Mud (FF)	Clay in FF	Silt in FF	E*	Salty WC (wt%)	Corr. Pycnometer. density	DBD	WBD
22057-1	560	0	2.880	97.120	39.661	60.339	5.8	52.846	2.566	0.675	1.432
22057-1	570	0	1.898	98.102	35.504	64.496	4.9	50.163	2.558	0.729	1.464
22057-1	580	0	1.055	98.945	41.027	58.973	5.7	49.474	2.576	0.745	1.475
22057-1	590	0	0.870	99.130	45.927	54.073	-1.4	50.162	2.543	0.728	1.461
22057-1	600	0	1.209	98.791	40.501	59.499	7.2	53.436	2.551	0.663	1.423
22057-1	610	0.133	2.765	97.101	32.632	67.368	5.6	48.590	2.568	0.764	1.485
22057-1	620	0	1.563	98.437	34.027	65.973	7.2	50.020	2.541	0.731	1.463
22057-1	630	0.133	1.596	98.271	40.019	59.981	6.0	50.142	2.543	0.729	1.461
22057-1	640	0	1.566	98.434	42.396	57.604	0.0	52.137	2.553	0.689	1.439
22057-1	650	0	0.888	99.112	43.087	56.913	7.5	48.524	2.556	0.764	1.484
22057-1	660	0.165	1.373	98.463	NN	NN	2.9	52.090	2.536	0.688	1.436
22057-1	670	0	2.067	97.933	35.744	64.256	5.8	46.960	2.571	0.799	1.507
22057-1	680	0	1.216	98.784	NN	NN	2.5	46.131	2.551	0.816	1.514
22057-1	690	0	3.066	96.934	31.751	68.249	10.0	50.520	2.550	0.721	1.458
22057-1	700	0.074	0.812	99.113	NN	NN	3.7	51.457	2.554	0.702	1.447
22057-1	710	0	1.068	98.932	48.633	51.367	-11.0	51.840	2.537	0.693	1.440
22057-1	720	1.039	1.206	97.755	NN	NN	3.5	49.189	2.559	0.750	1.476
22057-1	730	0	1.063	98.937	40.444	59.556	6.5	53.958	2.541	0.652	1.415
22057-1	740	0	0.368	99.632	NN	NN	3.1	51.000	2.551	0.712	1.452
22057-1	750	0	0.786	99.214	42.067	57.933	8.2	52.407	2.543	0.682	1.434
22057-1	760	0.092	1.099	98.809	NN	NN	2.6	47.014	2.580	0.799	1.508
22057-1	770	0	1.206	98.794	40.411	59.589	4.0	47.970	2.564	0.777	1.493
22057-1	780	0	0.322	99.678	NN	NN	3.8	50.942	2.543	0.712	1.452
22057-1	790	0	0.821	99.179	43.559	56.441	7.8	49.776	2.577	0.739	1.472
22057-1	800	0	0.946	99.054	NN	NN	2.4	49.061	2.568	0.754	1.479
22057-1	810	0	0.571	99.429	42.739	57.261	6.8	52.054	2.541	0.689	1.438
22057-1	820	0	0.657	99.343	NN	NN	3.4	48.276	2.574	0.771	1.490
22057-1	830	0	1.541	98.459	43.119	56.881	2.2	50.320	2.565	0.727	1.463
22057-1	840	0.135	1.833	98.032	NN	NN	3.4	47.326	2.588	0.793	1.506
22057-1	850	0.131	0.612	99.257	47.587	52.413	6.3	50.606	2.599	0.724	1.465
22057-1	860	0	0.500	99.500	NN	NN	3.2	44.962	2.586	0.846	1.537
22057-1	870	0.081	0.811	99.108	NN	NN	2.7	48.157	2.568	0.773	1.491
22058-1	0.5	0	0.319	99.681	NN	NN	7.1	64.586	2.448	0.458	1.292
22058-1	10	0	0.542	99.458	NN	NN	6.7	62.633	2.469	0.491	1.313
22058-1	20	0	0.283	99.717	NN	NN	10.4	62.533	2.463	0.492	1.314
22058-1	30	0	0.502	99.498	NN	NN	10.6	59.828	2.473	0.539	1.342
22058-1	40.5	0	0.225	99.775	NN	NN	5.4	56.508	2.537	0.603	1.386
22058-1	50	0.051	0.826	99.123	NN	NN	4.5	54.515	2.534	0.640	1.408
22058-1	60	0	3.181	96.819	36.778	63.222	6.9	53.072	2.526	0.668	1.423
22058-1	70	0	0.321	99.679	NN	NN	4.8	55.847	2.519	0.614	1.391
22058-1	80	0	0.574	99.426	NN	NN	5.8	58.892	2.504	0.557	1.356
22058-1	90	0.175	2.154	97.671	NN	NN	4.7	52.336	2.536	0.683	1.434
22058-1	100	0	0.806	99.194	NN	NN	3.6	56.077	2.557	0.612	1.393
22058-1	110	0.187	1.118	98.695	NN	NN	4.9	57.718	2.513	0.579	1.369
22058-1	120	0	0.892	99.108	NN	NN	5.1	58.013	2.497	0.573	1.364
22058-1	130	0	0.488	99.512	NN	NN	5.4	58.331	2.492	0.567	1.360
22058-1	140	0	0.359	99.641	NN	NN	4.4	55.046	2.542	0.631	1.403
22058-1	150	0.063	0.603	99.334	NN	NN	4.4	56.195	2.543	0.609	1.390
22058-1	160	0	1.632	98.368	39.921	60.079	7.4	56.316	2.551	0.607	1.390

Appendix C for Chapter 7

Core (GeoB)	Depth (cm)	Gravel	Sand	Mud (FF)	Clay in FF	Silt in FF	E*	Salty WC (wt%)	Corr. Pycno-meter. density	DBD	WBD
22058-1	170	0.094	0.953	98.953	NN	NN	4.0	52.344	2.559	0.685	1.437
22058-1	180	0	0.955	99.045	NN	NN	4.2	52.193	2.556	0.688	1.438
22058-1	190	0	1.648	98.352	NN	NN	6.9	55.249	2.571	0.629	1.405
22058-1	200	0	0.502	99.498	NN	NN	4.4	56.375	2.543	0.606	1.388
22058-1	210	0.022	0.820	99.159	NN	NN	4.3	55.532	2.536	0.621	1.396
22058-1	220	0	0.389	99.611	NN	NN	5.0	56.415	2.541	0.605	1.387
22058-1	230	0	1.864	98.136	NN	NN	4.4	52.822	2.548	0.674	1.430
22058-1	240	0	0.951	99.049	NN	NN	4.4	52.810	2.534	0.674	1.428
22058-1	250.5	0	0.606	99.394	NN	NN	5.1	59.184	2.519	0.553	1.354
22058-1	260	0	1.660	98.340	44.970	55.030	0.4	55.723	2.523	0.617	1.393
22058-1	270	0	1.369	98.631	NN	NN	4.2	52.913	2.539	0.672	1.427
22058-1	280	0	0.635	99.365	NN	NN	4.6	57.248	2.525	0.588	1.376
22058-1	290	0	0.442	99.558	NN	NN	4.4	56.833	2.527	0.596	1.381
22058-1	300	0.006	0.731	99.264	NN	NN	4.8	57.337	2.513	0.586	1.373
22058-1	310	0	2.178	97.822	NN	NN	3.9	53.208	2.549	0.667	1.425
22058-1	320	0	1.110	98.890	NN	NN	4.9	54.490	2.533	0.641	1.408
22058-1	330	0	1.013	98.987	NN	NN	4.8	55.670	2.522	0.618	1.393
22058-1	340	0	0.909	99.091	NN	NN	1.8	52.615	2.526	0.677	1.429
22058-1	350	0	0.951	99.049	NN	NN	5.7	53.393	2.534	0.662	1.421
22058-1	360	0	0.679	99.321	48.004	51.996	1.4	56.893	2.536	0.595	1.381
22058-1	370	0	2.377	97.623	44.074	55.926	-0.4	54.043	2.528	0.649	1.412
22058-1	380	0	4.414	95.586	33.400	66.600	7.4	49.417	2.554	0.745	1.472
22058-1	390	0	3.251	96.749	30.380	69.620	8.0	51.920	2.558	0.693	1.442
22058-1	400	0	6.437	93.563	41.082	58.918	-4.3	50.660	2.543	0.718	1.455
22058-1	410	0.463	19.09	80.449	50.784	49.216	-22.4	40.612	2.621	0.955	1.608
22058-1	420	1.308	8.990	89.702	37.165	62.835	6.7	47.777	2.570	0.781	1.496
22058-1	430	1.124	9.043	89.832	35.770	64.230	1.6	45.247	2.586	0.840	1.533
22058-1	440.5	0	0.749	99.251	43.248	56.752	12.6	70.114	2.480	0.372	1.245
22058-1	450	0	0.835	99.165	44.101	55.899	36.2	56.788	2.506	0.596	1.378
22058-1	460	0	0.609	99.391	44.451	55.549	-1.7	51.105	2.537	0.708	1.449
22058-1	470	0	1.477	98.523	39.956	60.044	9.7	55.065	2.529	0.629	1.401
22058-1	480	0	0.946	99.054	46.187	53.813	8.0	64.077	2.520	0.469	1.305
22058-1	490	0	1.290	98.710	48.045	51.955	1.0	60.115	2.528	0.537	1.346
22058-1	500	0	0.502	99.498	40.779	59.221	7.0	55.606	2.542	0.620	1.396
22058-1	510	0	0.694	99.306	NN	NN	4.1	52.557	2.546	0.680	1.433
22058-1	520	0	0.509	99.491	NN	NN	5.5	55.679	2.534	0.618	1.395
22058-1	530	0	0.784	99.216	45.692	54.308	1.4	56.537	2.535	0.602	1.385
22058-1	540	0	0.661	99.339	NN	NN	5.4	60.399	2.525	0.532	1.342
22058-1	550	0	1.822	98.178	NN	NN	5.1	54.386	2.547	0.644	1.411
22058-1	560	0	1.194	98.806	42.753	57.247	8.9	59.372	2.518	0.549	1.352
22058-1	570	0.215	1.006	98.779	NN	NN	7.2	70.618	2.467	0.364	1.239
22058-1	580	0	0.660	99.340	NN	NN	5.6	59.241	2.513	0.551	1.353
22058-1	590	0	1.529	98.471	45.912	54.088	12.4	61.675	2.527	0.509	1.329
22058-1	600	0	1.613	98.387	NN	NN	6.5	63.689	2.520	0.475	1.308
22058-1	610	0	1.040	98.960	NN	NN	5.9	59.388	2.520	0.549	1.352
22058-1	620	0	0.920	99.080	47.051	52.949	10.6	59.306	2.509	0.550	1.352
22058-1	630	0	0.491	99.509	NN	NN	5.6	59.792	2.511	0.542	1.347
22058-1	640	0	0.355	99.645	46.291	53.709	7.8	57.794	2.538	0.579	1.372

Appendix C for Chapter 7

Core (GeoB)	Depth (cm)	Gravel	Sand	Mud (FF)	Clay in FF	Silt in FF	E*	Salty WC (wt%)	Corr. Pycnometer. density	DBD	WBD
22058-1	650	0	0.931	99.069	52.827	47.173	1.3	62.463	2.529	0.496	1.322
22058-1	660	0	0.467	99.533	61.337	38.663	1.6	57.865	2.508	0.576	1.367
22058-1	670	0	0.898	99.102	53.028	46.972	1.5	63.360	2.499	0.480	1.309
22058-1	680	0	2.825	97.175	56.913	43.087	-0.5	62.420	2.530	0.497	1.322
22058-1	690	0	0.558	99.442	52.826	47.174	1.8	62.266	2.528	0.499	1.323
22058-1	700	0	0.546	99.454	50.050	49.950	1.6	59.118	2.520	0.554	1.355
22058-1	710	0	0.534	99.466	50.424	49.576	1.5	57.382	2.513	0.585	1.373
22058-1	720	0	1.317	98.683	55.148	44.852	1.0	62.863	2.489	0.488	1.313
22058-1	730	0	1.070	98.930	51.120	48.880	1.3	63.657	2.480	0.474	1.304
22058-1	740	0	0.538	99.462	53.298	46.702	1.6	57.906	2.516	0.576	1.368
22058-1	750	0	1.549	98.451	45.106	54.894	10.6	58.343	2.509	0.567	1.362
22058-1	760	0	0.635	99.365	58.465	41.535	1.8	66.347	2.471	0.430	1.278
22058-1	770	0	1.054	98.946	54.684	45.316	1.5	63.317	2.492	0.480	1.309
22058-1	780	0	0.487	99.513	52.592	47.408	1.7	68.528	2.457	0.396	1.257
22058-1	790	0	0.586	99.414	55.226	44.774	1.7	60.639	2.495	0.526	1.336
22058-1	800	0	0.620	99.380	56.844	43.156	1.4	59.031	2.511	0.555	1.355
22058-1	810	0	1.001	98.999	49.860	50.140	1.0	55.287	2.526	0.625	1.398
22058-1	820	0	1.155	98.845	54.129	45.871	1.4	54.414	2.531	0.642	1.409
22058-1	830	0.337	0.650	99.013	50.353	49.647	1.4	66.059	2.479	0.435	1.281
22058-1	840	0	1.221	98.779	42.984	57.016	7.8	64.514	2.496	0.461	1.298
22058-1	850	0	0.741	99.259	52.545	47.455	1.4	55.740	2.508	0.615	1.390
22058-1	860	0	0.429	99.571	62.825	37.175	1.7	57.853	2.520	0.577	1.369
22058-1	870	0	0.802	99.198	47.710	52.290	9.3	65.410	2.487	0.446	1.288
22058-1	880	0	1.622	98.378	51.499	48.501	0.6	60.013	2.513	0.538	1.345
22058-1	890	0	0.876	99.124	52.822	47.178	1.1	52.858	2.541	0.673	1.428
22058-1	900	0	0.687	99.313	51.603	48.397	1.5	54.665	2.540	0.638	1.407
22058-1	910	0	0.448	99.552	61.285	38.715	1.7	55.445	2.532	0.622	1.397
22058-1	920	0	0.855	99.145	50.292	49.708	14.4	53.593	2.547	0.659	1.420
22058-1	930	0	1.162	98.838	50.968	49.032	1.1	57.563	2.521	0.582	1.372

## Appendix C for Chapter 7

Table C.2: Chemical Properties for GeoB22056-1, GeoB22057-1, GeoB22058-1, featuring Total carbon, Total organic carbon and Carbonate

Core (GeoB)	Depth (cm)	TOC (wt%)	TOC(wt%)	Carbonate (wt%)	Core (GeoB)	Depth (cm)	TOC (wt%)	TOC(wt%)	Carbonate (wt%)
22056-1	1	1.0688	0.8691	1.6641	22057-1	554	0.7341	0.6802	0.4490
22056-1	10	0.8557	0.8098	0.3826	22057-1	560	0.7573	0.6658	0.7630
22056-1	19	0.8392	0.7684	0.5899	22057-1	570	0.6308	0.6196	0.0931
22056-1	29	0.8828	0.8226	0.5024	22057-1	579	0.5928	0.5687	0.2010
22056-1	40	0.8326	NN	NN	22057-1	580	0.8000	0.7040	0.8000
22056-1	54	0.7776	0.6993	0.6519	22057-1	590	0.6897	0.6280	0.5138
22056-1	60	0.8883	0.8337	0.4548	22057-1	600	0.8199	0.6917	1.0688
22056-1	70	0.9121	0.8108	0.8447	22057-1	604	0.7095	0.6649	0.3712
22056-1	84	0.7611	0.6679	0.7763	22057-1	610	0.6987	0.6452	0.4456
22056-1	99	0.7421	0.6836	0.4877	22057-1	620	0.8409	0.7541	0.7233
22056-1	110	0.9457	0.7667	1.4912	22057-1	630	0.7224	0.6809	0.3458
22056-1	119	0.6688	0.6107	0.4842	22057-1	640	0.9334	0.7181	1.7935
22056-1	129	0.7460	0.6973	0.4059	22057-1	650	0.8965	0.6344	2.1841
22056-1	140	0.5766	0.6938	-0.9767	22057-1	654	0.8359	0.7918	0.3674
22056-1	154	0.6858	0.6532	0.2713	22057-1	660	0.9234	0.8411	0.6863
22056-1	170	0.8054	0.7532	0.4351	22057-1	670	0.8177	0.7724	0.3780
22056-1	179	0.7267	0.6855	0.3433	22057-1	680	0.8092	0.7191	0.7501
22056-1	190	0.7503	0.7197	0.2555	22057-1	690	0.6986	0.6063	0.7687
22056-1	204	0.6854	0.6365	0.4081	22057-1	700	1.0746	0.7227	2.9321
22056-1	210	0.7254	0.6955	0.2489	22057-1	704	0.8281	0.7325	0.7966
22056-1	229	0.6055	0.5639	0.3465	22057-1	710	0.9848	0.6963	2.4043
22056-1	230	0.6622	0.6051	0.4754	22057-1	720	0.8331	0.7302	0.8573
22056-1	240	0.6674	0.6834	-0.1333	22057-1	730	0.7124	0.6389	0.6125
22056-1	255	0.6604	0.5946	0.5481	22057-1	740	0.8329	0.7654	0.5619
22056-1	270	0.7580	0.7120	0.3833	22057-1	750	0.7117	0.5972	0.9540
22056-1	280	0.6738	0.6187	0.4591	22057-1	754	0.8209	0.7763	0.3716
22056-1	290	0.7666	0.7078	0.4897	22057-1	760	0.8015	0.6822	0.9939
22056-1	305	0.7127	0.6439	0.5732	22057-1	770	0.6856	0.6185	0.5586
22056-1	321	0.6906	0.6231	0.5627	22057-1	779	0.6696	0.6514	0.1519
22056-1	331	0.6218	0.5736	0.4012	22057-1	780	0.8630	0.7578	0.8766
22056-1	340	0.6182	0.6633	-0.3757	22057-1	790	0.7400	0.6876	0.4365
22056-1	356	0.7123	0.6446	0.5643	22057-1	800	0.8014	0.6527	1.2389
22056-1	370	0.7392	0.6698	0.5783	22057-1	804	0.7591	0.7083	0.4232
22056-1	381	0.6501	0.6067	0.3619	22057-1	810	0.6715	0.6180	0.4455
22056-1	390	0.7373	0.6798	0.4798	22057-1	820	0.7166	NN	5.9711
22056-1	406	0.7011	0.6393	0.5144	22057-1	829	0.7535	0.7074	0.3838
22056-1	421	0.6814	0.6219	0.4958	22057-1	830	0.6849	0.6218	0.5258
22056-1	431	0.7290	0.6653	0.5303	22057-1	840	0.7733	0.6823	0.7582
22056-1	456	0.6932	0.6346	0.4881	22057-1	850	0.6383	0.5279	0.9198
22056-1	470	0.8110	0.7815	0.2463	22057-1	854	0.6576	0.5969	0.5056
22056-1	481	0.7380	0.6789	0.4927	22057-1	860	0.7780	0.6480	1.0834
22056-1	490	0.7980	0.7447	0.4442	22057-1	870	0.5709	0.5008	0.5845
22056-1	506	0.7156	0.6551	0.5041	22057-1	879	0.7729	0.7240	0.4074
22056-1	521	0.6440	0.6050	0.3251	22057-1	880	0.6781	0.5966	0.6789
22056-1	531	0.6858	0.6385	0.3943	22058-1	0.5	1.1810	0.9078	2.2770
22056-1	540	0.7348	0.6847	0.4177	22058-1	10	1.0656	0.9330	1.1051
22056-1	556	0.6782	0.6176	0.5048	22058-1	20	0.9602	0.9174	0.3571
22056-1	570	0.7526	0.6732	0.6612	22058-1	30	0.9074	0.7982	0.9102
22056-1	581	0.6633	0.6131	0.4187	22058-1	39	0.9100	0.8729	0.3092
22056-1	590	0.7000	0.6330	0.5583	22058-1	49	0.8753	0.8335	0.3485
22056-1	606	0.6867	0.6190	0.5640	22058-1	60	0.8383	0.6467	1.5970
22056-1	615	0.7566	0.7176	0.3253	22058-1	70	0.7119	0.6420	0.5824
22056-1	622	0.7932	0.7119	0.6777	22058-1	80	0.8874	0.7158	1.4296
22056-1	625	0.7298	0.7285	0.0106	22058-1	90	0.7696	0.6538	0.9656
22056-1	632	0.6610	0.5921	0.5738	22058-1	99	0.7792	0.7610	0.1513
22056-1	640	0.7639	0.7438	0.1670	22058-1	110	0.7941	0.7466	0.3963
22056-1	650	0.6909	NN	NN	22058-1	124	0.7288	0.6914	0.3113

Appendix C for Chapter 7

Core (GeoB)	Depth (cm)	TOC (wt%)	TOC(wt%)	Carbonate (wt%)	Core (GeoB)	Depth (cm)	TOC (wt%)	TOC(wt%)	Carbonate (wt%)
22056-1	657	-0.0091	-0.0071	-0.0167	22058-1	130	0.8297	0.7513	0.6532
22056-1	659	0.0795	0.0635	0.1336	22058-1	140	1.0679	0.8638	1.7003
22056-1	670	0.7744	0.7313	0.3595	22058-1	150	0.6759	0.5998	0.6342
22056-1	682	0.7871	0.7164	0.5889	22058-1	160	0.8221	0.7331	0.7418
22056-1	690	0.8753	0.8479	0.2289	22058-1	170	0.6845	0.6333	0.4265
22056-1	700	0.9124	0.8850	0.2284	22058-1	175	0.6357	0.6087	0.2252
22056-1	707	0.8660	0.7845	0.6787	22058-1	190	0.6117	0.5715	0.3348
22056-1	722	0.9140	0.8620	0.4331	22058-1	200	0.7338	0.6865	0.3939
22057-1	1	1.1260	0.8997	1.8857	22058-1	210	0.6873	0.6684	0.1575
22057-1	10	1.0040	0.8676	1.1373	22058-1	225	0.7526	0.7191	0.2794
22057-1	20	0.9773	0.8115	1.3812	22058-1	230	0.7161	0.6972	0.1574
22057-1	26	0.8572	0.8082	0.4085	22058-1	240	0.7593	0.6694	0.7497
22057-1	30	0.8485	0.7930	0.4625	22058-1	250	0.6490	0.5865	0.5206
22057-1	40	0.9624	0.8158	1.2217	22058-1	260	0.7848	0.6388	1.2167
22057-1	50	0.8500	0.7739	0.6338	22058-1	270	0.6608	0.5935	0.5615
22057-1	52	0.8384	0.7926	0.3824	22058-1	275	0.7468	0.6985	0.4027
22057-1	60	0.8765	0.7172	1.3281	22058-1	290	0.6672	0.5530	0.9519
22057-1	70	0.7611	0.6905	0.5888	22058-1	300	0.7034	0.6625	0.3410
22057-1	76	0.5978	0.5590	0.3231	22058-1	310	0.6627	0.5564	0.8864
22057-1	80	0.8457	0.6986	1.2258	22058-1	320	0.5617	0.5296	0.2680
22057-1	90	0.7290	0.6940	0.2919	22058-1	330	0.6202	0.5794	0.3397
22057-1	100	0.7418	0.6343	0.8955	22058-1	340	0.6379	0.5644	0.6129
22057-1	101	0.6754	0.6382	0.3106	22058-1	350	0.6105	0.5783	0.2689
22057-1	110	0.6319	0.5958	0.3010	22058-1	360	0.6294	0.5784	0.4253
22057-1	120	0.7637	0.6416	1.0177	22058-1	370	0.6781	0.5858	0.7689
22057-1	126	0.6676	0.6284	0.3263	22058-1	380	0.6100	0.5977	0.1026
22057-1	130	0.6448	0.6028	0.3496	22058-1	390	0.5927	0.5099	0.6900
22057-1	140	1.3435	0.6955	5.3994	22058-1	400	0.5977	0.5300	0.5642
22057-1	150	1.1566	0.6027	4.6158	22058-1	410	0.5966	0.5574	0.3267
22057-1	151	0.7427	0.6909	0.4314	22058-1	420	0.4703	0.0457	3.5386
22057-1	160	0.9609	0.5522	3.4058	22058-1	430	0.6975	0.5390	1.3213
22057-1	170	0.8361	0.6336	1.6878	22058-1	440	0.5571	0.4537	0.8612
22057-1	179	0.8318	0.7163	0.9628	22058-1	450	0.6274	0.5722	0.4599
22057-1	180	0.7963	0.6368	1.3295	22058-1	460	0.6212	0.5115	0.9142
22057-1	190	0.6669	0.6294	0.3125	22058-1	470	0.6251	0.5257	0.8287
22057-1	200	0.8112	0.6596	1.2628	22058-1	480	0.5401	0.4809	0.4927
22057-1	204	0.7125	0.6638	0.4059	22058-1	490	0.6143	0.5953	0.1582
22057-1	210	0.6921	0.6779	0.1182	22058-1	500	0.5781	0.5297	0.4035
22057-1	220	0.8221	0.6954	1.0551	22058-1	510	0.5567	0.5000	0.4727
22057-1	229	0.7038	0.6726	0.2598	22058-1	520	0.5327	0.4332	0.8291
22057-1	230	0.6974	0.6639	0.2791	22058-1	530	0.5601	0.5201	0.3333
22057-1	240	0.8401	0.7096	1.0877	22058-1	540	0.5521	0.4988	0.4445
22057-1	250	0.7126	0.6381	0.6201	22058-1	550	0.4955	0.4616	0.2824
22057-1	254	0.6941	0.6493	0.3739	22058-1	560	0.7275	0.4455	2.3497
22057-1	260	0.7453	0.5770	1.4027	22058-1	570	0.8185	0.7368	0.6809
22057-1	270	0.6188	0.5355	0.6942	22058-1	580	0.6958	0.6563	0.3296
22057-1	279	0.7679	0.7329	0.2917	22058-1	590	0.9861	0.6983	2.3984
22057-1	280	0.7900	0.6512	1.1562	22058-1	600	0.8809	0.5782	2.5224
22057-1	290	0.6620	0.6338	0.2346	22058-1	610	0.8561	0.6893	1.3902
22057-1	300	0.8023	0.6122	1.5837	22058-1	620	0.7475	0.5320	1.7958
22057-1	304	0.6882	0.6607	0.2294	22058-1	630	0.7908	0.6838	0.8921
22057-1	310	0.6854	0.5119	1.4458	22058-1	640	0.6774	0.6038	0.6136
22057-1	320	0.6444	0.6251	0.1604	22058-1	651	0.6709	0.5906	0.6691
22057-1	329	0.5800	0.5722	0.0646	22058-1	660	0.6377	0.5994	0.3192
22057-1	330	0.6216	0.5839	0.3141	22058-1	670	0.7664	0.7209	0.3791
22057-1	340	0.5316	0.4666	0.5416	22058-1	680	0.6560	0.6088	0.3929
22057-1	350	0.6627	0.6172	0.3794	22058-1	690	0.8440	0.7004	1.1968
22057-1	354	0.5880	0.5525	0.2956	22058-1	700	0.7238	0.5920	1.0986
22057-1	360	0.5865	0.5123	0.6182	22058-1	710	0.8642	0.7227	1.1799
22057-1	370	0.5578	0.5184	0.3283	22058-1	720	0.7453	0.6216	1.0306

Appendix C for Chapter 7

Core (GeoB)	Depth (cm)	TOC (wt%)	TOC(wt%)	Carbonate (wt%)	Core (GeoB)	Depth (cm)	TOC (wt%)	TOC(wt%)	Carbonate (wt%)
22057-1	380	0.5592	0.5064	0.4401	22058-1	726	0.7582	0.6847	0.6121
22057-1	390	0.5799	0.5273	0.4382	22058-1	740	0.7637	0.6291	1.1221
22057-1	400	0.7458	0.6333	0.9380	22058-1	751	0.8144	0.6335	1.5074
22057-1	404	0.6356	0.6018	0.2810	22058-1	760	0.7191	0.6102	0.9077
22057-1	410	0.6125	0.5665	0.3827	22058-1	770	0.8507	0.8514	-0.0054
22057-1	420	0.6352	0.5937	0.3457	22058-1	780	0.7477	0.6546	0.7753
22057-1	430	0.8163	0.7479	0.5706	22058-1	790	0.8552	0.7471	0.9014
22057-1	440	0.7098	0.6640	0.3813	22058-1	800	0.7500	0.6635	0.7211
22057-1	450	0.7084	0.4522	2.1343	22058-1	810	0.7979	0.6907	0.8934
22057-1	460	0.8740	0.7670	0.8918	22058-1	820	0.6808	0.6012	0.6636
22057-1	470	0.8498	0.7784	0.5948	22058-1	830	0.9739	0.8905	0.6948
22057-1	480	0.7509	0.7141	0.3064	22058-1	840	0.8512	0.7593	0.7653
22057-1	490	0.9788	0.7947	1.5343	22058-1	852	0.8663	0.8139	0.4364
22057-1	500	1.0127	0.8066	1.7174	22058-1	860	0.8299	0.7457	0.7014
22057-1	504	0.9020	0.8360	0.5499	22058-1	870	1.0302	0.9158	0.9536
22057-1	510	0.9027	0.8270	0.6302	22058-1	877	0.9405	0.8564	0.7012
22057-1	520	0.8814	0.8027	0.6558	22058-1	890	1.0683	0.9708	0.8124
22057-1	529	0.7656	0.7278	0.3152	22058-1	902	1.0270	0.9446	0.6862
22057-1	530	0.7668	0.6533	0.9460	22058-1	910	1.0975	1.0228	0.6222
22057-1	540	0.7722	0.6779	0.7860	22058-1	927	0.9992	0.9127	0.7211
22057-1	550	0.6506	0.6030	0.3967	22058-1	941	0.9061	0.8713	0.2901

Table C.3: *bSiO<sub>2</sub>* and biogenic opal content for GeoB22056-1, GeoB22057-1, GeoB22058-1

Kern	Tiefe (cm)	SiO <sub>2</sub> (wt%)	biogenic opal (wt%)
GeoB22056-1	1	21.8	24.22
GeoB22056-1	350	19.57	21.74
GeoB22056-1	705	22.16	24.62
GeoB22057-1	1	18.51	20.56
GeoB22057-1	170	19.51	21.67
GeoB22057-1	290	17.94	19.93
GeoB22057-1	440	15.74	17.48
GeoB22057-1	600	23.01	25.56
GeoB22057-1	830	16.23	18.03
GeoB22058-1	0.5	24.26	26.95
GeoB22058-1	120	22.66	25.17
GeoB22058-1	320	22.83	25.36
GeoB22058-1	410	16.78	18.64
GeoB22058-1	480	29.12	32.35
GeoB22058-1	800	27.65	30.72



## Appendix C for Chapter 7

Table C.4: Conventional radiocarbon ages with IntCal20 calibration results for this study (Reimer et al., 2020), MRA are based on Butzin et al. (2019, 2020). "Mollusc" refers to bivalve and gastropod (remains)

Sample details			Conventional radiocarbon ages					IntCal20 calibration			Lab Code AWI
Core (GeoB)	Depth (cm)	Carb. source	14C/12C (*10-12)	(14C ka BP)	Age error (ka)	MRA (ka)	MRA MAD (ka)	Min (cal ka BP)	Weighted mean (cal ka BP)	Max (cal ka BP)	
22056-1	60	Bryozoa	0.9504 ±0.65%	1.386	±0.059	1.03	<0.014	0.305	0.404	0.505	6164.1.1
22056-1	170	Bryozoa	0.9218 ±0.73%	1.55	±0.064	1.04	<0.014	0.34	0.548	0.651	6165.1.1
22056-1	270	Mollusc	0.9092 ±0.66%	1.72	±0.06	0.92	<0.014	0.652	0.731	0.902	4451.1.1
22056-1	380	Bryozoa	0.8756 ±0.66%	2.05	±0.059	0.93	<0.014	0.925	1.031	1.175	6166.1.1
22056-1	490	Mollusc	0.8618 ±0.70%	2.096	±0.063	0.94	<0.014	0.931	1.073	1.26	4452.1.1
22056-1	530	Mollusc	0.8456 ±0.69%	2.353	±0.062	0.88	<0.014	1.286	1.364	1.515	4453.1.1
22056-1	620	Mollusc	0.8297 ±0.65%	2.502	±0.06	0.89	<0.014	1.361	1.481	1.688	4454.1.1
22056-1	645	Mollusc	0.8268 ±0.65%	2.504	±0.06	0.89	<0.014	1.365	1.483	1.688	4455.1.1
22057-1	20	Mollusc	0.9649 ±0.68%	1.241	±0.061	1.07	<0.014	0	0.15	0.297	6167.1.1
22057-1	192	Mollusc	0.8433 ±0.66%	2.097	±0.062	0.94	<0.014	0.931	1.072	1.259	9972.1.1
22057-1	340	Mollusc	0.8109 ±0.74%	2.6	±0.066	0.85	<0.014	1.524	1.645	1.821	4456.1.1
22057-1	390	Mollusc	0.7605 ±0.74%	3.116	±0.066	0.86	<0.014	2.054	2.238	2.404	4457.1.1
22057-1	430	Mollusc	0.7431 ±0.74%	3.403	±0.066	0.87	<0.014	2.37	2.598	2.755	4458.1.1
22057-1	460	Mollusc	0.6460 ±0.75%	4.443	±0.067	0.85	<0.014	3.699	3.899	4.086	4459.1.1
22057-1	500	Mollusc	0.5966 ±0.78%	5.15	±0.069	0.88	<0.014	4.58	4.814	5.038	4460.1.1
22057-1	590	Mollusc	0.5125 ±1.28%	6.226	±0.108	1.02	<0.014	5.726	5.991	6.274	4461.1.1
22057-1	610	Mollusc	0.5286 ±0.84%	6.076	±0.074	0.93	<0.014	5.664	5.891	6.175	4462.1.1
22057-1	694	Mollusc	0.4644 ±0.67%	7.013	±0.078	0.99	<0.014	6.671	6.874	7.156	9973.1.1
22057-1	750	Mollusc	0.4561 ±0.90%	7.285	±0.079	1.05	<0.014	6.943	7.129	7.318	4463.1.1
22058-1	60	Mollusc	0.9237 ±0.65%	1.608	±0.06	1.04	<0.014	0.511	0.584	0.653	4464.1.1
22058-1	160	Bryozoa	0.8767 ±0.87%	1.938	±0.074	0.93	<0.014	0.739	0.9	1.061	6169.1.1
22058-1	260	Mollusc	0.8128 ±0.74%	2.618	±0.065	0.85	<0.014	1.535	1.658	1.821	6170.1.1
22058-1	380	Bryozoa	0.7759 ±0.70%	2.983	±0.062	0.84	<0.014	1.95	2.143	2.318	6171.1.1
22058-1	430	Benthic Foram	0.4203 ±1.01%	7.879	±0.087	1.01	<0.014	7.575	7.718	7.922	4465.1.1
22058-1	470	Benthic Foram	0.3906 ±1.03%	8.516	±0.09	1.03	<0.014	8.038	8.276	8.427	4466.1.1
22058-1	560	Mollusc	0.3732 ±0.95%	8.95	±0.083	0.94	<0.014	8.601	8.849	9.119	4467.1.1
22058-1	650	Benthic Foram	0.3539 ±1.03%	9.345	±0.09	0.88	<0.014	9.144	9.446	9.658	4468.1.1

Appendix C for Chapter 7

22058-1	690	Mollusc	0.3491 ±1.04%	9.44 1	±0.09	0.81	<0.014	9.468	9.646	9.903	4469. 1.1
Sample details			Conventional radiocarbon ages					IntCal20 calibration			Lab Code
Gravity core	Depth (cm)	Carb. source	14C/12C (*10-12)	(14C ka BP)	Age error (ka)	MRA (ka)	MRA MAD (ka)	Min (cal ka BP)	Weighted mean (cal ka BP)	Max (cal ka BP)	AWI
22058-1	800	Benthic Foram	0.3304 ±1.09%	9.89 6	±0.09	0.86	<0.014	9.898	10.167	10.486	4470. 1.1
PS133/2_17-13	30	Mollusc	0.9327 ±0.60%	1.42 3	±0.056	1.03	<0.014	0.314	0.422	0.518	10471 .1.1
PS133/2_17-13	60.5	Mollusc	0.8424 ±0.63%	2.22 2	±0.059	0.97	<0.014	1.012	1.182	1.294	10472 .1.1
PS133/2_17-13	101	Mollusc	0.8008 ±0.64%	2.62 4	±0.059	0.85	<0.014	1.538	1.66	1.82	10473 .1.1
PS133/2_17-13	183. 5	Mollusc	0.7383 ±0.68%	3.32 3	±0.062	0.84	<0.014	2.365	2.557	2.723	10474 .1.1
PS133/2_17-13	236	Mollusc	0.6834 ±0.69%	3.96 7	±0.063	0.88	<0.014	3.083	3.294	3.447	10475 .1.1
PS133/2_17-13	303. 5	Mollusc	0.6245 ±0.82%	4.65	±0.073	0.89	<0.014	3.927	4.144	4.404	10476 .1.1
PS133/2_17-13	434	Benthic Foram	0.3740 ±0.96%	8.69 6	±0.084	0.97	<0.014	8.367	8.511	8.722	10477 .1.1
PS133/2_17-13	636. 5	Mollusc	0.3762 ±0.93%	8.65 2	±0.082	0.96	<0.014	8.362	8.486	8.636	10478 .1.1
PS133/2_17-13	834. 5	Mollusc	0.3599 ±0.98%	9.09 2	±0.085	0.94	<0.014	8.778	9.119	9.41	10479 .1.2
PS133/2_17-13	885. 5	Fish scale	0.3563 ±0.38%	9.03 8	±0.036	0.94	<0.014	8.787	9.028	9.191	10480 .1.1
Recalibrated radiocarbon age from Graham et al. (2017)											
Sample details			Conventional radiocarbon ages					IntCal20 calibration			Lab Code
Gravity core	Depth (cm)	Carb. source	14C/12C (*10-12)	Age (14C ka BP)	Age error (ka)	MRA (ka)	MRA MAD (ka)	Min (cal ka BP)	Weighted mean (cal ka BP)	Max (cal ka BP)	ETH-
GC666	490	Benthic Foram	-	13.3 7	0.089	1.85	0.768	13.18 4	13.387	13.58	51519 .1
GC666	490	Benthic Foram	-	13.1 05	0.136	1.77	0.77	12.97 2	13.241	13.492	51519 .2

Table C.5: Bchron results with median ages and the respective lower and upper confidence levels.

Core	Depth (cm)	2.5% CL (ka)	Median age (ka)	97.5% CL (ka)
GeoB22056-1	722	1.47	1.62	1.9
GeoB22057-1	404	2.2	2.35	2.5
GeoB22057-1	414	2.28	2.4	2.58
GeoB22057-1	434	2.44	2.62	2.97
GeoB22057-1	446	3.01	3.82	4.09
GeoB22057-1	879	7.09	7.74	10.18
GeoB22058-1	400	2.02	2.25	2.88
GeoB22058-1	412	7.08	7.65	7.86
GeoB22058-1	941	10.02	10.8	12.54
PS133/2_17-13	197	2.57	2.76	3.05
PS133/2_17-13	308	3.32	8.16	8.56
GC666	200	2.26	6.15	9.85

Erklärung

**Versicherung an Eides Statt / *Affirmation in lieu of an oath***

**gem. § 5 Abs. 5 der Promotionsordnung vom 18.06.2018 /  
*according to § 5 (5) of the Doctoral Degree Rules and Regulations of 18 June, 2018***

Ich / I, \_\_\_\_\_  
(Vorname / *First Name*, Name / *Name*, Anschrift / *Address*, ggf. Matr.-Nr. / *student ID no.*, if applicable)

versichere an Eides Statt durch meine Unterschrift, dass ich die vorliegende Dissertation selbständig und ohne fremde Hilfe angefertigt und alle Stellen, die ich wörtlich dem Sinne nach aus Veröffentlichungen entnommen habe, als solche kenntlich gemacht habe, mich auch keiner anderen als der angegebenen Literatur oder sonstiger Hilfsmittel bedient habe und die zu Prüfungszwecken beigelegte elektronische Version (PDF) der Dissertation mit der abgegebenen gedruckten Version identisch ist. / *With my signature I affirm in lieu of an oath that I prepared the submitted dissertation independently and without illicit assistance from third parties, that I appropriately referenced any text or content from other sources, that I used only literature and resources listed in the dissertation, and that the electronic (PDF) and printed versions of the dissertation are identical.*

Ich versichere an Eides Statt, dass ich die vorgenannten Angaben nach bestem Wissen und Gewissen gemacht habe und dass die Angaben der Wahrheit entsprechen und ich nichts verschwiegen habe. / *I affirm in lieu of an oath that the information provided herein to the best of my knowledge is true and complete.*

Die Strafbarkeit einer falschen eidesstattlichen Versicherung ist mir bekannt, namentlich die Strafandrohung gemäß § 156 StGB bis zu drei Jahren Freiheitsstrafe oder Geldstrafe bei vorsätzlicher Begehung der Tat bzw. gemäß § 161 Abs. 1 StGB bis zu einem Jahr Freiheitsstrafe oder Geldstrafe bei fahrlässiger Begehung. / *I am aware that a false affidavit is a criminal offence which is punishable by law in accordance with § 156 of the German Criminal Code (StGB) with up to three years imprisonment or a fine in case of intention, or in accordance with § 161 (1) of the German Criminal Code with up to one year imprisonment or a fine in case of negligence.*

Bremen, . . . .2023

Ort / *Place*, Datum / *Date*

\_\_\_\_\_  
Unterschrift / *Signature*